Abstract of “Quality-Selected Lensing Analysis of Galaxy Clusters in Subaru Telescope Fields” by Ryan J. Michney, Ph.D., Brown University, May 2015.

In recent years, weak gravitational lensing has become an indispensable method for understanding the concentration of matter on the largest scales. Galaxy clusters, the largest virialized structures in the universe, provide a crucial environment in which to examine cosmological evolution. Because most matter is non-luminous, weak lensing provides an opportunity for direct measurement of large scale mass clustering, independent of considerations involving cluster dynamics.

This study takes advantage of the large amount of deep and high quality optical imaging freely available from the Subaru Telescope data archive to perform a semi-blind cluster search across an extraordinarily large field of view, 10.34 deg^2 of the sky, at high source density (utilizing 1.27×10^6 galaxies). Our precise 2D mass reconstruction, spanning five low-extinction Milky Way windows, detects 90 unique cluster candidates above S/N$\geq$3. Of these, 67 possess S/N$\geq$4, and 18 possess S/N$\geq$5. From the fields analyzed, 43 independently confirm prior detections, 6 of these match (but with offsets in the location of the cluster barycenter, while still indicating their existence within error tolerance), and the remaining 47 represent potential new cluster discoveries.

Previous cluster candidates in these regions were uncovered through non-WL techniques, therefore, our analysis represents a significant contrast against other wide-field cluster search methods, and is one of the largest lensing surveys completed to date.

Convergence reconstructions also confirm the detection of SZ & X-ray cluster candidate PLCK G100.2-30.4 in multiple independent waveband data, while failing to measure the more observationally difficult PLCK G18.7+23.6. We estimate the mass of the former, as well as that of clusters Abell 383, Abell 1672, and RXC J1651.1+0459.

The scale of this project necessitated the invention of numerous automated data reduction algorithms and a comprehensive pipeline optimizing the shape information and object detections of deep-field galaxies in available imaging. Most notably, a novel flux-independent identification system for stars was created in order to find ideal stellar objects necessary for accurate PSF circularization. Our techniques allow us to stack and circularize Subaru images to better than <0.5% mean ellipticity without introducing spurious effects.

Quality-Selected Lensing Analysis of Galaxy Clusters in Subaru Telescope Fields

by

Ryan J. Michney

A.B., Dartmouth College, 2006

M.S., Dartmouth College, 2008

Sc.M., Brown University, 2010

A dissertation submitted in partial fulfillment of the
requirements for the Degree of Doctor of Philosophy
in the Department of Physics at Brown University

Providence, Rhode Island

May 2015

This dissertation by Ryan J. Michney is accepted in its present form by the Department of Physics as satisfying the dissertation requirement for the degree of Doctor of Philosophy.

Date ______________ ______________________________
Ian Dell'Antonio, Director

Recommended to the Graduate Council

Date ______________ ______________________________
Ian Dell'Antonio, Reader

Date ______________ ______________________________
Richard Gaitskell, Reader

Date ______________ ______________________________
Gregory Tucker, Reader

Approved by the Graduate Council

Date ______________ ______________________________
Peter M. Weber
Dean of the Graduate School

Vita

Ryan James Michney was born in Providence, Rhode Island in June 1984. He was raised in Bristol, RI, studying at the Gordon and Met schools, and attended Tabor Academy in Marion, MA on the *H. Theodore Gregory Scholarship*, earning citations in AP Physics, Modern Physics, Latin, and the *Cum Laude Society.* He obtained a bachelors degree (A.B.) with *High Honors* in Physics in 2006 from Dartmouth College, double-majoring in Physics and Astronomy. Initially a researcher in the Lynch Rocket Lab, he subsequently developed a theoretical prediction of the anisotropy and properties of the cosmic neutrino background with Professor Robert Caldwell [72, 73]. He spent the summer of 2006 at the Harvard-Smithsonian Center for Astrophysics, modeling the conditions of water megamasers in active galactic nuclei with Dr. Lincoln Greenhill. In the following year he earned an M.S. at Dartmouth, and then began in the Ph.D. program at Brown University. In 2009 he joined the Observational Cosmology and Weak Lensing group under the mentorship of Professor Ian Dell'Antonio. He has served as an observer at both the WIYN 3.5-m and Mayall 4-m telescopes at Kitt Peak National Observatory in Arizona.

Michney was a teaching assistant for eight courses in the Physics Department and a representative for the department to the Graduate Student Council. He received the NASA RI Space Grant and NSF GK-12 STEM Education fellowships, teaching two summer courses and developing two year-long astronomy exhibits at the Roger Williams Park Museum of Natural History, as well as conducting outreach at Ladd Observatory, instructing at Brown Summer High School, and designing and teaching a 4th-grade space science module at Martin Luther King Jr. Elementary in Providence. He was involved with the RI Science Olympiad and the WiSE Athena Science Challenge, competitions encouraging high school students from underrepresented groups to study science. In 2014 he collaborated and performed with the Meridian Project, a multimedia concert/lecture series exploring astrophysics.

Acknowledgements

I must begin by thanking my graduate advisor, Professor Ian Dell'Antonio, for his kindness, encouragement, and expertise throughout my time here at Brown. He has been nothing less than a wellspring of knowledge and enthusiasm about all facets of astrophysics and beyond, and I've consistently struggled to find any topic, academic or otherwise, about which he does not know something. I was truly fortunate to work with him and be the beneficiary of his advice.

My fellow group members, Richard Cook, Van Dao, Paul Huwe, and Jacqueline McCleary, have been essential for their support and our many engaging conversations over the years, as well as undergraduate researchers Kate Alexander, Jesse, and Emmet Golden-Marx. It has been a pleasure to work alongside all of them and share in their insights and friendship.

I would like to thank my committee members, Professors Greg Tucker and Richard Gaitskell for their thoughtful suggestions into the drafting of this dissertation, and helpful comments strengthening this manuscript.

I have had the privilege of participating in many outreach experiences to better my home state of Rhode Island, and I am grateful to Professor Karen Haberströh, Mr. Mike Umbricht, Ms. Rene Gamba, Mr. Peter Neivert, Ms. Juliet Duyster, and to the teachers at Martin Luther King Jr. Elementary who have all been such a pleasure to work with on sharing our mutual passion for science with the general public. I thank Barbara Dailey for her work on behalf on myself and all the graduate students here, as well as Jane Martin and the rest of the department staff for making Brown Physics a cheerful place.

There are countless friends I have made here that have kept me sane and made me a better person, but I would especially like to thank David Malling, Michael Antosh, Andy Blaeser, Jeremy Chapman, John Macaluso, Scott Field, Shawna Hollen-Fischer, Julliette Alimena, Kyle Helson, and the rest of our championship physics softball team, Schrödinger's Bat[1], for making life in Providence a delightful experience. Jennifer Salcido and Christopher Hassan have raised my spirits on so many occasions that I cannot thank them adequately. Anyone who absorbs that many musings from Ryan Michney deserves an award that hasn't been invented yet. I owe them hundreds of tickets to robotic shark movies. They think about everything.

Most importantly, I am eternally grateful to my parents Sheila McLean and James Michney for their unceasing encouragement and love. Their support and wisdom have made me the person I am today, and there is no way that I could have accomplished a fraction of what I have so far without their unabating belief in me. Somehow, throughout my life, they have pushed me without pushing.

I also thank my future wife Andria Tieman for, for reasons I cannot fathom, staying by my side throughout the gauntlet that is graduate school. I love her more than words can express and I count myself lucky for each day I spend with the funniest, most beautiful, most midwestern woman I have ever met.

Lastly, I would like to remember the late Professor Hendrik Gerritsen who invited me to take his Introduction to Astronomy class here at Brown when I was only nine years old. He couldn't have known it at the time, but his willingness to share an infectious love of physics with anyone and everyone had a profound effect on the path of my life.

---

[1] 2009 Mid-level Intramural Champions!

To my parents,

who showed me how to love the search for knowledge

about life, the universe, and everything.

Contents

List of Tables

List of Figures

Chapter 1

Introduction: The State of Cosmology & Galaxy Clusters

"In the beginning the Universe was created.
This has made a lot of people very angry
and been widely regarded as a bad move."
Douglas Adams, *The Restaurant at the End of the Universe*

No field exceeds cosmology in ambition—the goal of which is an understanding of the history, contents and future of the universe as a whole. These are extremely vast and complex issues, but multiple directions of inquiry are finally carving out firmly established truths. "Precision cosmology," once considered an oxymoronic phrase, in addition to pinpointing the age, scale, and contents of the cosmos, now even assists in estimates of quantities in particle physics [2, 24, 51, 65, 103, 115, 116, 120]. Observations probing the origins of the universe are provided by a wider array of sources than ever before—from traditional ground-based observatories, networks of radio antennae, space-based telescopes, orbiting and balloon-bourne experiments, to sensitive particle detectors deep underground. Techniques are now powerful enough to determine much about the initial state and eventual fate of the universe through precise measurements of remnants of the cosmic microwave background [12, 87, 105], the formation of large scale structure [106], and elemental abundances forged in the first minutes of cosmic history [21].

These efforts are converging on a consensus of a homogeneous, isotropic, and spatially flat universe composed mostly of "dark" components, having recently transitioned from matter to dark-energy dominated expansion, which began approximately 13.8 Gyr in the past. The primary contents of this universe are: $<1\%$ radiation; $\sim 5\%$ luminous matter (consisting of everything which interacts via electromagnetism); $\sim 25\%$ dark matter (which is cold, non-relativistic, and likely made up of weakly-interacting particles exerting significant effects only through the gravitational force); and nearly $\sim 70\%$ dark energy, a poorly-understood substance which exerts negative pressure and currently drives the acceleration of the universe's expansion.

This dissertation deals with the intersection of advanced techniques of imaging the distant sky with a form of analysis, weak gravitational lensing (WL), which has only become possible within the last two decades. We explore a wide array of deep-sky imaging, applying weak lensing analysis as a means of revealing and measuring vast conglomerations of matter known as galaxy clusters. Cluster studies, which probe the largest gravitationally collapsed structures in the universe, serve as a significant cosmological test, and WL is increasingly a preferred tool to understand them as light-gathering and large-scale data processing abilities improve. Weak lensing is most often applied to targeted regions already understood to contain galaxy clusters, however, as we show, the staggeringly large amount of imaging which is about to become available to the astronomical community may be employed in a blind manner as a detection technique. We optimize our search to include only the most sensitive data, create a fast, responsive, and high-volume processing pipeline, and employ this robust sample towards detection and mass estimation of intermediate- and low-mass clusters, in large domains of the sky hitherto unstudied using WL.

1.1 Spacetime and Relativistic Cosmology

1.1.1 The Expanding Universe

Although astronomy may be the oldest science, it is only within the last century that we have gained any understanding of the universe outside our own galaxy. The recognition that separate galaxies exist outside our own, isolated by vast gulfs of empty space, rather than as "spiral nebulae," gravitationally bound to the Milky Way, dates to only the 1920s, when observations of Cepheid variables supplied a more accurate distance scale. Edwin Hubble then provided evidence that these newly distant galaxies are part of an expanding universe by demonstrating that they appear to be receding from our own at a rate proportional to our distance from them. Using known spectral lines as a benchmark and the redshift relation

$$z \equiv \frac{\lambda_{\text{observed}}}{\lambda_{\text{emitted}}} - 1 \tag{1.1}$$

and then plotting the redshift velocity, v, against the distance measurements he calculated, d, Hubble proposed the linear relation now known as *Hubble's Law*:

$$v = cz = H_\circ d \tag{1.2}$$

His original measurement of $H_\circ$, the Hubble constant, was nearly 500 km/s/Mpc (we now estimate it to be closer to 70 km/s/Mpc); however, his basic insight was correct—that the contents of the universe appear to move apart from one another as a function of distance. He argued that this recession cannot be a matter of actual galaxy motions, rather it must be apparent to observers at any point in the universe. The mounting evidence of subsequent decades confirmed that space itself is undergoing expansion, having originated from hot, dense, compressed state, billions of years in the past.

1.1.2 General Relativity

Einstein's theory of gravity remains the most satisfying explanation of matter's long-scale attractive force and of the geometry of the universe. First proposed in 1915, the general theory of relativity (GR) is a set of laws deriving from the ideas that: (1) mass and energy are equivalent quantities, and (2) that inertial bodies seek to follow straight paths through a space-time geometry which is curved by the presence of matter and energy.

It is a peculiar and heretofore unexplained fact that the inertial and gravitational masses of a body are equal to one another [96]. A concept known as the *equivalence principle*, this is the insight leading to the observation that acceleration due to gravitational force is functionally indistinguishable from that due to any other form of acceleration. Motion within an inertial frame must, itself, be indistinguishable from free fall in a gravitational potential. The laws of physics must remain the same locally, as they are in all reference frames. Moreover, the formulae of GR must reduce to Newtonian laws in regimes where gravity is weak and motion is non-relativistic. These are the basic

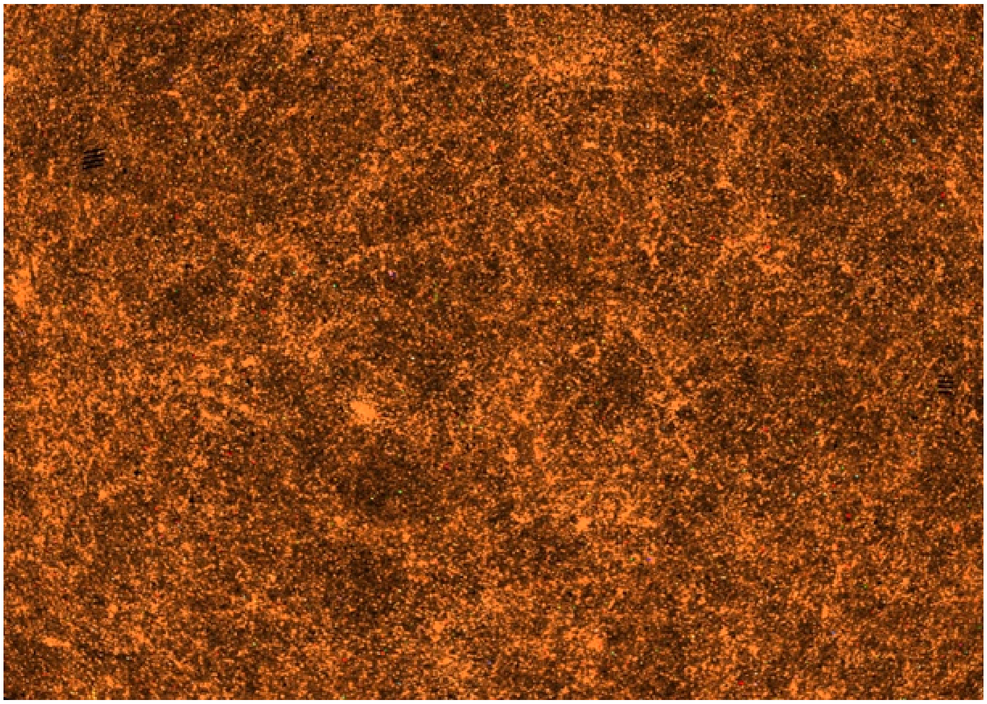

Figure 1.1: Part of the northern section of the Sloan Digital Sky Survey's final data release, showing millions of galaxies. Filaments, clusters, and walls are visible, but the overall homogeneity of the universe is apparent [55].

ideas governing the development of relativistic dynamics.

The consequences of relativity have been repeatedly verified over the years. Successful applications of general relativity include precession of Mercury's orbital perihelion, gravitationally lensed stars observed during eclipses, and gravitational redshifting of light. Despite these and numerous other tests, gravitational interactions on quantum scales and unification with the electroweak force at high-energy limits remain an active area of research. Some questions about the behavior of gravity on larger scales are still open to debate as well, however, modifications to GR, or "MOND" models as an explanation of the effects of dark matter and energy are increasingly disfavored, and no significant competitors to traditional GR-based cosmologies possess compelling evidence.

We therefore begin from the assumption that the evolution of our universe is well-described by the *cosmological principle*, the axiom which states that our position in the universe is not unique. This compels two important conditions when applied to cosmological distance scales. Firstly, that the universe is *homogeneous*, with a structure broadly uniform with respect to location, obeying the same laws at all points and containing the same forms of matter everywhere. Secondly, that it is *isotropic*, having no preferred directionality. Cosmological studies have verified both propositions, large scale structure maps show even distributions of mass above scales of ∼100 Mpc while relic cosmic background radiation exhibits an isotropic temperature distribution, containing variations of less than 10^{-5} (Figs. 1.1 & 1.2).

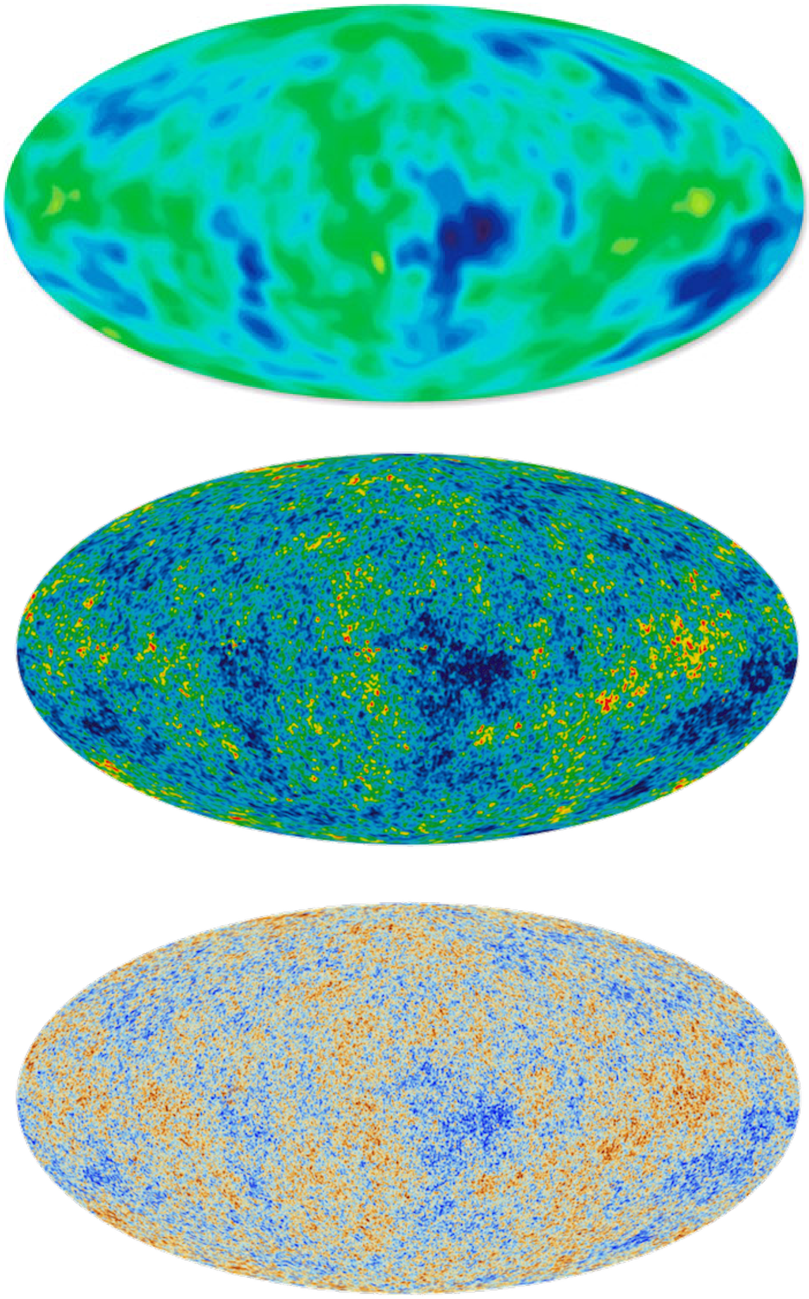

Figure 1.2: Increasingly precise measurements of the Cosmic Microwave Background as captured by COBE (1992), WMAP (2003), and Planck (2013) [67, 105, 87]. The CMB obeys a blackbody radiation curve with directional temperature variance below 1 part in 10^5, these maps display the deviation from uniformity.

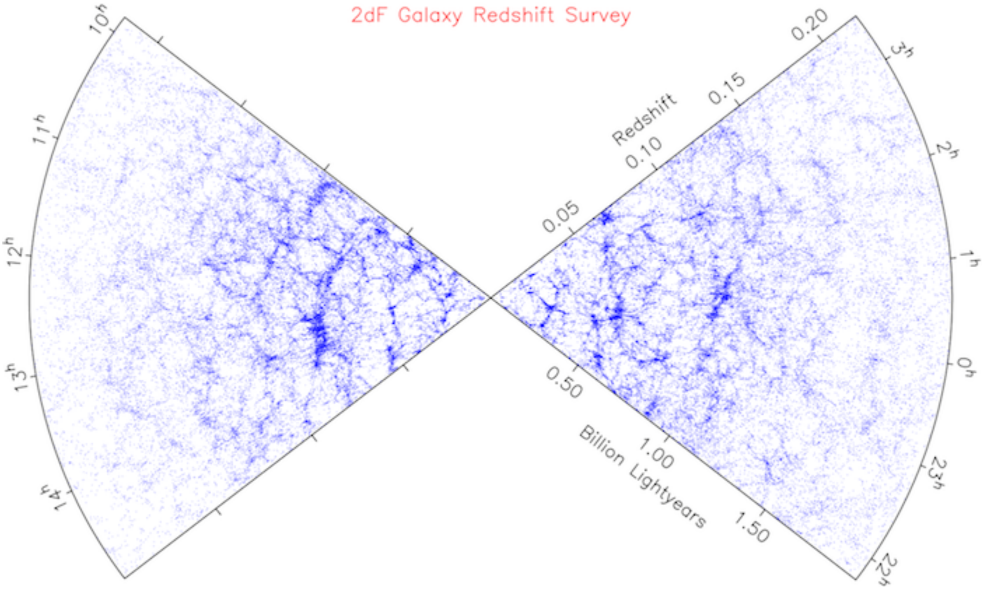

Figure 1.3: Overview from the 2dF Galaxy Redshift Survey, depicting a 1500 deg^2 swath of the sky [17]. Each dot is a single one of the 245,591 galaxies whose spectral redshift was obtained for the survey.

1.1.3 The Friedman-Robertson-Walker Universe

Space-time Geometry

The observed homogeneity and isotropy of the universe is well-described by the Friedman-Roberston-Walker metric:

$$\mathrm{d}s^2 = -\mathrm{d}t^2 + a^2(t)\left[\frac{\mathrm{d}r^2}{1-kr^2} + r^2(\mathrm{d}\theta^2 + \sin^2\theta\,\mathrm{d}\phi^2)\right] \tag{1.3}$$

In this description, the spherical coordinates are $(t,\, r,\, \phi,\, \theta)$, k is the spatial curvature parameter (which may be between -1$\leq k \leq$1, with a flat spatial geometry at $k = 0$), the time-dependent scale factor is $a(t)$, and $c = 1$. Without non-diagonal terms, this metric is rotationally invariant, obeying the condition of isotropy. Einstein's field equations may be used to solve for the time-evolution term, $a(t)$. The metric tensor $g_{\mu\nu}$ may be written in the form

$$g_{\mu\nu} = \begin{pmatrix} -1 & 0 & 0 & 0 \\ 0 & \frac{a(t)^2}{1-kr^2} & 0 & 0 \\ 0 & 0 & a(t)^2r^2 & 0 \\ 0 & 0 & 0 & a(t)^2r^2\sin^2\theta \end{pmatrix} \tag{1.4}$$

Einstein's field equations are

$$G_{\mu\nu} = R_{\mu\nu} - \frac{1}{2} R g_{\mu\nu} = 8\pi\, G\, T_{\mu\nu} + \Lambda\, g_{\mu\nu} \tag{1.5}$$

where $G_{\mu\nu}$ is the Einstein tensor, $R_{\mu\nu}$ the Ricci tensor, R is the scalar curvature, $T_{\mu\nu}$ is the stress-energy tensor, G is the gravitational constant, and Λ is a cosmological constant term. In order to describe the behavior of the space-time at large, we must relate these terms to the metric, $g_{\mu\nu}$. The Ricci tensor is a contraction of the Riemann curvature tensor, $R^{\rho}_{\sigma\mu\nu}$, which is, in turn, a sum of the affine connection terms which describe the curvature of space through derivatives in the metric tensor.

$$\Gamma^{\sigma}_{\mu\nu} = \frac{1}{2} g^{\sigma\rho} \left(\partial_{\mu} g_{\nu\rho} + \partial_{\nu} g_{\rho\mu} - \partial_{\rho} g_{\mu\nu} \right) \tag{1.6}$$

$$R^{\rho}_{\sigma\mu\nu} = \partial_{\mu} \Gamma^{\rho}_{\nu\sigma} - \partial_{\nu} \Gamma^{\rho}_{\mu\sigma} + \Gamma^{\rho}_{\mu\lambda} \Gamma^{\lambda}_{\nu\sigma} - \Gamma^{\rho}_{\nu\lambda} \Gamma^{\lambda}_{\mu\sigma} \tag{1.7}$$

This allows us to calculate the Ricci curvature tensor and scalar terms of the field equations:

$$R = R^{\mu}_{\mu} = g^{\mu\nu} R_{\mu\nu} \tag{1.8}$$

$$R_{\mu\nu} = R^{\rho}_{\mu\rho\nu} = g^{\rho\sigma} R_{\sigma\mu\rho\nu} \tag{1.9}$$

We now have the ability to solve the geometric portion of Eq. (1.5). Now we deal with the right-hand side, to relate the geometry to the matter and energy that shape it. The most important term there is the energy-momentum tensor, $T_{\mu\nu}$, containing the relativistic mass-energy, as well as the contributions via motion of the fluid. It may be thought of as "flux of four momentum p^{μ} across a surface of constant x^{ν}" [15]. We are interested in working with a collisionless, perfect fluid—the condition of isotropy requires spatial symmetry and therefore that $T_{\mu\nu}$ has only diagonal terms—thus we neglect those containing bulk motion, viscosity, and stress interactions. In this situation, our fluid retains only the rest-frame energy density, ρ, and the isotropic 3-D pressure components ($\langle \vec{p} \rangle = p_x = p_y = p_z$).

$$T_{\mu\nu} = \begin{pmatrix} \rho & 0 & 0 & 0 \\ 0 & p & 0 & 0 \\ 0 & 0 & p & 0 \\ 0 & 0 & 0 & p \end{pmatrix} \tag{1.10}$$

With our metric specified by Eq. (1.4), and time derivative of the scale factor denoted as $\dot{a}$, we can (after some effort) write the Ricci tensor components that correspond to the non-zero $T_{\mu\nu}$ terms:

$$R_{00} = -3\frac{\ddot{a}}{a} \tag{1.11}$$

$$R_{11} = \frac{a\ddot{a} + 2\dot{a}^2 + 2k}{1 - kr^2} \tag{1.12}$$

$$R_{22} = \left(a\ddot{a} + 2\dot{a}^2 + 2k\right) r^2 \tag{1.13}$$

$$R_{33} = \left(a\ddot{a} + 2\dot{a}^2 + 2k\right) r^2 \sin^2\theta \tag{1.14}$$

$$R = 6\left(\frac{\ddot{a}}{a} + \frac{\dot{a}^2 + k}{a^2}\right) \tag{1.15}$$

Additionally, $T^{\mu}_{\nu} = \text{diag}(-\rho, \vec{p})$ describing a perfect fluid, has the trace

$$T^{\mu}_{\mu} = T = -\rho + 3p \tag{1.16}$$

which allows us to write the field equation in the time-time ($\mu\nu = 00$), and space-space ($\mu\nu = ij$) cases as

$$-3\frac{\ddot{a}}{a} = 4\pi G\left(\rho + 3p\right), \qquad \text{and} \tag{1.17}$$

$$\frac{\ddot{a}}{a} + 2\frac{\dot{a}^2 + k}{a^2} = 4\pi G\left(\rho - p\right) \tag{1.18}$$

respectively. Solving for $\ddot{a}$ in Eq. (1.18) and rewriting the time-time equation give us the **Friedman Equations**:

$$\frac{\dot{a}^2 + k}{a^2} = \frac{4\pi G}{3}\rho \tag{1.19}$$

$$\frac{\ddot{a}}{a} = -\frac{4\pi G}{3}\left(\rho + 3p\right) \tag{1.20}$$

Mass-Energy Components

The conservation of energy dictates that,

$$\nabla_\mu T^\mu_0 \quad = \quad 0 \tag{1.21}$$

$$\partial_\mu T^\mu_0 + \Gamma^\mu_{\mu\lambda} T^\lambda_0 - \Gamma^\lambda_{\mu 0} T^\mu_\lambda \quad = \quad -\dot{\rho} - 3\frac{\dot{a}}{a}\left(\rho + p\right) \tag{1.22}$$

For the basic classes of "perfect fluid" matter and energy which we are interested in, the equation of state is simple:

$$p = w\rho \tag{1.23}$$

This means that by applying Eq. (1.22), and assuming that w is a constant, we find that ρ evolves as

$$\dot{\rho} \quad = \quad -3\frac{\dot{a}}{a}\left(1 + w\right)\rho \tag{1.24}$$

$$\rho(a) \quad = \quad \rho_\circ \, a^{-3(1+w)} \tag{1.25}$$

(where $\rho_\circ \equiv \rho(a{=}1)$, the current density.)

There are three basic elements contributing to the energy density: matter, radiation, and a term which we will refer to, for now, as a "cosmological constant" ($\rho = \rho_m + \rho_r + \rho_\Lambda$). The pressure contribution from "dust"—collisionless, non-relativistic matter effectively at rest, is zero. While for radiation, $w = \frac{1}{3}$, and a cosmological constant gives $w = -1$. Because matter's contribution to ρ is non-relativistic, it is proportional to the density of matter itself, going as $\rho_m \propto a^{-3}$. Likewise, the contribution of relativistic particles (which, in actuality, are predominantly massless photons) is $\rho_r \propto a^{-4}$. The cosmological constant must be a quantity that fills all space without regard to the total volume[1], $\rho_\Lambda \propto a^0$. As the universe expands, there is more space, increasing the importance of this term.

Because there is no compelling evidence for spatial curvature in recent cosmological measurements, from this point onward we assume $k \simeq 0$.

---

[1] This is the most popular mainstream perspective on Λ—alternate theories propose different types of behavior, such as, for example, scale factor dependent w.

The Hubble parameter, describing the evolution of the co-moving distance, $a(t)$, and the expansion of space, is defined as $H(t) \equiv \frac{\dot{a}}{a}$. Using this term, the Friedmann equations become:

$$H^2 = \left(\frac{\dot{a}}{a}\right)^2 = \frac{8\pi G}{3}\rho + \frac{\Lambda}{3} \tag{1.26}$$

$$\frac{\ddot{a}}{a} = -\frac{4\pi G}{3}(\rho + 3p) + \frac{\Lambda}{3} \tag{1.27}$$

Further simplification of the expansion rate may be accomplished by defining critical energy density for a spatially flat universe, the limit which balances expansion and collapse:

$$\rho_c \equiv \frac{3H^2}{8\pi G} \tag{1.28}$$

meaning that the overall energy densities for each type are of the form

$$\Omega_i = \frac{\rho_i}{\rho_c} = \frac{8\pi G}{3H^2}\rho_i \tag{1.29}$$

Hubble's constant, $H_\circ$, is the value of the Hubble parameter at our current time. Recent studies show it to be in the vicinity of $H_\circ = 70 \pm 5$ km/sec/Mpc (in dimensional units). From EQNS. 1.26 & 1.29 we find

$$\frac{H^2}{H_\circ^2} = \Omega_m + \Omega_r + \Omega_\Lambda \tag{1.30}$$

Substituting the ρ parameters at $a_\circ = 1$, and relating the densities to their critical values at current times (i.e. $\Omega_m(a{=}1) \equiv \Omega_{m,\circ}$), we can show that the universe evolves as,

$$\frac{H^2}{H_\circ^2} = \frac{\Omega_{m,\circ}}{a^3} + \frac{\Omega_{r,\circ}}{a^4} + \Omega_{\Lambda,\circ} \tag{1.31}$$

These relations imply that as the universe expands, the contribution of each component drives the energy density in turn as $\propto a^{-4}$ (radiation), in the very early universe, $\propto a^{-3}$ (matter), and eventually $\propto a^0$ (Λ), at late times.

To derive expressions for cosmological distances, we recall that light travels along null geodesics. Therefore, the proper distance, d_p (the metric distance at the current time), can be expressed as a time integral of $a(t)$. Defining $a = [1+z]^{-1}$ and setting the scale factor at the present time as $a(t_\circ) = 1$, the proper distance between an observer at $t_\circ$ and a galaxy at redshift z' can be written as

$$d_p = \frac{1}{H_\circ} \int_0^{z'} \left(\Omega_m (1+z)^3 + \Omega_r (1+z)^4 + \Omega_\Lambda\right)^{-\frac{1}{2}} \mathrm{d}z \tag{1.32}$$

Following the same approach, we are able to derive the angular diameter distance, d_A, the ratio between co-moving size (separation between two points at the same redshift) and angular size subtended:

$$d_A = \frac{1}{H_\circ(1+z')} \int_0^{z'} \left(\Omega_m (1+z)^3 + \Omega_r (1+z)^4 + \Omega_\Lambda\right)^{-\frac{1}{2}} \mathrm{d}z \tag{1.33}$$

Luminosity distance, d_L, describes the appearance of an object's brightness as a function of our distance to it, and is related to the prior two quantities by

$$d_L = (1+z) d_p = (1+z)^2 d_A \tag{1.34}$$

1.1.4 Parameter Constraints

The main source of radiation's contribution to the energy density parameter is a sea of photons left over from the era when the universe cooled to the point where photons decoupled from the primordial fluid. This occurred at the time when the overall temperature of the matter-radiation fluid decreased to the point where the ionization rate of electrons fell below that of recombination into atomic hydrogen. Since that time, around $z = 1089$ (~380,000 years after the Big Bang), the expansion of space has caused their energy to drop as $\rho_\gamma \propto a^{-4} \propto \lambda^{-4}$. Observations reveal a relic microwave temperature of $T = 2.72548 \pm 0.00057$ K [36]. The Stefan-Boltzman law then provides the energy density for a photon fluid of this temperature of

$$\rho_\gamma = \alpha T^4 \simeq 0.260 \text{ MeV m}^{-3} \tag{1.35}$$

Meanwhile, an analog to the photon background consisting of neutrinos which froze-out on the order of ~1 sec after the big bang also contributes roughly $\rho_\nu \simeq 0.23 \rho_\gamma$ per neutrino species (though this background has never been observed). Considering this, their contribution to the overall radiation energy density is likely to be less than a quarter of that of the CMB. Energy density from starlight is similarly negligible. Therefore radiation should be no greater than $\Omega_{r,\circ} \lesssim 5 \times 10^{-5}$.

Matter and dark energy are likely to have a more substantial contribution. Parameter fitting from combined CMB observations by *Planck* and *WMAP*, as well as baryon acoustic oscillation studies in several large scale surveys find energy densities of [83]

$$\Omega_{m,\circ} = 0.308 \pm 0.010 \tag{1.36}$$

$$\Omega_{\Lambda,\circ} = 0.692 \pm 0.010 \tag{1.37}$$

while similar findings indicate that cold dark matter dwarfs baryonic matter by a fraction of approximately $\Omega_{\text{baryons}}/\Omega_{\text{CDM}} \approx 1/5$. (Fig. 1.4.)

Dark Energy

Dark energy is observed in measurements exploring the cosmic expansion history of the universe. As a parameter in the Friedmann equations, Λ first arises as a free constant due to an anti-derivative in the solution of the field equations, however its exact nature is poorly understood and an active subject of research. In classical physics and special relativity, it would be inconsequential that a constant energy term appears in these equations, because only relative differences between two energy states are physically meaningful. However, GR emerges through relating space-time geometry to energy, and therefore the existence of a non-zero energy field pervading space becomes physically significant. Prior to the discovery of cosmic expansion, a cosmological constant was considered a "spatial" aspect of the universe, which preserved the steady-state universe against gravitational collapse. Once the Big Bang model became the prevailing cosmology, the expansion of the universe provided sufficient opposition against collapse, and the cosmological constant was relegated to the status of mathematical artifact—a non-physical term equal to zero[2]. From the 1990s onward, growing evidence of an accelerating expansion rate renewed interest in the cosmological constant term as a potential cause for this behavior. Popular opinion now places Λ on the "right-hand" side of the field equation, as an energy quantity constant throughout the universe.

Two basic forms of Λ are possible. The first would be a form of vacuum energy, constant over time, filling all space evenly. The second, a variable form, or "quintessence" evolves as a function of the scale-factor, like $w_\Lambda(a) = w_\circ + w_q(a)$, where at current times $w_\Lambda(a_\circ) \to -1$. This results in an energy density that varies (potentially non-linearly) as a function of a. Observations studying the evolution of the universe, especially at late times as Λ comes to dominate ρ_c governing the expansion,

---

[2] As a growing body of observations supplanted the concept of a steady-state universe, Einstein's inclusion of Λ to preserve static space-time famously became known as his "biggest blunder." This is interesting in light of the fact that Albert Einstein spent a significant fraction of his later career disputing the probabilistic nature of quantum mechanics and promoting hidden variable theories.

are of great importance in distinguishing between them.

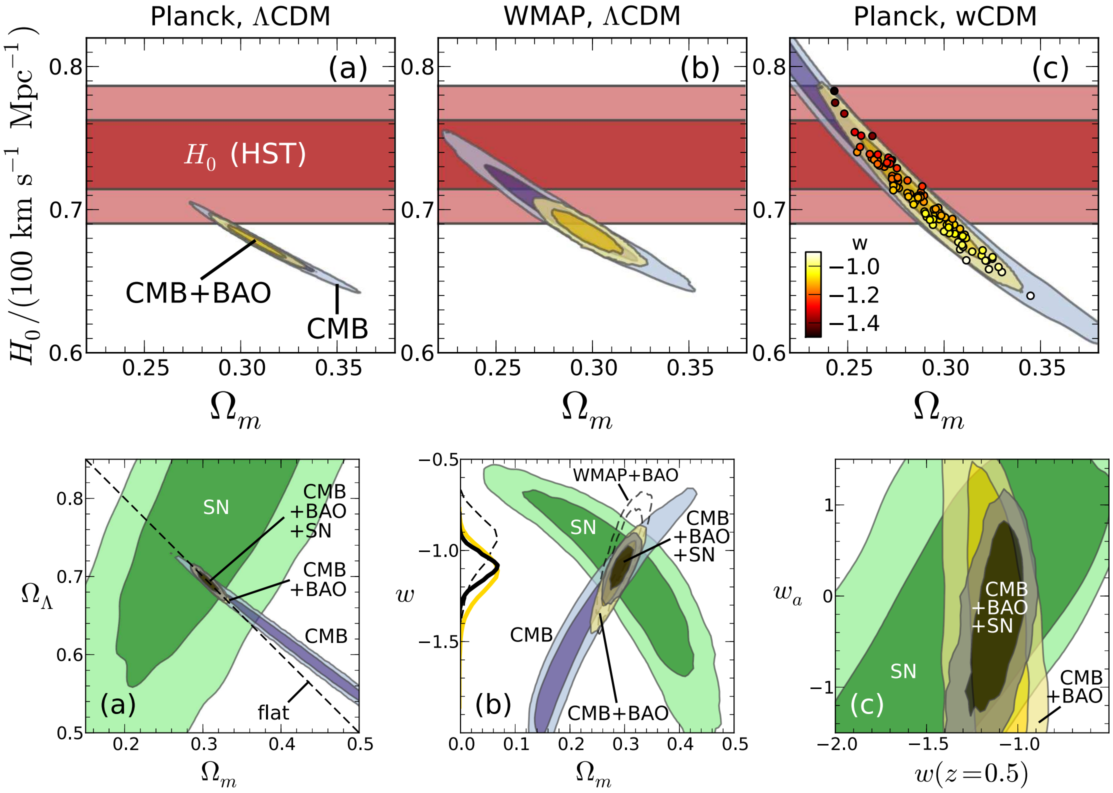

Figure 1.4: Compilation of limits on dark matter and dark energy parameters from WMAP9, Planck, BAO (SDSS-II, BOSS, 6dFGS), and Union2 (as "SN"). **(Top)** Recent constraints of Ω_m and the Hubble constant, $H_\circ$, based on the aforementioned observations, with the first two graphs depicting a flat Λ-CDM universe, and the third contrasting these measurements against 100 Monte Carlo simulations of w values based on CMB+BAO results. **(Bottom)** Total matter in the universe plotted against dark energy (and quintessence) parameters. The right plot depicts a time-varying equation of state for quintessence. **(Both)** The dashed contours show the 68.3% and 95.4% CL regions for the combination of WMAP9 and BAO data [78].

1.2 Galaxy Clusters & the Development of Structure

1.2.1 Cosmological Importance of Galaxy Clusters

The gravitational collapse of matter, baryonic and dark, leads to extended structure of galaxies. Large groupings of these galaxies, filamentary chains, gravitationally-bound clusters, and enormous empty gulfs between them are evident in even simplistic n-body experiments modeling the evolution of the universe, and confirmed by large scale structure observations [55, 17]. Clusters of galaxies

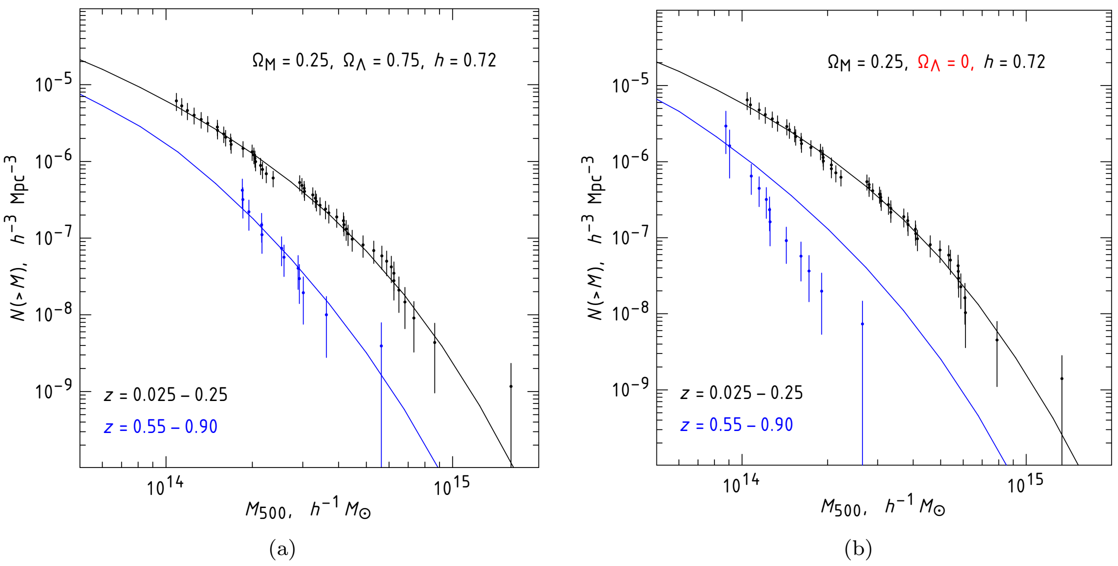

(a)

(b)

Figure 1.5: 2009 plots demonstrating the sensitivity of cosmological models to the cluster mass function [122]. Cluster counts based on ROSAT X-ray measurements of cluster weight and redshifts. Aggregate mean cluster figures for two different z ranges are seen plotted against predicted curves in **(a)** well- and **(b)** poorly-fitting cosmologies.

form at the overlapping bounds of filaments of matter. Sophisticated simulations predict even more specific aspects of this structure and its development over time.

The significance of galaxy cluster abundance and features in cosmological measurements are twofold: Firstly, they are the universe's largest virialized structures. (Larger conglomerations of matter, such as superclusters, may be gravitationally bound, however they have not yet had the time to collapse under gravity and come to virial equilibrium.) Their size makes it possible to find them despite vast cosmological distance scales in a variety of different methods. Plus, having multiple independently-verifiable observation techniques improves the accuracy of mass measurements. Secondly, clusters are the most recently-formed aspects of structure. Because the changeover to Λ-dominated expansion of the universe occurred only recently (cosmologically speaking), cluster formation, which is similarly recent, is particularly sensitive to it. For this reason they provide an excellent laboratory with which to study late-time evolution and the influence of dark energy. The cluster mass function (mean virialized cluster mass as a function of redshift) is an especially good test of cosmological parameters (Fig. 1.5).

1.2.2 Measurements of Clusters

There are several methods for detecting and determining the properties of galaxy clusters. Each has its own strengths and weaknesses, and the strongest results in this effort typically combine two or more approaches to verify detection and weigh the cluster.

Coincidence and Color-Matching

Coincidence surveys simply seek out regions of over-density in large galaxy catalogs. Verification of clustering and measurement of radial scale is then performed by calculating photometric galaxy redshift values. Because galaxies within the same cluster typically have similar stellar compositions, color-matching serves as an indication that they are located at the same line-of-sight distance and gives the angular extent of the cluster. At high redshifts, color searches can identify clusters composed mostly of faint red ellipticals, which are populated by older stars which formed relatively early in the universe's history. Clusters of these bodies may be found by locating them in the "red-sequence" of galaxy color maps.

Difficulties in this method include coincidental overdensities, correctly estimating photometric redshifts, and velocities along the line-of-sight adding uncertainty to distance measurements. There are also numerous technical considerations in performing wide-angle surveys; however, recent innovations have allowed the construction of ever larger telescopes with enough light-gathering power to resolve ever fainter objects and storage capabilities for massive amounts of data-collection. The Dark Energy Survey [37] is among upcoming projects which will utilize this approach (among others) to hunt for cluster candidates.

Spectral Surveys

Similar to optical methods, surveys of spectral profiles attempt to detect overdensities in large numbers of galaxies by providing a more accurate line-of-sight distance with which to locate each object in three-dimensional space. Obtaining spectral redshifts allows an effective measurement of the distance, as well as providing proper motions along the line-of-sight to identify sets of members moving around a common center of mass. In strongly-bound clusters, galaxy motions are strongly influenced by the gravity of the cluster. Therefore, clusters appear as regions with a notable dispersion in galaxy velocities.

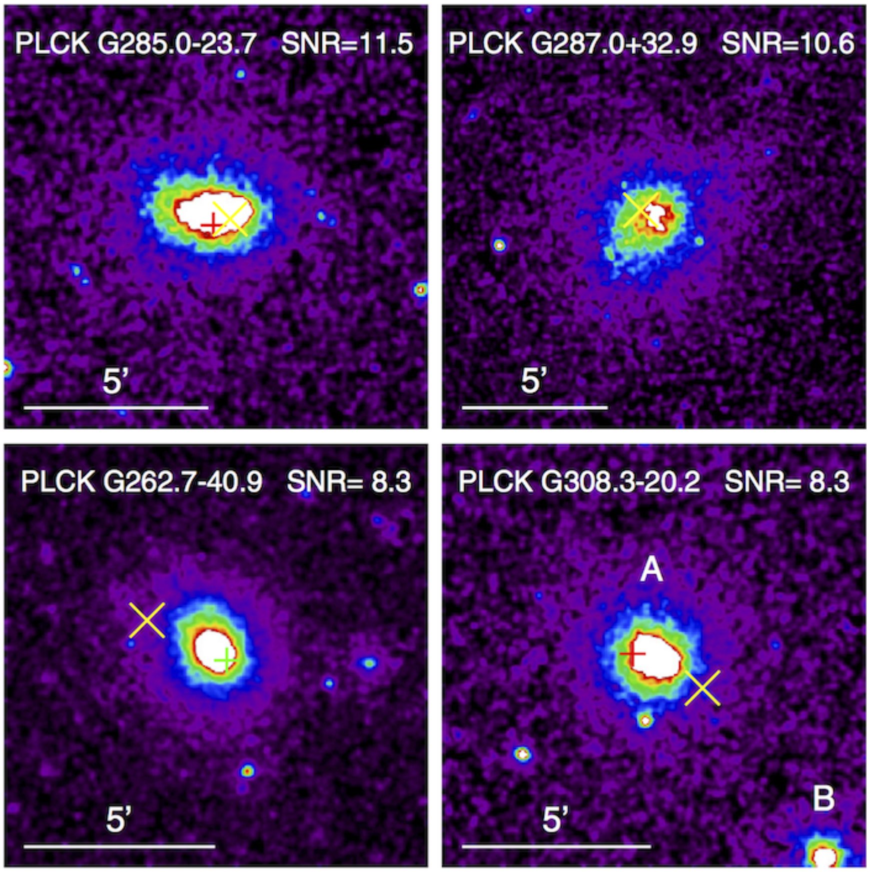

Figure 1.6: X-ray imaging of 4 clusters taken by the orbiting X-ray observatory, *XMM-Newton*, showing the extended structures of hot intergalactic gas [89]. The yellow X's mark the location of SZ-cluster-detections found by the *Planck* experiment, red and green crosses indicate RASS-BSC and -FSC (ROSAT all-sky X-ray survey, bright and faint source catalogues) survey detections, respectively.

As in coincidence surveys, spectral methods require an outside source for calibration of the mass-observable relation to provide accurate cluster weights. They are highly sensitive to the luminosities of the cluster galaxies, and therefore correlate to, but do not directly reveal the amount of dark components or intergalactic gas that make them up. Thus, in general, the value of such cluster surveys is primarily in aggregate rather than as a targeted method to estimate mass values of specific clusters. The increased velocity dispersions seen in merging clusters and those undergoing dynamical relaxation may also complicate attempts at mass estimates via this method.

X-ray Observations

Intergalactic gas collects in the gravity wells of galaxy clusters and heats by giving up an enormous amount of gravitational potential energy during infall. Bremsstrahlung emission from this virially heated inter-cluster medium may span a large area around the cluster's center of mass, allowing observers to find galaxy clusters by locating non-point-like X-ray sources. Because other sources of X-rays are typically compact, they subtend only the angular size of the telescope's smallest resolved PSF. Cluster emissions, on the other hand, appear as extended structures. Information about the properties of the cluster may be evaluated by using the angular size of the cluster, its estimated temperature, and the emission strength.

X-ray studies have the advantages of avoiding false detections in superposition seen in optical surveys, as well as being independent of cluster galaxy luminosities and sensitive to overall mass distribution. They provide spectral redshift information targeted to the source emitter as well. Typically, X-ray based mass estimates are founded on an approach which treats the intra-cluster medium as a relaxed fluid at hydrostatic equilibrium. Mass calculations are then fit to a model for radiative emission which depends on the temperature, extent, and density of the source, as well as some empirical values. However, because factors other than the cluster mass alone may influence conditions of the gas, dynamical uncertainties about the cluster effect the strength of the measurement. Mergers are of particular consequence, as they may create significant bremsstrahlung signals far greater than would be accounted for in a dynamically-relaxed cluster of the same overall mass[3].

Sunyaev-Zel'dovich Effect

When CMB photons encounter hot plasma, inverse Compton scattering of the light off of ionized electrons results in the scattered photon coming away with a slight energy increase. As significant reservoirs of super-heated gas, galaxy clusters can show up in measurements of the cosmic microwave background as regions where fewer (or more) CMB photons are observed, depending on source wavelength. The plasma of the cluster is effectively reducing the flux of certain background photons

---

[3] Famously, in the case of the Bullet Cluster [16], this has had the beneficial result of demonstrating the collisionless nature of dark matter, as X-ray emissions from the interacting gas at the mid-point of the cluster merger lag behind the mass distribution of the galaxies and dark matter shown through gravitational lensing to have passed through one another. More self-interactive dark matter would have given a lensing result closer to the X-ray peak, and most versions of modified gravity theories (MOND) are unable to account for a system where the lensing mass reconstruction tracks the galaxies rather than the X-ray gas which makes up the bulk of the baryonic matter in the system.

which reach us, for wavelengths which would be associated with CMB temperatures overall. Most importantly, because the key observable is a backdrop signal of light from the early universe, there is no redshift dependence of this effect, as the temperature of ionized electrons dwarfs that of source photons at any z that could contain a cluster. Rather, the only properties which determine the strength of the observation are those related to source strength variance or the apparent angular size of the cluster's ionized plasma distribution, (and therefore, in a general sense, the overall mass, as well as the resolving power of the instrument). SZ detection is therefore the most successful approach to finding clusters at high-redshift.

Weak Gravitational Lensing

Weak lensing (WL) studies evaluate the aggregate warping of background galaxies caused by large intermediary groups of matter. The bending of light due to the gravitational well of this matter leads to magnification and shear distortion in the appearance of the background shapes. Because no overall mean ellipticity ought to be seen among large samples of galaxy shapes, overall deviations reveal hidden mass. Due to the 2-dimensional nature of our perspective, thorough calibration methods are necessary to assure that background source galaxies truly lie behind the potential cluster in question. Care must also be taken to conduct precise measurements of shapes, as they may be affected by scores of observational factors like wind or instrument systematics. Furthermore, some knowledge of the distances involved is necessary to accurately estimate cluster masses (either through multi-band imaging that provides photometric redshift, direct spectroscopy, or knowledge of aggregate distance-magnitude relations). This dissertation deals with cluster detection through weak lensing, and the methodology and technical issues will be discussed in detail in Chapters 2 & 3.

Unlike mass measurements based on optical clustering and spectroscopy, weak lensing methods are immune to issues regarding the proper velocity dispersions amongst cluster galaxies or the fraction of luminous to non-luminous matter. Unlike those based on X-ray emission, they are immune to issues related to the gas dynamics or merger status of the cluster. WL study is therefore of particular importance in setting the mass-observable relations of these other methods. WL is solely responsive to the distribution of mass and geometry.

Weak lensing as a blind attempt to find clusters is a relatively new effort, due to the necessity to accurately resolve shapes of numerous objects over a wide enough field to make a survey effort worthwhile. Insufficiently accurate preparation steps reduce signal-to-noise, and highly precise corrections must be employed at each stage of the data reduction process to reduce factors which contaminate measurement. It is for this reason that WL is almost always used in a targeted fashion, calibrating mass measurements of specific clusters against other methods. Nonetheless, WL measurements across large sections of the sky were primary goals of missions like the Deep Lensing Survey (DLS) and are among those of the upcoming Large Synoptic Survey Telescope (LSST) and Dark Energy Survey (DES) projects.

We continue in the next chapter with a discussion of the methodology behind weak lensing techniques.

Chapter 2

Weak Gravitational Lensing

"Relativity is just science's way of flip-flopping.
Space or time? Mass or energy? Which is it?
Pick a side. We're at war."
Stephen Colbert

Matter and energy curve spacetime, and light follows a "straight" path through that curved spacetime. This is the central idea behind gravitational lensing. An essential prediction of General Relativity, it was one of the first to be tested observationally (Fig. 2.1) when Arthur Eddington photographed the light of stars passing behind the eclipsed sun in 1919 [30]. In modern use, this phenomenon has several astrophysical implications. The first, known as "microlensing," refers to using alignments of individual compact objects with some stellar background source to study the populations of faint and non-luminous bodies within the Milky Way. Strong and weak lensing, on the other hand, are most commonly applied to extragalactic physics to understand the distribution of mass in galaxies and clusters of galaxies. Because weak lensing measurements depend only on the total cluster mass, including dark matter, and do not rely on the dynamical state for calibration, They are a vital tool in ongoing efforts to understand the evolution of the universe on the largest scales.

The increased rate of growth in the number of weak lensing studies in recent years can be attributed to: (1) the improving availability of large instruments at astronomical sites with outstanding observing conditions (which are necessary to accurately resolve galaxy shapes); (2) recently

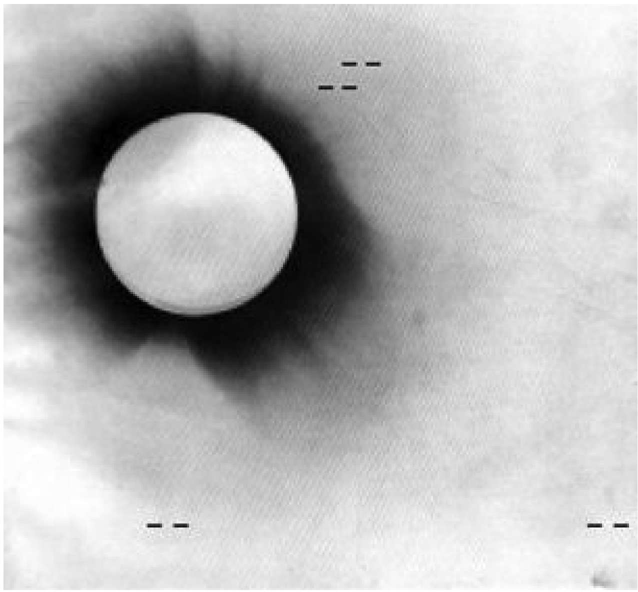

Figure 2.1: Negative photographic plate from Eddington's observation of the May 29, 1919 eclipse taken at Principe island [30]. Stars are marked by the horizontal hashes. Calculations demonstrated a 2″ deviation in the position of the background stars. Eddington's expedition confirmed the gravitational lensing aspect of general relativity, and formed a significant piece of evidence in support of the nascent theory of gravity.

constructed large telescopes with high-resolution cameras, wide fields of view, and powerful light-gathering capabilities; (3) more precise computational methods for reconstructing galaxy shapes and making weak lensing measurements across dense galaxy fields; and (4) the improving precision of cosmological techniques which provide supporting information necessary for reliable weak lensing results (such as large redshift catalogs, distance ladder measurements, and accurate measurements of cosmological parameters from multiple sources).

Strong lensing measurements were first made in 1979 when multiple images of the quasar *QSO 0957+561* were observed [124], while the first weak lensing signal was confirmed 11 years later with the successful measurement in 1990 of the Abell 1689 and CL1409+52 galaxy clusters [118]. Observations demonstrated that a preferentially directed ellipticity signal was found relative to the center of the cluster, indicating that the cluster introduced a shearing effect to the otherwise randomly oriented background of galaxies. WL measurements have now been made of hundreds of galaxy clusters with increasing precision.

2.1 Theoretical Basis

We will begin with the Schwarzschild metric to describe the space around a spherically symmetric point source of mass, M, at some distance r,

$$\mathrm{d}s^2 = \left(1 - \frac{2MG}{rc^2}\right) c^2 \mathrm{d}t^2 - \left(1 - \frac{2MG}{rc^2}\right)^{-1} \mathrm{d}r^2 - r^2 \mathrm{d}\theta^2 - r^2 \sin^2\theta \mathrm{d}\phi^2 \tag{2.1}$$

To describe the motion of a photon around this source, we calculate a null geodesic traveling on a planar path within a plane of constant $\theta = \frac{\pi}{2}$. Solving the geodesic equation gives us two constants of motion:

$$\xi = a \left(1 - \frac{2GM}{c^2 r}\right)^{-1} \frac{\mathrm{d}s}{\mathrm{d}t} \tag{2.2}$$

where,

$$a = r^2 c \frac{\mathrm{d}\phi}{\mathrm{d}s} \tag{2.3}$$

At the points of closest and furthest approach, $\frac{\mathrm{d}s}{\mathrm{d}t} = 1$, and $\frac{\mathrm{d}\phi}{\mathrm{d}s} = 1$, respectively. (Thus, a and ξ are analogous to the apogee and perigee of an orbit.) Substituting these relations into the metric and integrating along the path of a light ray traveling from $r = -\infty$ to $r = \infty$ provides a deflection in ϕ (which we define as α):

$$\begin{aligned} \delta\phi = \alpha &= \int_{-\infty}^{\infty} \frac{\mathrm{d}r}{\sqrt{\frac{r^4}{\xi^2} - \left(1 - \frac{2GM}{c^2 r}\right) r^2}} && (2.4) \\ &= \frac{4GM}{c^2 \xi} && (2.5) \end{aligned}$$

Without the ability to see this distortion in three-dimensions, we are limited, observationally, to measuring this phenomenon solely as demonstrated through the 2D appearance on the plane of the sky. With the light path distances dwarfing the physical size of the deflectors by many orders of magnitude, we may approximate the lensing mass as being within a thin plane, orthogonal to the observer. This is known as the *thin lens approximation.*

Lensing Equation

The physical arrangement is diagrammed in Fig. 2.2. Because the space between the objects is cosmological, the distances are taken to be angular diameter distances. They are *defined* such

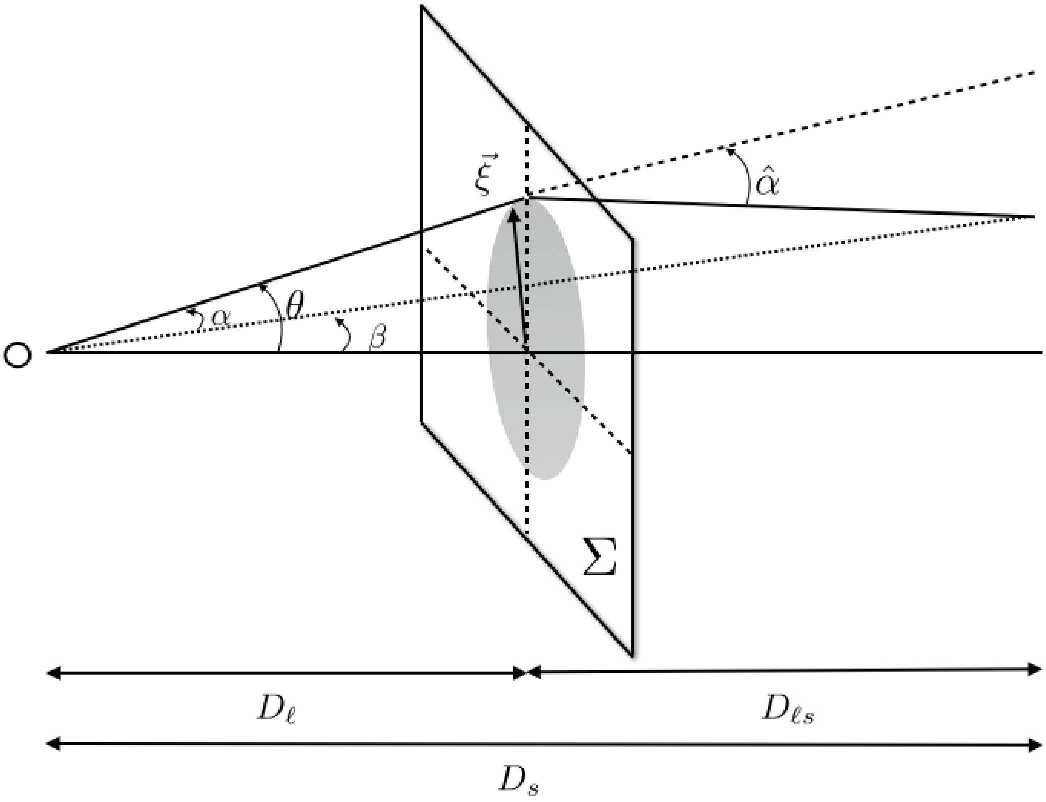

Figure 2.2: Geometry of gravitational lensing. Original source depicted in solid red, outlined star is apparent position.

that our lensing formulae are true, however they may not obey other Euclidean geometric relations independently (i.e. $D_\ell + D_{\ell s}$ may not be—and in practice is almost never—equal to D_s).

In the thin lens approximation, the mass warps the approach of a light ray from the unknowable "real" position of the source $\vec{\beta}$ into the *observed* angle $\vec{\theta}$.

$$\vec{\beta} = \vec{\theta} - \vec{\alpha} \tag{2.6}$$

The "reduced" lensing angle, $\vec{\alpha}$, is related through simple geometry to the actual deflection angle, $\hat{\alpha}$, through

$$\vec{\alpha} = (D_{\ell s}/D_s)\,\hat{\alpha} \tag{2.7}$$

in the limit of a small angle. Thus we get the *lens equation*:

$$\vec{\beta} = \vec{\theta} - \vec{\alpha} = \vec{\theta} - \frac{D_{\ell s}}{D_s}\hat{\alpha} \tag{2.8}$$

Mass Distribution

Now we wish to understand the potential which creates this deflection. Given a distribution of mass, $\rho(\vec{x})$, we are interested primarily in the situation where the distances of the light's trajectory are significantly larger than those within the distribution itself, meaning that we restrict the dimensions to the two within a "lens plane" orthogonal to the light path. As such, we take $\Sigma(\vec{\xi})$ to be the surface mass density as a projection of the distribution on this plane passing through the center of mass and orthogonal to the line-of-sight to the observer. $\vec{\xi}$ is the two-dimensional vector describing position within the plane of the lens.

$$\Sigma(\vec{\xi}) = \int \mathrm{d}z\, \rho(\vec{\xi}, z) \tag{2.9}$$

The total deflection is a sum of all the tiny deflections produced by a great number of individual masses—the deflection of light is related to this distribution through the integral

$$\hat{\alpha}(\vec{\xi}) = \frac{4G}{c^2} \int \mathrm{d}^2\vec{\xi}'\, \Sigma(\vec{\xi}') \frac{\vec{\xi} - \vec{\xi}'}{\left|\vec{\xi} - \vec{\xi}'\right|^2} \tag{2.10}$$

In the case of a radially symmetric mass distribution,

$$\hat{\alpha}(\xi) = \frac{4\pi G}{c^2 \xi} M(\xi) \tag{2.11}$$

where $M(\xi)$ is mass within the radius ξ, and $\xi = |\vec{\xi}|$.

We define the quantity *convergence* to be:

$$\kappa(\vec{\theta}) = \frac{\Sigma(\vec{\theta})}{\Sigma_{cr}} \tag{2.12}$$

where Σ_{cr} is the *critical surface mass density.* We define it as

$$\Sigma_{cr} \equiv \frac{c^2}{4\pi G} \frac{D_s}{D_{\ell s} D_\ell} \tag{2.13}$$

This is the mass density required to produce a deflection angle identical to the apparent projection angle. It is the threshold between the strong and weak lensing regimes. $\Sigma \geq \Sigma_{cr}$ is the case where Einstein rings or multiple images may be visible. Likewise, cases where $\kappa \ll 1$ constitute weak lensing scenarios, while strong lensing takes place in the regime where $\kappa \geq 1$.

Using Eqns. (2.7) & (2.12), we can then express the deflection in terms of the convergence as

$$\vec{\alpha}(\vec{\theta}) = \frac{1}{\pi} \int \mathrm{d}^2\vec{\theta'}\, \kappa(\vec{\theta'})\, \frac{\vec{\theta} - \vec{\theta'}}{\left|\vec{\theta} - \vec{\theta'}\right|^2} \tag{2.14}$$

The deflection angle is related to the 2D projected or "lensing" potential, which is, in turn related to the 3D gravitational potential, $\Phi(\vec{\theta}, z)$, by

$$\psi(\vec{\theta}) = \frac{2}{c^2} \frac{D_{\ell s}}{D_\ell D_s} \int \mathrm{d}z \Phi(\vec{\theta}, z) \tag{2.15}$$

This potential satisfies the lensing form of the Poisson equation,

$$\nabla^2 \psi(\vec{\theta}) = -2\kappa(\vec{\theta}) \tag{2.16}$$

and may be written in terms of the convergence and the observed angle as

$$\psi(\vec{\theta}) = \frac{1}{\pi} \int \mathrm{d}^2\vec{\theta'}\, \kappa(\vec{\theta'})\, \ln \left|\vec{\theta} - \vec{\theta'}\right|^2 \tag{2.17}$$

Therefore, we can relate the deflection to the potential,

$$\vec{\nabla}\psi(\vec{\theta}) = \vec{\alpha}(\vec{\theta}) \tag{2.18}$$

2.2 Observable Quantities

Distortion of galaxy shapes via lensing takes three forms: deflection, magnification, and shear. Deflection is unmeasurable without *a priori* knowledge of the system as it would appear without an intervening lens unless there are multiple images of the same object. In weak lensing scenarios however, there are other measurable quantities in ensemble systems. As we will describe, magnification and shear may be employed to understand the potential.

Using Eq. (2.18) we can rewrite the lens equation in terms of the 2D potential as,

$$\vec{\theta} = \vec{\beta} + \vec{\nabla}\psi(\vec{\theta}) \tag{2.19}$$

This allows us to link the distortion of source objects by a gravitational lens with the potential through the Jacobian transformation matrix, $\mathbf{A}(\vec{\theta})$, which acts on the "unlensed" shapes and modifies them into the shapes we see.

$$\mathbf{A}(\vec{\theta}) = \frac{\partial \vec{\theta}^i}{\partial \vec{\theta}^j} = \left(\delta_{ij} - \frac{\partial^2 \psi(\vec{\theta})}{\partial \vec{\theta}^i \partial \vec{\theta}^i} \right) \tag{2.20}$$

This measures the "stretching" of the lens equation, mapping the original angle to the lensed image. We define this transformation to be

$$\mathbf{A}_{ij} = \frac{\partial \vec{\theta}^i}{\partial \vec{\theta}^j} \qquad \longrightarrow \qquad \mathbf{A} = \begin{pmatrix} 1 - \kappa - \gamma_1 & -\gamma_2 \\ \gamma_2 & 1 - \kappa + \gamma_1 \end{pmatrix} \tag{2.21}$$

where γ_1 & γ_2 are known as the complex shear. Shear itself can be expressed as a spinor function, with complex terms

$$\vec{\gamma} = \begin{bmatrix} \gamma_1 \\ 0 \end{bmatrix} + i \begin{bmatrix} 0 \\ \gamma_2 \end{bmatrix}. \tag{2.22}$$

Thus our Jacobian matrix becomes

$$\mathbf{A} = (1 - \kappa) \begin{pmatrix} 1 & 0 \\ 0 & 1 \end{pmatrix} - |\vec{\gamma}| \begin{pmatrix} \cos 2\phi & \sin 2\phi \\ \sin 2\phi & -\cos 2\phi \end{pmatrix} \tag{2.23}$$

where ϕ is the angle between the deflection angle $\vec{\alpha}$ and the x-axis of the chosen coordinate system. In subsequent sections we will explore how to extract this information about the lensing distortion in a manner that is useful to a real-world observer.

Magnification

Magnification, μ, is the increase in observed flux as a function of the original value. Magnification can be calculated from the determinant of the lensing Jacobian:

$$\mu = \frac{1}{\det|\mathbf{A}|} = \frac{1}{(1 - \kappa)^2 - |\vec{\gamma}|^2} \tag{2.24}$$

The strength and magnification of the lens is related to the convergence, $\kappa(\vec{\theta})$, which may be calculated from the potential

$$\kappa(\vec{\theta}) = \frac{1}{2}\nabla^2\psi = \frac{1}{2}\left[\frac{\partial^2\psi(\vec{\theta})}{\partial\theta_1^2} + \frac{\partial^2\psi(\vec{\theta})}{\partial\theta_2^2}\right] \equiv \frac{1}{2}\left[\psi_{,11} + \psi_{,22}\right] \tag{2.25}$$

where $\psi_{,i}$ is a partial derivative in the i-th direction. Unfortunately, as is the case with deflection, we have no *a priori* knowledge of individual galaxy shapes which would provide an insight into the original sizes of the background sources. Nonetheless, convergence calculations in combination with shear measurements may provide an insight into estimating κ.

Shear

The shear, $\vec{\gamma}$, measures the shape distortion of an object from its original form. The complex shear terms of Eq. (2.21) are sensitive to the second derivative of the potential ψ:

$$\begin{aligned}
\gamma_1(\vec{\theta}) &= \frac{1}{2}\left[\frac{\partial^2\psi(\vec{\theta})}{\partial\theta_1^2} - \frac{\partial^2\psi(\vec{\theta})}{\partial\theta_2^2}\right] = \frac{1}{2}\left(\psi_{,11} - \psi_{,22}\right) && (2.26)\\
\gamma_2(\vec{\theta}) &= \frac{1}{2}\left[\frac{\partial^2\psi(\vec{\theta})}{\partial\theta_1\partial\theta_2} + \frac{\partial^2\psi(\vec{\theta})}{\partial\theta_2\partial\theta_1}\right] = \psi_{,12} = \psi_{,21} && (2.27)
\end{aligned}$$

The directional aspect of the shear in terms of ϕ (the angle between the principal angle of the shear and that of the coordinate system) is, via extension of Eqns. (2.26) & (2.27),

$$\begin{aligned}
\gamma_1(\vec{\theta}) &= \gamma(\vec{\theta})\cos\left(2\phi(\vec{\theta})\right) && (2.28)\\
\gamma_2(\vec{\theta}) &= \gamma(\vec{\theta})\sin\left(2\phi(\vec{\theta})\right) && (2.29)
\end{aligned}$$

We want to relate the shear to the measured ellipticity. First, we define the object ellipticity and orientation in terms of spinors e_1 and e_2 (depicted in Fig. 2.3):

$$e_1 = -\mathrm{Re}\left[\vec{e}\,e^{-2i\phi}\right] \tag{2.30}$$

$$e_2 = -\mathrm{Im}\left[\vec{e}\,e^{-2i\phi}\right] \tag{2.31}$$

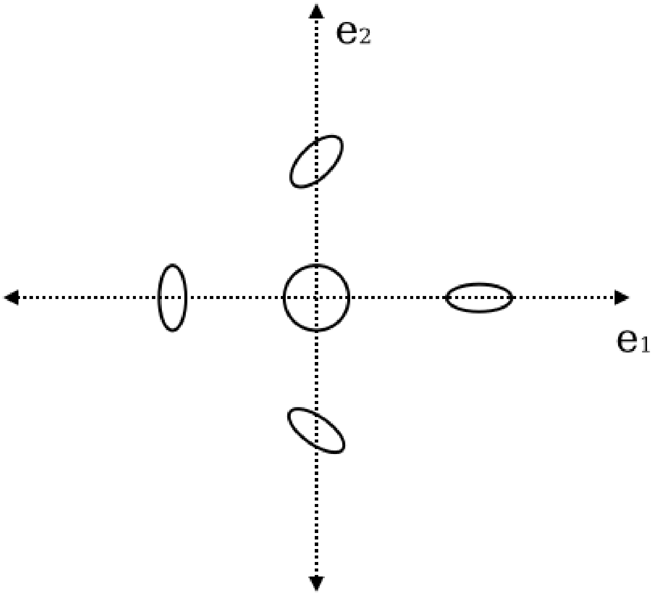

Figure 2.3: Graphical depiction of e_1–e_2 observable shape distortion.

The reverse relationship gives the angle of the major axis in terms of the e–components,

$$\phi = \frac{1}{2}\arctan\frac{e_2}{e_1} \tag{2.32}$$

We define a quantity, $\vec{g}$, *reduced shear*, for which $\vec{g} \simeq \vec{\gamma}$ in the weak lensing limit (where $\kappa \ll 1$).

$$\vec{g} = \frac{\vec{\gamma}}{1-\kappa} \tag{2.33}$$

Reduced shear, like $\vec{\gamma}$, is a complex, two-component quantity describing the shape distortion of images through lensing. The initial ellipticity of a background source, $\vec{e_I}$, is distorted to that of the source we observe through interaction with the reduced shear, $\vec{g}$ (at small ellipticities) as:

$$\vec{e} = \frac{\vec{e_I} + \vec{g}}{1 + \vec{g}^*\vec{e_I}} \tag{2.34}$$

Although galaxies exhibit no mean $\vec{e}$, this is not to say that the average galaxy *itself* is circular, rather it is the ensemble which is, when summed for a wide field. Galaxies typically have an intrinsic RMS ellipticity greater than $\geq$0.3 depending on their morphology. Nonetheless, in large numbers the mean initial ellipticities obey $\langle\vec{e_I}\rangle \simeq 0$. An appropriately large ensemble of background galaxies leaves us with an equivalent to the average shear,

$$\langle \vec{e} \rangle \simeq \langle \vec{\gamma} \rangle \simeq \langle \vec{g} \rangle \tag{2.35}$$

2.2.1 Measuring Ellipticity Moments

The surface brightness distribution of an observed source is defined as $I(\vec{\theta})$, where $\vec{\theta}$ is defined as the position vector. The second order (quadrupole) brightness moments are then found through the expression

$$Q_{ij} \equiv \frac{\sum W_I(\vec{\theta}) I(\vec{\theta}) \theta_i \theta_j}{\sum W_I(\vec{\theta}) I(\vec{\theta})} \tag{2.36}$$

where W_I is a function that weights the flux distribution. W_I is a weighing that allows one to account for pixelization and maximize S/N in the shape measurement by de-weighting the pixels near the sky noise level.

The weighing function must take into account several types of error, such as pixelization and shot noise. The former is a limiting factor produced by the finite extent of CCD pixels. Small galaxies may approach the limits of pixel size. The latter consideration concerns the accuracy of intensity measurements. As astronomical imaging is a pixel-by-pixel light collection process, there is inherent randomness in how many photons will be detected by an exposure of a given time. This variation is described by a Poisson distribution, which governs the shot noise of the intensity measurement, and is reduced with longer exposure times. The technical aspect of approaches for measuring object shapes will be explored further in Ch. 3.

The moment tensor can be used to parameterize the size and shape of any object in the form of the *complex ellipticity*:

$$\vec{e} \equiv \frac{Q_{11} - Q_{22} + 2iQ_{12}}{Q_{11} + Q_{22} + 2\sqrt{Q_{11}Q_{22} - Q_{12}^2}} \tag{2.37}$$

2.3 Mass Reconstruction

Weak lensing analysis is capable of constructing a surface projection of relative convergence across a field of lensed galaxies—an analogous quantity to mass contained along the line of sight direction. This would, however, merely be a map of the relative mass densities. As already stated, further information is necessary to obtain an independent mass estimate.

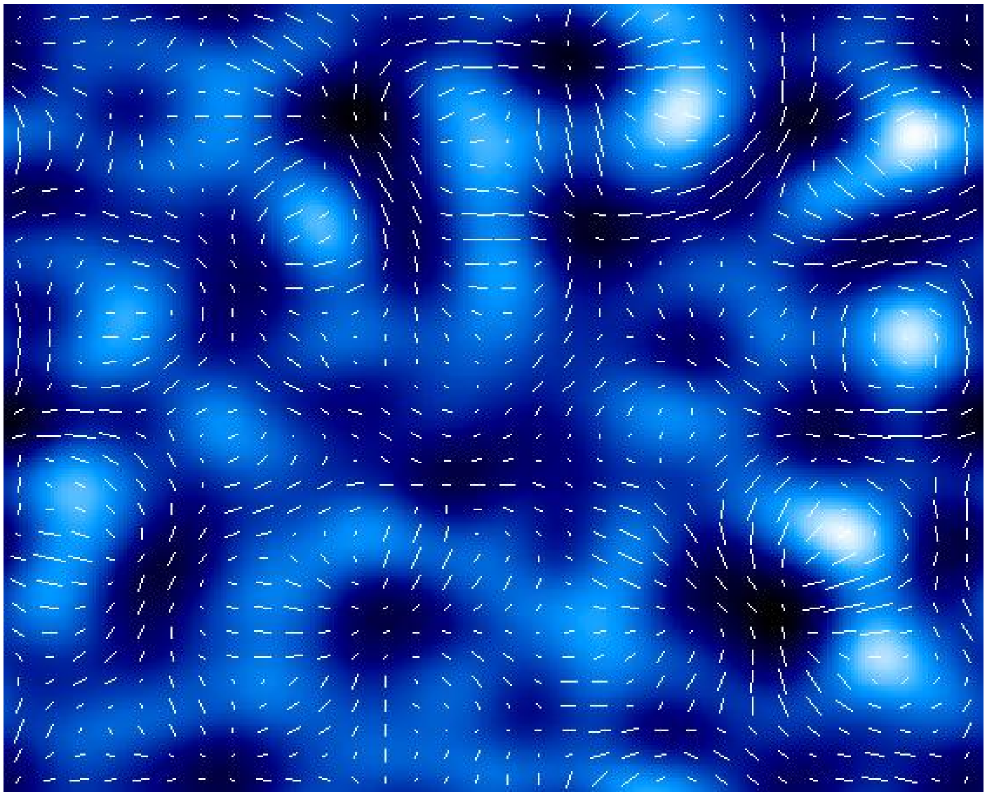

Figure 2.4: Convergence (white) and shear fields (whiskers) displayed for an example matter distribution. This map displays the relationship between these quantities and mass (located within the high convergence regions), showing tangental shear values around mass concentrations, whereas underdense areas display radial shear [5].

2.3.1 Aperture Masses

Having evolved formulae for $\vec{\nabla}\psi(\vec{\theta})$ and $\kappa(\vec{\theta}) = \frac{1}{2}\nabla^2\psi(\vec{\theta})$ we can use the 2-dimensional form of Gauss's Law to solve for mass within a given radius θ. Within a plane, Gauss's Law is

$$\int_0^\theta \vec{\nabla}F\mathrm{d}^2\vec{r} = \theta \oint \mathrm{d}s\,\vec{F}\cdot\hat{n} \tag{2.38}$$

By making $\vec{F} = \nabla\psi$, and choosing $\hat{n}$ to be normal to the circle of radius θ, we find

$$\int_0^\theta \mathrm{d}^2r\,\kappa(r) = \theta \oint \mathrm{d}s\,\vec{\nabla}\psi\cdot\hat{n} \tag{2.39}$$

Evaluating this integral over a circle centered on the origin of our coordinate system we see that the mass contained within the circular aperture may be written,

$$M_{ap}(\theta) = \int_0^\theta 2\kappa(r)\,\mathrm{d}^2\vec{r} = \theta \oint \frac{\partial\psi}{\partial\theta}\mathrm{d}s \tag{2.40}$$

Differentiating the right hand side and recalling that,

$$\frac{\partial^2\psi}{\partial\theta_1^2} = \psi_{,11} = \kappa + \gamma_1 \tag{2.41}$$

we eventually find that the (dimensionless) mass within the aperture is,

$$M_{ap}(\theta) = 2\pi \int_0^\pi 2\langle\kappa(r)\rangle r\mathrm{d}r = 2\pi\theta^2\bar{\kappa}(\theta) \tag{2.42}$$

having defined $\bar{\kappa}(\theta)$ as the mean mass density within the θ–sized aperture. (This is $\bar{\kappa}(\theta) = \frac{1}{2\pi}\left[\langle\gamma_t(\theta)\rangle + \langle\kappa(\theta)\rangle\right]$ where $\langle\gamma_t(\theta)\rangle$ is the mean tangential shear within θ.)

As given in Eqns. 2.26, 2.27, & 2.25 the shear can be written in terms of convergence,

$$\vec{\gamma}(\vec{\theta}) = \frac{1}{\pi}\int \mathrm{d}^2\vec{\theta'}\,\mathcal{D}(\vec{\theta}-\vec{\theta'})\kappa(\vec{\theta'}) \tag{2.43}$$

where $\mathcal{D}(\theta-\theta')$ is the complex conjugation kernel. Convergence may then be found by taking the Fourier transform

$$\kappa(\vec{\theta}) = -\frac{1}{\pi}\int \mathrm{d}^2\vec{\theta'}\,\mathrm{Re}\left[\mathcal{D}(\vec{\theta}-\vec{\theta'})\vec{\gamma}^*(\vec{\theta'})\right] \tag{2.44}$$

In practical terms, we are taking a sum of contributions to κ, galaxy-by-galaxy. This reconstructs the lensing potential, and thus the mass, through the cumulative addition of shear moments. As such, a sum over the collection of galaxies better reflects the calculation in practice,

$$\kappa(\vec{\theta}) = \frac{2}{\pi n}\sum_{\text{galaxies}} \frac{W(\vec{\theta}-\vec{\theta_i})|\vec{e}_{\tan}(\vec{\theta_i})|}{|\vec{\theta}-\vec{\theta_i}|^2} \tag{2.45}$$

The weight function, $W(\theta)$, must deal with the fact that the kernel $\mathcal{D}$ diverges at the origin $\theta = 0$, exaggerating the significance of ellipticities of galaxies approaching the convergence peak (which are randomly aligned). Conversely, it also de-weights galaxies at θ's far from the peak. In particular, galaxy contributions well outside the virial radius add noise without improving the signal strength. A weight function which goes to zero on scales lower than the mean cluster galaxy separation distance, and substantially higher than the virial cluster radius, is empirically determined to be most successful.

We opt to employ the weighting approach of Wittman *et al.* (2006) [129]

$$W(\vec{\theta}) = \left(1 - e^{-|\vec{\theta}|^2/2r_{in}^2}\right) e^{-|\vec{\theta}|^2/2r_{out}^2} \tag{2.46}$$

where $\vec{\theta_i}$ is the angular distance of that galaxy from the point $\vec{\theta}$, for which we want to find the convergence, and r_{in} & r_{out} are the radial distance limits from $\vec{\theta}$. To detect and locate surface mass densities via the *fiatmap* algorithm [56], we adopt this approach.

2.4 Sources of Error

We have briefly touched on pixelization and shot noise effects as they relate to the estimation of galaxy shapes in weak lensing, but there are additional issues that a careful study must take into account. The mentioned effects depend on camera specifics, but there are also telescope-specific effects on shape measurement. Mirror, focal plane distortion, as well as atmospheric seeing and telescope shake effects can introduce spurious shape noise. Ch. 3 will deal with technological considerations more thoroughly.

Weak lensing is predicated on the assumption that the intrinsic orientations of galaxies are random and uncorrelated. In the presence of non-zero intrinsic ellipticities this is true only in the limit of very large N_{gal}. Without large enough background sample sizes, coincidence is capable of dwarfing the physical effect. There is also reason to believe that galaxies exhibit a slight tendency to arrange themselves preferentially to the tangent of a cluster halo [95]. Despite correlating to the presence of a cluster, this is not a lensing effect *per se*, and therefore it is a priority to remove cluster galaxies from the sample to avoid a biased result.

Of course, real observations with ground-based telescopes result in images where the galaxy is convolved with a significant atmospheric and telescope PSF, spreading the light (often anisotropically). This has the dual effects of dimming the central flux, and of blurring the shape itself. Light from faint galaxies may be scattered below the necessary threshold for detection, and the strength of the lensing signal can be reduced by the increased circularization of the galaxy shapes and altered by the PSF anisotropy. Plate-wide and regional PSF distortions can be corrected to some extent in the image reduction/stacking process, but galaxies lost from the sample are not recovered.

Because telescope optics and observing conditions are influenced by dozens of sometimes interdependent effects which each must be carefully examined and corrected for, the solutions for these issues are often pragmatic in nature, and may be most efficiently dealt with through a comprehensive approach to measurement calibration. We will now proceed to an in-depth discussion of weak lensing observing in the real world.

Chapter 3

The Subaru Telescope

"Yet nature is made better by no mean
But nature makes that mean: so, over that art
Which you say adds to nature, is an art
That nature makes."
William Shakespeare, *A Winter's Tale*

3.1 Motivation

Low mass clusters are much more numerous and are therefore capable of assisting in an improved measurement of mass clustering. For this reason, gains in low mass cluster detection enable a strong enhancement in cosmological constraints, based on the cluster-mass function (§1.2.1). Furthermore, they can potentially be applied to providing the establishment of a low mass threshold for viable measurements of substructure in future surveys. In order to reliably detect these galaxy clusters, deep imaging with atmospheric seeing below $\sim 0.7''$ is required [58]. A survey performed on data of this quality can, additionally, be helpful in understanding biases in upcoming studies like LSST, which will have worse spatial resolution but cover more area. With more precise galaxy shapes, sizes, and colors for faint sources, future observers can better calibrate the effects of source crowding, intrinsic alignments of neighboring galaxies, and magnification of the expected shear signal. Because the majority of galaxies in any survey are at the faint and small limit, this calibration is essential to optimizing the success of WL measurements with LSST and other future surveys [63].

3.1.1 Instrument Choice

Measurements of clusters at high source density require cameras capable of reaching the maximum number of faint and small galaxies. Instruments such as LSST and the Thirty Meter Telescope are in development with this goal in mind, and DECam and several others are about to be employed in this direction. The Hubble Telescope achieves very high levels of galaxy resolution, but has a narrow field of view, ill-suited for wide surveys. Furthermore, most large ground-based instruments built in areas of clear atmospheric conditions have proprietary data dissemination policies. However, there is one source for high-resolution images covering multiple degrees at significant depth: the Subaru Telescope data archive, SMOKA [48].

Subaru's data release rules are favorable: regardless of the objective or observers, all data is made available to interested researchers within 18 months [110] (§3.2.2). Additionally, despite being relatively new, its optical qualities and imaging system are well understood. pODI and DECam are, as yet, underdeveloped, and do not contain a substantial public archive for a large lensing study focusing on high background density fields. Thus, we chose the Subaru Telescope archive to fulfill these objectives.

Selecting fields as a function of image quality is functionally similar to performing a high resolution wide-field cluster lensing survey. Similarly, for the study of individual objects (as opposed to large-scale correlation functions) it is of paramount importance to accurately calculate object shapes and exclude cluster members while attaining the highest possible resolved galaxy density within the region of interest. Data selected by seeing depth also permits exploration into lower mass scales than an untargeted analysis of cluster observations. Because the surface density of clusters with mass $\sim$1–2$\times 10^{14} M_{\odot}$ is greater than 1 per deg^2 (as opposed to rare $\sim 10^{15} M_{\odot}$ clusters targeted by most WL studies) we can choose our target fields based on the image quality rather than their location and still expect to make a significant number of detections [57, 74].

3.2 Suprime-Cam

The Subaru Telescope is an 8.2 meter optical-infrared telescope with a wide-field primary focus, on Mauna Kea, Hawaii. The National Astronomical Observatory of Japan was formed to construct and oversee the project in 1988, and in January 1999, Subaru saw first light. Since then, the prime-focus camera has been upgraded twice, and at the time of this writing, the installation of a new

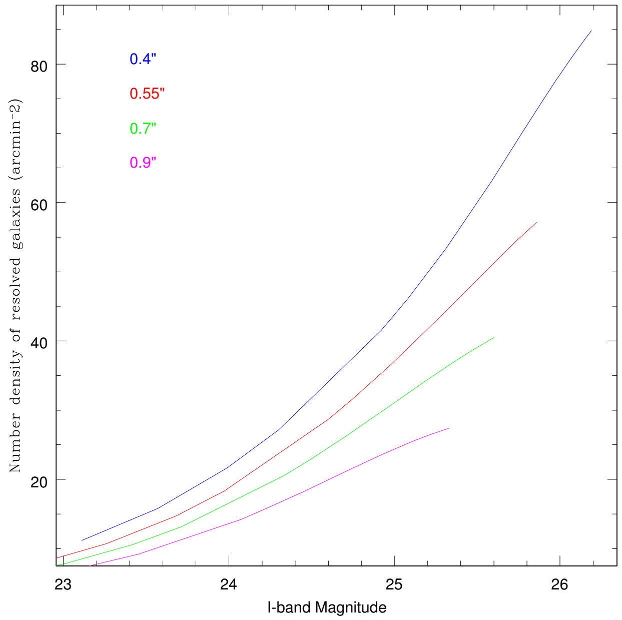

Figure 3.1: Resolved galaxy density as a function of i'-band magnitude, in terms of different instrumental seeing [25].

prime-focus imager, HYPER-SUPRIME-CAM, is underway.

Subaru is one of the largest single-mirror observatories in the world (though several with segmented or combined mirrors are larger). It employs a Ritchey–Chrétien configuration, with the primary reflective surface consisting of a 20 cm thick mirror, weighing 22.8 tons, whose optical figure is corrected through a series of 261 active optics motors. The mirror is mounted in an altitude-azimuth configuration.

The Subaru Prime Focus Camera (Suprime-Cam) consists of ten rectangular 2048 × 4096 pixel charge coupled devices (CCDs), located at the objective mirror's primary focus (FIG. 3.8). The total span of the imaging plane (including chip gaps) is 10848 × 8373 pixels, with a view subtending $34' \times 27'$ of the sky. Because the edges receive less light, however, the effective field coverage is considered to be nearer $24' \times 24'$, with a pixel scale of $0.20''$/pixel. Standard wide-band filters, FIG. 3.4a, are used with the primary focus instrument, and first-guess astrometric coordinate data are provided in the header data of the image files.

The peak of Mauna Kea is one of Earth's best locations for ground-based astronomical observations. Atmospheric conditions which contribute to degradation in seeing, such as turbulence and

Figure 3.2: The dome of the Subaru Telescope at sunset on Mauna Kea in 2010 [49].

differential temperature layers along the line of sight, are reduced by the unique topology and climate of a mountain rising out of the sea without nearby landmasses. Differences between lower and upper atmospheric wind patterns are less significant than over inland mountains, as are temperature variations. Cloud cover is also infrequent, optimizing potential observing time.

3.2.1 Data Selection

For the goals we have described, large numbers of images of lensing-quality depth and resolution are needed to reach a high surface density of resolved galaxies. To preserve a quality threshold, we focused our search on the following criteria:

- Observations totaling at least $\gtrsim$1000 sec of exposure time in each area.
- Average stellar FWHM of $0.5''$ or lower[1].
- Pointings $\geq 30°$ above or below the galactic plane, where galactic gas, dust, and stars do not obscure our view of extragalactic objects.

---

[1] As measured by Subaru's on-site data archive system. As we describe in §3.2.2, this information is overly optimistic, however, in terms of real stellar PSF, this translates to $\lesssim 0.7''$, which is sufficiently well-resolved for WL measurements.

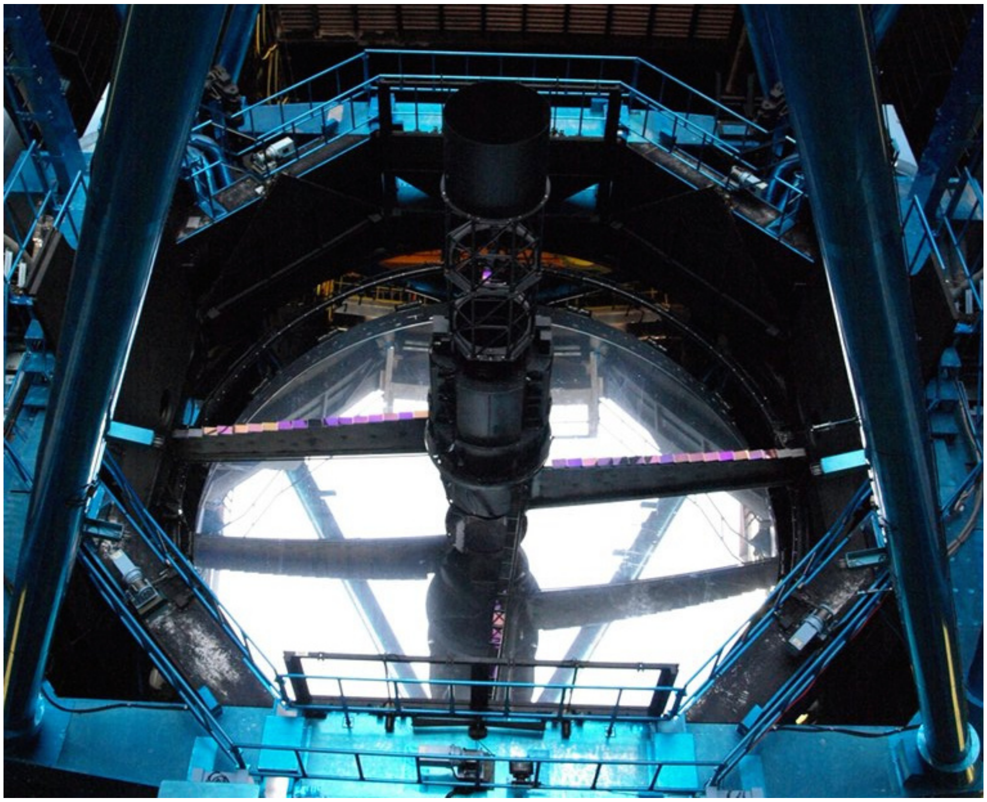

Figure 3.3: Subaru's 8.2 meter primary mirror in daylight.

- Red and near-IR bands, where the transmission and seeing of the atmosphere, and thus our opportunity to resolve faint objects, is best. The most desirable data in terms of minimal atmospheric dispersion and ability to resolve small background galaxies in the appropriate redshift range are within r', R_C, i', I_C, z', & z_R passbands. When possible, we opted to utilize fields for which there was data in more than one filter. Multiple passband fields provide additional verification of cluster detections, as data from separate filters function as isolated data sets. For this reason, V and g' imaging was sometimes considered useful when paired with red and near-IR filters.

In observations from the last 6 years there is more than ~ 30 deg^2 of wide-band images meeting these criteria in the SMOKA catalog. Optimal images of this quality provide a number density of $\gtrsim$25 resolved galaxies per arcmin^2 (Fig. 3.1).

An incident resulting in CCD replacement at Subaru took place in early 2008, so we focused on data taken after July 2008, when ten new CCDs were installed there to ensure consistency in reduction and analysis across data sets. The reduction software developed subsequently was specifically tuned to interpret this data, and our utilization of it took these changes into account. We were also interested in data which was less likely to have been subjected to weak lensing analysis prior to this work, and consideration for this was undertaken in the sample selection. We elaborate further on field choice in Ch. 4.

3.2.2 SMOKA Data Archiving System

The policy of the National Observatory of Japan is to make data freely available to interested researchers following a proprietary period of 18 months [110]. This archive, SMOKA[2], is searchable across multiple detailed parameters, including sky clarity, seeing quality, filters used, etc, allowing a comprehensive targeted search for quality data. With conditions at Mauna Kea permitting a large number of clear, low-seeing nights, and the light-gathering capabilities of an 8-meter telescope, it is a certainty that observers were inadvertently imaging clusters in our area of interest, whether they were looking for them or not.

One issue that arose was the unreliability of SMOKA in correctly describing the seeing of images. Mountaintop measurements are provided as a criteria of SMOKA database queries and we routinely measured values differing from estimates of the true stellar FWHM. Most typically, these initial values (which are contained in image headers) report seeing somewhat lower than what we eventually find, though their *relative* differences are consistent, and useful in identifying outlier or glitched exposures. Nonetheless, because seeing is a major criteria for our image selection, we independently performed seeing tests immediately prior to stacking exposures (Fig. 3.9b) to obtain more accurate values, avoid excluding good data with misreported seeing, or including flawed images.

3.3 Image Processing

To prepare astronomical images for scientific analysis, numerous processing steps must be performed on the raw data to create an unbiased picture of the observed target. Weak lensing studies, in particular, require an emphasis on the accuracy of shape information of galaxies, which may be relatively faint and therefore more susceptible to minor processing errors. Extreme care must be taken to improve the signal-to-noise of fields used for weak lensing in order to accurately resolve the

---

[2] http://smoka.nao.ac.jp

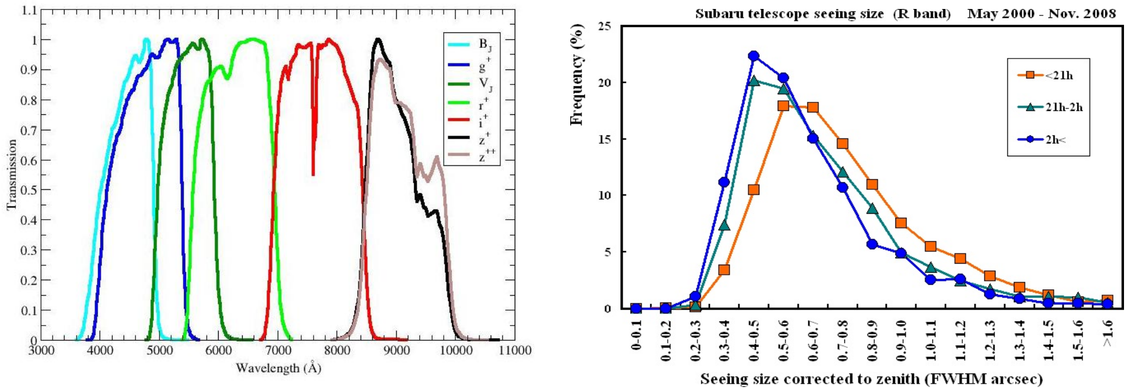

(a) (b)

Figure 3.4: **(a)** Broad passband frequency responses for Suprime-Cam. [113] **(b)** Distribution of seeing FWHM measured during focus checks compiled for the first 8 years of Subaru's operation. The different colored trend lines correspond to the time of night. [111]

largest number of galaxies possible.

The standard set of astronomical reductions to prepare raw data for analysis is a complex and delicate process. Dozens of computational steps are needed to remove electronic noise, calibrate for differing observational conditions, compensate for unavoidable artifacts of the engineering, and normalize separate detectors and exposures to one another.

Bias and overscan subtraction remove fixed electronic noise, patterns, and a pedestal voltage. Flat fields, calibration images taken of evenly illuminated screens, are necessary to understand the varying response of different parts of the detector to light. Faulty pixels, stray light, and regions not appropriately responsive to photon collection must be masked out of the image. Corrections for the distortion by telescope optics, which warp the representation of the sky, are also applied. The CCDs must undergo sky background subtraction, then be scaled relative to one another and combined into a single imaging field, at which point, corrections to the astrometric coordinates of the data are made, to increase the accuracy of the dimensions and locations of objects.

At this point, images are cataloged, with stellar objects selected in preparation for modeling the PSF (and the necessary circularizing corrections to it) prior to stacking. Exposures which do not meet our standards of seeing FWHM are then removed from the sample. PSF correction and relative photometric corrections are then applied at the image stacking step. This step also removes aberrant objects, clipping outlying shapes only found in single exposures. Post-stacking, after verifying circularization of stellar PSFs, additional atmospheric corrections are performed at the

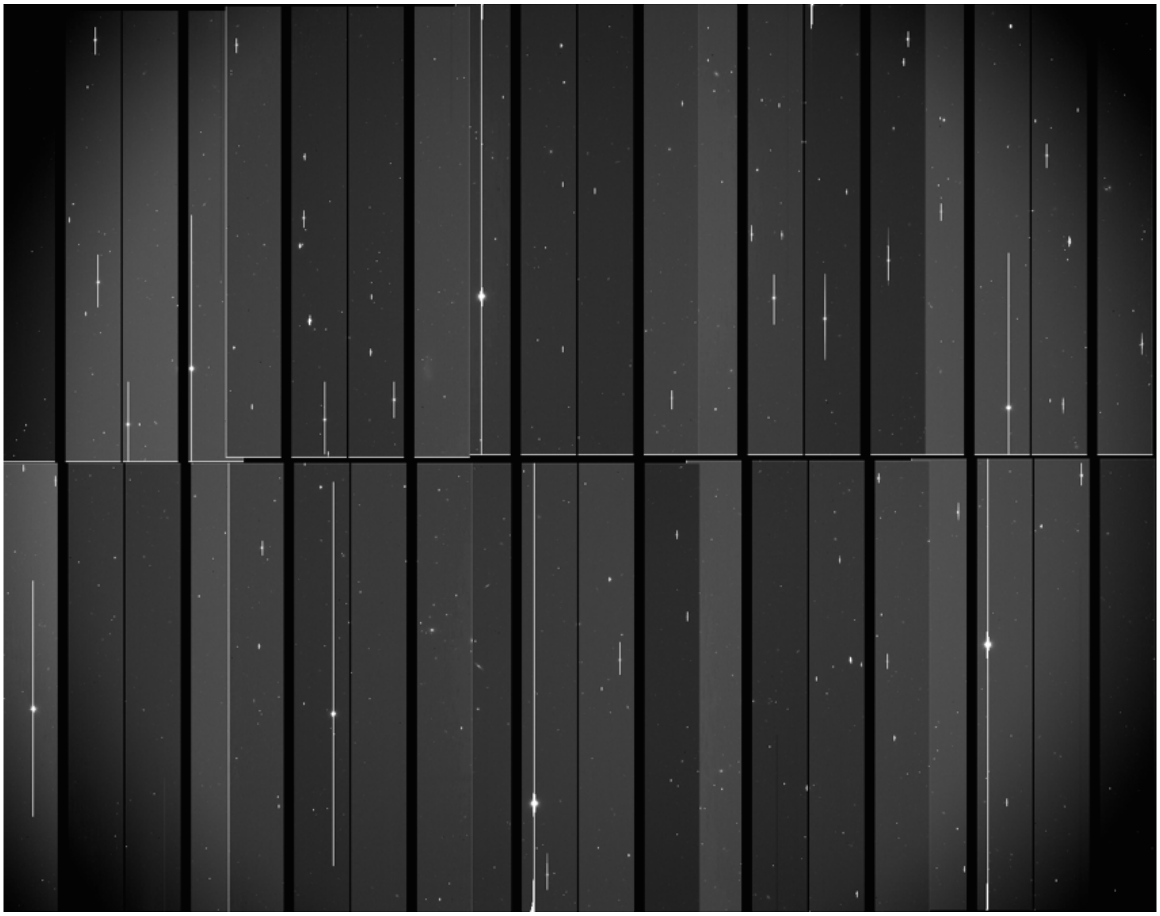

Figure 3.5: Raw field of view, prior to image reduction. Each CCD has 4 different readout areas (Fig. 3.8), accounting for the jagged (apparent) discontinuities (described in §3.3.1). Vignetting is visible near the edges.

catalog level, the object magnitudes are normalized, and finally pruned to compile galaxy catalogs free of stars, extended/unresolved objects, and foreground galaxies.

Large-Scale Processing Challenges

The nature of this project required implementing a large-scale data reduction routine. However, astronomical data is extremely variable—there are imperfections in atmospheric conditions, temperature, airmass, satellite and airplane trails, reflected light, dust, electrical gain, cosmic rays, telescope shake, tracking errors, etc. Images are taken with filters of different transmission efficiencies, exposure times—and choices of calibration frames may vary based on the availability for that particular date.

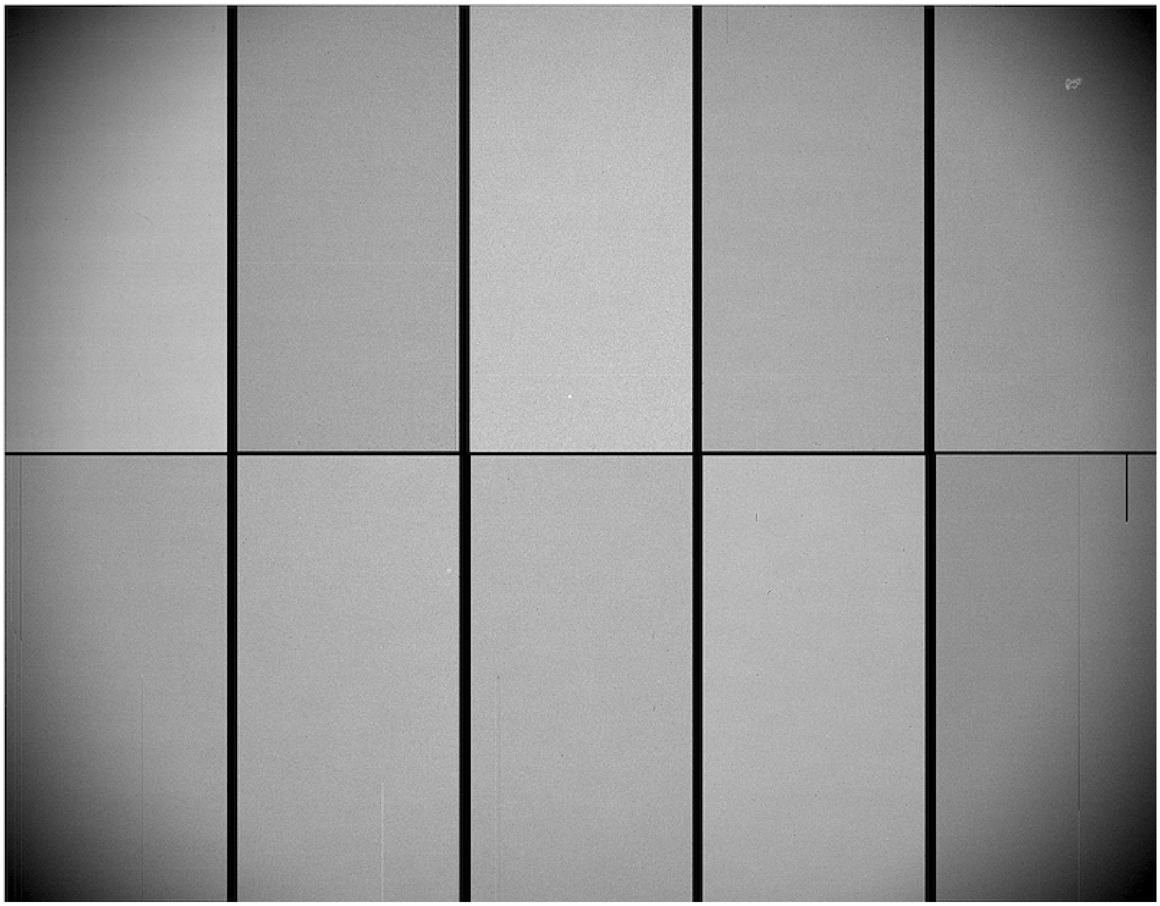

Figure 3.6: Example of a composite domeflat image.

We are using data collected by dozens of different observers, with different goals, choices of filters, and observing strategies. Therefore we are subject to differences that are the result of their interests. Most observers utilizing the Subaru telescope are interested in extragalactic astrophysics, however, someone studying an active galactic nucleus or a star-forming region will necessarily have different priorities than one studying weak lensing. Observers studying objects within the solar system track motion that blurs the background. Those who are collecting photometric differences may tolerate imperfect focus—where objects are detectable, but have sub-optimal shape resolution. Goals such as ours emphasize field-depth and spatial resolution, so sub-optimal data was aggressively pruned from our sample, and care was taken to not rely on SMOKA metadata, as well as to determine the function of an observing run first.

In order to efficiently reduce large quantities of data, a software pipeline was created to do so in a versatile but rigorous manner. Our Python suite, *subarutools*, consists of a systematic execution and

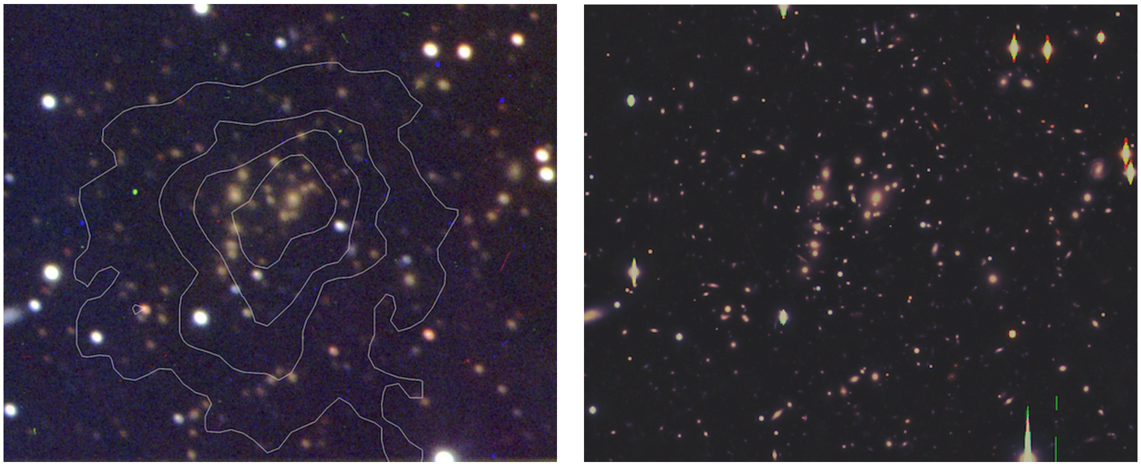
(a) (b)

Figure 3.7: Color composite views of PLCK G 100.2-30.4, as imaged with the previously best resolution via the 0.82-m IAC80 telescope for ∼3000 sec in g', r', and i'-bands [89] (overlaid with *XMM-Newton* iso-contours), compared to Subaru imaging for the same region of the sky (§5.3.1).

quality check sequence for every reduction step from data sorting to astrometric correction. After simple organizational steps, it selects the optimal form of calibration flats, constructs them, runs the full detrending process, measures alignments and corrections, and ultimately creates a wide-field image of the entire imaging plane. Because intermediate files generated during the reduction process consume a substantial amount of disk space, the routine performs checks of the success or failure of each step, and, at certain points, deletes unnecessary files, and organizes those selected for preservation. (Raw files, and those created prior to astrometry, masking, and stacking, are always retained so that the procedure is repeatable.)

SDFRED Software

Reduction software developed by the Subaru Telescope Collaboration, known as SDFRED [80, 84], is a C-based suite of programs facilitating detrending of astronomical imaging from the primary Subaru cameras. It runs specialized processing scripts as command-line executables on FITS data files, as opposed to a system like IRAF [117] (an extensive set of astronomical reduction tools) which creates its own execution environment.

In order to deal flexibly with a large quantity of data, a complex reduction pipeline was required for the initial reduction steps. The need for a general, scriptable, set of routines which would reliably (and with low rates of failure and human interaction) produce high-quality images for stacking, as well as the consideration that SDFRED was developed for issues specific to the Subaru telescope and its camera, motivated our adoption of this system. The scriptable, Python wrapper for IRAF known as PyRAF [100], would be an alternative system, and certain later reduction steps utilize PyRAF. However, SDFRED's corrections for Suprime-Cam's unique qualities, such as the unusual readout system (FIG. 3.5), mirror distortions, flat fielding, and the efficient combination of CCDs, were additional reasons for utilizing the specialized software.

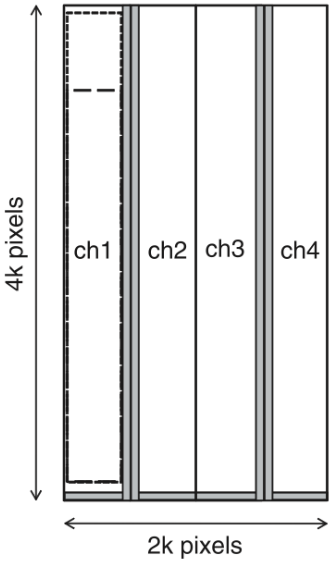

Figure 3.8: Readout areas for each CCD [38].

3.3.1 Initial Reduction Steps

Sorting & Overscan Subtraction

To organize the files which can be of various filters, flat types, targets, and dates, a routine was constructed which creates a folder system and organizes data hierarchically by necessary criteria based on header information. Based on the available calibration frames and total exposure times available for each filter in question, the program determines which type of flat fielding data will be optimal (§3.3.1). The files are also renamed.

Each of the 10 CCDs reads out charge data through four separate channels at the edges of the chip detection boundaries. Overscan regions on the edges measure line charge not exposed to light, for calibration of the readout electronics. The median pixel values of each overscan line are thus subtracted line-by-line for the corresponding pixels (for each channel independently), to remove the bias. The overscan regions and known blank pixels are then trimmed off, leaving gapless image frames for each CCD. Known hot pixels and bad regions are also masked out by this step.

Flat Fielding

CCD pixels exhibit different response rate behaviors to light, sometimes even within the same narrow waveband. Small engineering imperfections are unavoidable with such a large number of independent cells, so it is necessary to account for these differences by creating flat frames of each chip. These images consist of exposures of different lengths taken at twilight (when the sky is not completely dark), known as *sky flats*, or those taken of an evenly lit white screen inside the telescope enclosure, known as *dome flats*. Images of the target fields may be used as well to create *object flats*, as long as their contents do not repeatedly appear at the same positions and do not contain large extended objects. In all three cases, the flat frames must have been taken within several weeks of the observation (or optimally within a few days) to ensure calibrating against chip behavior which may vary over time, and must match the filter of the target data, as the detectors have different response rates to each waveband.

Flats are constructed by first normalizing the counts of each pixel, dividing by median of the image; then, having done this for each exposure, combining them into a final flat frame by taking the median of each pixel value and removing outlier pixels having offsets greater than 3σ from the median. Having made the flat, the pixel value of each data frame is divided by that of its corresponding flat frame pixel.

Creating flat frames is computationally expensive, and one of the longest steps, time/processing-wise, of the initial reduction process. The greater the number of flats, the longer it takes; however, the result is marginally better. A minimum of 3 flats is necessary, but we never used any for which there were fewer than 5 (and in situations where less than 10 flats were available but more object frames existed, object flats were preferred). Dome flats were preferred over sky flats because they are more evenly illuminated, and to save time and computing constraints, a database of completed flats organized by filter, type, and date, was maintained for fast completion of this step for data taken within 3 weeks of the previously created flat frames.

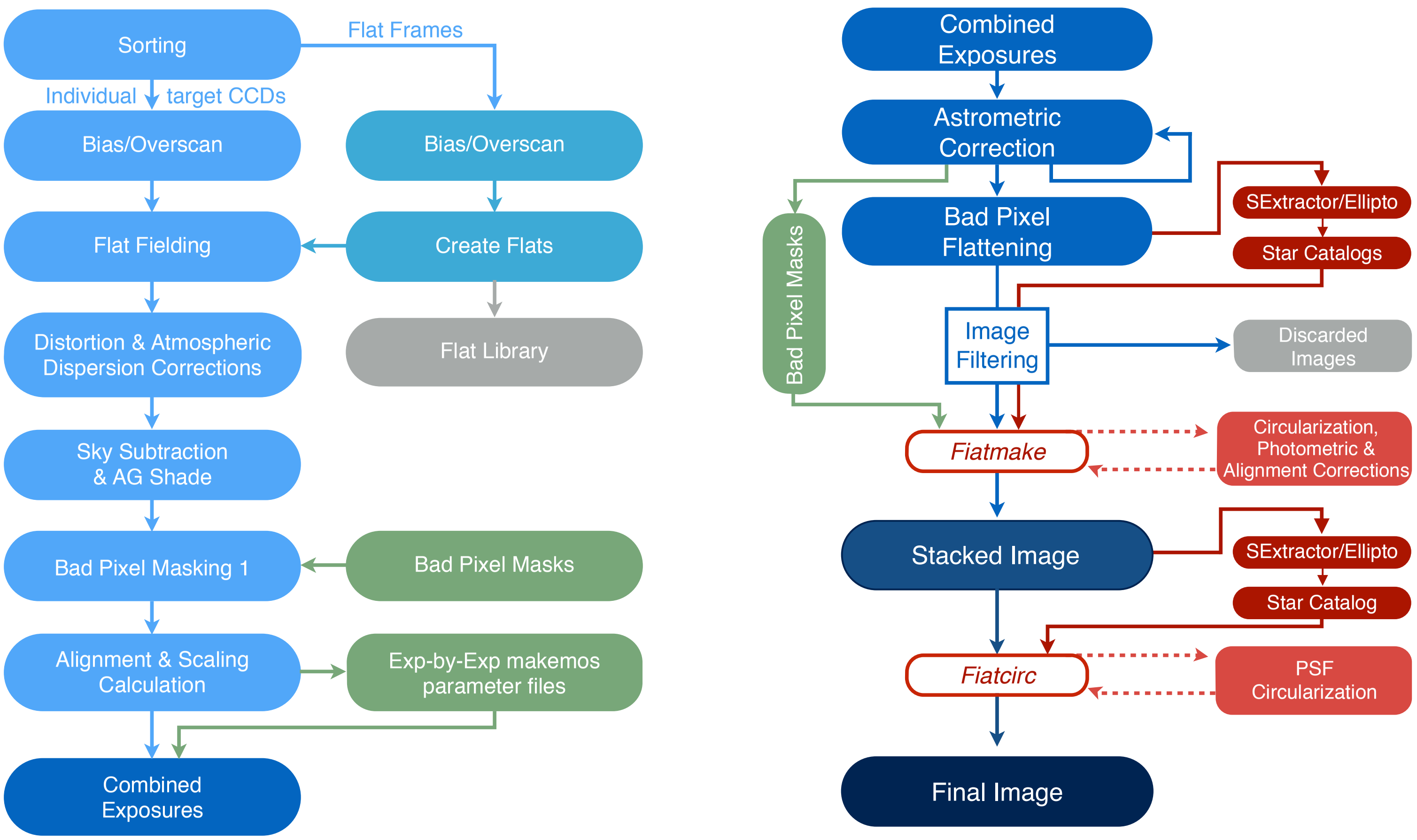

(a)

(b)

Figure 3.9: Image reduction framework. **(a)** Initial stages, performed in a fully automated process via the author's *subarutools* module, from downloading raw data to combined 10-CCD images of individual exposures. Left column shows operations on target frames while the right are calibration files (§3.3.1). **(b)** Actions taken from the creation of full-exposure frames to the eventual stacked and twice-circularized complete stack of quality images (§3.3.2–3.4.3). (Note that the "Bad Pixel Masks" differ. The first are standard to each CCD, the second are uniquely generated for each exposure.)

Distortion & Atmospheric Dispersion Correction

This step accounts for warping of the field created by the specific optics of the mirror. It also corrects for differential dispersion by the atmosphere, using the airmass value stored in the image header.

In the prescribed SDFred reduction process [80], this point would be where the PSF of each chip is computed, and the lowest-seeing images are degraded via Gaussian smoothing, to match the worst, high-seeing, frames, for eventual stacking by the *imcio2a* step. Although useful for certain astronomical objectives, this step runs counter to our goal of achieving the highest quality seeing data, necessary for the accurate shape resolution vital to weak lensing measurements. Moreover, our stacking process (§3.4) is completely different from the simplistic method performed by SDFred, and image degradation is unnecessary. Because of the number of images being analyzed, wherein it is not atypical to encounter several defective exposures as part of a large data set, the likelihood of over-smoothing a great deal of high-quality images would be significant. Instead, we choose to simply discard large-seeing images at a later step, rather than including them in the final data set.

Sky Subtraction

Light diffusion from the atmosphere creates a low level of mostly uniform luminosity across the night sky. Though greatest in areas near large amounts of man-made light sources, astronomical sources contribute as well, and some level of background is always evident. It is necessary to remove the artifact of this background noise from the exposure. This algorithm computes sky noise in overlapping grid boxes, and, after rejecting outlying values, subtracts it from the image. This leaves an image with mean background values of approximately zero and no spatial gradient.

AG shade

Subaru employs a guiding probe that, in certain alignments, may cause vignetting over a portion of the top edge of the field. This script uses the telescope orientation to determine whether to mask this area. This is a very straightforward process, however, the fact that it causes certain images to have different sizes (sometimes within the same set of target frames) necessitated a flexible procedure for mask creation in later reduction steps.

Bad Pixel Masks

In addition to the AG probe, regions near the chip edges are masked because they display a bizarre "frame"-like appearance. Parameter files generate these masks, which, depending on the CCD, mask between 20-50 pixels around the edges of the images. SDFRED masks regions by setting the specified pixels to -32768 ADU, which is low enough to be far below the range of usable data values. The scripts therefore ignore all points with this value throughout the reduction. A later step, §3.3.3, will reset the bad data value to 0 and instead designate these areas with linked mask files.

Alignment, Scaling, and Chip Combination

At this stage, the 10 CCDs of each exposure field are still separate. Suprime-Cam's 10 CCDs all have a different relative flux scale, with the further unfortunate tendency of even these flux ratios to exhibit minor variations with respect to one another from exposure to exposure[3]. Furthermore, precise relations between the position and relative rotations of the chips to one another are also important for any process of combining them. These remain nearly totally constant, but minor variations do exist.

SDFRED provides a two part routine for correctly combining CCDs and stacking them. The first, *makemos*, measures these aspects for each frame, to correctly stack them, and generates a parameter file with the necessary quantities. This file instructs how to alter the flux for each chip, and what their relative positions/rotations are to one another, in order for the second routine, *imcio2a*, to build them into a single composite stack of every chip. This (as intended) results in a single complete-field image.

These tools posed a particular challenge, as well as an opportunity. On the one hand, an automated method for quickly normalizing the flux between chips, designed for, and already tested extensively on, precise shift, rotation, and flux corrections, is very appealing. On the other, the original purpose of the system is for *stacking* the chips: overlaying them to combine the total light of each and create a deeper image, which uses the entire exposure time. It eliminates gap areas between chips. Our goal includes shape correction of the PSF, a correction that may necessarily vary between separate exposures (weather conditions at the ground and in the upper atmosphere

---

[3] A star on the reference chip, #6, would, on average, readout at ∼80% of its flux when imaged by the chip below it, #8. However, one day that exact ratio may be 80.5%, and the next, 79.8%—so the ratio must be found on a case-by-case basis.

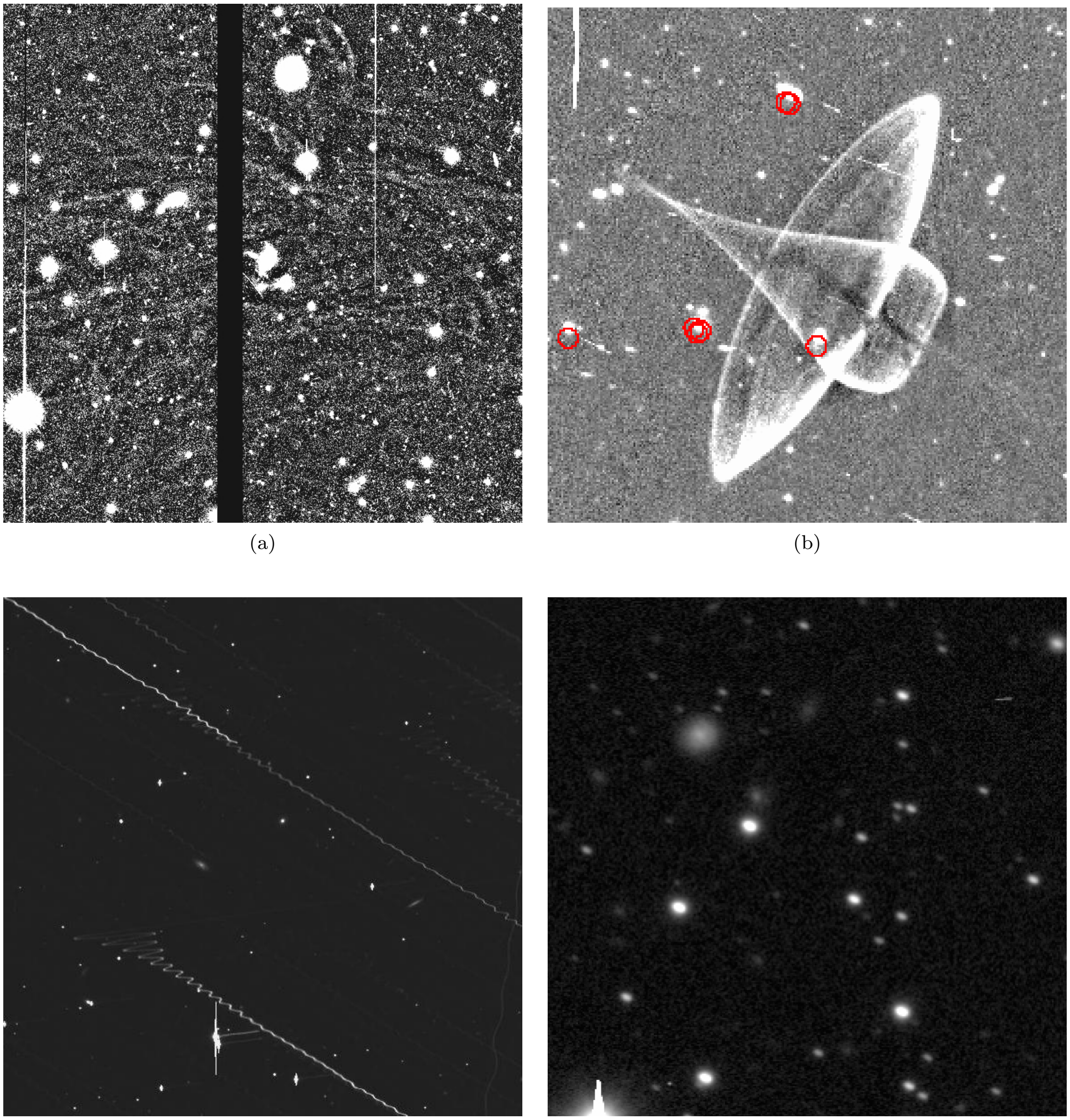

(a) (b)

(c) (d)

Figure 3.10: Various subtle image reduction difficulties. **(a, b)** Scattered light artifacts. The former is too significant to correct, the latter (showing a far smaller area) is clipped out in the stacking process. **(c, d)** Catastrophic and subtle tracking errors—both indicating unusable exposures.

often change over the course of an observing run). Although post-stacking corrections may be helpful, shape information is better maintained (and S/N strongly improved) by performing them prior to co-addition of the frames. The SDFRED stacking routine, as originally intended, is not optimal for weak lensing data. Nonetheless, there is nothing wrong with using the alignment and scaling adjustments (intended for stacking multiple exposures and *every* chip at once) for combining *only the chips associated with a single exposure* into images that contain the entire field for that exposure.

In addition to extremely accurate flux and chip location adjustment, there are many benefits to this approach:

1. Because low-order shape distortions occur outside the instrument, these effects are best measured and ameliorated in the PSF-correction stage by using frames which encompass the imager's entire field of view.
2. Astrometric corrections are frequently of this same nature, so lower-order corrections are more accurate, and full-plate solutions have a greater number of objects to optimize the fit.
3. Both of the previous factors are most significant for the edge frames, which receive less light and have a worse signal-to-noise condition. Corrections relying solely on these chips have an increased probability of failure because nearly 50% of their area is unusable.
4. Computing time for subsequent steps (astrometry, mask generation, cataloging, star selection, PSF correction, and stacking) is an order of magnitude faster, and the amount of disk space necessary for masks (which can be roughly equal to that of the data frames) is reduced.
5. Our star selection routine (§3.4.2) is better able to function reliably without human intervention when given an entire field rather than a single CCD.
6. Identification of fields where an issue (such as a tracking failure) ruined every chip in the exposure are far easier to find and discard when they are grouped in a single image.

For these reasons, the reduction process partially utilizes the SDFRED combination routine by breaking the parameter file into 10-CCD chunks and then using it to scale, shift, and combine the chips into single-exposure wide-fields. Subsequent reductions are performed on these single-exposure frames.

3.3.2 Astrometry

The Subaru Telescope data system attempts to add World Coordinate System (WCS) information about the astrometric coordinates of the pointing to the header of the FITS data file. This is a first-guess at the sky coordinates based on the pointing of the telescope and some knowledge of

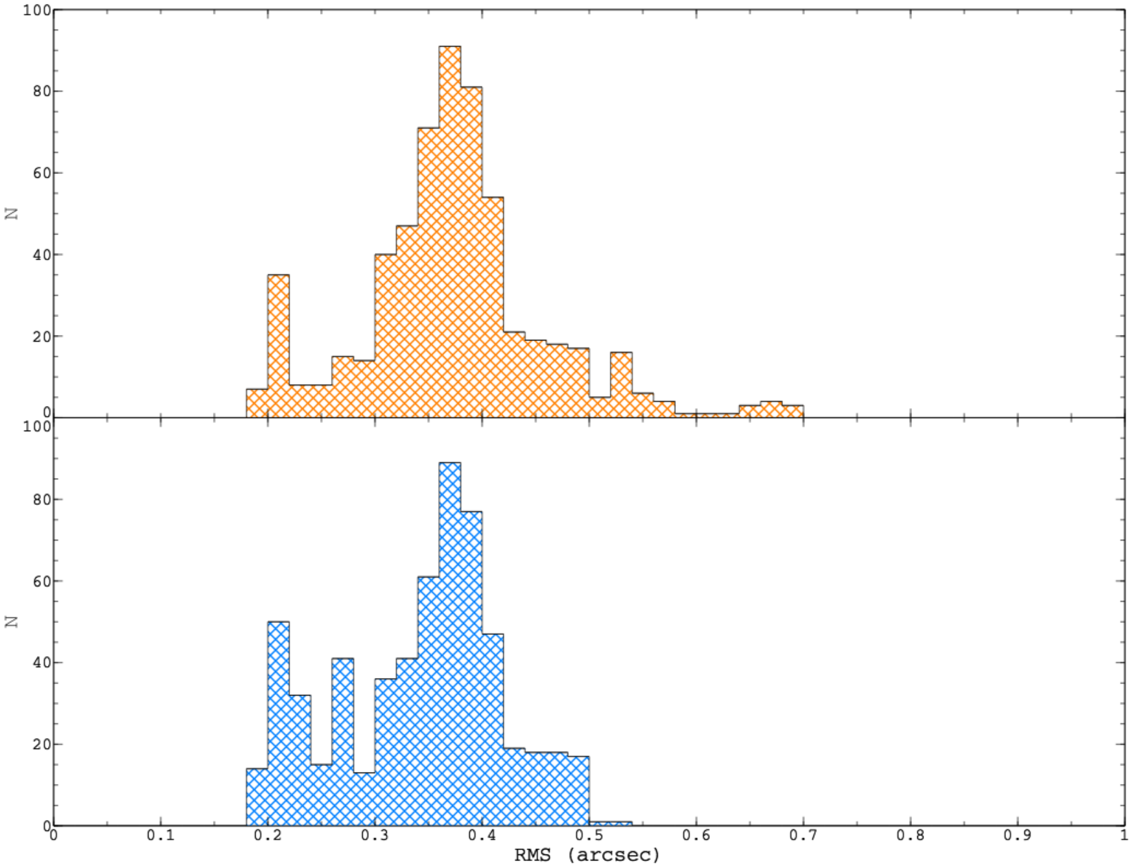

Figure 3.11: Average displacement RMS in arcsec of *msccmatch* astrometric fits for 590 fields. **(Top)** Values following the initial iterative astrometric correction routine, with up to 4 attempts. **(Bottom)** Final fit, with $> 0.5''$ fields having been further corrected using more aggressive object rejection.

the field geometry, and is relatively close to the actual right ascension (α) and declination (δ) of the objects captured, but minute adjustments are necessary to ensure exact agreement between the fields when stacking.

Astrometric correction was performed by use of PyRAF routines constructed to iteratively attempt an *msccmatch* fit [117] until the RMS dispersion of the external difference between the catalog position and the coordinates of the object in the FITS image was below $0.5''$ in both the x and y

dimensions[4]. The program retrieves the relevant portion of the US Naval Observatory all-sky object catalog (USNO-B1.0) [77], containing the position, proper motions, and magnitudes of the well-measured objects within the field of view. It first applies large corrections, then attempts successively fine-tuned ones. The iterative attempts are based on the output log of each subsequent attempt. If, after 4 tries, it has failed to match the image to within an RMS of $0.5''$, fitting attempts are performed with a more stringent object rejection criteria. The resulting correction is verified using an overlay of the USNO-B catalog over the final image, by the IRAF program *mscimage*. Due to the similar field size of the Mayall 4-meter MOSAIC Camera to that of Suprime-Cam, the MOSAIC-based programs were successful at achieving an astrometric solution to within a sufficient degree of accuracy in nearly all cases. Rare failed images were discarded from the data set.

3.3.3 Bad Pixel Zeroing and Mask Creation

Prior to exposure stacking, we generate masks corresponding to this value and reset the -32768 (error) pixels to 0, as the extremely negative values have undesired effects within our stacking routine. Having the mask generation method correspond to the specific bad pixel values allow automated programs to respond to heterogeneities between frames, such as size differences which are due to the variable nature of the AG probe masking routine, as well as saturation effects which are screened out in this manner (∼2% of the area of the frames). A pre-determined set of masks would not account for these correctly, and having chip gaps set to -32768 would cause blotchy stripes and remnants at unphysical high values around the field after stacking[5]. Using values of 0 (the average of the frame after sky correction) and associated bad pixel masks solves both issues.

In practice, bad pixel masks typically consist of FITS or pixel list (.pl) files with the the coordinates of good pixels having a value of zero, and the masked pixels having a non-zero value. (Though in our stacking routine, *dlscombine*, mask files must have this condition reversed.) The name of the mask is then added to the header of the data image. To make them in our process, a PyRAF routine duplicates the original target frame, then uses the IRAF *imreplace* command to create mask frames where corresponding good data pixels are “1” bad pixels are “0” and updates the header of

---

[4] A perfect solution is never possible, and would not actually be preferable due to the fact that the astronomical objects used for the fit have peculiar velocities which change their position over time (gradually reducing the accuracy of the USNO-B catalog astrometry). There is also an unavoidable level of measurement inaccuracy in the catalog itself and the routines analyzing the image. Fits between 0.2–$0.5''$ are generally considered the limit of astronometrical accuracy for these calibration datasets.

[5] Due to a peculiar behavior of our stacking routine *dlscombine*.

the target to indicate the mask's path.

We then set to zero the regions of the target images with bad pixels (while maintaining the association of masks for the images to be used in the final stacking process). This is necessitated by an anomaly in the *dlscombine* stacking program, which generates spurious high pixel values in areas where large discontinuities in pixel values occur in only one or several images of a stack. Upon co-adding, bands of incorrect values then occur in parts of the image which disagree widely on the value at certain coordinates of the images. The associated masks prevent the data in regions of chip gaps and masked areas from being incorporated into the final stack, and the zero values match the average sky value of the data, leaving nearby pixels unaffected by the anomalous co-adding behavior.

3.4 Alignment and Stacking

PSF correction and distortion subtraction is a vital aspect of any gravitational lensing analysis. Of recent innovations permitting weak lensing measurement to become an important tool for probing cosmology, post-observational shape correction is one of the most significant. As atmospheric dispersion and instrument effects can distort object shapes at a similar order to those created by lensing shear, a method of accounting for them with a ground-based instrument is required. This section describes the method of correcting for atmospheric and instrument error which would, if left unaccounted for, undermine many weak lensing results undertaken from ground-based observatories.

3.4.1 Object Cataloging & Shape Measurement

A vital step in both obtaining stellar properties for stacking and analysis of galaxy shapes is the construction of object catalogs. These bridge the gap between raw image files and manipulatable data. Astronomical catalogs take the form of text files with arrays of measured quantities for each detected object. SOURCE EXTRACTOR [9], a highly configureable source analysis program, is responsible for generating catalogs of resolved objects and their properties, while ELLIPTO [104], has a more specialized purpose of measuring the intensity moments of ellipticity (and associated quantities). ELLIPTO bases calculations on the SEXTRACTOR-generated catalog as well as the image, and reduces bias, particularly in the case of larger FWHM objects (such as galaxies), by modulating the shapes with a weight function of an elliptical gaussian profile (as opposed to a circular gaussian used by windowed mode SEXTRACTOR). Ellipticity moments (§2.2.1) are calculated in terms of intensity as

$$I_{xx} = \frac{\sum_i I_i x_i^2}{\sum_i I_i} \tag{3.1}$$

$$I_{yy} = \frac{\sum_i I_i y_i^2}{\sum_i I_i} \tag{3.2}$$

$$I_{xy} = \frac{\sum_i I_i x_i y_i}{\sum_i I_i}. \tag{3.3}$$

In turn, allowing us to describe the ellipticity qualities as,

$$e_1 = \frac{I_{xx} - I_{yy}}{I_{xx} + I_{yy}} \tag{3.4}$$

$$e_2 = \frac{2I_{xy}}{I_{xx} + I_{yy}} \tag{3.5}$$

$$e = \sqrt{e_1^2 + e_2^2} \tag{3.6}$$

$$\theta = \frac{1}{2} \arctan 2(2I_{xy}, I_{xx} - I_{yy}) \tag{3.7}$$

Utilizing different weighting functions is an important consideration which depends on the aim of the cataloging measurement. Weighting functions attempt to account for pixel noise and overlapping or nearby objects, and must be applied in differentiating between stars and galaxies—given that galaxies tend to have comparatively diffuse and elongated flux profiles, in contrast to stars, which exhibit more uniform characteristics. Stars, which are ideally circular in ground-based imaging, are best modeled as circular gaussian profiles, with a scale dictated by the seeing size and pixel scale. Elliptical profiles of exponential or "de Vaucouleurs" types best model elliptical and spiral galaxies respectively (convolved by a circular gaussian to account for atmosphere). At different stages of our analysis both approaches are important: accurately modeling and removing stellar PSF is best accomplished through use of a circular gaussian weight appropriate for measuring stars (employed by windowed-mode SExtractor), while Ellipto, optimized for weak lensing, employs elliptical gaussian weights in catalog construction which are better suited for measuring galaxy shapes.

3.4.2 Star Selection

Stars, in ideal conditions, should exhibit a circular shape profile in ground-based observations. However, all observations are subject to conditions like atmospheric turbulence, focal variations,

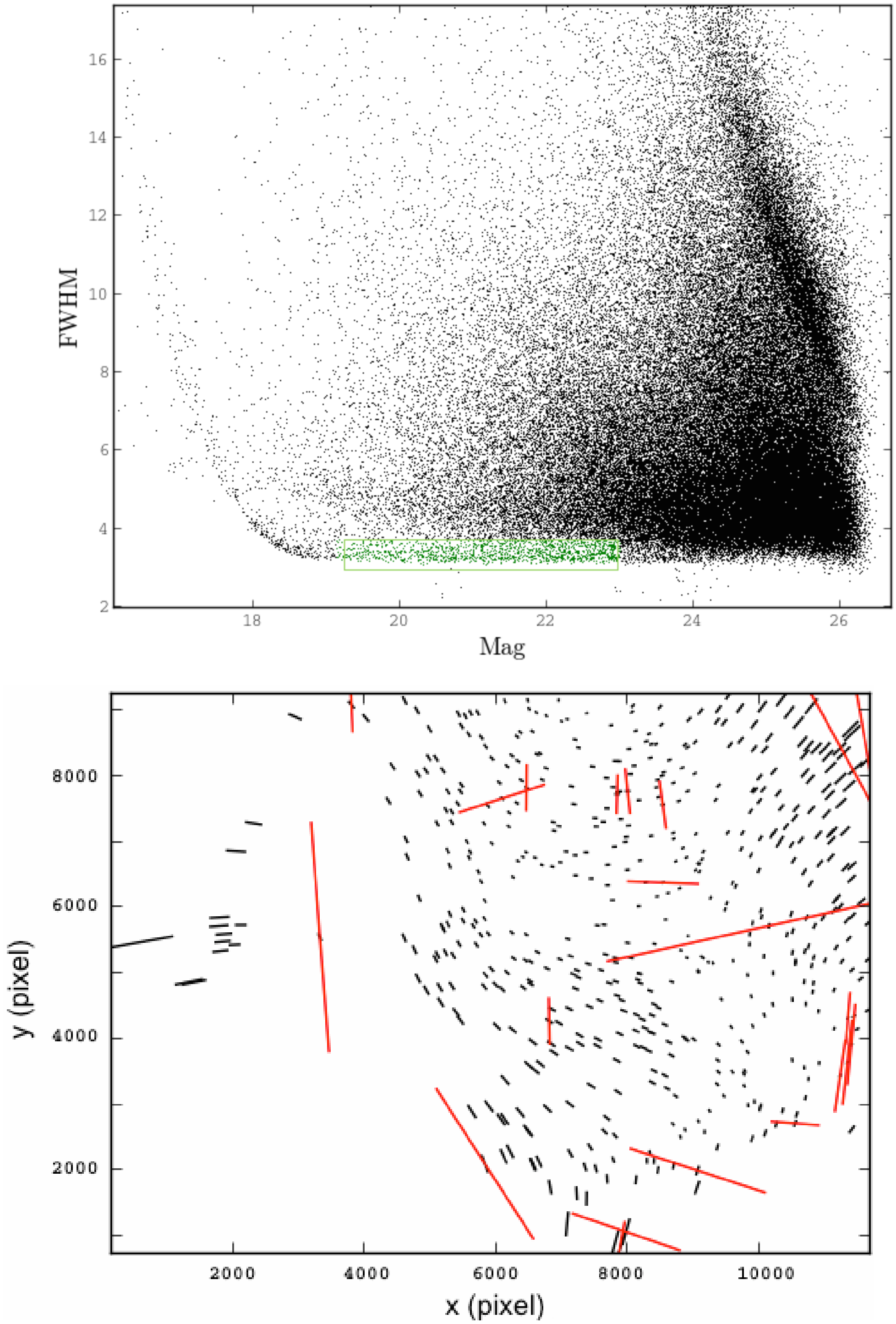

Figure 3.12: **(Top)**: Size-magnitude diagram for objects in an example field, taken from a single exposure. The box indicates the region of likely stellar objects. (FWHM in pixels.) **(Bottom)**: Whisker plot showing the unsuitably small area of the image that previous tools recognize as stars due to spatial PSF variation. (Highly elliptical objects in red.)

and instrument defects which warp their appearance. Therefore, deviation from circularity may be used to model local PSF distortion across the field and reconstruct an image as it would appear without these effects. Stellar ellipticities are further used as a diagnostic of overall image quality and suitability for lensing analysis. Therefore, a method of reliably detecting stellar objects from image catalogs are vital in the preparation of data.

Prior methods utilized a set of programs (*fiattools*/*dlstools*), originally developed for the Deep Lens Survey, that rely on choosing stars within a rectangular slice of the size-magnitude diagram, where the flat branch of the distribution denotes a class of objects of different flux values but constant size—a quality of stars, which, without atmospheric dispersion, would present themselves as point sources, and therefore display no increase in size as a function of brightness[6] (as opposed to galaxies, whose flux is proportional to their size, because it results from a diffuse collection of sources, when they are of resolvable extent). The FWHM of these objects depends on the atmospheric seeing conditions, but the primary sequence is approximately between 18th and 23rd magnitudes (depending on exposure time and filter). Nonetheless, the appropriate catalog section cannot be chosen automatically, due to variance in both seeing, and inability of the prior technique along with (*elliptostar*) to detect stars reliably (see Fig. 3.12).

This approach was unsatisfactory, because spatial variations in stellar PSF across Suprime-Cam's wide fields make it impossible to select clean star catalogs in this manner. Most samples left out stars from large sections of the image, or the catalogs contained far too many galaxies (PSF-correcting for which would degrade the lensing signal). Additionally, this method requires a very great deal of human supervision, sometimes repeatedly for the same exposure. The scope of this work required stacking on the order of $\sim 10^3$ frames. Even if it had been effective, visual interaction with each size-magnitude plot for every frame would be necessary. This would not, in itself, motivate a new star selection algorithm, however, it does add additional preference for replacement rather than modification of the original approach if possible.

SDFred possesses a means of selecting bright stars from an image, but this method is only effective for the very brightest (~15) stars per CCD, and does not behave reliably on a combined 10-chip image. It is intended for a different purpose than modeling subtle measurements of stellar PSF across a frame [38]. Their method lacks the necessary information to find minute PSF changes across the field with sufficient accuracy. Furthermore, using only the brightest stars of an image is

---

[6] Until they become luminous enough to saturate the detector.

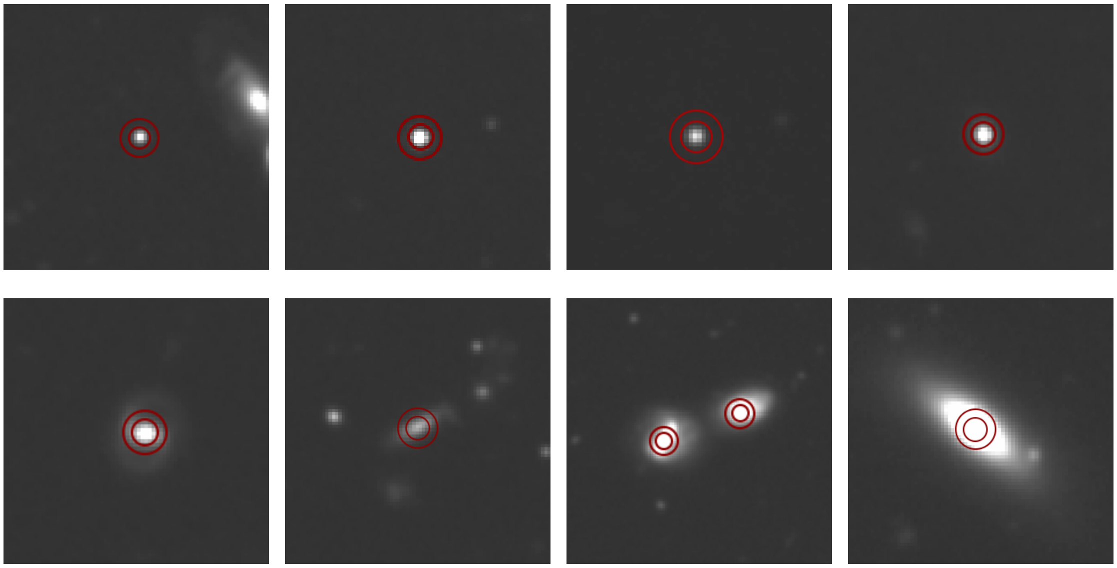

Figure 3.13: Various stars **(Top Row)** and galaxies **(Bottom Row)** showing the differential aperture technique used to classify stellar objects. Inner and outer photometric apertures are at $1.4''$ to $2.4''$ in diameter, creating the characteristic object parameter via $\delta_m = m_{\text{inner}} - m_{\text{outer}}$. As this demonstrates, a substantial difference between the value of the outer apertures versus the inner is the result of isolated, non-saturated stars only increasing in aperture flux due to the sky background, as opposed to galaxies which have irregular extended structure. (Sampled from 3600 sec EN1n1n1 stack in i', §4.4).

not appropriate for measuring PSF distribution because saturation may become an issue effecting the shape, and the response of CCD electronics to brighter extended objects is not fully representative of the local PSF distortion.[7]

Instead of either of these, a new approach, *subarustar*, providing a more accurate, efficient, and automated procedure for star selection was created. Based on the work of [93] and [82], *subarustar* employs Source Extractor to measure the magnitude of objects at two differently-sized circular apertures (in our case, $1.4''$–$2.4''$, though a range of similar values could be used, depending on the seeing resolution and pixel scale of the instrument). It then calculates the net difference, δ_m, and assigns this parameter to each pre-selected object in the catalog. As visible in plots of δ_m vs. total flux (Fig. 3.14), stars are clearly resolved as a distinct line, which allows for star selection which is independent of regional PSF and across a range of flux values.

---

[7] In order to select stars for the purpose of SDFred processing, the software catalogs each chip with Source Extractor (with a 2σ detection threshold). Then they count every object as a function of magnitude, and take 50 objects from the 15% percentile of brightest objects which are between $0.3''$–$2.4''$ in FWHM. Of these 50 objects, they have a new FWHM range which will be close to the seeing of that exposure. Having done this, Source Extractor now uses this value of SEEING_FWHM to run a test of the classification measurement CLASS_STAR, a parameter that seeks to identify how "star-like" an object is on a scale from 0 to 1. The SDFred routine ultimately chooses everything with CLASS_STAR > 0.9 and a size of the average seeing value within $\pm 0.3''$.

After building a catalog of the image, *subarustar* first removes any objects with erroneous measurements (those flagged by SOURCE EXTRACTOR or ELLIPTO with any code indicating an abnormality). It also filters any object near the edges of the image, where the distortion due to telescope optics is too great. Objects with an ellipticity greater than 0.3 are screened out (stars are never this elliptical in usable exposures). Saturated stars are removed (as well as streaks of large negative flux values created by the stellar bleed trails). Having pre-filtered these objects, *subarustar* then calculates δ_m values for each candidate and adds it to the catalog file. At this point, an iterative filtering algorithm bins the stars by δ_m and determines the flat trendline of the δ_m–FLUX_MAX plot, thus revealing the stars. Dispersion in optimal δ_m bin size varies as a function of the image's seeing and exposure length, so a range of bin widths is tested (this allows the algorithm to function on images where the PSF varies significantly across the field). The algorithm performs these tests at a higher flux range than is ultimately selected, because stars dominate the high-flux range of these catalogs. Having fit a satisfactory trendline at these values, the program uses the optimal δ_m fit and dispersion to extend the catalog cut to objects down to 1500 ADU, and only up to 30000 ADU, where saturation effects begin to appear (alternate boundaries accounting for passband or exposure time may be used).

The resulting selection is a cleaner star catalog than one generated through any previous approach. Fitting stars to a fixed δ_m value, as described by Richard (2005) [93] does not account for variable PSF values, which may increase or decrease within the overall trendline. Rather, an algorithm for treating large catalog sets must be responsive to the viewing conditions from night to night, and adapt to the sensitivity of the CCD for different filters. Furthermore, examination of sequential δ_m–FLUX values provides an easy test of seeing evolution over the course of observation, as δ_m fluctuations are shorthand measurements of the atmospheric dispersion when considered relative to other images taken that night.

Resultant catalogs were well in agreement with both size-mag and CLASS_STAR techniques, with tests demonstrating a SEXTRACTOR stellarity index $\geq$0.90 for 96.1% of 8125 objects in 10 randomly-selected fields with pre-measured stellar FWHM. Only 2.5% lay outside acceptable mag-size tolerances as judged by manual star selection. *Subarustar* catalogs are also more selective than either previous approach, excluding a substantial number of contaminating sources which could potentially degrade the PSF estimation and correction.

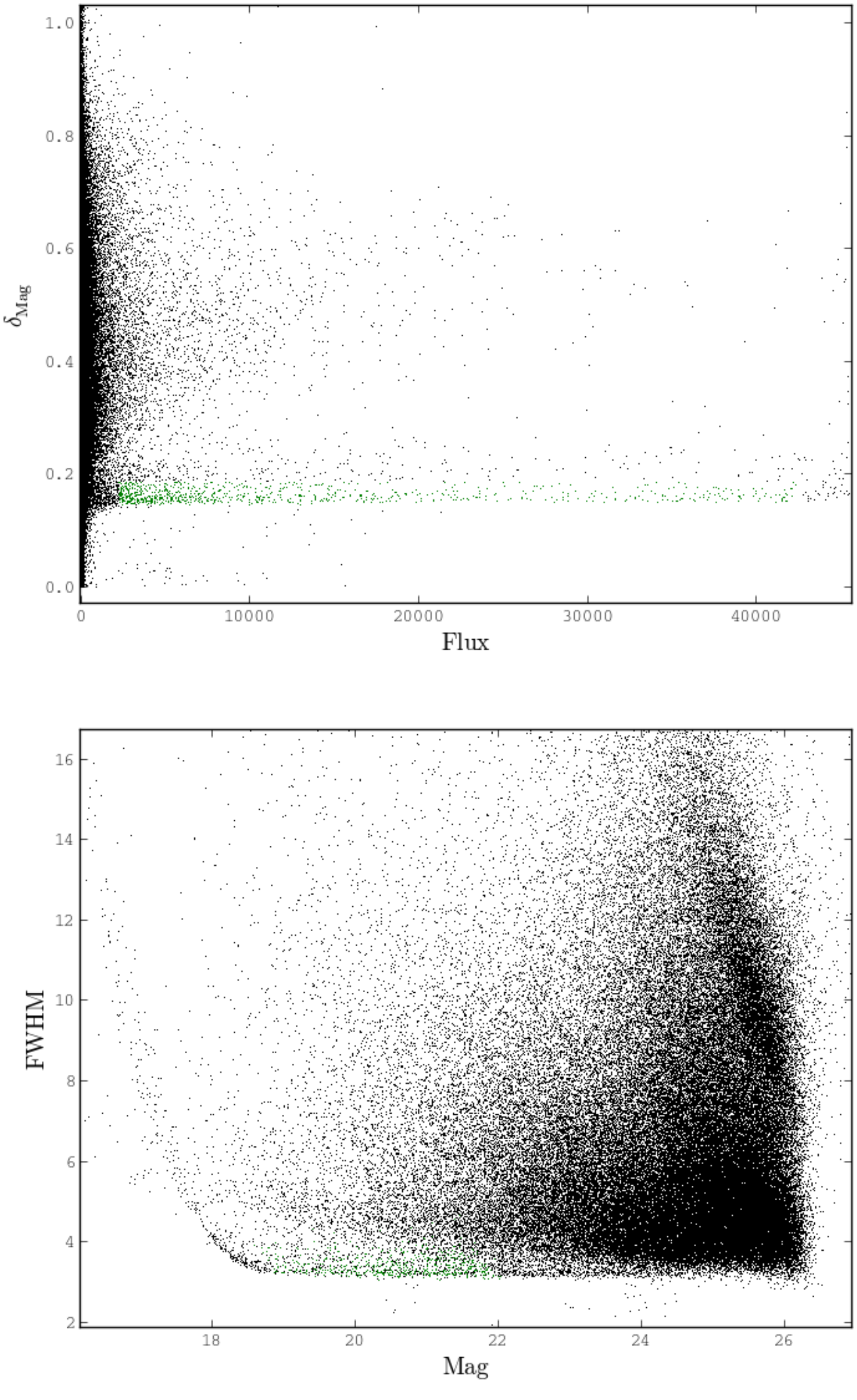

Figure 3.14: **(Top)** δ_m–FLUX_MAX plot of the same FIG. 3.12 catalog. The colored horizontal trendline is stellar objects. **(Bottom)** Selected stars via *subarustar* overlaid in green upon the original size-mag diagram. Note the exclusion of many objects within the selected "stellar" region as well as the differing magnitude cut-off (a judgement impossible to discern by eye, and a possible source of non-uniform star selection from frame to frame).

3.4.3 Exposure Stacking and PSF Correction

Ultimately combining reduced data frames into a full stacked image is a challenging task. Best methods for stacking and correction are often a matter of trial and error, however, our robust set of stacking algorithms, *fiatmake*, provides an adaptive framework for precise calibrations and co-addition of exposures. The primary steps it executes are:

1. Star selection via size-magnitude plot (in my process, replaced by *subarustar* before execution of *fiatmake*).
2. Optional astrometry catalog created from the SDSS database.
3. Polynomial fitting to the PSF in each exposure, as measured from the stellar catalog.
4. Coordinate transformation derived to translate each pixel of the input frames to a final point in the resultant stack.
5. Photometric scaling calculated through relative flux measurements of common objects.
6. Creation of the final image with these corrections taken into account. This final image is built through use of a predecessor routine known as *dlscombine* [35], which inputs original frames, scaling, the polynomial translation, associated bad pixel masks, and writes the output frame pixel-by-pixel.

We have the fortunate circumstance of dealing with a relatively homogeneous set of images at this stage of the process—Subaru data from a relatively narrow timescale, the same camera, pixel scale, optical distortions (within images of the same passband), field of view, and approximately similar numbers of useful stars. However, there are still some variances between filter responses, exposure lengths, field density, and seeing conditions. Each stack is subject to post-*fiatmake* examination to verify satisfactory improvement to the PSF distribution and visual follow-up to check for unusual artifacts or extraneous effects.

PSF Convolution

Although we pre-select on the basis of FWHM seeing size, atmospheric and optical distortions still warp the true object shapes. To recover them, we resample the data pixels through the application of a correction kernel. Having measured the stellar PSF shape across the field through the I_{xx}, I_{yy}, and

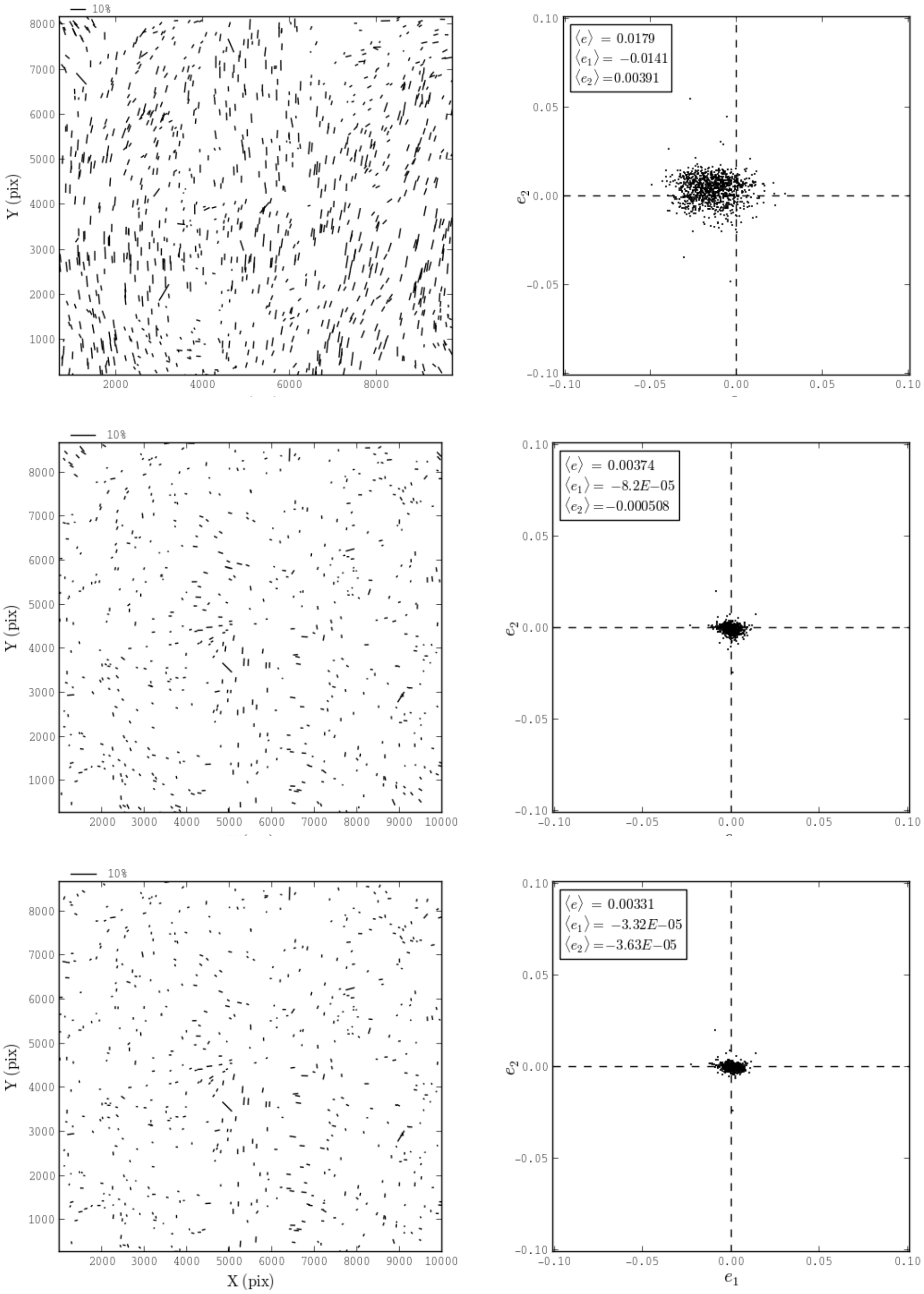

Figure 3.15: Stellar ellipticities of three successive corrections to the PLCK G100 field. (Plotted via my *vectron* ellipticity measurement tool.)

I_{xy} intensity moments, a localized circularizing solution is calculated for each frame. The correction, based on Fischer & Tyson's approach [35] utilizes a flux-conserving, analytically determined, 3 × 3 pixel convolution kernel (which is appropriate for the scale of high-resolution Subaru imaging, where a $0.2''$/pixel scale and $\lesssim 0.7''$ seeing results in stellar FWHM values in in the $\sim$2.5–4 pixel range).

The analytic correction is calculated as complementary moments to the stellar PSF measurements and interpolated across the field [19]. Taking $I_{ii} > I_{jj}$ (where i, j are x or y):

$$I^*_{ii} = |I_{ij}| \tag{3.8}$$

$$I^*_{jj} = |I_{ij}| + I_{ii} - I_{jj} \tag{3.9}$$

$$I^*_{ij} = -I_{ij} \tag{3.10}$$

The kernel is

$$k_{00} = \min(1 - I^*_{xx}, 1 - I^*_{yy}) \tag{3.11}$$

$$k_{-10} = k_{10} = 0.5[I^*_{yy} + (1 - k_{00})] \tag{3.12}$$

$$k_{0-1} = k_{01} = 0.5[I^*_{xx} + (1 - k_{00})] \tag{3.13}$$

$$k_{-1-1} = k_{11} = 0.25[I^*_{xx} + I^*_{yy} + I^*_{xy} - (1 - k_{00})] \tag{3.14}$$

Cross-Ellipticity Irregularity

The primary difficulty detected among stacked fields was that of stellar "flattening" across the e_1 and e_2 ellipticity modes. Although circularization to both e_1 and e_2 were below RMS values of 0.5%, a relative spread in e_1/e_2 between $\sim$1.2–1.8 was occasionally found. The improvements to stellar PSF based on standard PSF-correction methods were significantly greater than the resultant ellipticity distortion and there was no spatial correlation to this effect—aggregate ellipticity moments exhibiting this phenomenon were consistent across images, with no spatial variance—meaning that lensing measurements could potentially be suppressed, but not exaggerated.

The primary reason for this effect is the slight irregularity and rectangularity of pixels on the post-2008 Suprime-Cam CCD imager [123]. The aforementioned reference, von der Linden *et al.* (2014), contains an unofficial description of this instrumental defect (which is under-reported in literature about Suprime-Cam). To quote: "These have the unusual [artifact] that the pixels vary in shape and size; the divisions between pixels are not straight lines, but are curved (Miyazaki, private communication)." As such, when stellar resolution closely approaches the CCD pixelization limit (as in cases of very clear seeing often selected by choice in this work), e_1–e_2 tests of circular objects, measuring "up–down" versus diagonal moments, lose accuracy when weighted by their elliptical convolution kernel in windowed-mode SExtractor and Ellipto. Circular weighting functions more accurately fit inherently circular stellar shapes, and are less prone to this effect.

The consequential test of this instrumental aberration against WL measurements are further explored in §4.2 & 5.2, where we demonstrate the agreement of circularized fields with prior independent measurements of known clusters.

Post-stacking Measurements

Following initial stacking, secondary correction is applied by *fiatcirc* circularization at higher order[8] to remove any further trace ellipticity. If the resultant field is satisfactorily circularized, object detection and cataloging is performed, with filters for flagged, saturated, and non-physical measurements. The intensity moments based on this initial catalog are remeasured by Ellipto with an elliptically weighted gaussian kernel, and filtered again. A sharpening transformation on the catalog shapes developed for ground-based measurements, based on Bernstein & Jarvis (2002), *seeingcorrect* [8], is applied, as a correction to the shape profile degradation of the atmosphere. This process utilizes measured parameters based on the sky background noise, seeing PSF, and shape measurement error, to reconstruct a set of ellipticity moments as they would appear without the atmosphere.

The next chapter continues with discussion of galaxy filtering constraints, mass map generation, calibration, and large field detections.

---

[8] 4th or 5th depending on which yielded the best stellar circularization on a case-by-case basis

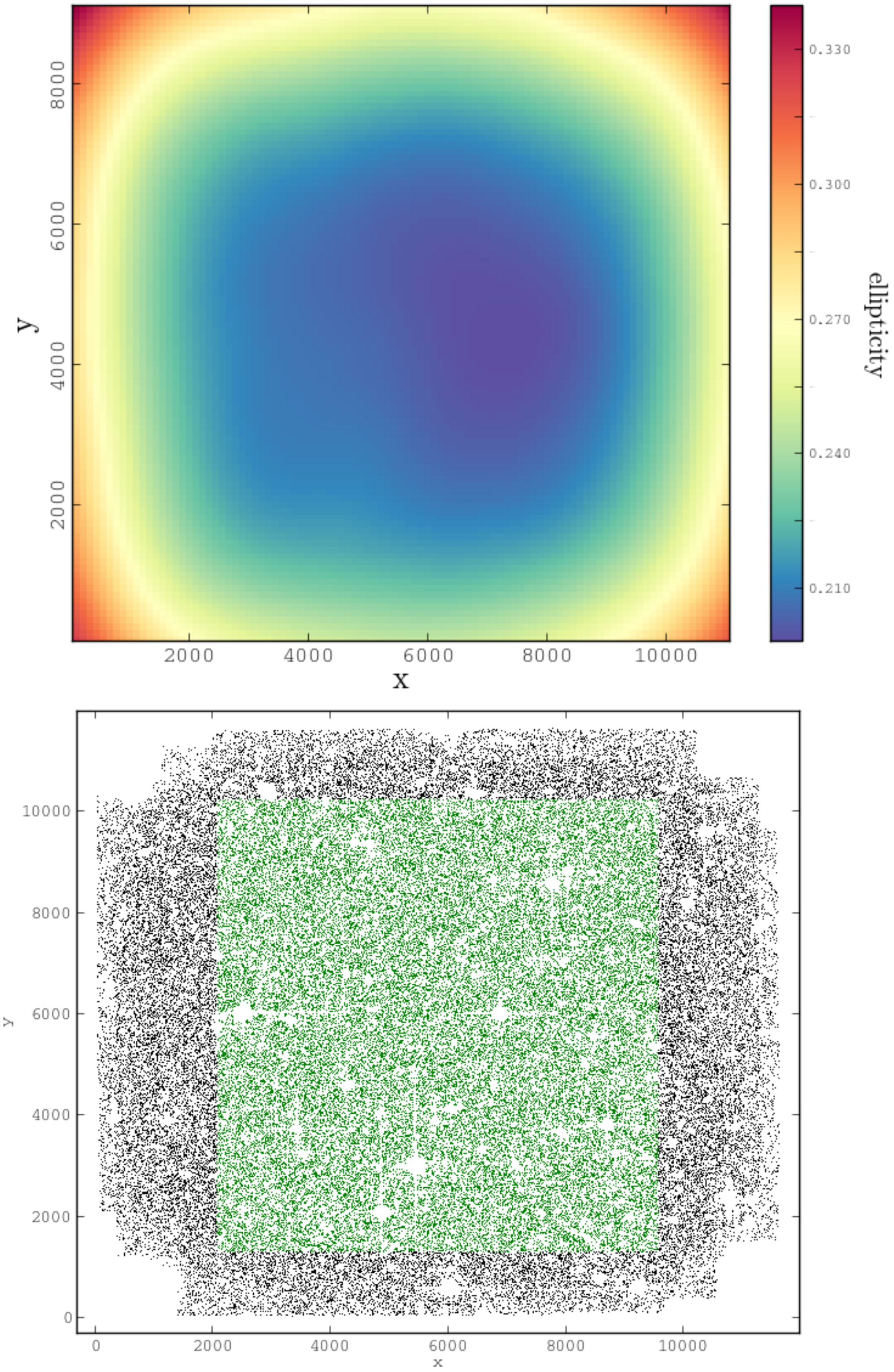

Figure 3.16: **(Top)** Overall mean ellipticity, for all detected objects measured across the entire field of view in an example image. (Note: rectangular field rescaled for a square plot.) **(Bottom)** Size, in pixels, of the useful, $24' \times 24'$, region of the Suprime-Cam imager.

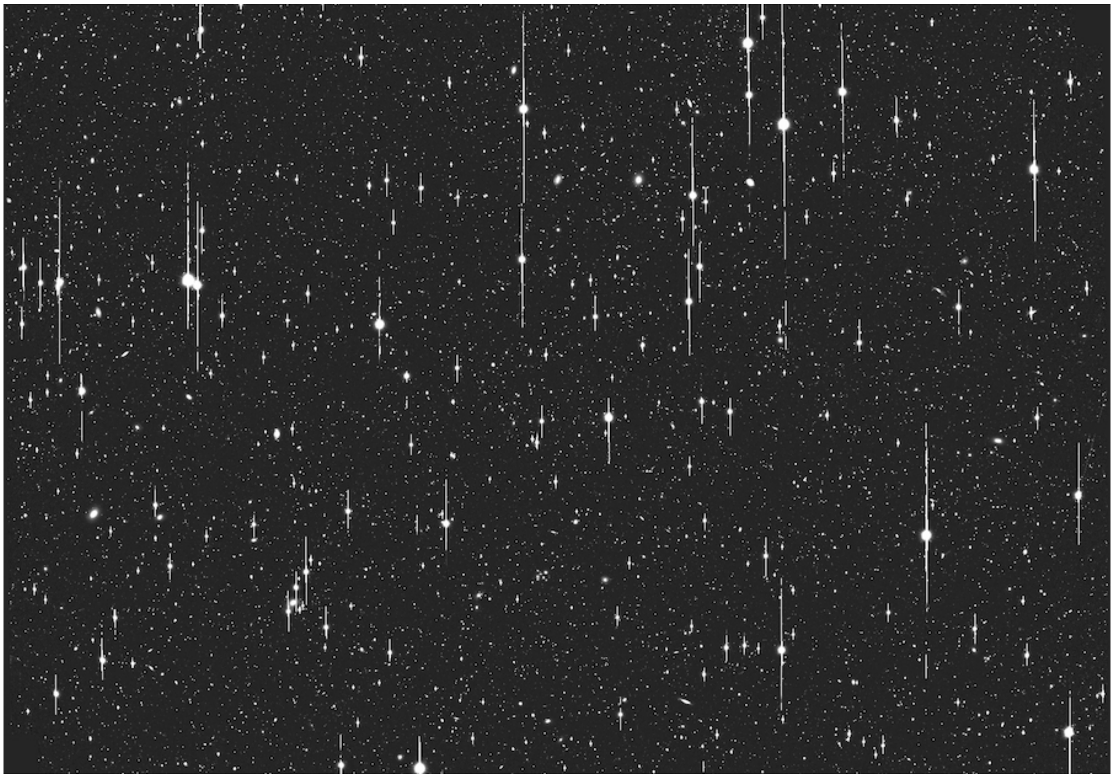

Figure 3.17: Example of a complete wide-field stack. This frame depicts the region near the Hercules Dwarf Sph Galaxy in the I_C band. 3200 sec from ten 320 sec exposures.

Chapter 4

Wide-Field Cluster Calibrations and Detections

"It's like a jigsaw puzzle, all one color.
No key to where the pieces fit in.
Why?"
Captain Kirk, *Star Trek*, "This Side of Paradise"

The raw survey sample consisted of over 120 separate fields, and $\gtrsim 25$ square degrees of the sky. Nearly 13 TB of data were reduced. To meet quality standards, however, the final sample was pruned significantly, and only the highest-quality data taken under self-similar observational conditions is presented here. We rejected every field with seeing $\geq 0.75''$ to create our own survey, pre-selected for galaxy densities above $20 \geq$ gal/arcsec^2.

Our initial intention was to capture the greatest amount of non-cluster-specific images and perform a blind study on it. However, so much Subaru imaging is oriented towards cluster studies that human selection-bias led to the realization that selected fields would find an unnaturally high number of clusters, and massive intermediate redshift clusters will obscure the signal from smaller unseen clusters. Thus, we oriented our search, in particular, towards fields which had no cluster-specific purpose: proposals focused on high-z objects such as AGN, Quasars, Lyman-alpha blobs, and, most usefully, follow-up observations of large regions of the sky covered by previous studies.

This chapter is devoted exclusively to the large congruent regions of the sky meeting these standards, on which we perform a wide-field cluster detection effort. First, we describe catalog filtering methodology, generation of convergence maps, statistical quality measures. Then we provide a verification check of our pipeline and analysis techniques through a detailed examination of a single cluster, Abell 781, well-studied in independent work, as a comparison. We then give a general description of the data sample, and the results of this survey for each of the five areas of the sky explored. Charts of our candidate clusters are provided, and discussion of measurement precision and selected comparisons with other cluster surveys.

4.1 An Independent Subaru Survey: Goals & Approach

Galaxy cluster observations are among the most common applications for Suprime-Cam [112], due to the exceptional suitability of the instrument for wide-field multi-band extragalactic astrophysics. Therefore, a straightforward number density survey of clusters would not be possible, owing to human selection bias in telescope pointings favoring cluster-rich regions. (Especially among those consisting of $\gtrsim$1000 sec of exposure time in red and near-IR bandpasses.) Thus, we divided the complete sample into 3 regions of interest:

- Large-angle uniform observations lacking well-known clusters
- Known clusters lacking weak lensing measurements
- Known galaxy clusters with lensing measurements (as a calibration check, and potential refinement of earlier results)

This chapter explores the first category, broadly speaking. Five areas of the sky comprise the largest self-similar areas of the sky imaged by Subaru since 2008. They are each wide enough to encompass previous work where cluster searches (using other techniques) have been performed. However, the cluster detection methods used are extremely varied in both quality and redshift range explored. Among a subclass of the third category were previously discovered clusters possessing redshifts not sufficiently distant to contaminate a potential WL signal at the higher redshift scale probed. Secondly, because of the wide field-of-view, some regions can contain multiple structures at distances which interest us. Due to the public availability of the data used in this project, we emphasized relatively new data, as being the most profitable to all 3 categories. We return to a specific description of these areas in §4.3.

4.1.1 Catalog Filtering

Mass reconstruction by weak lensing, particularly when dealing with large field samples where cluster detection itself is the primary objective, necessitates a rigid constraint strategy for filtering undesirable objects which degrade or bias the lensing signal. To select for background galaxies, our clipping scheme has three main goals:

- Elimination of objects too faint or small to have accurately measured shapes
- Removal of galaxies likely to be in the foreground of the sample or be members of the cluster
- Removal of stars and bad detections

As described in §3.4.3, object detection in the final stacked images is performed with SExtractor and Ellipto; we then attempt to remove non-galaxy objects. We cut objects with an error code greater than zero, reverse exclusion of the stars (based on the star selection method described in §3.4.2), objects of size greater than SIZEE=50 (which are too large to constitute background objects), erroneous negative size measurements, outliers in shape measurement error[1], and all remaining magnitude and size outliers. Image edges, particularly along the x-axis, were clipped aggressively because the rectangular nature of the imaging field results in signal degradation more than ∼4000 pixels from the center of the plane. The effective field coverage is $24' \times 24'$ for single exposures, and can be slightly wider with substantial dithering and depth, so this was accounted for on a case-by-case basis by inspection of variance in background sky noise.

In order to select for reliably shape-measured galaxies, we only include objects with PSF size more than 20% above minimum local PSF size for small objects in the field. Faint objects are discarded as well, with removal of the faintest 10% of the effective magnitude range.

Because this chapter focuses on blind, wide-field attempts at convergence peak detection, we do not apply aggressive filtering of foreground galaxies, as these fields are not targeted at specific clusters or redshift domains. In the next chapter, where the goal is measurement of cluster weights, the foreground is aggressively pruned through removal of objects with estimated redshift below the known cluster redshift (see §5.1.1).

---

[1] "mean_rho_4thE" and "sigma_eE"

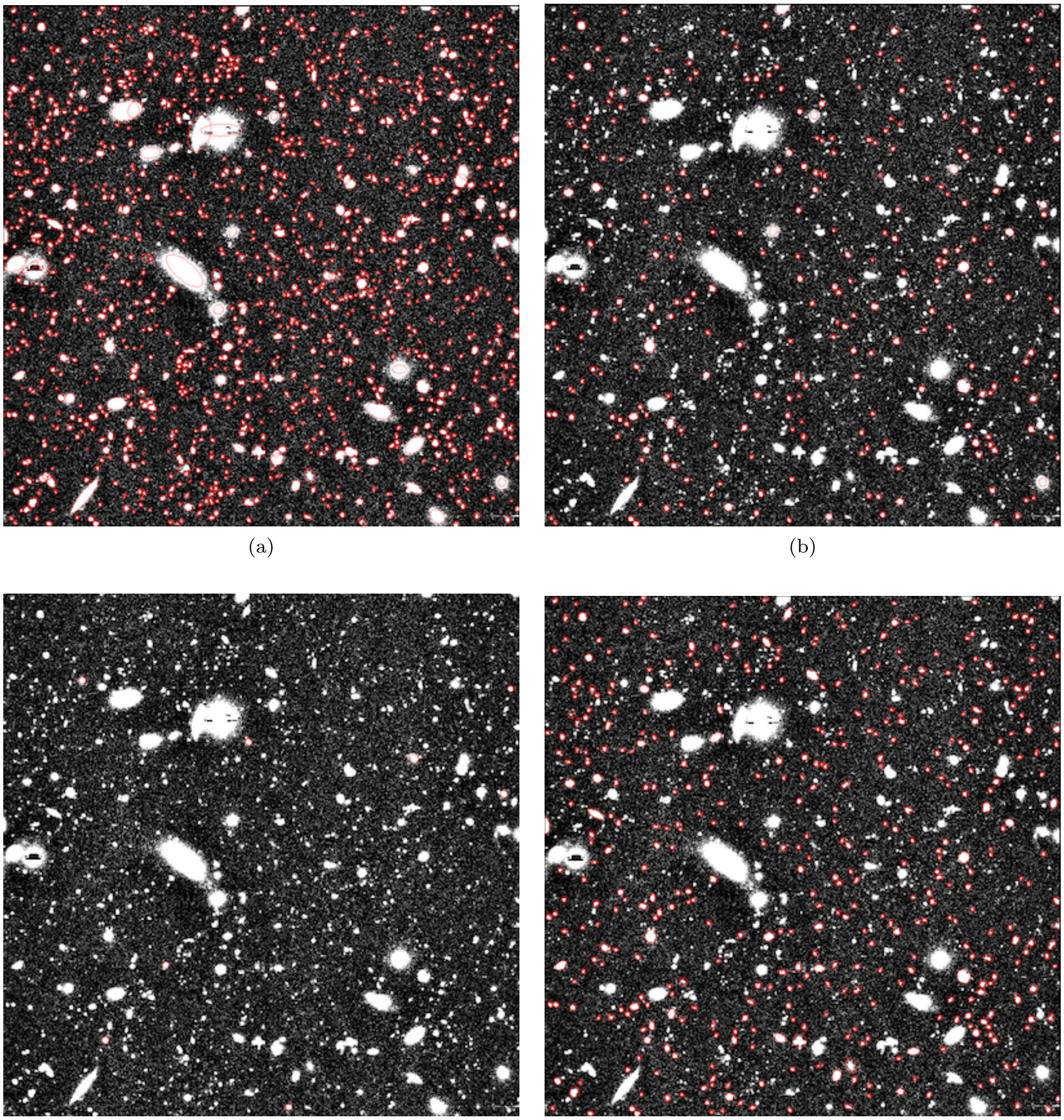

(a) (b)

(c) (d)

Figure 4.1: Succession of catalog filtering stages for a portion of the EN1n1n1 field stack (3600 sec in i', §4.4). **(a)** Raw SExtractor catalog, (144,610 objects). **(b)** Ellipto'ed catalog filtered to potential stellar objects, prior to execution of the *subarustar* star-selection algorithm (29,192 objects). **(c)** Automatically determined stellar objects (798 stars). **(d)** Filtered galaxy catalog (28,427 objects).

4.1.2 Generating Convergence Maps

We generate convergence maps based on the approach of Wittman *et al.* (2006) [129]. The *fiatmap* algorithm [56] finds convergence values within particular "blocks"[2] sampled across the field in question (supplied via a catalog of weighted galaxy moments calculated by Ellipto) (Fig. 4.3a).

---

[2] Not to be confused with *pixel* blocks, assigned only in order to specify the resolution of the S/N sample.

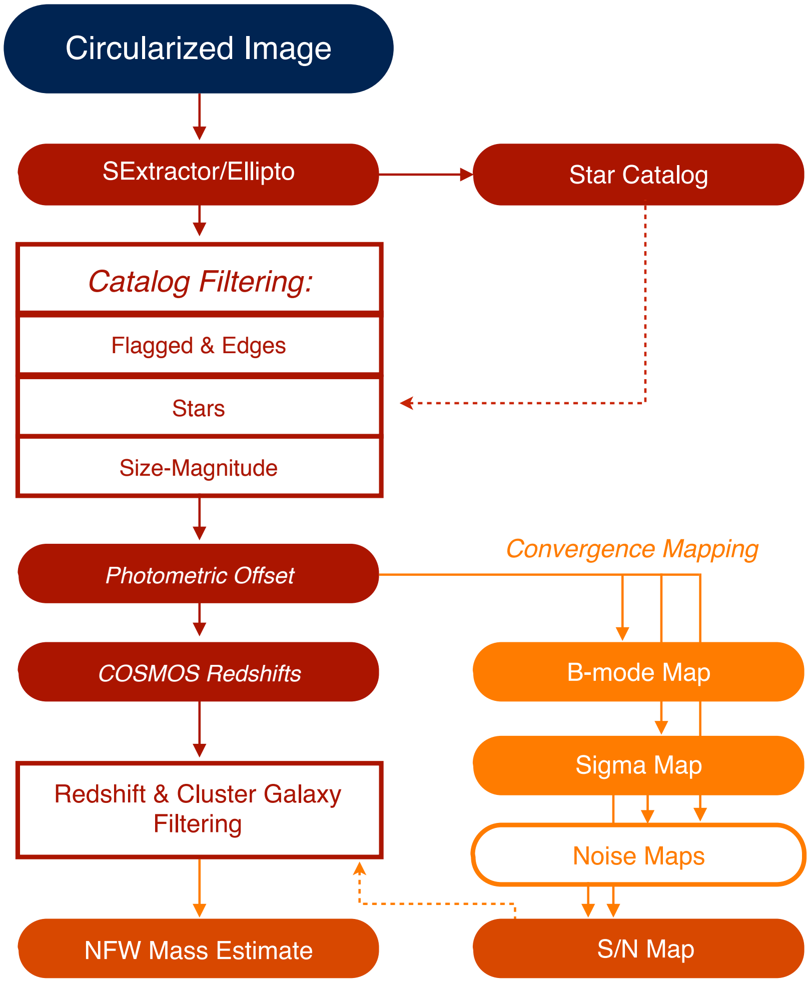

Figure 4.2: Catalog filtering, S/N map, and mass estimation process. (Continued from FIG. 3.9).

The convergence measurement, (as described in §2.3.1) is

$$\kappa(\vec{\theta}) = \frac{2}{\pi n} \sum_{\text{galaxies}} \frac{W(\vec{\theta} - \vec{\theta}_i)|\vec{e}_{\tan}(\vec{\theta}_i)|}{|\vec{\theta} - \vec{\theta}_i|^2} \tag{4.1}$$

where $\vec{\theta}$ is the location of the measurement and $\vec{\theta}_i$ is the location of the galaxy being summed. The weight function, $W(\vec{\theta})$, is given by

$$W(\vec{\theta}) = \left(1 - e^{-|\vec{\theta}|^2/2r_{in}^2}\right) e^{-|\vec{\theta}|^2/2r_{out}^2} \tag{4.2}$$

The structure of this weight function suppresses the fluctuations at small radii, where the contribution of a small number of galaxies can strongly influence κ. The r_{out} parameter, the outer radius, prevents the shape noise from the much larger number of distant galaxies from overwhelming the signal.

The strength of the mass reconstruction signal is subsequently gauged through comparison against estimated noise maps. These are created through a Monte Carlo-type approach: *fiatmap* generates 100 convergence maps based on the input catalog but with randomized galaxy shapes. In the generation of noise maps, position information is preserved, however, and the variance between the signal at corresponding pixels across the set is used to assign each pixel an average noise value dominated by shape noise. Assuming aggregate randomness in the 100 maps, the variance of the signal ought to provide Gaussian shape noise error, and gives a 1σ level of the measurement at each point (Fig. 4.3b). Dividing the genuine signal by the noise at each pixel produces a signal-to-noise map (Fig. 4.3c).

Replacement of the tangental ellipticity (E-mode) used in the generation of convergence mapping, with that of the B-mode (curl-like) ellipticity, rotated at 45°, gives an additional check in systematic distortion in background galaxies. B-mode signals ought to vanish when substituted for their E-mode ellipticity counterparts in calculations of κ, therefore finding significant peaks approaching the strength of E-mode signal indicate flaws in the galaxy catalog. B-mode ellipticity is given by:

$$e_B = e_2 \cos 2\phi - e_1 \sin 2\phi. \tag{4.3}$$

Since WL does not generate a residual B-mode signal, anomalous peaks corresponding to those found in E-mode maps are an important check on the creation of lensing maps. *Fiatmap* creates them as well, in the same method as S/N maps (Fig. 4.3d). In practice, such B-mode signals are often seen to some extent among 2D mass reconstructions which accurately model the lensing system. Because they are essentially random fields which do not correspond a physical lensing quantity *per se*, in wide sky areas with many source galaxies, the large number of samples means that $\gtrsim$3 S/N B-mode peaks are not so rare. Nonetheless, a small B-mode signal in comparison to the E-mode peaks is a good indication of successful detection, while B-modes comparable to or greater than the lensing signal cast the signal into doubt.

We define the spatial extent of sampling around each pixel as r_{in}. Nearby pixels provide similar results, as they share the majority of the objects within this block, but as we vary r_{in}, we can examine the S/N of signal peaks to optimize the correlation scale of the sampling. The maximum

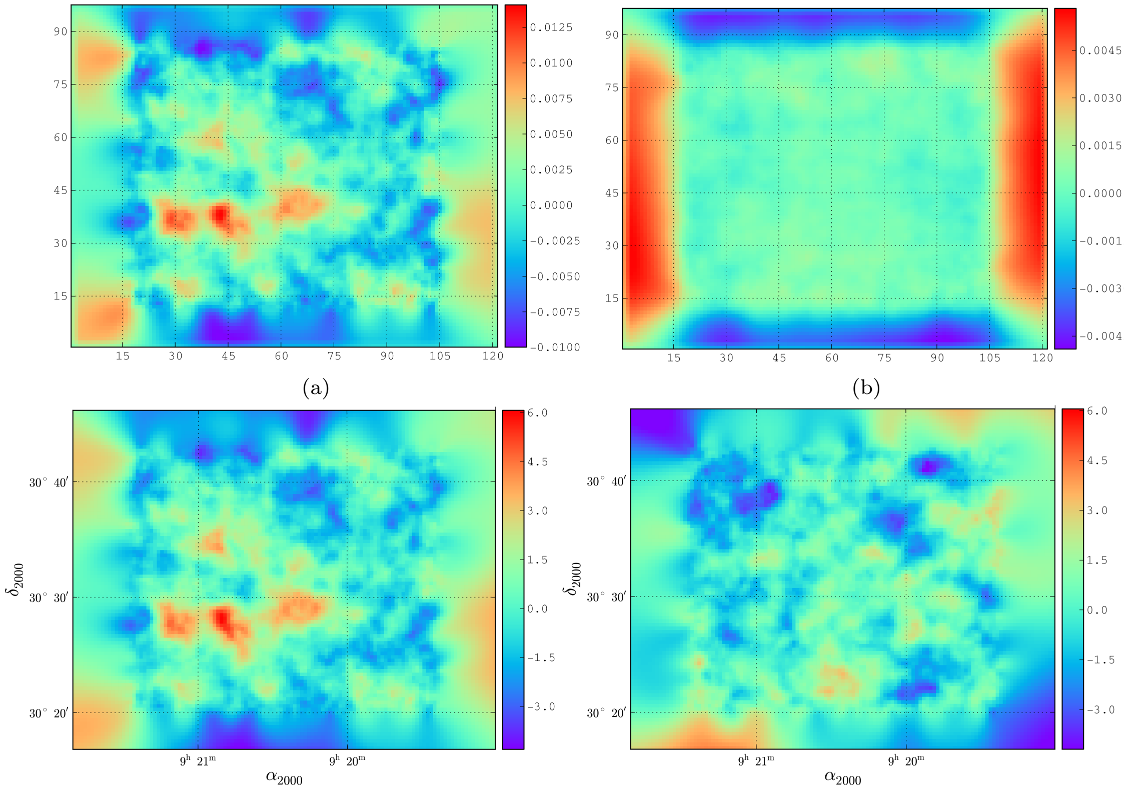

(a) (b)

(c) (d)

Figure 4.3: *Fiatmap* results. **(a)** Convergence signal map, **(b)** Noise map, **(c)** Signal-to-noise map, **(d)** B-mode S/N. Note edge effects due to mismatch between galaxy catalogs and extent of FITS stack which provide the WCS. Edge regions do not correspond to data catalogs and are trimmed in subsequent analysis. (Taken from Abell 781 data, §4.2.)

S/N will occur at an r_{in} which matches the angular extent, or "characteristic scale" of the peak. In our wide-field sample, we measure the convergence at 4 different scales to detect clusters in a varied size range. We chose to use a range of the following scales: $1'$ (300 pix), $1.67'$ (500 pix), $2.33'$ (700 pix), and $3.33'$ (1000 pix), and only select out the highest detection signal to indicate the angular scale of the potential cluster found.

The resulting output of *fiatmap* are FITS files, with each "block" represented by a pixel, and the WCS values inherited by comparison to the header of the original stacked image from which catalogs are drawn (as well as the RA & DEC values of the images in those catalogs). The catalog is trimmed substantially, both in terms of characteristics for selecting suitable galaxies (§4.1.1), and to remove the edges, where quality is suspect. However, output maps extend to the full size of the original image, including the regions trimmed out of the catalog, so a clipping process is performed to match the final maps to the size of the catalogs.

The resolution size utilized for wide-field regions of this chapter are within several pixels of ∼150 pix[3]. Providing pixel blocks 2-6 times smaller than the characteristic scale being examined, while also limiting the substantial processing resources required to produce over 200 maps, allowed for an effective measurement process. This resolution size does, however, result in a relative uncertainty of $0.5'$ for any given peak location. Larger pixel block sizes, because they span more of the section area, can have a slight tendency to reduce the signal strength of convergence peaks—though block sizes on this scale are sufficient to avoid correlation with suppressed signal on our narrow scale (300 pix, 500 pix) measurements *relative* to the wider ones (700 pix, 1000 pix)—but it is worth noting.

Furthermore, because of the unscriptable nature of the *SeeingCorrect* routine, this was not implemented in the generation of maps in this chapter (though it is used in mass estimates in the next). De-convolving object shapes to reconstruct atmospheric blur (effectively "sharpening" the objects) is primarily relevant to measurements estimating cluster mass—attempting to match the sky to the true object shapes prior to atmospheric distortion in order to calculate lensing shear. The goals of Ch. 4, the generation of 2D mass maps via convergence, are based on *relative* difference in ellipticity across the field of study; therefore, this type of *en masse* shape alteration will not effect the proportional strength of the lensing peaks used to locate cluster candidates.

4.1.3 Statistical Methodology

Though S/N calculations are already inherently based on systematically-sensitive noise measurements, we added an additional metric to gauge the extent to which convergence peaks were found outside of the normal distribution created by random shape noise of the sampled galaxies. Due to the fact that the overwhelming number of pixels in any map do not correspond to a lensing signal, the S/N maps exhibit a normal distribution in terms of $N_{\rm pix}$ vs. S/N. Signal peaks occur at the maxima of the S/N-distribution, so quantifying their value in terms of standard deviation to a fitted gaussian gives a further gauge of their significance, relative to each map. Departures from gaussianity, as seen in Fig. 4.4 (particularly clear in the logarithmic plot), represent the true convergence signal. To calculate this, histograms of each field are created based on the FITS–format convergence maps, and fitted to a normal distribution (pruned by 2% at the edges to account for departures from

---

[3] As a result of the specific behavior of the *Fiatmap* software, it was simplest to assign the $1'$,$1.67'$, $2.33'$, & $3.33'$ maps to block sizes each offset by one pixel from 150-153 pix for identification purposes. Because fields are approximately ∼8000 pix on each side, the variance in pixel scale is essentially negligible.

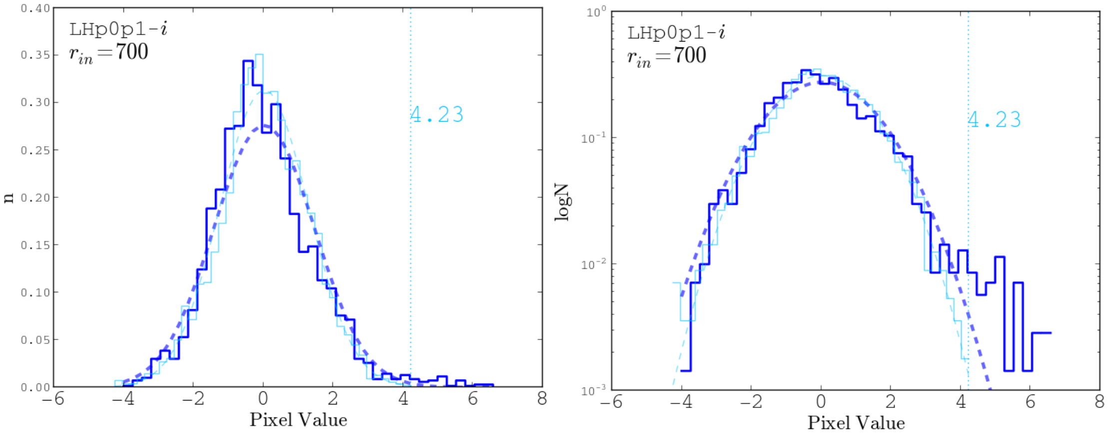

(a) (b)

Figure 4.4: Example S/N histograms displayed with gaussian fit to E-mode S/N (dark blue) and B-mode (light blue) maximums. Linear and logarithmic versions. Residual from gaussianity is visually obvious, and upper-bound of B-mode signal is shown via dotted vertical line.

non-gaussianity characteristic of lensing peaks). The pixel S/N value is then translated to its corresponding standard deviation value, σ_{fit}, in terms of the map's fitted normal distribution. The error in σ_{fit} estimation is the residual standard mean error of the gaussian fit.

Additional plots and tables for each field in this chapter may be found in Appendix A.

4.2 2D Mass Reconstruction Calibration Field: Abell 781

Abell 781 is a system of four subclusters centered at $9^{h}20^{m}25^{s}$ $+30°31'$ (J2000). Studied extensively in the prior work of this group, Richard Cook's thesis and subsequent articles dealt with this area in great detail [19, 20]. Cook used multiple imagers to analyze this galaxy cluster; OPTIC on the WIYN 3.5-m telescope, Deep Lens Survey (DLS) data from MOSAIC at the Mayall and CTIO Blanco 4-m telescopes, and 2003 Subaru data, with a particular focus on Abell 781D, (or "A781 West"). This subcluster presented convincing evidence for its existence in X-ray and dynamical studies, but was not detected via WL. Wittman *et al.* (2014) [128] showed that random intrinsic alignments prevented its measurement, and used redshift information to improve filtering techniques needed to resolve the cluster's lensing signal. Prior work by Sehgal *et al.* (2008) [101] used Deep Lens Survey, *Chandra*, and *XMM-Newton* data to study the cluster.

We chose this cluster as the ideal test region to compare the efficacy of our analysis pipeline with multiple independent measurements of the cluster's structure. Firstly, several X-ray studies confirm the complex substructure of the region. Secondly, independent methods of WL analysis using other datasets identify these sub-groups. And lastly, analysis *within our own group*, using the same algorithms on different imaging data, and under a totally different reduction approach, give us a final benchmark for systematic differences in our tools. Success reproducing these results will allow us to gauge confidence of our application of our techniques to other regions in our sample.

Our dataset is Suprime-Cam imaging taken in i', on March 15, 2010. Nine 240 sec exposures (2160 sec) were available, with only six meeting quality standards for a total of 1440 sec. We reduce, astrometrically correct, stack, and circularize residual stellar e_1 & e_2 ellipticity moments to below $\leq$0.2%. Mean seeing of our final sample is 0.73″, with 21,182 galaxies in our final, filtered, sample across 0.17 deg^2 of the sky, for a galaxy density of $\langle n_{\rm gal} \rangle = 34.9$ gal/arcmin^2, and sample depth of 25.23 magnitudes.

Sub-Cluster	S/N	$\sigma_{\rm fit}$	RA, DEC$^{\rm a}$	RA, DEC (X-ray)$^{\rm b}$	Separation
Abell 781A	6.012	3.795	[09:20:24.6, +30:28:28.5]	[09:20:24.8, +30:30:20.4]	1.872′
Abell 781B	6.381	3.992	[09:20:51.4, +30:28:13.9]	[09:20:52.5, +30:28:08.4]	0.252′
Abell 781C	5.287	3.408	[09:21:06.8, +30:27:55.6]	[09:21:10.9, +30:28:04.2]	0.894′
Abell 781D	0.173	0.093	[– , –]	[09:19:23.3, +30:31:35.6]	–

[a] Detected in our analysis.
[b] *Chandra* [101].

Table 4.1: Abell 781 WL results in terms of 2010 Subaru Data.

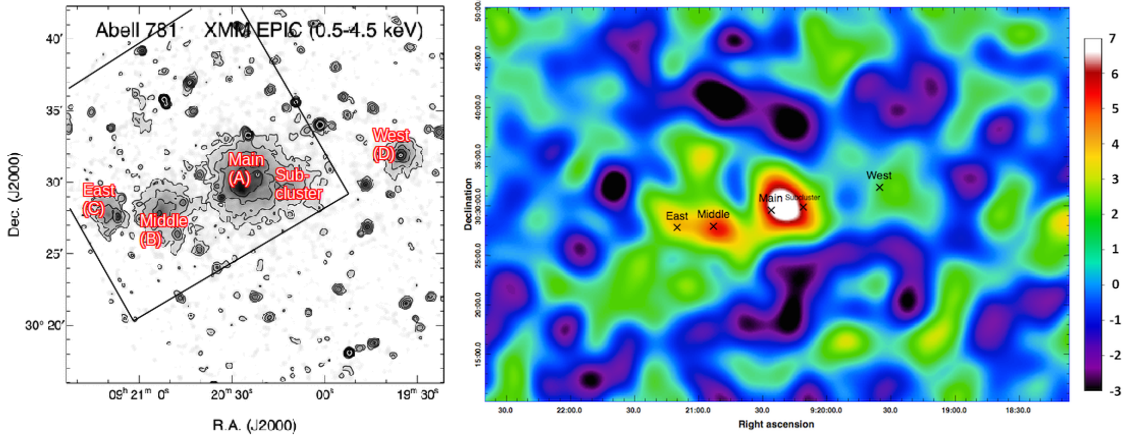

(a)

(b)

Figure 4.5: Wittman (2014) [128] figures based on Sehgal *et al.* (2008) X-ray measurements [101], depicting the Abell 781 cluster. **(a)** X-ray map, showing sub cluster lumps. *XMM-Newton* imaging. **(b)** Weak lensing map of A781 region, without correction for photo-z galaxy calibration.

Convergence mapping at several scales gives the greatest mutual 3-subcluster signal structure at 900 pix characteristic scale, or $r_{in} = 3'$. At this scale length, the Main (A), Middle (B), and East (C) subclusters are each uniquely resolved and found at 6.012, 6.381, 5.287 S/N respectively (FIG. 4.6). No significant B-mode peaks were identified, and fits to the Gaussian S/N provided standard deviation detections above $\geq 3\sigma_{\mathrm{fit}}$ for all three peaks. Comparison to *Chandra* emission peaks demonstrated low separation in WL center-of-convergence from the X-ray source (TABLE 4.1). In terms of subtler shape recognition, the substructure mass to the right of the Main (A) cluster, is seen as well, and is the reason for the $\sim 1.87'$ peak separation to *Chandra* imaging—likely due to the presence of this mass extension.

With each subcluster closely identified at high accuracy, we find our sample provides an excellent verification of our methods. Multiple independent measurements in this region are in close agreement, as seen in FIG. 4.7, where different analyses are overlaid upon our map. Furthermore, they agree with the Cook (2012) and Cook & Dell'Antonio (2012) [19, 20] results, which utilized OPTIC, *DLS* (Mosaic & CTIO), and different 2003 Subaru data. The quality of the imaging used in his analysis is comparable to ours, with far longer exposure times in the non-Subaru data, though with less powerful telescopes and slightly worse atmospheric conditions. For Mosaic, OPTIC, and Suprime-Cam, Cook's sample consisted of: (R-band, R-band, z'-band) filters, exposure time=(14000 sec, 6000 sec, 780 sec), galaxy density=(24, 21, 11 gal/arcmin^2), limiting magnitudes=(27, 26.6, 24.5 mag), and seeing=($0.9''$, $0.84''$, $0.79''$), respectively. They, similarly, detected the primary A, B, & C cluster peaks, but not the D "West" peak, yet effectively ruled out systematic telescope, instrumentation, and PSF-residual causes for the lack of signal. Because they utilized multiple data sets, with different pixel-scales, qualities, and instrumental features, they determined that the non-detection of Abell 781D was the result of unique alignments in the distribution of source galaxies, while Wittman *et al.* (2014) later used a more detailed redshift analysis to show that contamination effects from foreground galaxies also contributed to the masking of the lensing signal.

We also note the same issue that prevents the detection of A781D. Because this is a systematic feature of intrinsic galaxy alignments in the regional lensing conditions themselves, seen in every independent measurement, this systematic feature is to be expected. Carefully targeted application of redshift information can reveal it, as in Wittman *et al.* (2014), but because we do not have photo-z information for the fields in our sample, we must accept some incompleteness in this sense. We are more interested in accurate positive detections, than in potentially missing a small number of candidates due to effects undiagnosable without specific knowledge of any one particular cluster. It is of note, however, that the quality of resolved shape information for our calibration dataset is on par with Cook's somewhat deeper, longer-timescale imaging. Their combined DLS, OPTIC, and Suprime-Cam imaging managed to barely resolve the strong lensing arc near the A781D center of mass. Our 1440 sec i'-band stack, processed through our completely different data-reduction pipeline easily shows the same feature, (Fig. 4.8). This further indicates that our reduction methodology is successfully reconstructing faint and extremely subtle galaxy shapes with high-accuracy.

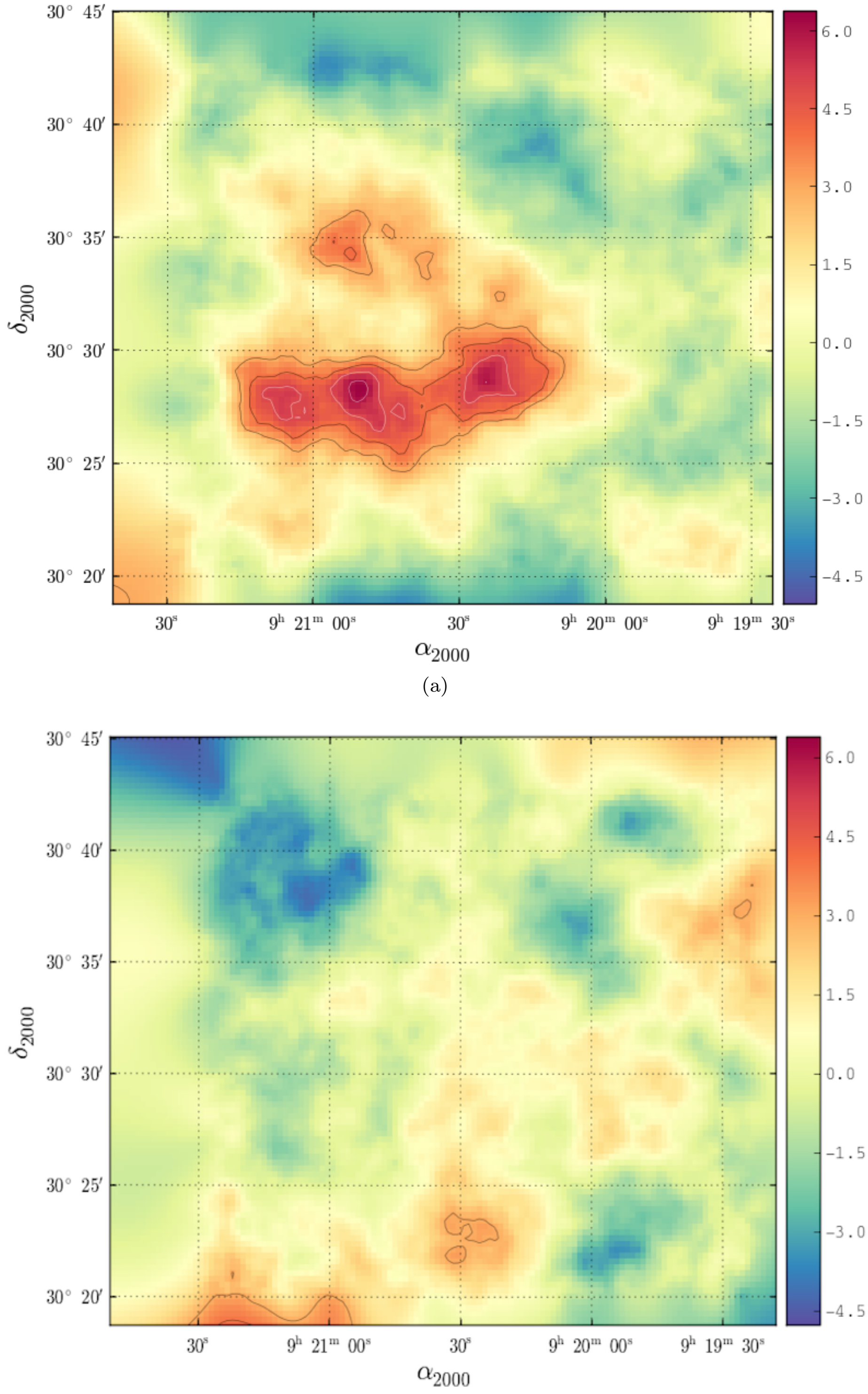

(a)

(b)

Figure 4.6: **(Top)** 2D Mass reconstruction map of Abell 781. Contours at levels of 3, 4, 5, & 6 S/N. **(Bottom)** *B*-mode calibration map. Contour at 3 S/N

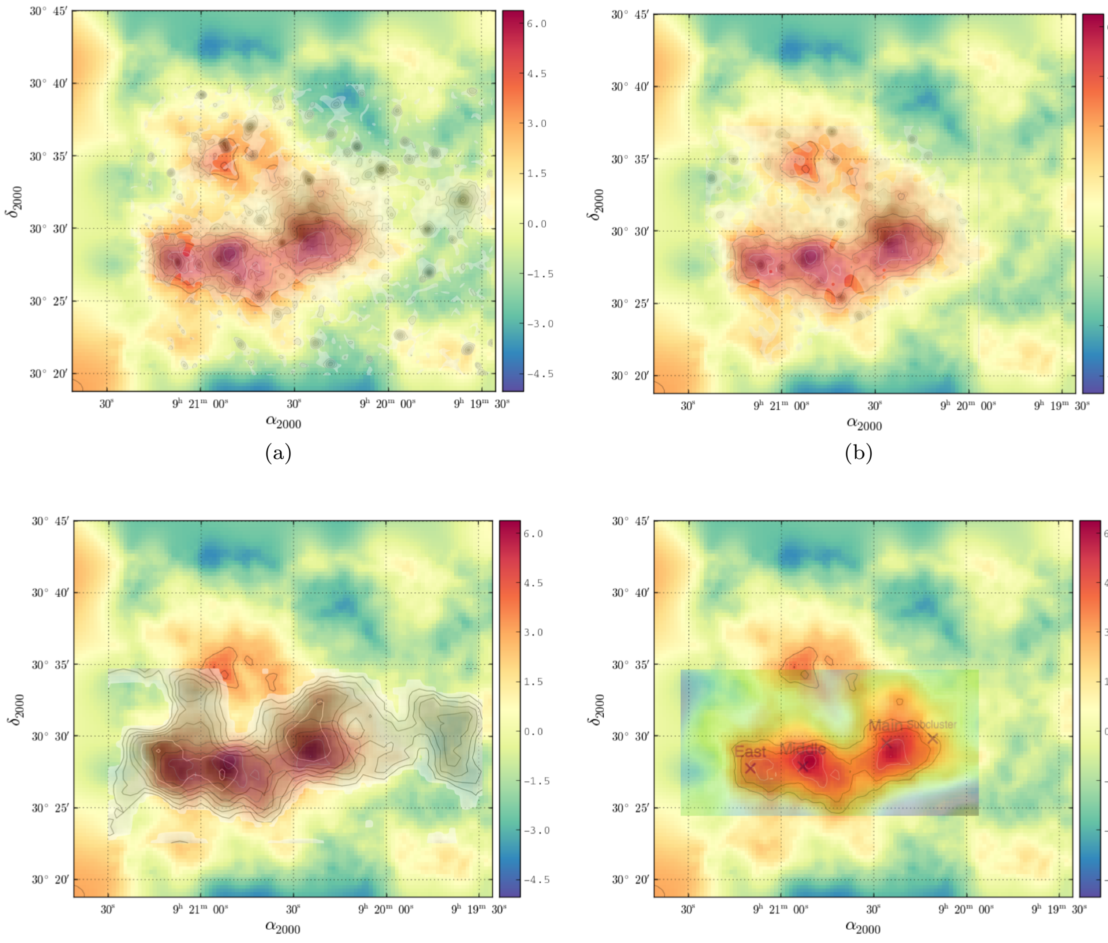

(a)

(b)

(c)

(d)

Figure 4.7: Peak comparisons across multiple comparison fields based on Abell 781 (at characteric scale 3′). The top two superimpose X-ray measurements of Abell 781 [101], while the bottom fields show weak lensing comparisons. **(a)** *XMM-Newton*. **(b)** *Chandra*. **(c)** *DLS-Mosaic*, Sehgal *et al.* (2008) [101]. **(d)** *Optic-Mosaic-Subaru*, Wittman *et al.* (2014) [128].

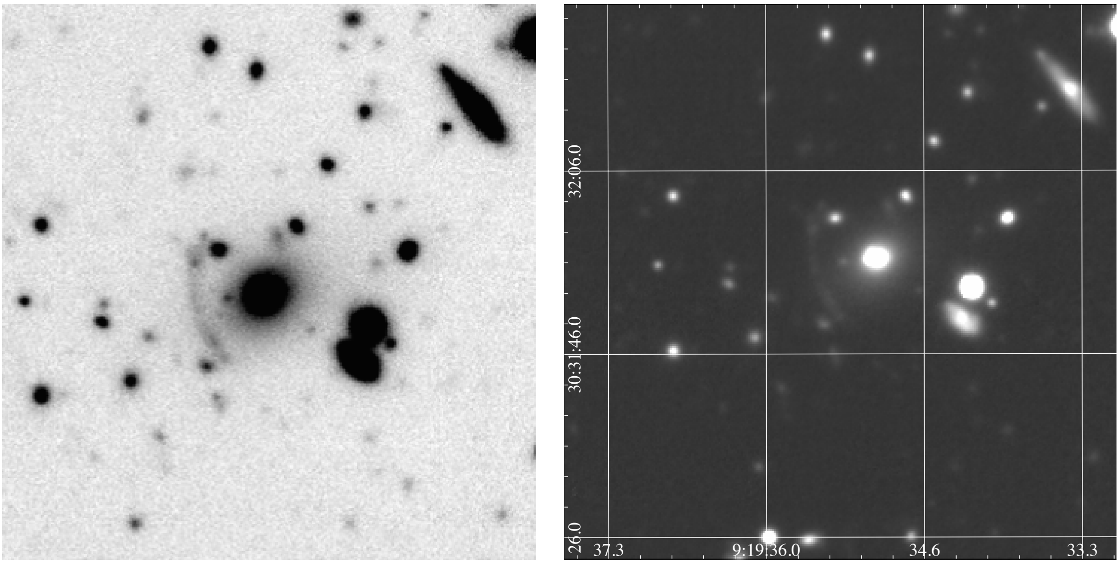

(a) (b)

Figure 4.8: Lensing arc around A781D. **(a)** Combined OPTIC (r'-band, 6000 sec, $0.84''$ seeing) and Subaru Telescope (z'-band, 780 sec, $0.79''$ seeing) data, from Cook & Dell'Antonio (2012) [20]. **(b)** Our 1440 sec, $0.74''$ seeing i'-band stack. Though we do not detect the West cluster through weak lensing (due to intrinsic alignment effects beyond our limitations), the ability to accurately resolve this extremely faint lens, on par with a deeper-imaged analysis at similar atmospheric conditions, serves as an indication that our reduction, stacking, and circularization pipeline is effective at accurately imaging subtle field objects.

4.3 Wide-Field Regions

As touched upon in §4.1, we select on depth and quality parameters from post-2008 Suprime-Cam data:

- $\gtrsim 1000$ sec of total exposure time
- Galactic latitude $\gtrsim \pm 30^\circ$
- Reported seeing $\lesssim 0.6''$ according to initial SMOKA estimates
- Red and near-IR bandpasses
- Contiguous fields taken in single observational runs given preference

The last standard marks our emphasis on large contiguous regions with similar characteristics, and thus results in our selection of these five particular regions, as opposed to different, scattered fields selected fully at random. For consistency, we focused on images taken on shorter timescales in similar conditions. Among these are the Lockman Hole (LH) and ELIAS North 1 (EN) fields (§4.4), because they represent optimum extragalactic viewing lines-of-sight due to low galactic dust column density, and multiple filter exposures in at different dates, as well as two of the CFHTLS-Wide areas (W2 & W3) (§4.5), and a field located midway between the Boötes void, and the Boötes supercluster structure (referred to as "F") (§4.6) areas, chosen for high quality seeing and substantial depth ($\geq$1000 sec).

Our selection criteria, as first outlined in §3.2.1, are slightly expanded to be marginally more inclusive. We have done this for several reasons. Firstly, standards for measuring stellar seeing vary somewhat within the astronomical community. Although we maintain an approach which is consistently self-similar and uniform, to account for different standards, we opted to be slightly more inclusive. Secondly, as our *goal* is to achieve high source density, and we are able to find $\langle n_{\rm gal} \rangle$ and depth values for each field, the built-in quality statistics are reported and permit us to assess the value of each detection. Since we are interested in optimizing an approach in cluster detection, including some range of quality values gives us a way of evaluating the worthiness of each parameter.

Due to being taken for a variety of different purposes, this is a diverse sample. In terms of galactic density (Fig. 4.9), area, and waveband, these regions are somewhat different. EN1 and the Lockman Hole (§4.4) are, on average, the highest quality regions, with excellent depth and low extinction, while the two CFHTLS areas, W2 & W3 (§4.5), are relatively large with sufficient seeing and exposure time and the lowest average galaxy density. The Boötes, or F–fields (§4.6), are both large and imaged with exceptionally good seeing.

While Subaru imaging, as a general trend, is aimed at cluster observations at a much higher than random rate, none of these five areas, broadly speaking, were originally selected for that goal *per se*. Rather, most areas seem to have been selected as follow-ups to prior larger studies of a variety of extragalactic interests, and due to generally low-background regions at high galactic latitude, few stars, and as clear windows out of the Milky Way. Nonetheless, the collected data is, in the case of the W and F regions, only a fractional subset of those regions as a whole, and may have been selected to examine local features.

Our methodology has been to reduce the largest possible number of fields, discard those with problematic aspects, and then create convergence maps at a range of four characteristic scales (300, 500, 700, and 1000 pixels). Peaks in detection S/N typically occur across multiple scales at the same location, however, the peak on the map with the scale yielding the highest significance signal is the size most likely to represent the true extent of a cluster at this location (§4.1.2).

Region	Area [deg^2]	Exp. Time [sec]	Seeing [$''$]	$\langle n_{\rm gal} \rangle$ [arcmin^{-2}]	Depth [mag]	Obs. Date	Peaks
LH	2.66	3600-6000	0.62	48.66	25.97	Various 2009-2011[1]	28
EN1	0.73	3600,4200	0.60	44.10	25.72	April 13-14, 2010	8
W2	1.26	1200	0.66	22.18	24.81	April 17-19, 2010	12
W3	2.73	1200	0.53	27.74	24.97	April 17-19, 2010	25
F	2.97	1200-1440	0.52	33.17	25.21	April 26-27, 2011	19

[1] See Table 4.3.

Table 4.2: Summary of region information. LH are z'-i'-r' bandpasses, EN is i', and the others are z'.

Several extragalactic surveys have provided data used for other types of cluster studies (all of far larger scope and intention), including SWIRE, which examined LH and EN1; HerMES (using SPIRE on the Herschel instrument), which studied LH, EN1, and F; the SCUBA-2 Cosmology Survey (S2CLS) which looked at Boötes; and the CFHTLS surveys of which W2 and W3 were two of the four wide-field regions.

Each section includes:

- A table of galaxy statistics by subfield

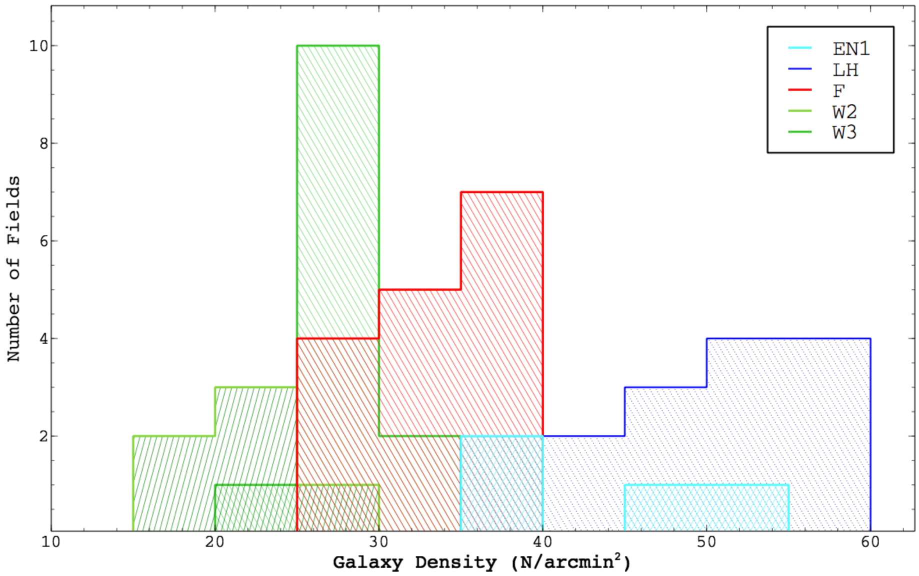

Figure 4.9: Galaxy density histogram of the 5 wide-field regions of the sky included in this survey.

- A table of highest S/N peaks by characteristic scale
- Convergence maps at $r_{in} = 700$ pixels ($2.33'$) scale
- Charts of candidate cluster detections (at every scale) overlaid upon sky and previous candidates existing on the NED database of extragalactic objects
- Detailed subimages of relevant, high S/N regions in optical, overlaid with convergence contours

We also include void measurements—peaks of extreme negative signal which are unlikely to contain a cluster within the redshift range sensitive to WL analysis.

Full tables of every recorded peak at each scale, all convergence maps, and additional optical zooms are included in APPENDIX A.

Our measurements are sensitive to clusters at intermediate redshift ($z \sim 0.05$-0.6 at most, depending on depth). Our detections are shown contrasted with cluster candidates suggested through several methods, pruned to the same redshift range, almost none of which include wide-field weak lensing analysis. Therefore, *our survey presents a unique WL-based contrast against other cluster search techniques.*

Candidates already existing in extragalactic databases originate in a diverse array of survey techniques, with different sensitivities and signal strengths—some of which are found via methods sensitive to different redshift scales. The outside candidate clusters are only provided for reference—not all of them are detectable through WL techniques using our data, nor do they all necessarily represent reliable cluster measurements. In particular, optically-selected cluster samples are prone to false positivity.

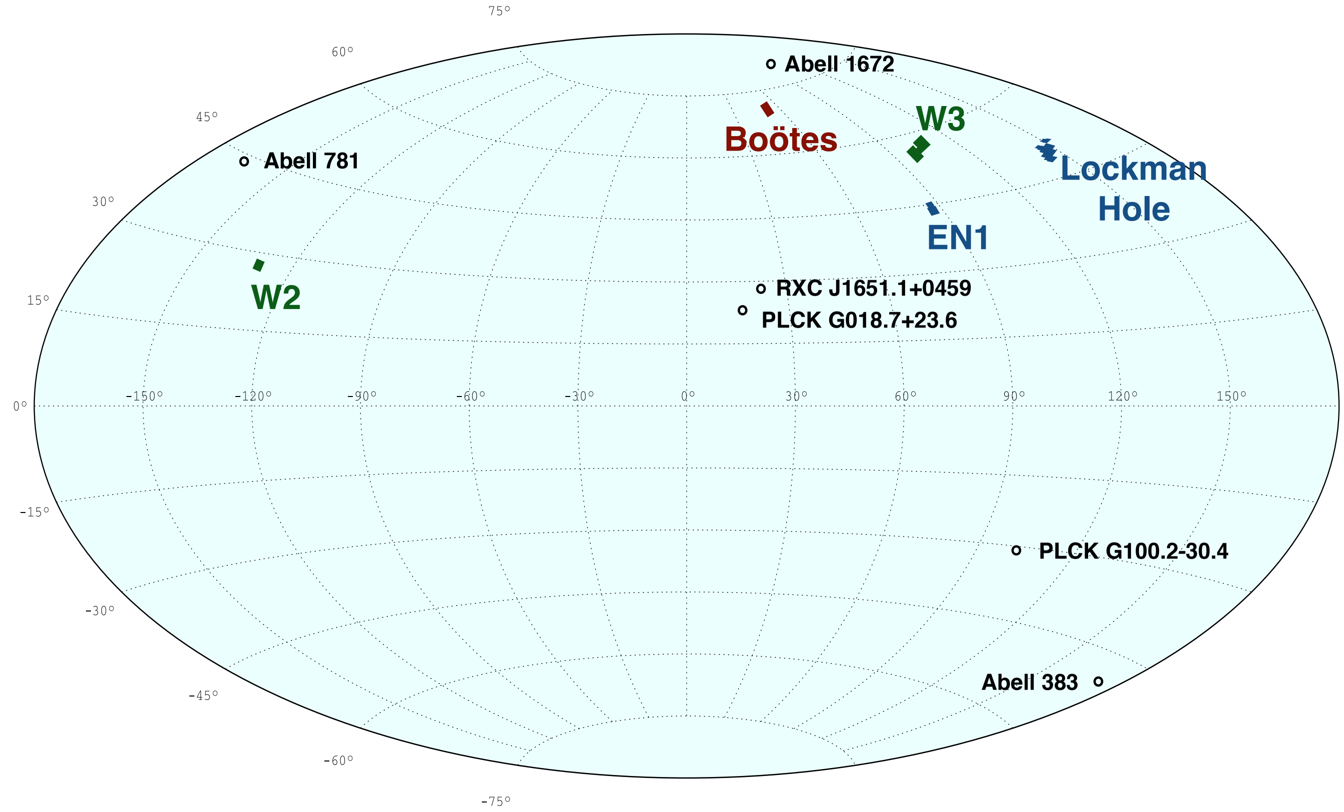

Figure 4.10: Distribution of fields analyzed in this work, displayed in galactic coordinates in Aitoff projection (not to scale).

4.4 Low Extinction Fields

This section features two areas of the sky with very clear views out of the Milky Way, with lines of sight minimally contaminated by interstellar gas and therefore containing low amounts of infrared background [97] and low line-of-sight extinction [61, 60].

Parts of three of the seven SWIRE fields were found imaged in the post-2008 SMOKA archive, the Lockman Hole (LH), the European Large-Area ISO Survey "ELAIS" North 1 region (EN1), and the XMM Large-Scale Structure Survey. All three regions were downloaded and processed by our pipeline. After reduction, much of LH and EN1 met lensing quality standards. Of the fields available, twenty were of sufficient quality and depth for lensing measurements (3.24 deg^2). The XMM-LSS region, 2^h20^m -4°48′, possessed seeing and observational difficulties too significant for inclusion in the final sample, with only a single usable field, so it was discarded.

The Lockman Hole, located within Ursa Major, is a gap in the galactic medium with a low concentration of neutral hydrogen [59]. Almost entirely devoid of foreground contamination, it provides an excellent view of extragalactic objects and is a frequent observational target. Its angular dimensions are approximately $3.66° \times 3.00°$ (11.0 deg^2), centered at 10^h45^m +58°. We obtained fourteen such fields, in r', i', and z' bands, and selected for depth and best residual stellar ellipticity among them.

The ELIAS North 1 field is $3.08° \times 3.00°$, (9.2 deg^2) in size, centered at $16^h11^m00^s$ +55°00′, in Draco. Our sample within this region is only four fields, because we discarded several additional pointings at insufficient seeing/exposure time. In those remaining fields, the seeing is $0.60''$, and the galaxy density is quite high, averaging 44.1 gal/arcmin^2.

As evident in Fig. 4.9 and Table 4.3, these constitute the highest resolution portion of the wide-field sample, containing the deepest and highest galactic density regions (due both to long exposure time and low extinction). The pointings in these regions consist of some of the greatest exposure depth and galaxy density, averaging $0.62''$ and 48.66 gal/arcmin^2, respectively (Table 4.3).

The Spitzer Wide-area InfraRed Extragalactic project (SWIRE) [61, 60] surveyed seven regions of the sky with low background. Exploring galaxy formation and evolution, AGN, and cosmic structure formation, SWIRE surveyed nearly 65 deg^2. They sought out large neighboring regions with low galactic emission, low contamination by bright stars and objects, large clusters, radio sources, especially those located at northern or southern galactic latitudes, overlapping other observations in

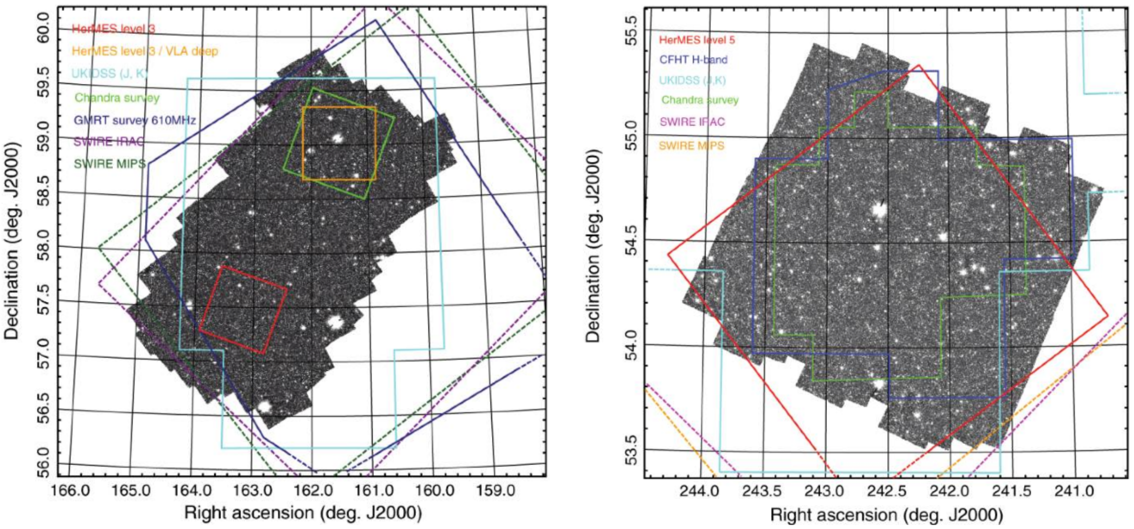

(a)

(b)

Figure 4.11: Existing coverage from prior studies of Lockman and EN1 as of 2012, [69]. (Note this does not necessarily reflect coverage from clustering surveys, specifically).

non-infrared wavebands.

Ground-based follow-up imaging was taken under a Subaru-Keck timeshare proposal across five observation dates in 2009-2011 in service of the Spitzer Extragalactic Representative Volume Survey (SERVS) [69], an IRAC Legacy project (with a scope of 18 deg^2)[4] focusing on galaxy evolution. Subaru supplied optical imaging of three northern SERVS fields to improve photometric-z measurements. Wavebands r',i',z' imaged 2 deg^2, 6 deg^2, and 5 deg^2, respectively, at magnitudes mag(z')=25, mag(i')=26, mag(r')=27 [114].

4.4.1 Lockman Hole

LH field key located on Pg. *152.*

---

[4] Subaru proposals: o09419, o09420, o10203, o10223, o11202

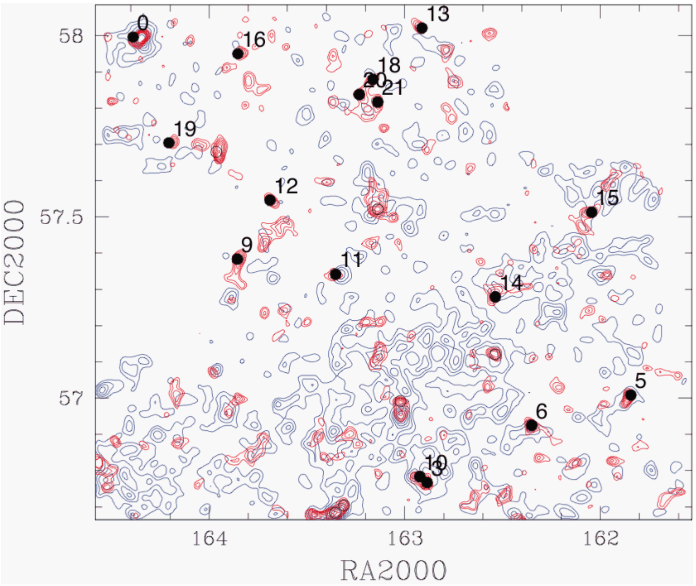

Figure 4.12: Miyazaki *et al.* (2007) [74] mass reconstruction map for a portion of the Lockman Hole region, based on Subaru imaging. This map overlaps with parts of our LHn1n1, LHn2n2, LHp0n2, and LHp0n3 fields.

Region	RA	DEC	Filter	t_{exp}	Seeing	N_{gal}	$\langle n_{\mathrm{gal}} \rangle$
	[J2000]	[J2000]		[sec]	[$''$]		[arcmin^{-2}]
LHn1n1[§]	10:53:30	+57:47	$\boldsymbol{z'}$	2700	0.60	30665	46.3
–[†]	-	-	r'	3600	0.70	38429	57.7
LHn1p0[†]	10:53:30	+58:15	i'	2400	0.48	30483	48.0
LHn2n2[⋆]	10:57:30	+57:20	i'	3900	0.71	33985	50.5
LHp0n1[⋆]	10:49:30	+57:47	z'	3600	0.61	27592	43.4
LHp0n2[‡]	10:49:30	+57:20	$\boldsymbol{r'}$	3600	0.70	36427	56.5
–[†]	-	-	z'	5700	0.73	28203	43.6
LHp0n3[⋆⋆]	10:49:30	+56:55	z'	3600	0.73	24668	37.7
LHp0p0[†]	10:49:30	+58:15	i'	3600	0.51	34459	53.4
LHp0p1[†]	10:49:30	+58:45	$\boldsymbol{i'}$	2400	0.56	29726	44.7
-[‡]	-	-	r'	4400	0.57	36431	54.2
LHp1n1[§]	10:45:30	+57:47	z'	3600	0.60	30678	45.7
LHp1p0[‡]	10:45:30	+58:15	$\boldsymbol{r'}$	3600	0.71	37461	55.6
–[†]	-	-	z'	3600	0.62	32112	48.2
LHp1p1[‡]	10:45:30	+58:45	$\boldsymbol{r'}$	3600	0.65	38374	57.1
LHp1p2[‡]	10:45:30	+59:20	r'	3600	0.62	33056	50.3
LHp2p1[†]	10:41:00	+58:45	$\boldsymbol{i'}$	6000	0.61	36189	53.8
LHp2p2[†]	10:41:00	+59:20	i'	6000	0.65	25269	38.3
EN1n1n1[‡]	16:07:00	+53:55	i'	3600	0.55	28427	50.6
EN1p0n1[‡]	16:10:00	+53:55	i'	3600	0.58	24682	37.2
EN1p1n1[‡]	16:13:00	+53:55	i'	3600	0.74	32405	48.6
EN1p2n1[‡]	16:16:00	+53:55	i'	4200	0.54	27254	39.9

[⋆] Observed November 16, 2009

[†] Observed January 18-19, 2010

[‡] Observed April 13-14, 2010

[§] Observed December 5, 2010

[⋆⋆] Observed April 2, 2011

Table 4.3: Lockman Hole Fields. LH is 2.66 deg^2 (out of a potential 3.42 deg^2 analyzed for this area across multiple filters), while EN1 comprises 0.76 deg^2 of the sky. (Second line describes filter not chosen for primary lensing measurement.)

Region	S/N	$\sigma_{\rm fit}$	RA	DEC	r_{in}	
			[J2000]	[J2000]	[pix]	[arcmin]
LHn1n1	5.93	5.68±0.021	10:52:35.2	+57:36:46.2	300	$1'$
LHn1p0	4.92	4.74±0.021	10:52:46.9	+58:05:35.5	300	$1'$
LHn1p0	3.89	3.52±0.022	10:54:11.6	+58:05:48.0	500	$1.67'$
LHn2n2	4.22	4.40±0.019	10:55:48.1	+57:20:14.7	300	$1'$
LHn2n2	5.04	4.05±0.025	10:58:15.4	+57:25:37.2	1000	$3.33'$
LHp0n2	5.26	3.49±0.030	10:49:56.8	+57:21:32.8	700	$2.33'$
LHp0n2	4.55	3.39±0.027	10:47:48.8	+57:21:01.9	500	$1.67'$
LHp0n2	5.00	3.03±0.033	10:48:19.8	+57:29:08.3	1000	$3.33'$
LHp0n3	4.46	4.27±0.021	10:49:29.1	+57:04:54.3	300	$1'$
LHp0n3	4.45	3.53±0.025	10:49:28.3	+57:04:50.4	700	$2.33'$
LHp0n3	4.63	3.37±0.028	10:49:03.9	+56:53:38.0	1000	$3.33'$
LHp0p0	4.84	3.06±0.032	10:50:55.9	+58:08:45.1	1000	$3.33'$
LHp0p0	4.17	2.64±0.032	10:50:18.9	+58:19:40.6	1000	$3.33'$
LHp0p0*	-6.03	-	10:49:08.4	+58:15:37.2	1000	$3.33'$
LHp0p1	6.57	5.37±0.024	10:48:40.7	+58:32:45.6	700	$2.33'$
LHp1n1	4.01	3.33±0.024	10:44:08.3	+57:54:37.1	700	$2.33'$
LHp1n1	4.34	3.61±0.024	10:45:17.5	+57:57:22.6	700	$2.33'$
LHp1p0	5.13	3.71±0.027	10:44:40.7	+58:08:20.0	700	$2.33'$
LHp1p0	4.40	3.54±0.024	10:45:08.1	+58:09:19.7	500	$1.67'$
LHp1p0	5.15	3.43±0.030	10:45:31.9	+58:02:46.7	1000	$3.33'$
LHp1p0	4.28	3.44±0.024	10:46:32.9	+58:02:53.7	500	$1.67'$
LHp1p1	4.17	2.87±0.029	10:46:03.4	+58:38:53.4	700	$2.33'$
LHp1p1	4.10	2.82±0.029	10:45:13.2	+58:50:38.2	700	$2.33'$
LHp1p2	4.27	3.82±0.022	10:45:48.7	+58:56:06.4	700	$2.33'$
LHp2p1	4.33	3.64±0.023	10:41:53.2	+58:37:25.2	500	$1.67'$
LHp2p1	4.69	3.29±0.028	10:41:48.6	+58:37:08.0	1000	$3.33'$
LHp2p2	4.69	3.75±0.025	10:40:54.3	+58:55:51.9	1000	$3.33'$
LHp2p2	3.88	3.61±0.021	10:39:50.3	+58:54:51.8	500	$1.67'$
LHp2p2	3.51	3.26±0.021	10:41:47.7	+58:59:15.1	500	$1.67'$

Table 4.4: Highest signal peaks in the LH field

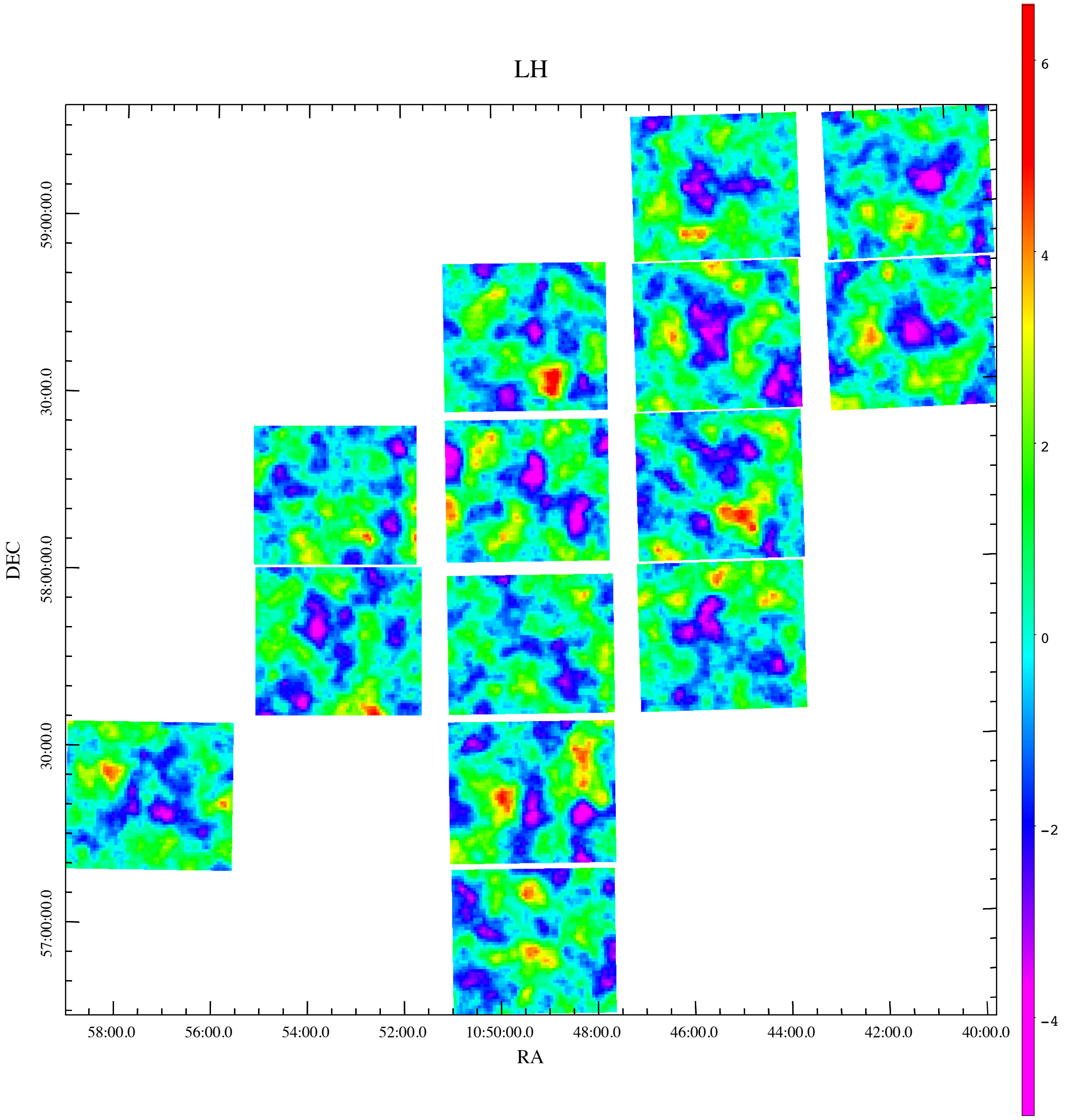

Figure 4.13: $r_{in} = 700$ pix convergence map of the Lockman Hole region. The other 3 maps can be found in A.2

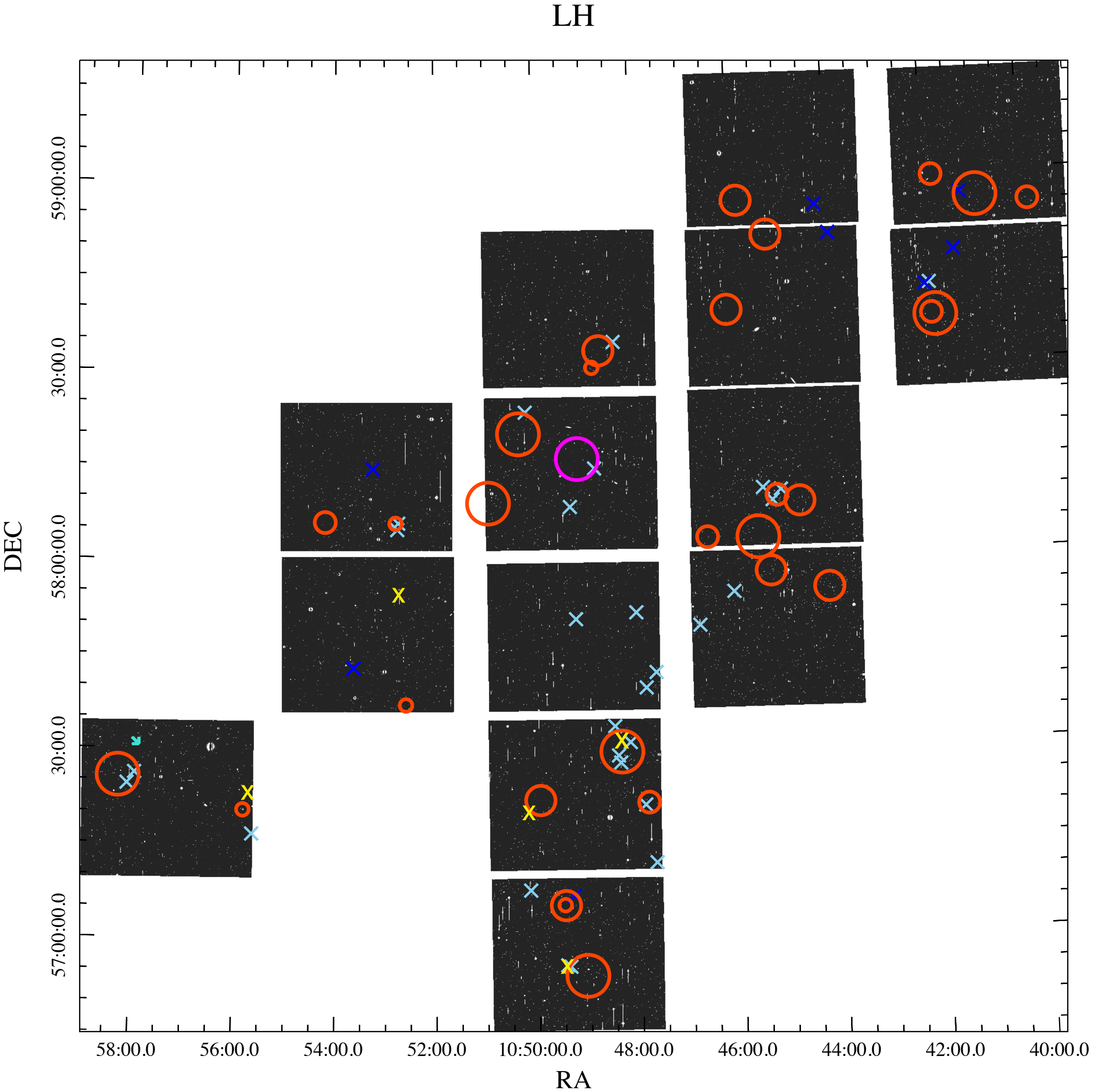

Figure 4.14: Signal peaks (red circles) shown at different characteristic scales overlaid on the Lockman field, with known candidate clusters from outside surveys marked by light blue crosses. Cluster candidates at the perimeter or our detectable range, at z=0.5-0.7 are shown in dark blue. Miyazaki *et al.* (2007) [74] weak lensing peaks are yellow. Voids are magenta. Strong lens shown as turquoise arrow.

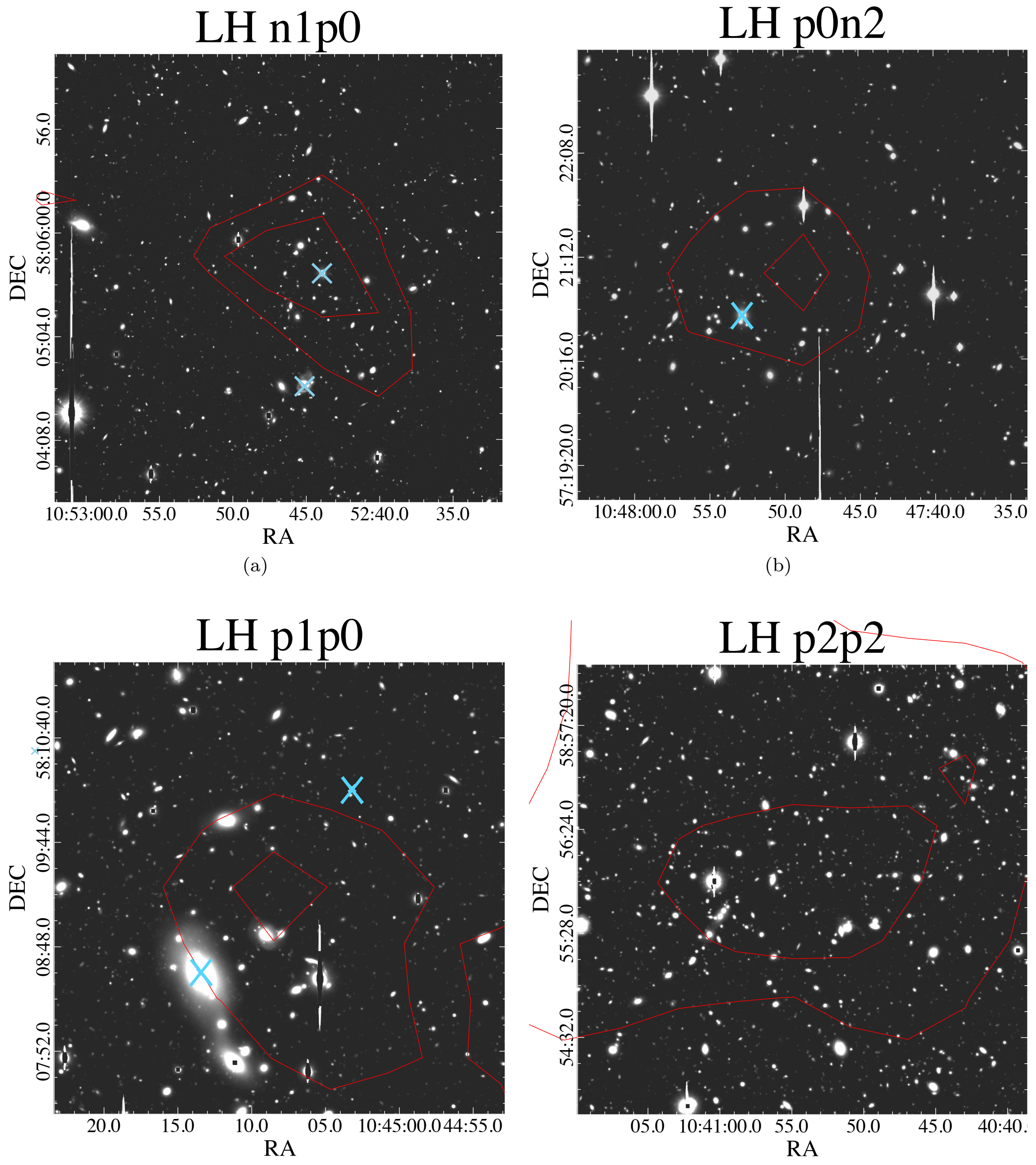

(a)

(b)

(c)

(d)

Figure 4.15: Signal peaks in the LH fields. **(a)**: 4.92 S/N peak at 1′ scale (300 pix). Contours at 3, 4. **(b)**: 4.55 S/N peak at 1.67′ scale (500 pix). Contours at 3, 4. **(c)**: 4.40 S/N peak at 1.67′ scale (500 pix). Contours at 3, 4. **(d)**: 4.69 S/N peak at 3.33′ scale (1000 pix). Contours at 3, 4.

4.4.2 ELAIS North 1 Peaks

EN1 field key located on Pg. *160.*

Region	S/N	σ_{fit}	RA	DEC	r_{in}	
			[J2000]	[J2000]	[pix]	[arcmin]
EN1n1n1	4.53	4.20±0.023	16:06:34.4	+53:54:05	300	$1'$
EN1n1n1	3.71	2.56±0.031	16:08:20.2	+53:54:32	1000	$3.34'$
EN1n1n1*	-4.99	-	16:07:07.0	+53:56:57	1000	$3.34'$
EN1p0n1†	6.37	5.15±0.024	16:10:33.1	+54:05:51	500	$1.67'$
EN1p0n1†	4.67	3.77±0.024	16:10:05.5	+53:47:56	900*	$3'$
EN1p1n1	5.11	4.66±0.022	16:12:10.1	+54:00:45	300	$1'$
EN1p1n1	5.08	3.43±0.030	16:13:39.6	+54:02:53	700	$2.33'$
EN1p1n1*	-5.49	-	16:11:46.5	+54:08:42	1000	$3.34'$
EN1p2n1	4.69	3.64±0.025	16:15:46.8	+53:47:24	700	$2.33'$
EN1p2n1	4.74	3.47±0.027	16:15:12.3	+54:08:25	1000	$3.34'$

Table 4.5: Dominant signal peaks in the EN1 field.
†Due to a software glitch, the EN1p0n1 field could only be singly (rather than doubly) circularized, and a previous analysis scheme substituted scales of 400 pix and 900 pix for 300 pix and 1000 pix, respectively, in the map-generation process.

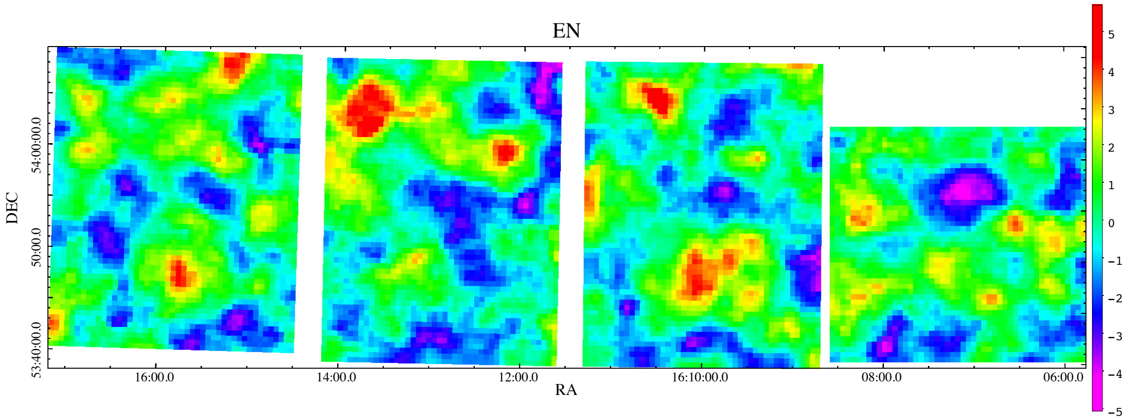

Figure 4.16: Convergence map of the EN region for $r_{in} = 700$ pix (Note: EN1p0n1 is 700 & 900 pix, respectively). The other 3 maps are in A.3.

4.4.3 LH & EN1 Results

Prior Work

Prior cluster detection attempts in these regions utilized photometric-redshift [55, 127, 125, 125] and color-matching techniques [94, 43] applied to catalogs generated by SWIRE and SDSS. Because those observations are most sensitive to infrared galaxies at high-z, the majority of clusters they locate are outside our detection range, with increasing density at $z < 1$. For our comparison chart,

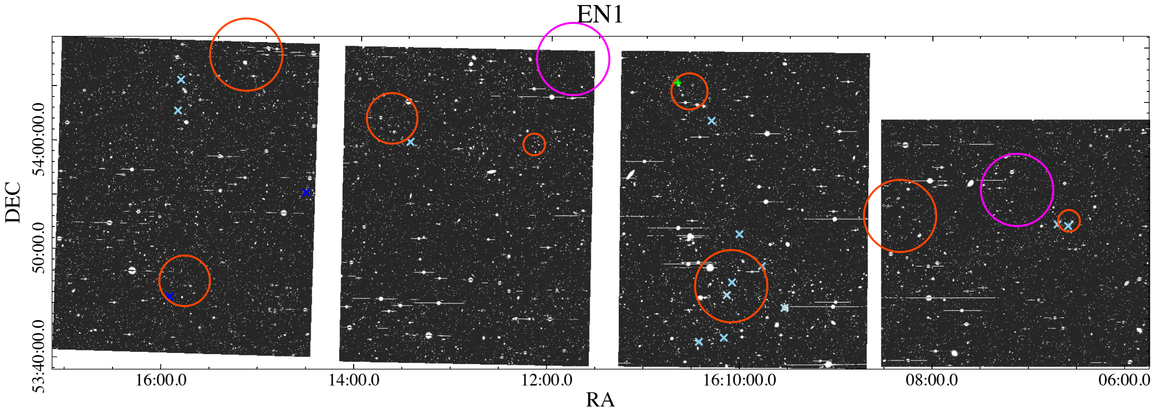

Figure 4.17: Signal peaks (red circles) shown at different characteristic scales overlaid on the EN1 field, with known candidate clusters from outside surveys marked by light blue crosses. Cluster candidates at borderline redshifts within this region are dark blue. 2XMM J161040.5+540638 is in green.

we restrict to "known" clusters within $0.05 \leq z \leq 0.6$, however the bias in these samples may still be influential because these methods are also sensitive to groups and filaments, in addition to truly gravitationally-relaxed structures.

Portions of this area have also been imaged by Subaru. Miyazaki *et al.* (2007) [74] studied 1.57 deg^2 of the field in R_C to produce a WL convergence map in search of cluster candidates (Fig. 4.12). They reported seeing of $0.60''$ and 39.3 gal/arcmin^2, and identified 16 potential clusters above 3.72 S/N.

Results

The first notable feature of our Lockman Hole & EN1 maps (Fig. 4.13 & 4.16) is the continuity of measurements across neighboring (but independently calculated) fields. Because catalogs are created independently, visual inspection of signal trends across gaps, even at lower S/N values, is an initial test for systematic flaws.

In existing extragalactic databases[5], for the redshift range in which we are sensitive, our LH regions, (Fig. 4.14), contain 26 uniquely resolved clusters, of which we confirm 13 prior detections. 13 are unique to our survey and independently resolved spatially. In EN1 regions (Fig. 4.17), 8 cluster candidates from prior studies exist in extragalactic databases. We confirm 5 of these and propose 3 of our own.

---

[5] http://ned.ipac.caltech.edu/

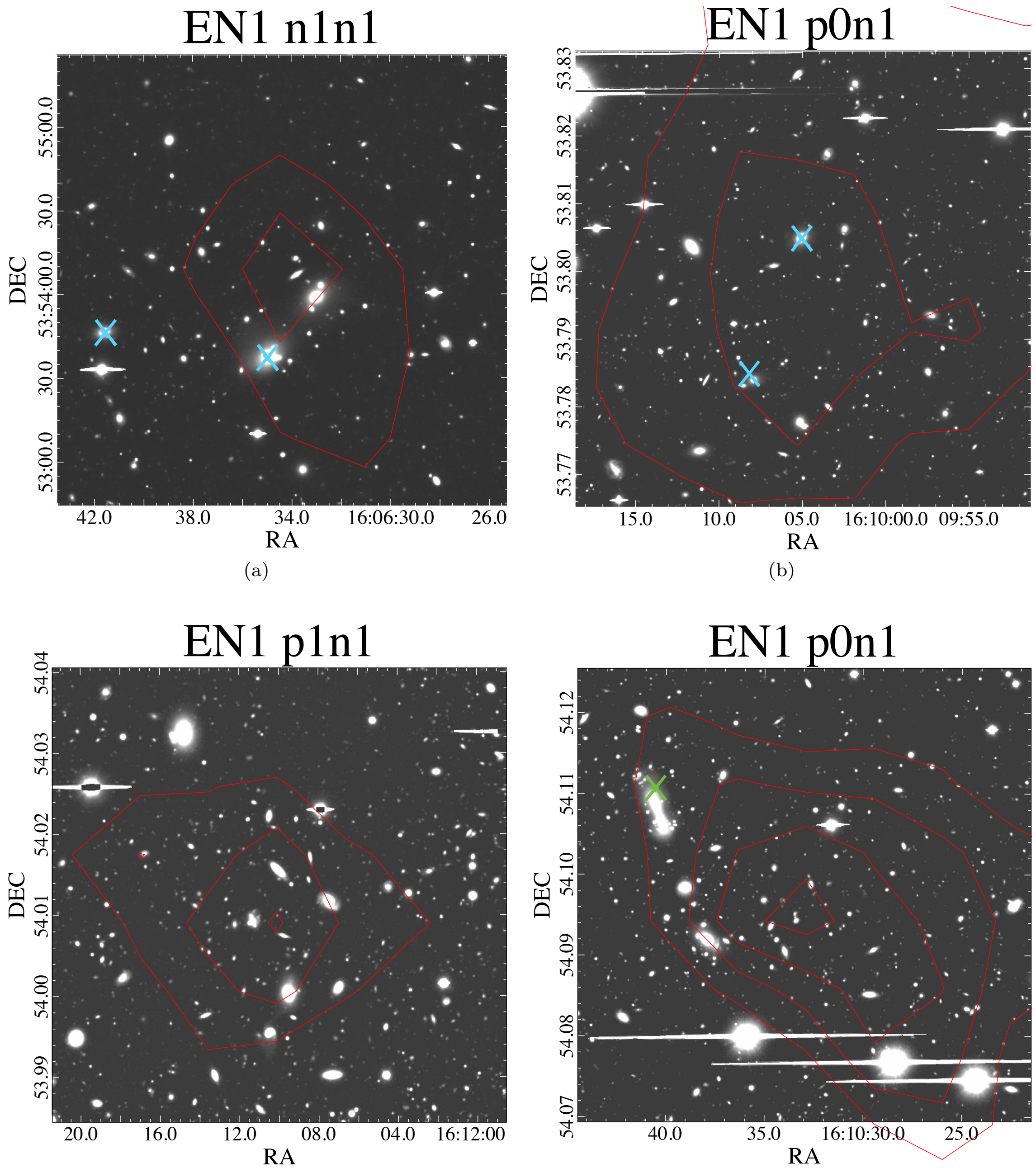

(a)

(b)

(c)

(d)

Figure 4.18: Signal peaks in the EN1 fields. **(a)**: 4.53 S/N peak at 1′ scale (300 pix), contours at 3, 4. **(b)**: 4.67 S/N peak at 3.33′ scale (1000 pix), contours at 3, 4. **(c)**: 5.11 S/N peak at 1′ scale (300 pix). Contours at 3, 4, 5. **(d)**: 6.37 S/N peak at 1.67′ scale (500 pix), contours at 3, 4, 5, 6.

We find strong agreement to clusters in EN1n1n1, LHn1p0, LHp0p1, LHp1p0, LHn2n2, and LHp0n2, with an additional source with 1′ offset in that field. Both the X-ray source and the apparent extended structure near the bottom of EN1p0n1 correspond to our lensing peaks. The X-ray source, 2XMM J161040.5+540638, is our highest S/N detection for the entirety of the wide-field sample. Matching cluster detections are seen at higher redshifts in EN1p2n1, LHp2p2, LHp0n3. We detect matches, with center coordinate discrepancy differences against clusters located in LHp0p0, LHp0n3, LHp0p0, LHp2p, EN1p1n1, and EN1p2n1 (8 LH, 3 EN1).

We also find excellent agreement with the independent lensing results of Miyazaki *et al.* (2007) [74], which were performed using the Subaru Telescope. Four of our fields overlap their imaging region: LHn1n1, LHn2n2, LHp0n2, and LHp0n3. We detect 4 of the 5 clusters they find in these fields. The cluster detection we do not confirm holds the lowest S/N among their Lockman Hole clusters. The peak we detect in LHn1n1 (but which is not included in their final results), at $10^h52^m35^s$ $+57°36'46''$, coincides with a convergence peak in the Miyazaki map which was below their threshold for inclusion (FIG. 4.12), but significant enough to be marked as $\geq$3.69 S/N. This agreement with independent lensing results is a strong independent check on our approach.

We make 13 unique detections and 6 center-of-mass corrections in Lockman and 3 of each in EN1. Our matches are highly significant, with 34 of 36 clusters detected above S/N $\geq$4. Within our sample, these two subsamples represent the most profitable of the five wide-field regions studied, at 10.53 & 10.96 peaks/ deg^2, respectively.

(Complete tables and additional figures dealing with this region may be found in §A.2 & §A.3)

4.5 Two CFHTLS Wide Fields

These areas, W2 & W3, are both subsets of the four Canada France Hawaii Telescope Legacy Survey (CFHTLS) Wide fields [45]. The four areas of the sky in this survey were selected by the CFHTLS leadership for low dust extinction, intersection with other extragalactic surveys and visibility from VLT for potential follow-up. Each of the four corresponds to a season in which they are azimuthally located (W2 in winter, and W3 in spring). Our portion consists of 2 large regions of the sky imaged in z'. Observed on April 17th and 18th, 2010 by Karl Glazebrook under proposal S10A-083 ("Is Dark Energy an Illusion? Measuring the growth of structure to z=1.5")[6]. These fields (particularly those of the W3 group) were observed under excellent seeing conditions in 1200 sec dithering groups. Six of the eleven W2 pointings were of sufficient shape resolution, with average seeing of $0.66''$ and average galaxy density of 22.18 gal/arcmin^2. Meanwhile, the W3 sample was both larger and deeper, consisting of thirteen pointing of average $0.52''$ and 27.74 gal/arcmin^2 (Table 4.6).

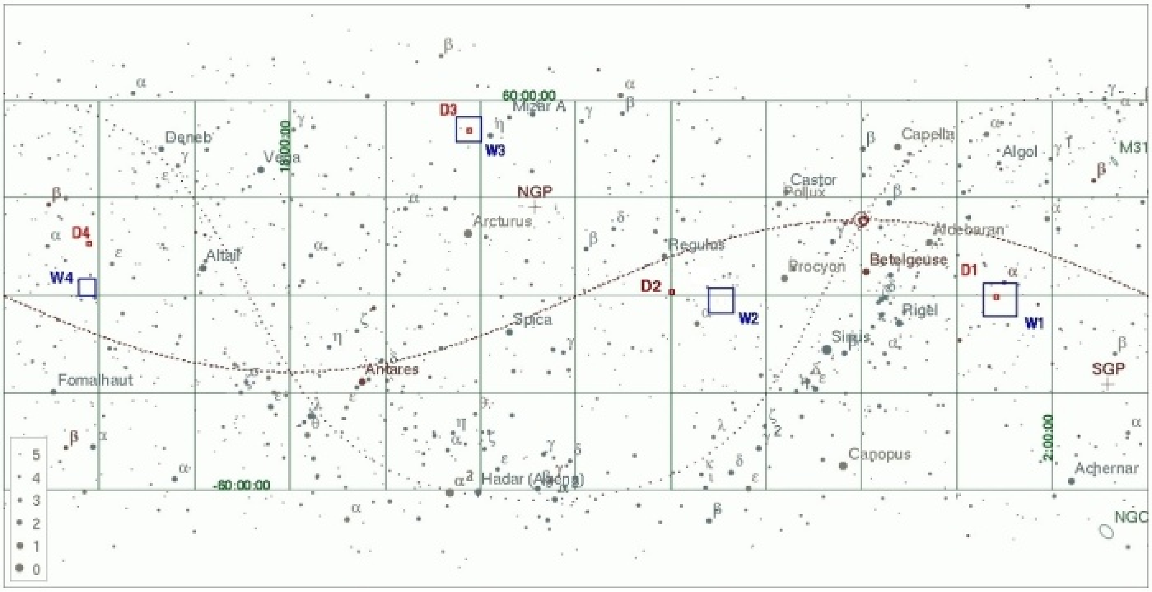

Figure 4.19: CFHTLS Deep and Wide survey fields on the whole sky [13].

W2 Fields

W2 field key located on Pg. *165.*

---

[6] http://www.naoj.org/Observing/Schedule/s10a.html

Region	RA [J2000]	DEC [J2000]	Seeing [$''$]	$N_{\rm gal}$	$\langle n_{\rm gal}\rangle$ [arcmin^{-2}]
w2_52	09:02:02	-03:18	0.94	-	-
w2_53	09:04:09	-03:18	0.83	-	-
w2_54	09:06:15	-03:18	0.96	-	-
w2_61	09:02:02	-02:55	0.74	15670	20.7
w2_62	09:04:09	-02:55	0.61	18030	23.8
w2_63	09:06:16	-02:55	0.78	15000	19.8
w2_70	09:02:02	-02:25	0.70	14307	19.6
w2_71	09:04:09	-02:25	0.58	18062	23.8
w2_72	09:06:15	-02:25	0.56	19273	25.4
w2_79	09:02:02	-02:03	1.04	-	-
w2_80	09:04:09	-02:03	1.22	-	-
w3_126	14:14:17	+56:10	0.51	20473	27.0
w3_127	14:17:55	+56:10	0.53	22422	29.5
w3_128	14:21:32	+56:10	0.53	19375	26.4
w3_137	14:14:17	+56:36	0.45	23178	31.0
w3_138	14:17:55	+56:36	0.46	23139	30.5
w3_139	14:21:33	+56:36	0.52	20559	27.2
w3_140	14:25:11	+56:36	1.36	-	-
w3_149	14:17:55	+57:00	0.48	21774	28.7
w3_150	14:21:33	+57:00	0.48	19911	27.7
w3_151	14:25:10	+57:00	0.66	17118	22.6
w3_159	14:14:18	+57:26	0.55	19284	25.4
w3_160	14:17:56	+57:26	0.51	20531	27.3
w3_161	14:21:33	+57:26	0.48	22222	29.3
w3_162	14:25:10	+57:26	0.59	21221	28.0

Table 4.6: W-Fields quality statistics. 1200 sec stacks (5×240 sec exposures) taken in z' on April 17-19th, 2010. W2 is 1.26 deg^2. W3 field is 2.73 deg^2. Stacks with seeing $> 0.8'$ were discarded.

Region	S/N	σ_{fit}	RA	DEC	r_{in}	
			[J2000]	[J2000]	[pix]	[arcmin]
w2_61	3.63	3.67±0.018	9:01:53.4	-2:45:34.0	500	1.67′
w2_61*	-4.02	-	9:02:00.5	-2:54:5	700	2.33′
w2_62	3.78	3.94±0.017	9:03:41.8	-3:01:15.8	300	1′
w2_62	4.01	4.18±0.017	9:04:32.5	-2:55:23.1	300	1′
w2_63	3.56	3.81±0.017	9:07:10.1	-3:01:20.4	300	1′
w2_63	3.32	3.39±0.018	9:07:10.2	-3:01:22.0	500	1.67′
w2_63	3.87	3.83±0.019	9:06:37.4	-2:47:03.9	700	2.33′
w2_70	3.31	3.33±0.018	9:01:17.3	-2:28:44.0	300	1′
w2_70	3.95	3.70±0.020	9:02:27.1	-2:25:30.2	1000	3.33′
w2_71	4.25	3.61±0.022	9:04:36.5	-2:21:23.1	700	2.33′
w2_71	4.26	4.37±0.018	9:03:26.2	-2:40:14.5	300	1′
w2_72	3.80	3.76±0.018	9:06:32.9	-2:36:34.5	300	1′
w2_72	3.27	2.94±0.021	9:05:52.0	-2:22:13.8	700	2.33′
w2_72*	-4.18	-	9:06:16.2	-2:31:03.0	500	1.67′

Table 4.7: Highest signal peaks in the W2 field

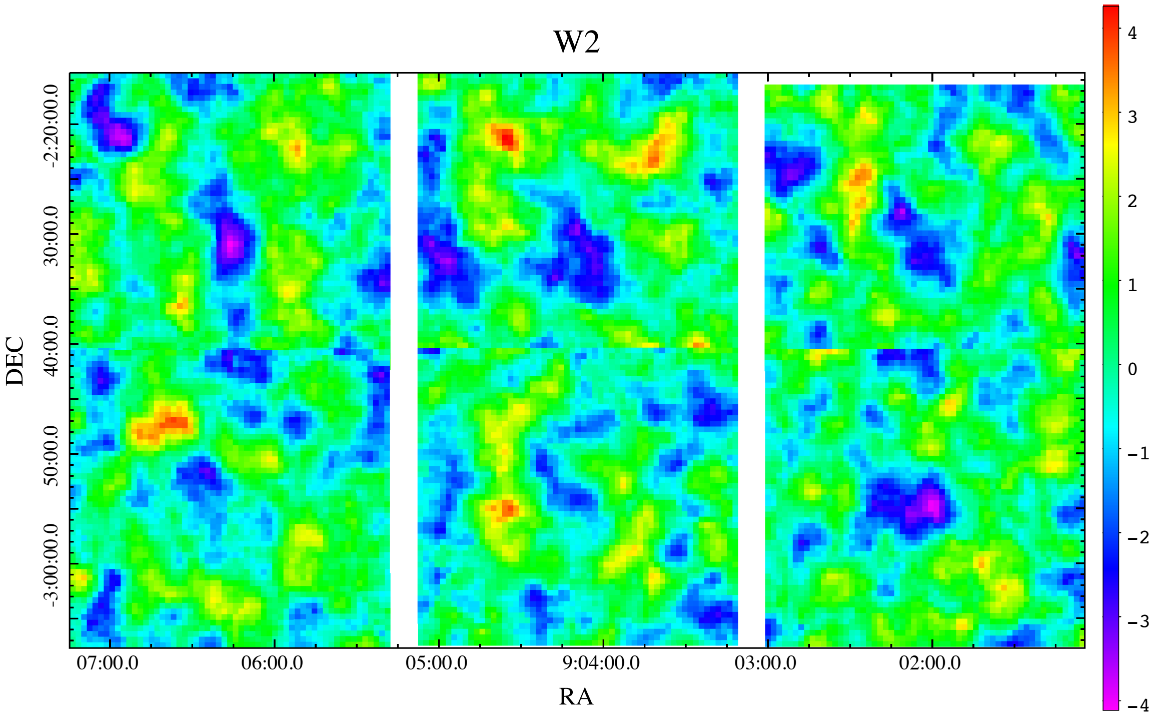

Figure 4.20: $r_{in} = 700$ and 1000 convergence maps of the W2 field region.

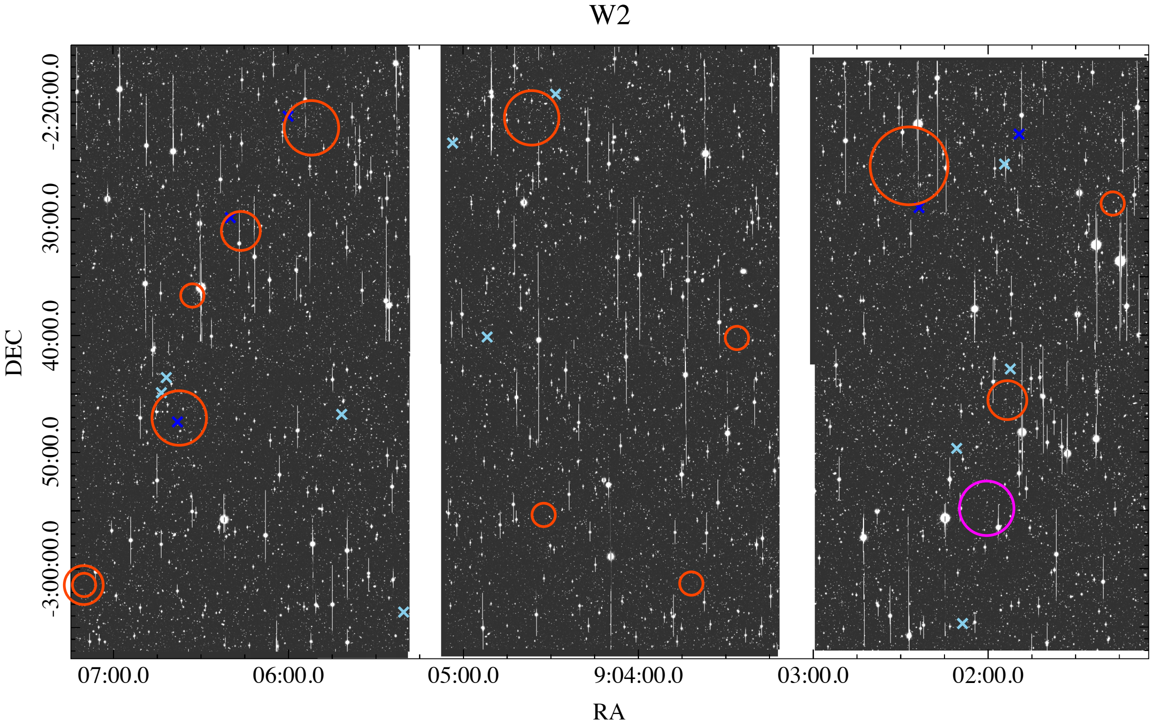

Figure 4.21: Signal peaks (red circles) shown at different characteristic scales overlaid on the W2 field, with known candidate clusters from outside surveys marked by light blue crosses, other potential candidates are shown as green crosses. Detections at the borderline redshifts of this dataset are dark blue. Voids are magenta.

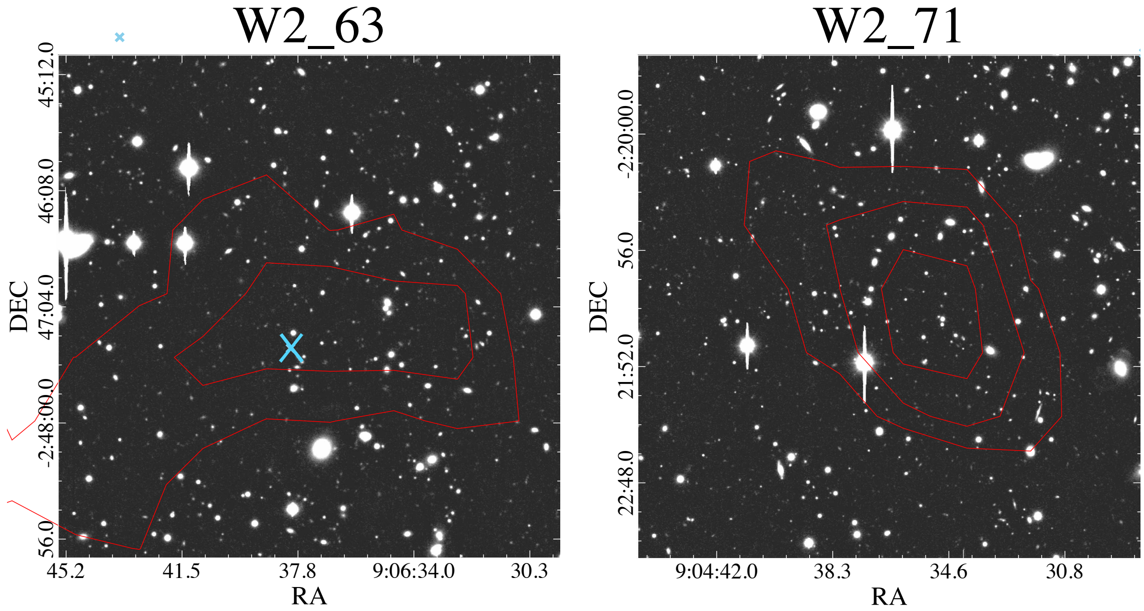

(a)

(b)

Figure 4.22: Signal peaks in the W2 fields. **(a)**: 3.87 S/N peak at 2.33′ scale (700 pix). Contours at 3, 3.5. **(b)**: 4.25 S/N peak at 2.33′ scale (700 pix). Contours at 3, 3.5, 4.

W3 Fields

W3 field key located on PG. *171.*

Region	S/N	$\sigma_{\rm fit}$	RA	DEC	r_{in}	
			[J2000]	[J2000]	[pix]	[arcmin]
w3_126	3.55	3.44±0.019	14:15:58.9	+56:20:15.4	500	1.67′
w3_126	4.17	3.71±0.021	14:13:37.9	+56:19:35.0	700	2.33′
w3_127	4.23	3.83±0.020	14:17:16.4	+56:15:30.4	500	1.67′
w3_127	4.46	4.46±0.018	14:18:38.5	+56:09:08.0	300	1′
w3_128	3.56	3.19±0.021	14:22:28.5	+56:19:52.2	1000	3.33′
w3_137	4.01	4.01±0.018	14:12:49.6	+56:38:17.7	300	1′
w3_137	3.53	3.34±0.019	14:14:41.4	+56:48:00.1	500	1.67′
w3_137*	-4.21	-	14:15:51.2	+56:34:59.0	700	2.33′
w3_138	4.38	4.01±0.020	14:17:04.0	+56:39:33.0	500	1.67′
w3_138	4.06	3.72±0.020	14:18:53.1	+56:41:33.2	500	1.67′
w3_138	4.15	3.77±0.020	14:17:21.0	+56:38:36.3	700	2.33′
w3_138*	-5.30	-	14:17:58.8	+56:36:41.9	500	1.67′
w3_139	3.90	3.79±0.019	14:21:46.1	+56:31:27.8	500	1.67′
w3_139	4.17	3.86±0.020	14:21:06.8	+56:47:26.9	700	2.33′
w3_139	3.69	3.74±0.018	14:22:18.2	+56:41:10.5	300	1′
w3_139	5.59	5.18±0.020	14:23:18.0	+56:39:47.0	700	2.33′
w3_139	3.68	3.58±0.019	14:16:27.5	+56:56:01.2	500	1.67′
w3_150	4.43	4.58±0.018	14:20:41.2	+56:51:22.6	300	1′
w3_150	3.96	3.56±0.021	14:20:33.6	+57:12:25.9	700	2.33′
w3_150	5.84	4.91±0.023	14:23:19.5	+57:12:59.7	1000	3.33′
w3_151	4.64	3.88±0.022	14:26:03.1	+57:05:23.6	1000	3.33′
w3_159	5.10	5.12±0.018	14:13:05.0	+57:35:45.8	500	1.67′
w3_159*	-5.19	-	14:14:23.9	+57:23:18.9	700	2.33′
w3_160	3.96	4.36±0.017	14:18:38.3	+57:29:53.2	300	1′
w3_160	4.16	4.46±0.017	14:19:04.8	+57:25:38.5	700	2.33′
w3_161	4.91	4.30±0.021	14:22:15.3	+57:27:39.3	700	2.33′
w3_161	3.84	3.36±0.021	14:20:27.1	+57:31:22.1	700	2.33′
w3_162	4.39	4.18±0.020	14:23:50.5	+57:26:47.3	1000	3.33′

Table 4.8: Highest signal peaks in the W3 field.

4.5.1 CFHTLS W2 & W3 Results

From the NED extragalactic database, our W2 fields contain 12 uniquely-located cluster candidates within the redshift range of detectability, of which we confirm 6, and propose 6 in addition to these. In W3, of the 5 non-CFHTLS candidates which exist, we detect 2. 30 unique, non-extended-structure cluster candidates originate from the CFHTLS study, of which we confirm 6. 13 of our peaks suggest unique cluster detections.

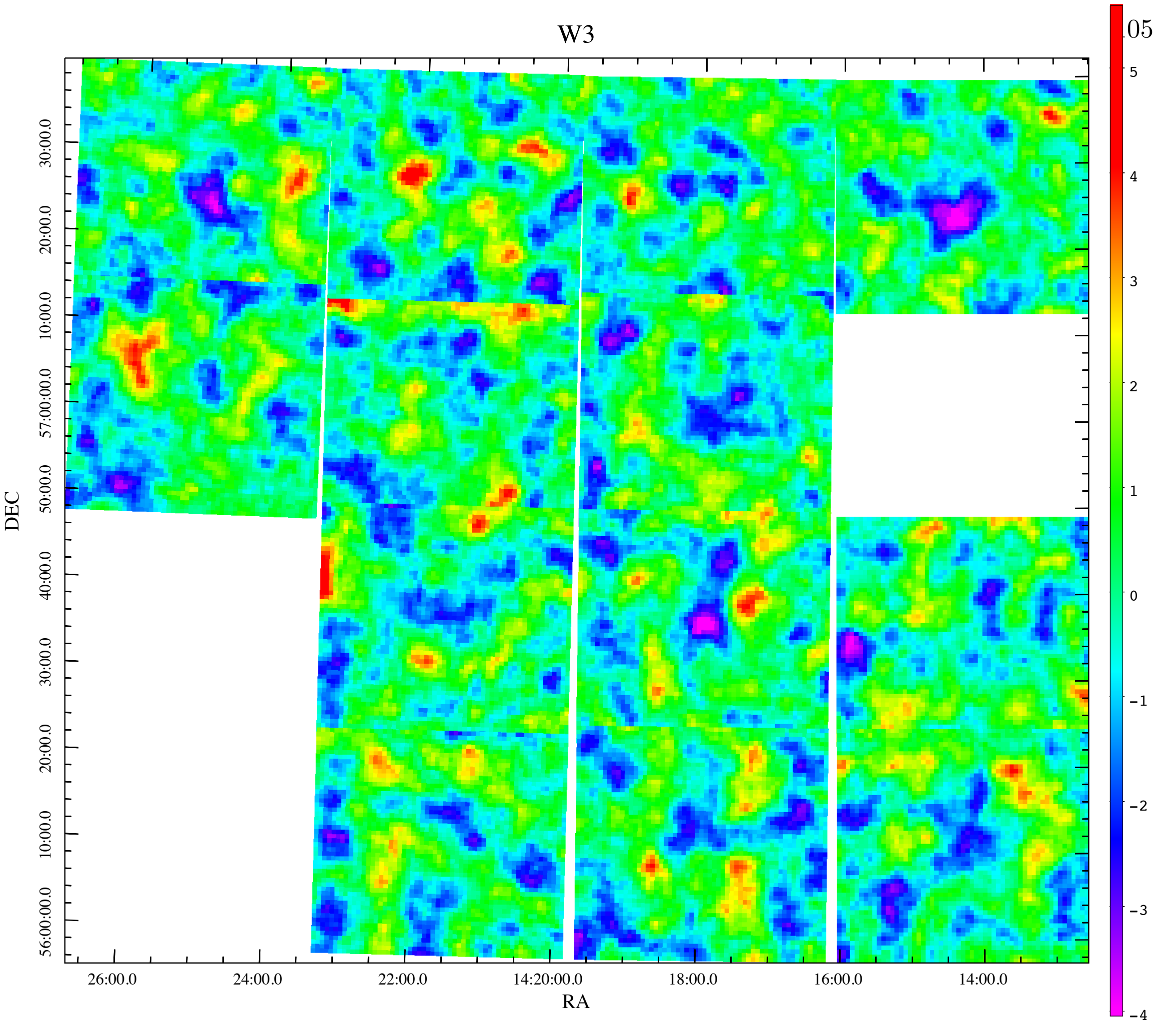

Figure 4.23: $r_{in} = 700$ pix convergence map of the W3 field region.

The vast majority of previously cataloged cluster candidates from these fields (every one from W2, and all but 5 in the regions covered by our W3 sample), are candidate clusters attributed to a photometric cluster survey conducted on the four CFHTLS regions by Durret *et al.* (2011), [29]. They proposed a total of 6802 possible cluster candidates over 154 deg^2 via photometric redshift counts. Their methodology is sensitive to clusters from $0.1 \leq z \leq 1.15$, with the bulk of detections above $z \gtrsim 0.5$, and four times as many intermediate mass ($10^{14} M_\odot$) clusters in the high redshift $0.5 \leq z \leq 1.15$ range than the range $0.2 \leq z \leq 0.5$, which overlaps our WL sensitivity. Their catalog also contains a large number of 2σ detections, which they attribute to "catastrophic redshift clustering" in their photo-z calculations. They also found their measurements unreliable below $z = 0.35$, and were unable to cross-correlate detections at these low redshifts (though this is the well within our most sensitive region). Therefore, our findings allow a useful contrast with photometric

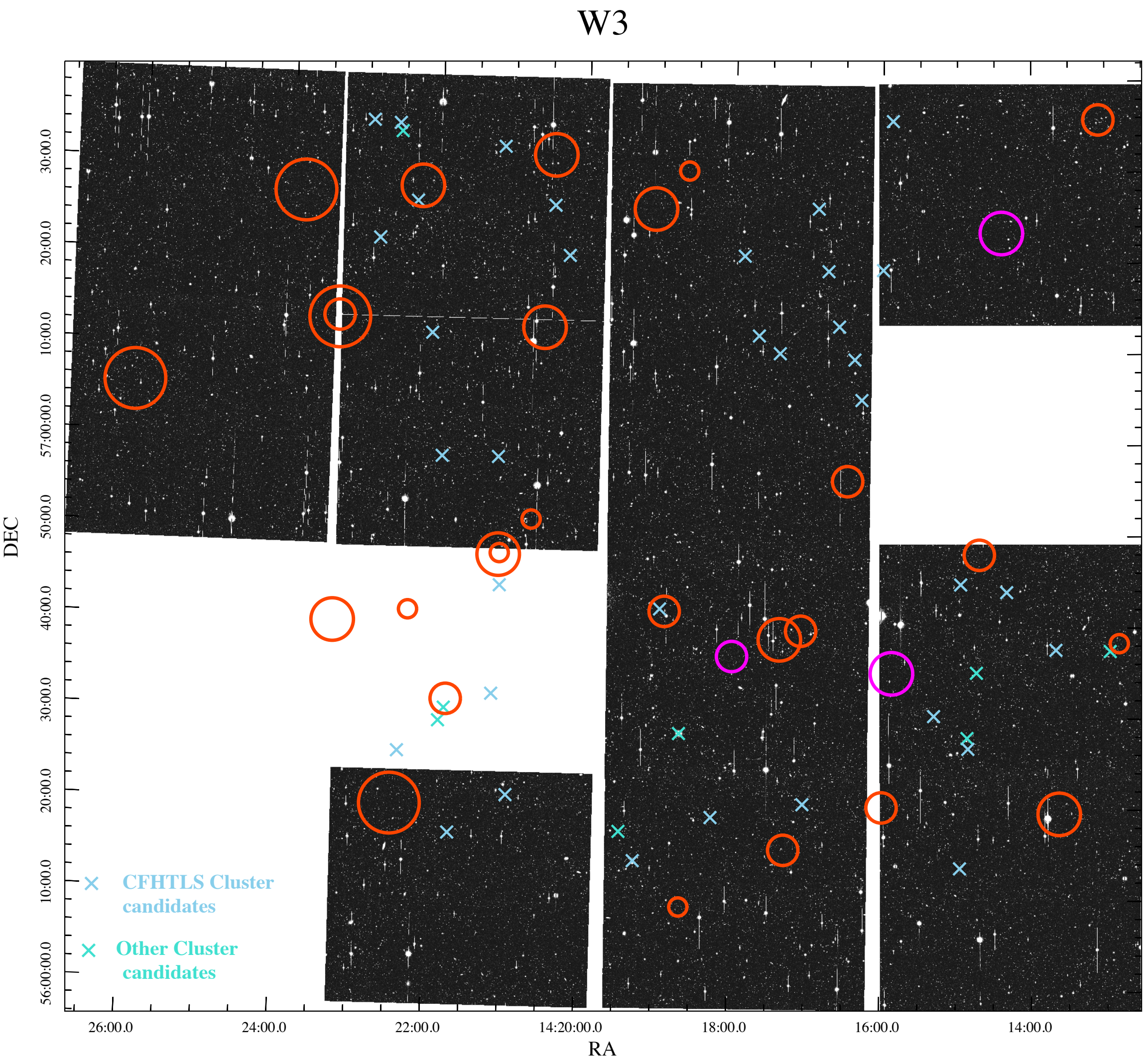

Figure 4.24: Signal peaks (red circles) shown at different characteristic scales overlaid on the W3 field, with known candidate clusters from outside surveys marked by light blue crosses. Voids are magenta. Cluster candidates at borderline redshifts within this region are dark blue. (Note: W3_139 does not display as background in this imaging projection.)

galaxy cluster searches at this redshift scale.

(Complete tables and additional figures dealing with this region may be found in §A.4 & §A.5)

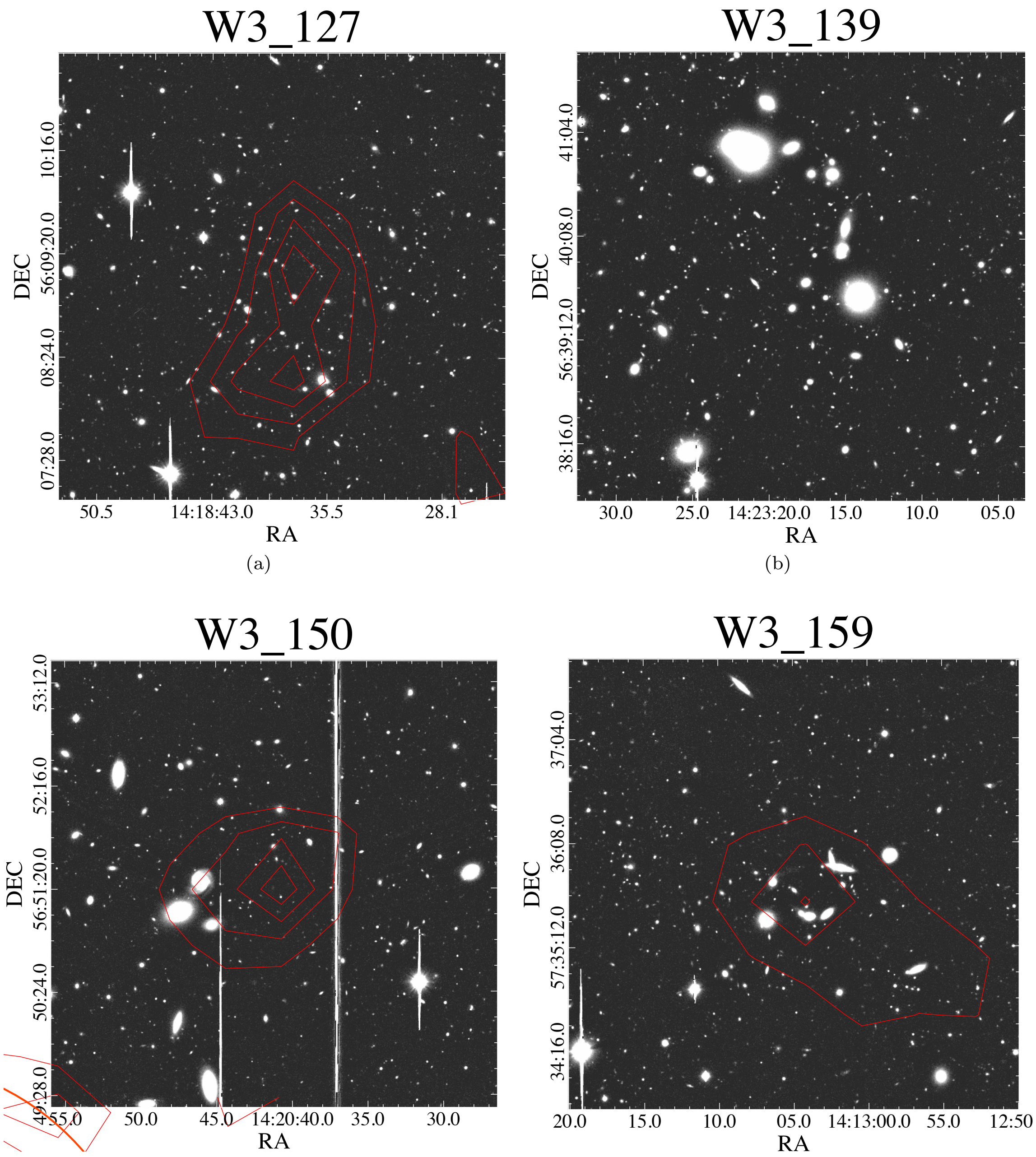

(a)

(b)

(c)

(d)

Figure 4.25: Signal peaks in the W3 fields. **(a)**: 4.46 S/N peak at 1′ scale (300 pix), contours at 2.5, 3, 3.5, 4. **(b)**: 5.59 S/N peak at 2.33′ scale (700 pix), (contours outside field of view). **(c)**: 4.43 S/N peak at 1′ scale (300 pix), contours at 2.5, 3, 3.5, 4. **(d)**: 5.10 S/N peak at 1.67′ scale (500 pix), contours at 3, 4, 5.

4.6 Boötes Void

Boötes field key located on PG. *179.*

Another large area of high-quality data lies in a region adjacent to the so-called Boötes void, a nearby spherical expanse approximately 75 Mpc in diameter with an extreme underdensity of galaxies (less than 100 have been observed) [54]. However, it borders the Hercules and Boötes superclusters, and the data obtained is a 2.96 deg^2 section of the sky nearly equidistant from the centers of the void and the Boötes supercluster (FIG. 4.26). (We refer to this region as *Boötes* or *F-fields* for convenience.)

Observations were performed April 27th & 28th, 2011, under proposal S11A-083 "A Suprime View of Clusters in Bootes" by P.I. Yen-Ting Lin[7]. Sky conditions were measured as extremely clear, with seeing reported between $0.2''$-$0.6''$ (though our more thorough analysis shows it closer to $0.5''$ on average). Observers sought imaging between 3-5, 240 sec exposures in z'. Our analysis restricted these to those pointings of greater than 720 sec and sub-$0.6''$ seeing. Of 16 usable stacks, 13 exceeded 1200 sec, and 12 contained $\geq$31 resolved galaxies per arcmin^2 (TABLE 4.9). Despite exceptionally good seeing, and having been imaged in 2011, there is as yet no published literature crediting the P.I. of the imaging proposal (a convention used to credit the particular observation, particularly in the case of the first use of images).

This area was initially one of two observed in deep optical and near-infrared by the NOAO Deep Wide-Field Survey (NDWFS) [50], each covering 9.3 deg^2 of the sky and aimed at understanding large scale structure and evolution at $z > 1$. Boötes was one of these two fields, centered at $14^h32^m05^s \ \ +34°16'$, near the north galactic pole, while the other, not used in our dataset, was found in Cetus in the southern hemisphere. The regions were originally imaged by the MOSAIC camera on the Mayall Telescope at KPNO (and Blanco at CTIO), while infrared observations were first made via other KPNO instruments. It was later observed by Spitzer as parts of the IRAC Shallow Survey [32], and by the Chandra X-ray Observatory [79]. Spitzer later conducted a multi-epoch survey, the "Spitzer Deep Wide-Field Survey" (SDWFS) [108], over the same region.

These regions were selected for low IRAS cirrus emission, relatively small amounts of neutral hydrogen, and due to expected later observation of the areas by the VLA FIRST radio survey. It is part of HerMES study listed as "NDWFS/Bootes" and as "Bootes-SCUBA2."

---

[7] http://www.naoj.org/Observing/Schedule/s11a.html

Quality

This area consists of sixteen fields, with numerous others from this data set having been rejected because of low-exposure times or aberrant seeing and three (F43, F61, and F72) included for completeness, despite including only 720 sec of exposure time. Results from these areas, though included in this section, are to be considered more skeptically due to their poorer depth. Further, data irregularities resulted in only half of F81 stacking correctly (though the remaining area was otherwise unaffected), and F62 only able to be subjected to a single circularization. The once (rather than doubly) circularized stack exhibited no particularly interesting features (high significance WL detections would have been evident in this field even prior to a 2nd circularizing step). $15^{1}/_{2}$ pointings were successfully reduced, with $12^{1}/_{2}$ meeting all quality criteria. Of the best fields, seeing averages $0.52''$ and 34.80 gal/arcmin^2. Including the three substandard areas the quality is $0.53''$ and 33.17 gal/arcmin^2, in total (the three 720 sec areas yield comparable seeing but lower, 26.40 gal/arcmin^2, galaxy density figures). Though the stellar resolution varies the least from pointing to pointing of all 5 major wide-field analysis regions, the exposure times (due to both observer choice and our own selection for inclusion in stacking) vary more greatly, with 1200 sec, 1440 sec stacks and a single 2880 sec field, F63. (Table 4.9)

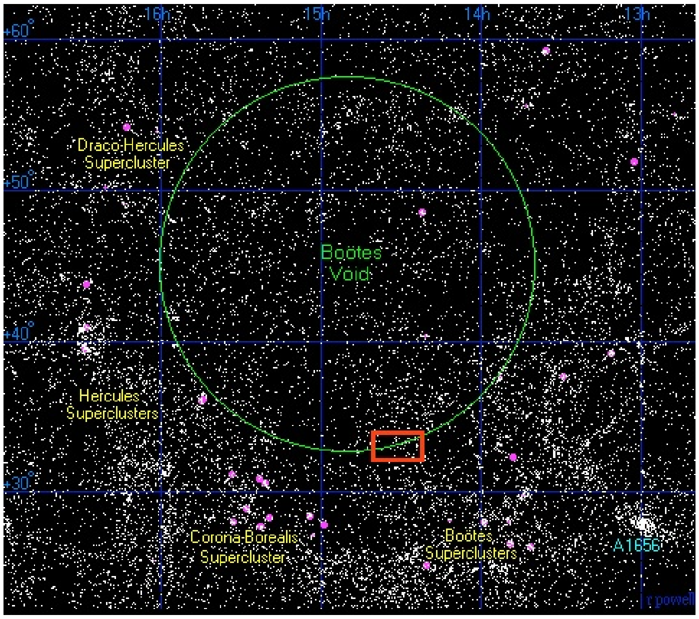

Figure 4.26: Location of “Boötes Void” data (red box) relative to the void itself and adjacent superclusters [91].

Region	RA	DEC	t_{exp}	Seeing	N_{gal}	$\langle n_{\mathrm{gal}} \rangle$
	[J2000]	[J2000]	[sec]	[$''$]		[arcmin^{-2}]
f43	14:30:21	+34:15	720	0.52	18049	27.7
f44	14:32:39	+34:15	1440	0.57	25508	38.7
f45	14:34:57	+34:15	1440	0.46	24151	36.9
f46	14:37:16	+34:15	1440	0.48	25562	39.4
f52	14:28:22	+33:50	1200	0.51	22705	35.3
f53	14:30:59	+33:50	1440	0.49	24359	37.0
f54	14:33:35	+33:50	1200	0.58	22509	34.2
f56	14:37:42	+33:47	1440	0.59	21160	31.7
f61	14:25:48	+33:24	720	0.53	16815	25.8
f62†	14:28:26	+33:24	1200	0.54	21299	32.9
f63	14:31:04	+33:24	2880	0.53	23959	36.3
f64	14:33:42	+33:24	1440	0.47	23541	35.8
f71	14:25:59	+32:58	1200	0.52	20762	31.6
f72	14:28:37	+32:58	720	0.53	16363	25.7
f73	14:31:14	+32:58	1440	0.54	20540	31.2
f81	14:25:59	+32:25	1440	0.56	9197	28.0

†Field only stacked and circularized once.

Table 4.9: Boötes Fields. 1200 sec (5 × 240 sec stacks) taken in z'. Subtends 2.96 deg^2 of the sky.

4.6.1 Boötes Results

Within our redshift range, 25 isolated candidates exist within our imaged regions. Our peaks correspond to only 4 of these, while 15 are unique compared to prior work.

In previous studies, F46 (upper-left) appears to contain some extended structure, which we positively confirm (Fig. 4.30). Our highest detection is in F43 (rightmost of upper row), where we obtain a 6.30 S/N cluster. We also obtain a clear image of a strong lens in F64, at the location of a 3.70 S/N peak with r_{in}=1$'$ (Fig. 4.30).

Similar to the case of Lockman and EN1 regions, the existing cluster candidates in these fields come almost exclusively from photometric methods utilizing SDSS data [127] as well as earlier work looking for galaxy overdensities based on the digitized Second Palomar Observatory Sky Survey [62, 40, 39, 62]. And though we select for candidates with expected cluster redshift within 0.05-0.5, some bias may still be present.

(Complete tables and additional figures dealing with this region may be found in §A.6.)

Region	S/N	$\sigma_{\rm fit}$	RA	DEC	r_{in}	
			[J2000]	[J2000]	[pix]	[arcmin]
f43	6.30	5.64±0.022	14:30:50.9	+34:21:12.2	500	1.67′
f44	4.43	2.97±0.030	14:32:41.5	+34:27:04.7	700	2.33′
f44	4.28	2.59±0.033	14:33:03.3	+34:21:31.5	1000	3.33′
f44*	-6.92	-	14:32:40.6	+34:16:12.4	1000	3.33′
f45*	-4.56	-	14:34:51.2	+34:15:59.7	500	1.67′
f46	4.86	4.35±0.022	14:37:08.5	+34:19:05.3	700	2.33′
f52	4.49	3.76±0.024	14:28:07.6	+33:45:22.9	500	1.67′
f52	4.35	3.19±0.028	14:29:19.5	+34:00:34.6	1000	3.33′
f53	3.71	3.71±0.020	14:31:29.3	+33:53:45.9	300	1′
f54	4.00	4.16±0.019	14:33:08.0	+33:50:25.2	300	1′
f54	4.44	4.62±0.019	14:32:45.8	+34:01:00.1	300	1′
f56	4.88	5.10±0.019	14:38:18.2	+33:55:27.9	300	1′
f61	5.22	4.94±0.021	14:25:29.1	+33:14:39.8	500	1.67′
f63	4.40	4.06±0.021	14:32:08.7	+33:15:10.4	500	1.67′
f63	4.19	3.61±0.023	14:31:43.2	+33:31:45.9	700	2.33′
f63*	-4.51	-	14:31:05.3	+33:24:49.0	500	1.67′
f64[†]	3.70	3.57±0.020	14:33:53.1	+33:30:15.6	300	1′
f64	4.53	3.91±0.023	14:34:19.2	+33:27:17.3	700	2.33′
f71	4.63	3.51±0.027	14:26:41.5	+33:00:53.5	1000	3.33′
f71	4.44	3.90±0.023	14:25:41.1	+32:51:49.4	500	1.67′
f71*	-5.32	-	14:25:01.2	+32:57:59.8	500	1.67′
f73	4.37	3.20±0.028	14:31:50.6	+32:51:44.5	1000	3.33′
f73	4.04	3.13±0.026	14:30:54.4	+32:49:29.1	700	2.33′

[†] Exhibits strong lensing arc.

Table 4.10: Highest signal peaks in the Boötes field.

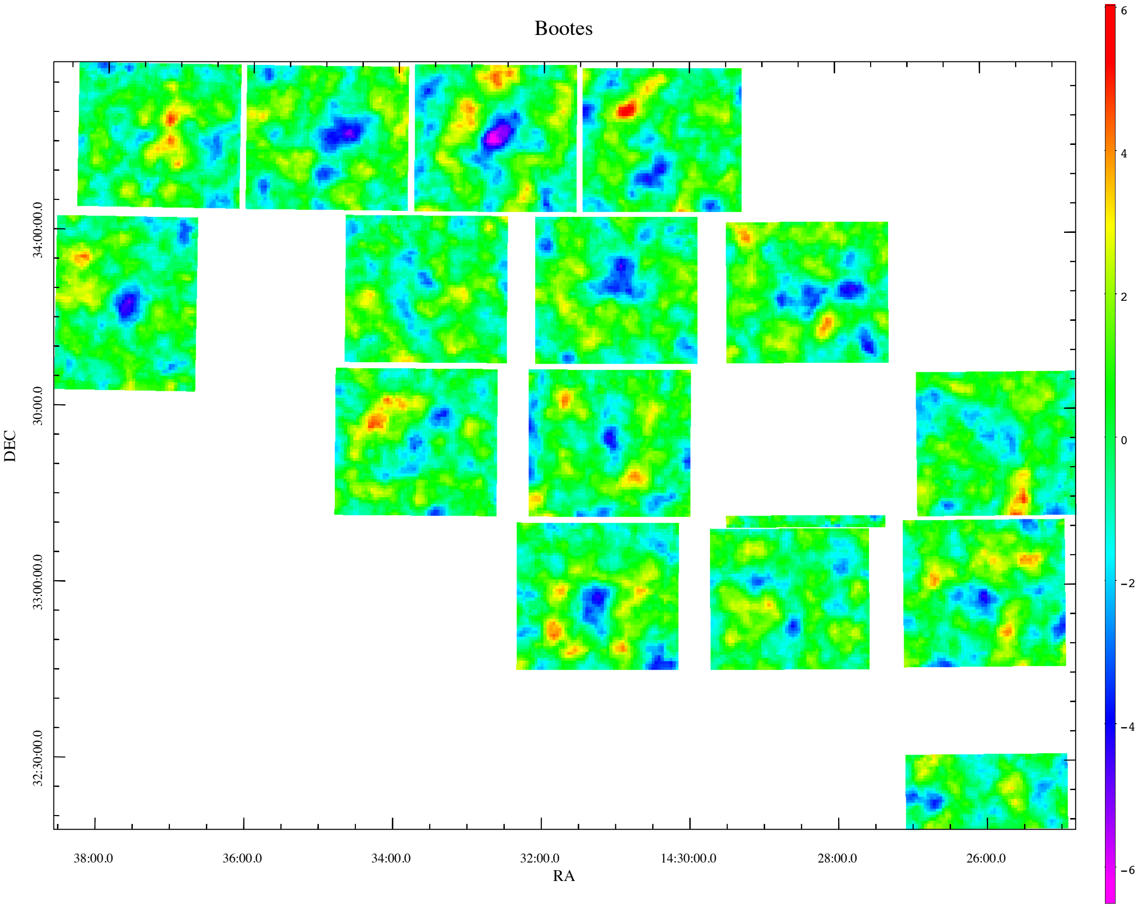

Figure 4.27: $r_{in} = 700$ pix convergence map of the Boötes Void field region.

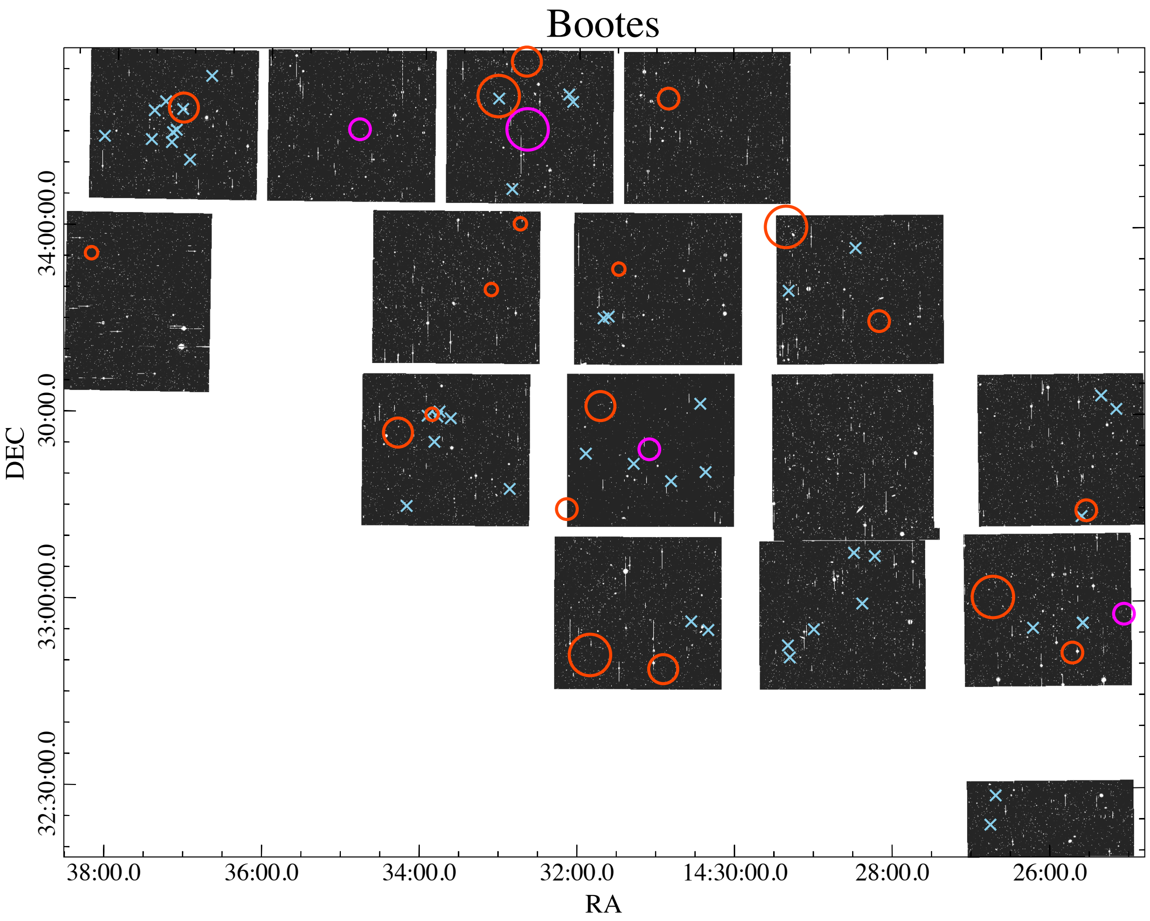

Figure 4.28: Signal peaks (red circles) shown at different characteristic scales overlaid on the Boötes field, with known candidate clusters from outside surveys marked by light blue crosses. Voids are magenta.

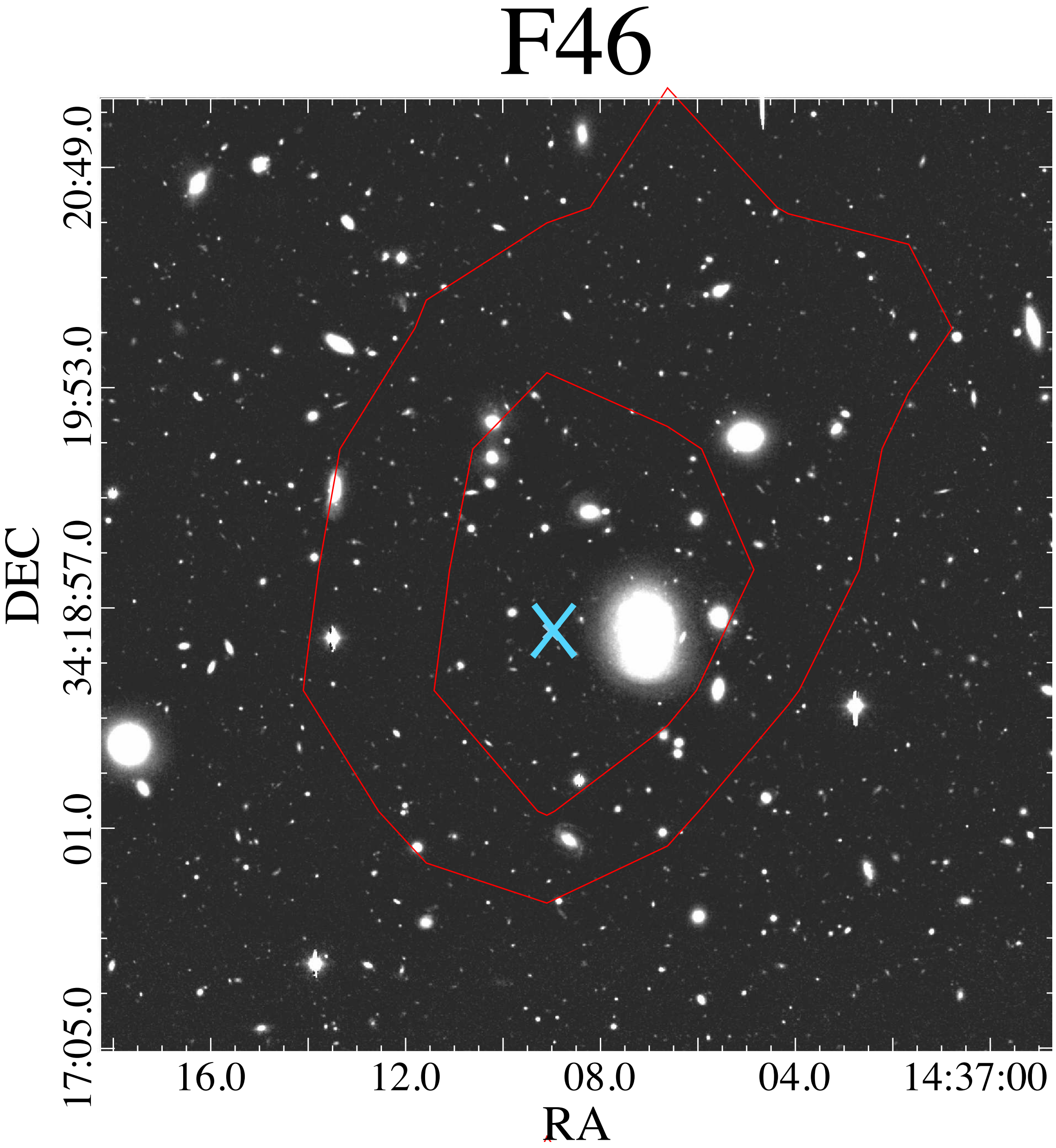

Figure 4.29: 4.86 S/N peak at 2.33′ scale (700 pix), contours at 3, 4.

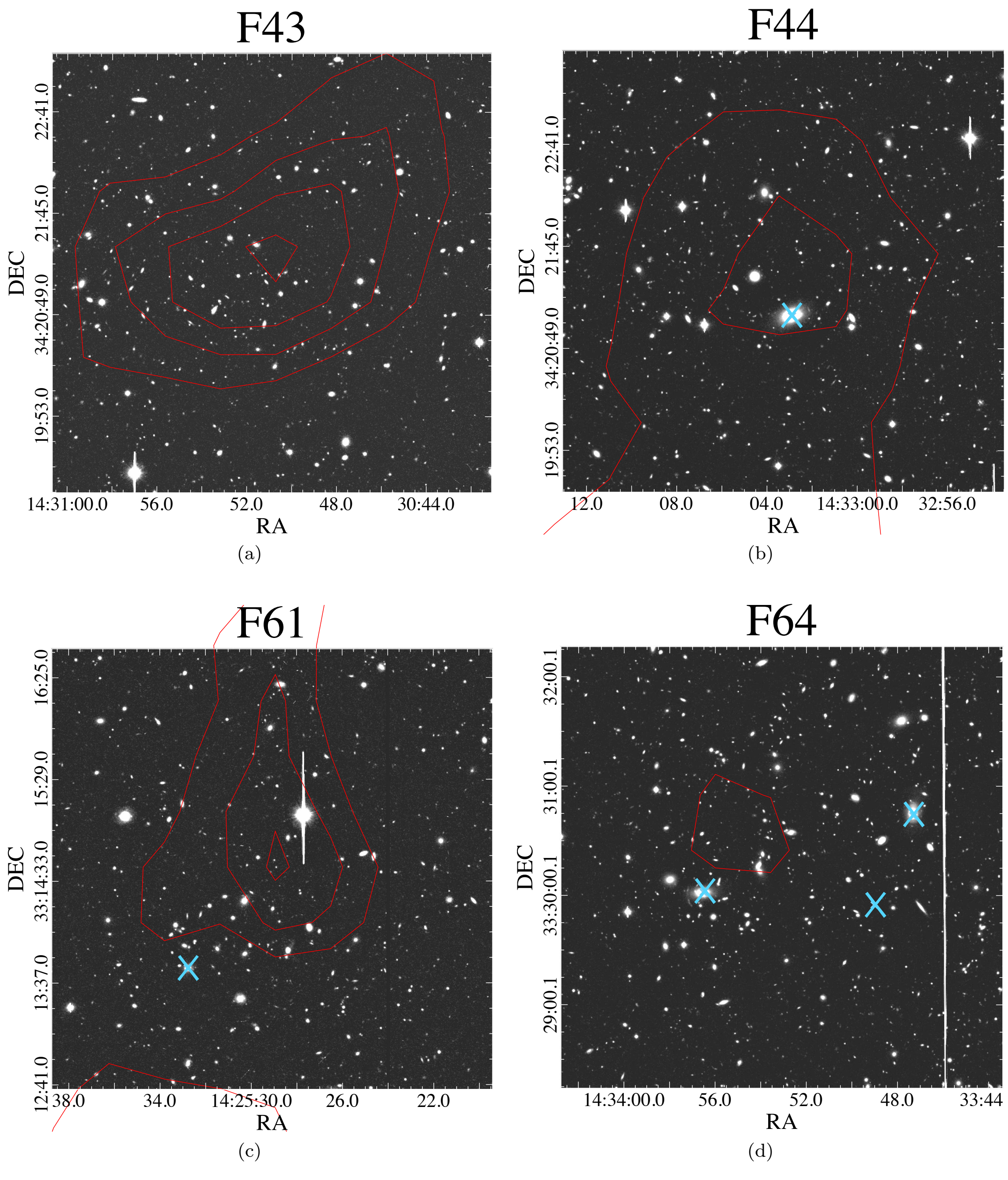

(a) (b) (c) (d)

Figure 4.30: Signal peaks in the Boötes fields. **(a)**: 6.30 S/N peak at 1.67′ scale (500 pix), contours at 3, 4, 5, 6. **(b)**: 4.28 S/N peak at 3.33′ scale (1000 pix), contours at 3, 4. **(c)**: 5.22 S/N peak at 1.67′ scale (500 pix), contours at 3, 4, 5. **(d)**: 3.70 S/N peak at 1′ scale (300 pix), contour at 3. Gravitational lens evident near leftmost X.

4.7 Summary of Results

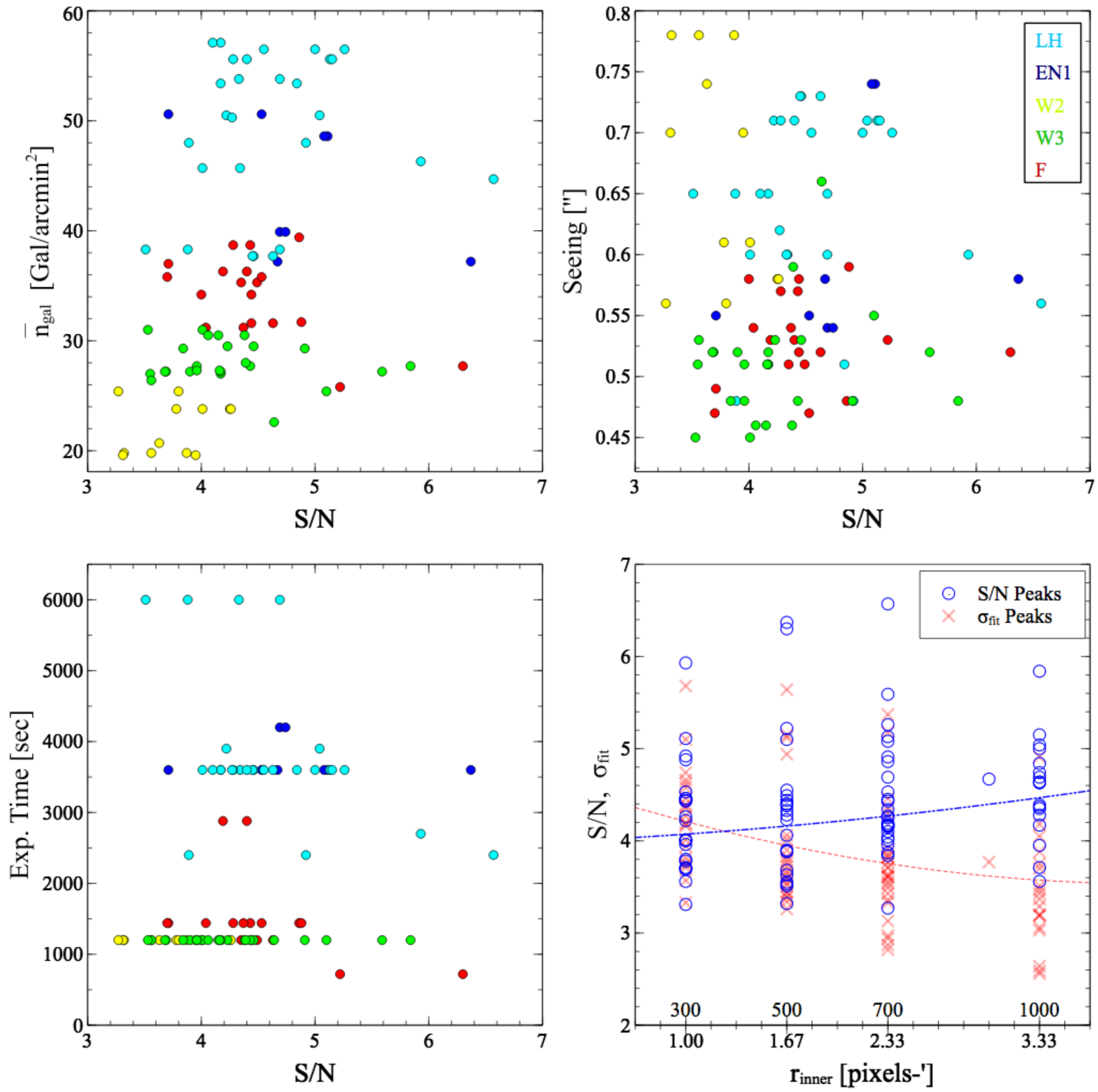

Figure 4.31: Summary of quality statistics for each of the 92 candidate peaks across all scales. Boötes is red, W2 & W3 are yellow and green, and the light and dark blues are LH and EN1.

In all, with some variance in image quality, (Fig. 4.9), this chapter contains WL measurement of 10.34 deg^2 of the sky from 53 separate pointings, imaging 1,268,828 source galaxies. We find 92 candidate peaks of S/N $\geq$ 3.0 (with 2 duplicate couples measured at identical S/N for two different r_{in} values, and both included on the chart of final candidates). 43 of our cluster candidates correspond to known candidate clusters, while 47 are unique, hitherto unknown structures. Our

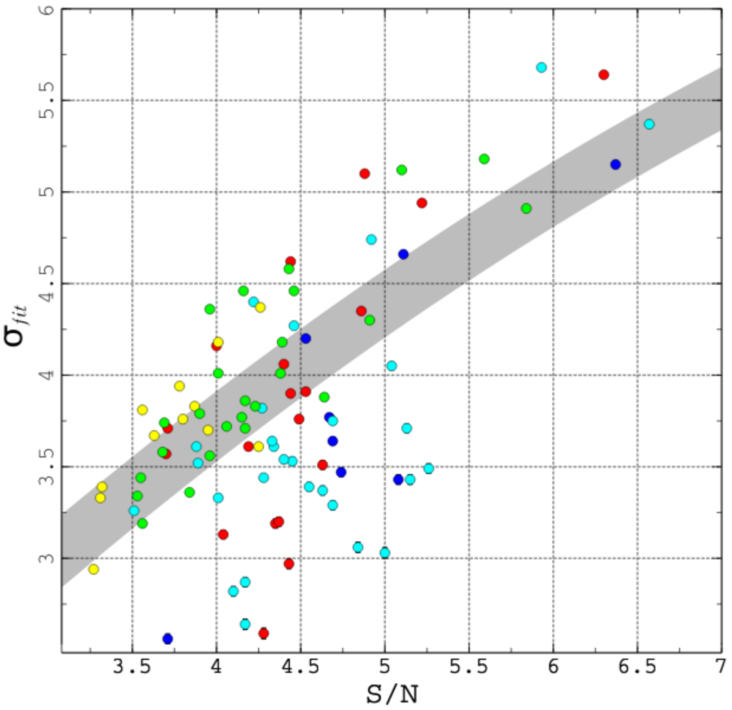

Figure 4.32: Relation of S/N to σ_{fit} values.

frequency of detection is 8.704 peaks-deg^{-2}, with Boötes the emptiest of the five regions. LH, EN1, W2, and W3 possess a convergence peak density of 10.53, 10.96, 9.52, 9.12 peaks-deg^{-2}, respectively, while Boötes only contains 6.42 peaks-deg^{-2}.

In total, including all measured peaks (not just the highest S/N selected to determine the characteristic extent) we find similar numbers of detections across each scale—54, 70, 64, 50 at scales of $1'$, $1.67'$, $2.33'$, and $3.33'$, respectively—showing that no systematic factor is biasing the application of the *fiatmap* algorithm.

We also see that the relationship between the S/N values and our gaussian assurance parameter, σ_{fit}, is approximately linear (Fig. 4.32), with similar distributions (Fig. 4.31d), demonstrating that the σ_{fit} is a useful value for gauging signal strength. We find the strongest determinant of S/N strength is resolved galaxy density, $\langle n_{\text{gal}} \rangle$, (Fig. 4.31). However, the inherent regional variability is significant enough to provide a possible alternative explanation. Though seeing and exposure depth are determinative in attaining high source-density, we find that they do not correlate noticeably with lensing signal strength *per se* among a self-selected dataset pre-selected above certain quality parameters. This is somewhat unexpected; however, we note that our sample is comparatively

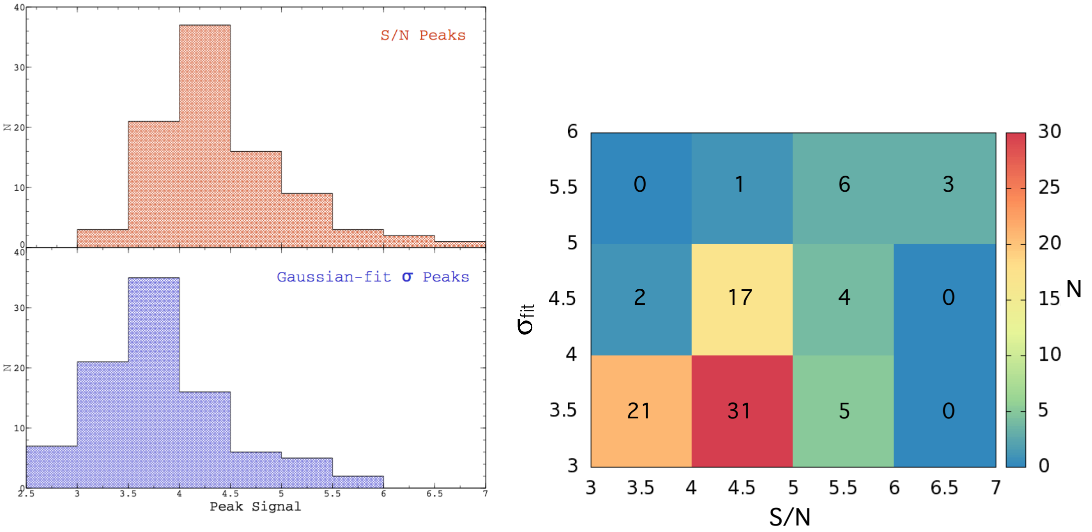

(a) (b)

Figure 4.33: **(a)** Correlation between S/N convergence peaks and their value in terms of standard deviations to the fitted normal distribution. **(b)** Two-dimensional histogram of peaks in terms of S/N and σ_{fit}.

homogeneous in terms of seeing because we set a high quality threshold for inclusion. Mean field stellar FWHM only ranges between $0.47''$-$0.78''$; this is nearly the best ground-based seeing possible for a sample of this size. Therefore, it is likely that among fields with excellent seeing, with all other quality parameters being equal, WL detection likelihood does not measurably increase as seeing improves. A wider range of values may be necessary to discern a significant effect in terms of WL detection.

Our results are in strong agreement with previous weak lensing study of a portion of the Lockman Hole by Miyazaki *et al.* (2007) [74]. We independently identify all but one of their detections in overlapping regions, providing a good external check of our cluster detection method. Our detections do not match optical samples as well—likely due, in part, to the large numbers of false positives found in those methods. Best agreement with previously-known cluster candidates (found via any method) is seen in the Lockman and EN1 regions. Prominent X-ray sources found in LH and EN1 are detected at high significance as well.

Though our goals and the scope of this work is substantially different, we note that in terms of total sky analyzed through lensing techniques, our 10.34 deg^2 subtended is comparable to the scale of far better-funded projects with substantially more personnel[8]. Furthermore, it also comprises only

---

[8] DLS: 21 deg^2; Weighing the Giants: 12.5 deg^2; CFHTLS-Deep: 4 deg^2; etc.

one of a handful of large-scale lensing cluster surveys attempted so far, a number which is certain to grow as ever larger instruments and enormous data-handling abilities come online over the next decade.

Chapter 5

Selected Cluster Weights

> *"...As we know, there are known knowns; there are things we know we know.*
> *We also know there are known unknowns.*
> *That is to say, we know there are some things we do not know.*
> *But there are also unknown unknowns—the ones we don't know we don't know.*
> *And if one looks throughout [history]...*
> *it is the latter category that tend to be the difficult ones."*
> Donald Rumsfeld

This chapter employs the numerous data handling and analysis tools developed for large-scale Subaru WL processing to obtain mass measurements of several clusters that have no previous published lensing results (as well as one cluster with both WL and other mass estimates, for calibration of our technique). In addition to the reduction methods performed to generate 2D mass maps as in the previous chapter, several additional catalog preparation steps are needed. First, because mass measurements require source redshifts, we construct an ensemble approach to redshift estimation for the galaxies in our sample (§5.1.1). We then create high-resolution 2D mass reconstruction maps of each cluster to locate the central lensing peak and mass distribution. We utilize an NFW-fitting approach to find shear-derived M_{200} values (§5.1.2). We calibrate our approach by comparison with a well-studied cluster, Abell 383 (§5.2), and proceed to mass estimates. We make measurements of the four galaxy clusters PLCK G 100.2-30.4, PLCK G 018.7+23.6, Abell 1672, & RXC J1651.1+0459—and are able to generate mass estimates of three of them.

Region	$\langle n_{\mathrm{gal}} \rangle$ [arcmin^{-2}]	Exp. Time [sec]	Seeing [$''$]	Depth [mag]	S/N	z	M_{200} [$\times 10^{14} M_{\odot}$]	Filters
Abell 383[a]	37.3	6300	0.52	25.62	10.21	0.187	7.65±1.61	$\boldsymbol{z'}$
PLCK G 100.2-30.4	39.9	3420	0.60	27.06	11.37	0.38[b]	8.17±2.12[c]	$\boldsymbol{r'}g'i'z'$
PLCK G 018.7+23.6	20.4	2700	0.66	26.93	4.72[d]	0.09	-	$\boldsymbol{r'}g'i'z'$
RXC J1651.1+0459	37.0	2160	0.63	26.30	5.39	0.15	3.37±1.96	$\boldsymbol{i'}, V$
Abell 1672	46.1	1920	0.69	26.41	5.34	0.19	5.61±2.81	$\boldsymbol{i'}, V$

[a] Calibration field.

[b] Published values range between 0.31-0.38. See §5.3.1.

[c] For $z_{\mathrm{Phot}} = 0.38$. We calculate a range of values.

[d] S/N of likely subcluster, rather than primary object.

Table 5.1: Cluster summaries. Quality figures refer to the lensing band (bold).

5.1 Methodology

5.1.1 Photometic Calibration & Simulated Redshifts

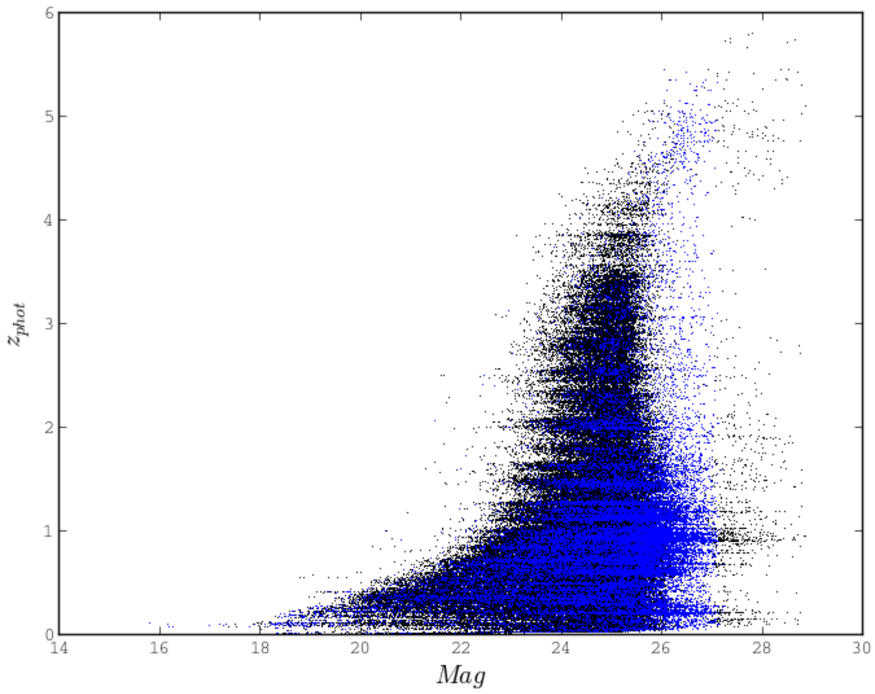

Figure 5.1: Monte Carlo estimated PLCK 100 mag-z distribution overlaid on COSMOS-derived value distributions for the r'-bandpass, in blue and black[1], respectively.

In order to assign redshifts to the galaxies in our catalogs, we need accurate photometric zeropoint data. We achieve this by calibration of SExtractor-measured magnitudes against known SDSS magnitudes for objects found in our field. Corrections to within ≤0.05 magnitude accuracy were sufficient, as color-dependent photometric redshifts could not be utilized to high-accuracy with only several wavebands. Object redshifts are then found via an ensemble matching approach to the COSMOS field photometric redshift catalog, which was compiled largely using multi-band Subaru observations (and thus uses the same camera and filters as our fields).

The COSMOS photometric redshift catalog was obtained from their data archive [14]. The catalog covers 2 deg^2 of combined space-based and ground-based observations, including with Subaru. As a result, it contains detailed magnitude and photometric redshift information for over 3×10^5

---

[1] Or white and gold.

galaxies taken in z', i', r', g', V, and B passbands with the Suprime-Cam imager. Because of the large number of galaxies in the catalog, it provides the best estimate of the redshift distribution for galaxies in any given Subaru magnitude range. Thus, it may be used as a means to form a magnitude-redshift correlation for the background galaxies in our fields.

The COSMOS data was prepared by re-formatting the catalog and header information to match SExtractor-recognized values, and the catalog was then filtered to exclude stars, masked/flagged objects, and entries with null values for photometric-z's and Subaru magnitudes. The Subaru magnitudes were measured with $3''$ apertures, so matching of galaxy catalogs utilized apertures of the same size and SExtractor cataloging parameters. After performing the galaxy filtering steps (§4.1.1), the objects are matched to the redshift distribution via a Monte Carlo approach, associating each galaxy with a COSMOS galaxy redshift from within 25 nearest neighbors in terms of magnitude, for the catalog of that bandpass. Because our catalogs are on the order of $\sim 10^5$ objects, the ensemble approach simulates the z distribution to an accuracy sufficient to make shear measurements. Photometric-z estimates would only be possible in fields which include multiple bandpasses at high source-density, and could suffer from systematic biases not controlled for in our analysis. Because our catalogs are relatively large (as they have been pre-selected for high-quality observing conditions), we can employ a statistical approach to z-estimation relying on a catalog already compiled for the same instrument with more accurate photometric redshift determinations.

Our approach necessarily means that some foreground galaxies are mistakenly classified as background and vice-versa. However, the distribution of redshifts should be robust, and because galaxy magnitudes correlate well with redshift the mean lensing signal should be largely unaffected. Our calibration measurement of Abell 383 serves as a partial test of this approach.

5.1.2 NFW Fitting Protocol

Assuming a Navarro-Frenk-White density profile [81], a halo mass within a radius of R_{200} is

$$M_{200} \equiv M(R_{200}) = \frac{800\pi}{3}\rho_c R_{200}^3 = \frac{800\pi}{3}\frac{\overline{\rho}(z)}{\Omega(z)}R_{200}^3 \tag{5.1}$$

where $\rho_c(z)$ is the critical density of the universe (Eq. (1.28)), $\overline{\rho}(z)$ is the mean energy density, and $\Omega(z)$ is the cosmological density parameter, all at the cluster redshift z. This profile has a characteristic radial scale, for which R_{200} is defined as the distance from the center of the cluster at which the concentration of mass equals 200 times that of the critical density of the universe. It has a surface mass density, $\Sigma_{NFW}(r)$, which varies radially in terms of the characteristic scale. To estimate a M_{200} mass value, we follow the methodology of Wright & Brainerd (2000) [132], calculating the predicted shear at the position of each galaxy and comparing it against our measurements. We then vary the R_{200} value to find the minimum χ^2 residual via the parabolic extrapolation approach of Press *et al.* (2007) [92]. The best fit of the measured shear profile of that to the NFW model allows us to calculate the mass. The R_{200} radius associated with that fit describes the physical extent of the cluster, and is sensitive to both the cluster density and the cosmology [28].

It should be noted that R_{200} values are not derived independently, they are the result of the value associated with the parametrically-derived fit to the measured tangental ellipticities of the galaxies alone. Additionally, we point out that best-fit χ^2 values are the minima for the fit itself, and are dependent on the intrinsic shape noise of the catalog. Therefore, they are not an independent gauge of the quality of the measurement, but rather a relative figure compared to other potential values of M_{200} for the sample.

Angular diameter distance measurements are calculated based on the redshift information matched to each object (and independent redshift measurements of the lensing cluster itself), under current *Planck*-derived ΛCDM model cosmological parameters (Ω_m, Ω_Λ, Ω_k, h)=(0.306, 0.692, 0.0, 0.678) [87].

In order to calculate error bars for our mass values, we employ a jackknife approach, calculating the best NFW fit to each of 5000 catalogs, as described, but having randomly resampled each to include only 50% of the background galaxies. This is useful as an internal consistency check, and variance among these measurements determines the error range in M_{200} measurement. Moreover, it ensures that our shear signal is not dominated by a small fraction of shape outliers.

5.2 Calibration Field: Abell 383

Due to the potential for bias in WL measurements it is important to provide benchmarks that will expose systematic errors within the reduction and analysis framework. To this end, we utilized a well-studied cluster with independent mass measurements via multiple analysis techniques, Abell 383, as a calibration cluster.

Though Abell 781 (used as a calibration field in our previous chapter) represents a cluster with

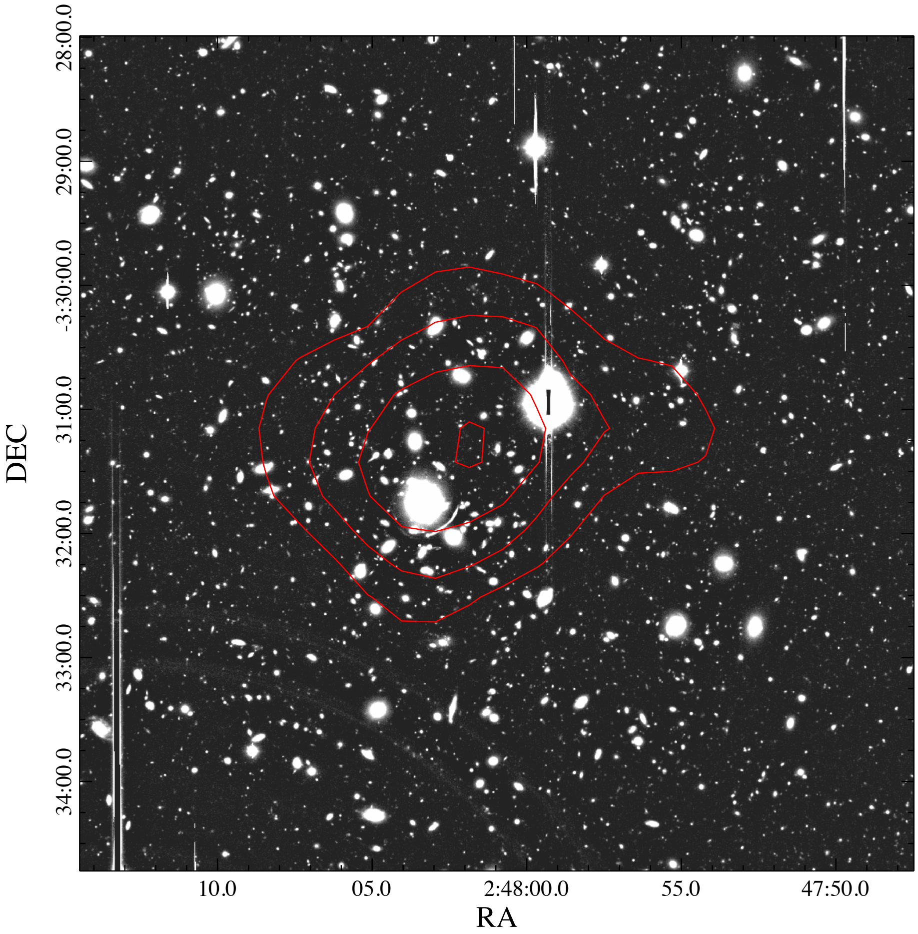

Figure 5.2: Abell 383 region. Contours are of 4, 6, 8 & 10 S/N, and a strong lens is visible to the lower left of the 10.2 S/N peak. (Maps have a tolerance of $\pm 5''$.)

highly-resolvable WL features, the subcluster structure creates the possibility of degeneracy in mass measurements [70]. For the purpose of calibration, a dense, centralized cluster is more appropriate. Abell 383 is the paradigm of this—as an extraordinarily well-studied field with a compact mass distribution.

5.2.1 Previous Measurements

Optical observations of the galaxy distribution place the cluster center at $2^{h}48^{m}06.9^{s}$ $-3^{\circ}29'32''$ [99], and mean redshift $z \simeq 0.1871$ [34]. Several strong lensing features have been identified in the heart of the cluster (Fig. 5.2).

There are a wealth of mass measurements of Abell 383, many utilizing WL. Mass estimates of the cluster vary slightly, with weak lensing measurements typically finding an approximately $\sim$30% lower mass estimate than X-ray observations, likely due to cluster-cluster contamination from an offset high-redshift ($z \simeq 0.9$) background cluster[2] [134]. Nonetheless, because we are not completing a precise redshift-complete cluster weighing study, we are satisfied to confirm M_{200} agreement to within 20%. A 2007 weak lensing study by Bardeau *et al.* [7] used CFH12K to measure $M_{200} = 5.98 \pm 2.08 \times 10^{14} M_\odot$ for A383. *Chandra* X-ray observations that same year fit cluster halo observations to an NFW profile, finding a virialized mass $M_{\rm vir} = 9.16^{+1.89}_{-1.85} \times 10^{14} M_\odot$ [98]. The CLASH project finds an M_{200} mass of $8.1 \pm 2.2 \times 10^{14} M_\odot$ [119], while *Weighing the Giants* estimates $M(< 1.5{\rm Mpc}) = 7.3 \pm 1.4 \times 10^{14} M_\odot$, [6] (using a methodology that finds cluster weights within 1.5 Mpc of the cluster center, rather than the M_{200} figure). Huang *et al.* (2011) [46] test a variety of approaches for galaxy selection, using multi-band data from CFHT and Subaru, finding a range of M_{200} values between 6.30–7.44$\times 10^{14} M_\odot$.

5.2.2 Mass Measurement

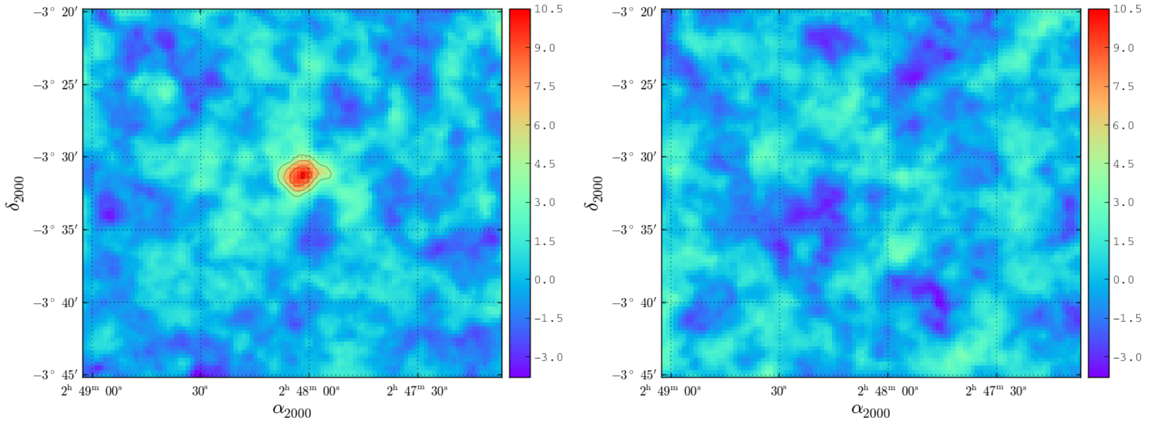

(a)

(b)

Figure 5.3: 2D mass reconstruction maps of the Abell 383 cluster. **(a)** E-mode S/N, peaking at 10.207 at the cluster center. (Contours at 4, 6, 8, & 10). **(b)** B-mode systematic check, peaking at 3.32 (plotted on the same scale).

Abell 383 was observed on November 5th, 2011 by Umetsu, Bruursema & Medezinski under proposal S10B-059 "A unique cluster mass profile dataset from an HST-Subaru Survey" (effectively, the CLASH lensing study). 6300 sec of data was obtained in z'-band (a mix of 150 sec & 300 sec

---

[2] In principle, our measurement could help resolve this discrepancy, but this would require more precise redshifts for the background galaxies.

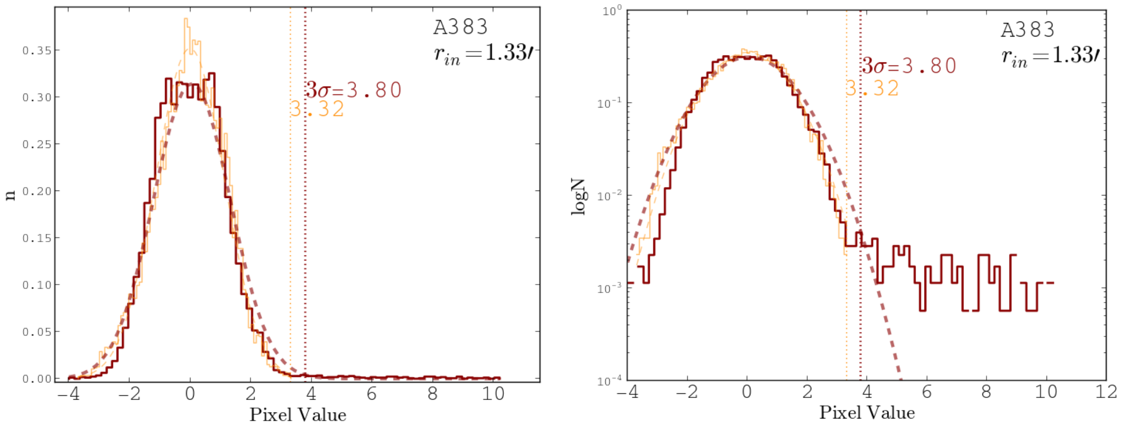

(a) (b)

Figure 5.4: Linear and logarithmic plots of S/N pixel distribution in our Abell 383 mass reconstruction map. E-mode in red, B-mode in orange, with vertical lines at B maxima and $3\sigma_{\rm fit}$.

exposures). The SMOKA archive reported mountaintop seeing between $0.22''$-$0.35''$, but in actuality, we find the seeing in this region to be $0.52''$.

After circularizing to <0.4% e_1-e_2 stellar ellipticity, assigning and then cutting on estimated redshift, and filtering to remove foreground objects, we map a field with 26931 galaxies (37.3 gal/arcmin^2). Unsurprisingly, we detect this cluster at S/N= 10.21, with a central peak of $2^h48^m01.7^s$ - $3^\circ31'21.5''$. Signal distribution places the peak at $\sigma_{\rm fit}$=8.056±0.03, and a B-mode maximum far below measured S/N at 3.32 (Fig. 5.4).

Our sample selected from a magnitude cut of $20.39 < mag < 25.62$, and redshift estimate $z > 0.1871$. Reconstruction maps include the entire quality region of the field, while our NFW measurement selects a circular annulus of the $10.2'$ extent of the cluster centered on the peak of detection (a 100 pixel circle at the cluster center is removed because the galaxy density makes distinguishing source from background impossible here).

We measure a minimized–χ^2 fit of $M_{200} = 7.65 \pm 1.61 \times 10^{14}\ M_\odot$ (with $\chi^2 = 0.724$). This value is well within the range of recent lensing measurements. We also find the cluster extent to be $R_{200} = 1.81$ Mpc. For comparison, Bardeau *et al.* (2007) [7] find $R_{200} = 1.89$ Mpc. We provide a 2D histogram of mass-χ^2 values generated by our 5000 iteration jackknife measurement, Fig. 5.5, showing the maximum-likelihood M_{200} values, produced from catalogs sampling 50% of the galaxies used in the NFW fit. (Note that, as described in §5.1.2, χ^2 is linked to the shape noise of the catalog itself, therefore the range of χ^2 values is an illustration of shape noise variability among resampled catalogs.) It shows a measurement centered on our final result, confirming that our estimate is not dominated by a small fraction of galaxies. FIG. 5.6 displays this comparison graphically. Therefore, our pipeline is capable of producing accurate mass estimates.

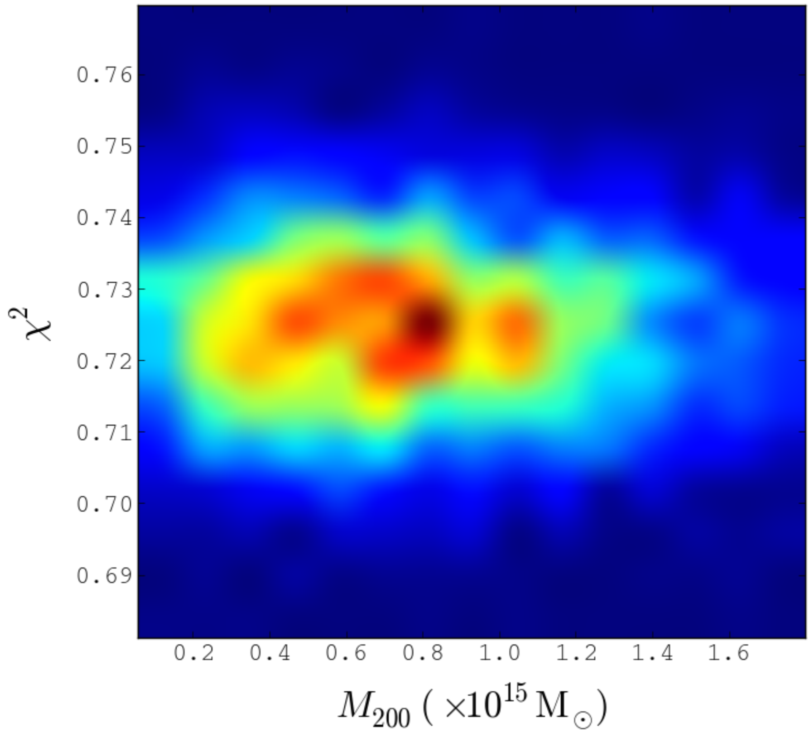

Figure 5.5: M_{200}-χ^2 maximum likelihood plotted over 5000 resampled iterations of the Abell 383 lensing catalog. Centered at a mass of $M_{200} = 7.65 \pm 1.61 \times 10^{14} M_\odot$.

5.3 Planck-XMM Clusters

The *Planck* Collaboration identified dozens of potential galaxy clusters through application of the Sunyeav-Zel'dovich effect. Many of these have been selected for follow-up by the X-ray observatory *XMM-Newton*, and several were selected for WL study with Subaru. Among them are two observed in 2012, but, as of the time of this writing, having no published weak lensing results. They consist of PLNK G 100.2-30.4 and PLCK G 018.7+23.6[3], as identified by SZ signal [89]. The fields were imaged by observers Radovich and Formicola on the evening of July 24, 2012, under proposal S12A-059 (o12122) "A weak-lensing analysis of two new clusters discovered by the *Planck* survey"[4] this

---

[3] also known as "PLCKESZ G100.2-30.4." and "PLCKESZ G100.2-30.4." For convenience, we refer to these areas as "PLCK 100" & "PLCK 018."

[4] http://www.naoj.org/Observing/Schedule/s12a.html

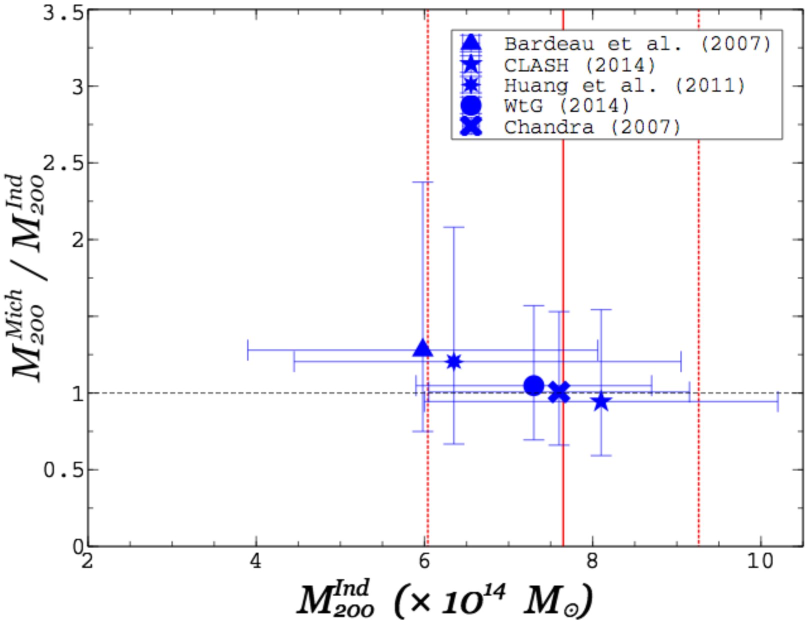

Figure 5.6: Comparisons with previous measurements of Abell 383 masses. Y-axis plots ratio of our result, M_{200}^{Mich}, to figures seen in other work (error bars show extrema of possible results), while the X-axis shows independently reported masses, M_{200}^{Ind}. Our result is displayed as a vertical red line with error limits the dotted lines. (Note that *Chandra* and *Weighing the Giants* values have been scaled from M_{vir} and $M(< 1.5\text{Mpc})$, respectively.)

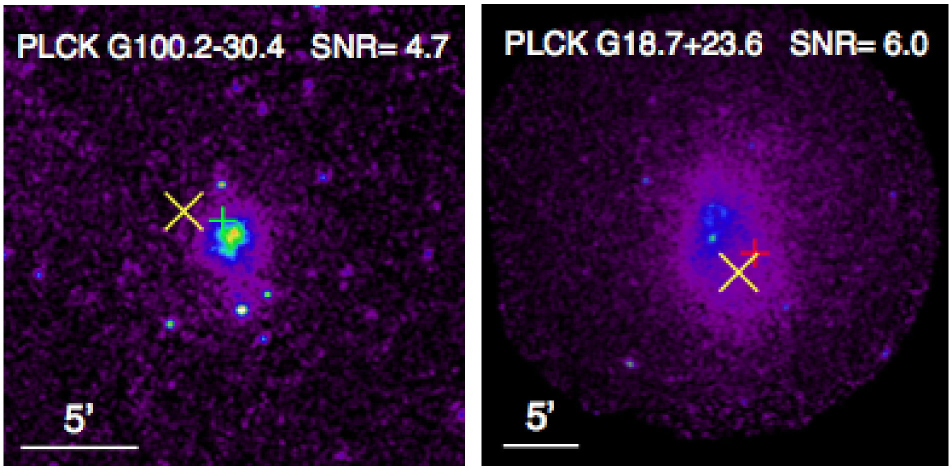

(a)

(b)

Figure 5.7: *XMM-Newton* imaging of the central mass distribution regions of the two Planck-detected clusters. Yellow crosses indicate *Planck* SZ-derived positions, and green/red indicate X-Ray peaks found in the ROSAT BSC/FSC catalogs [89].

imaging is the third in a sequence of follow-up observations on these cluster candidates.

Our analysis strongly confirms the detection of the former, while the latter is more problematic.

5.3.1 PLNK G 100.2-30.4

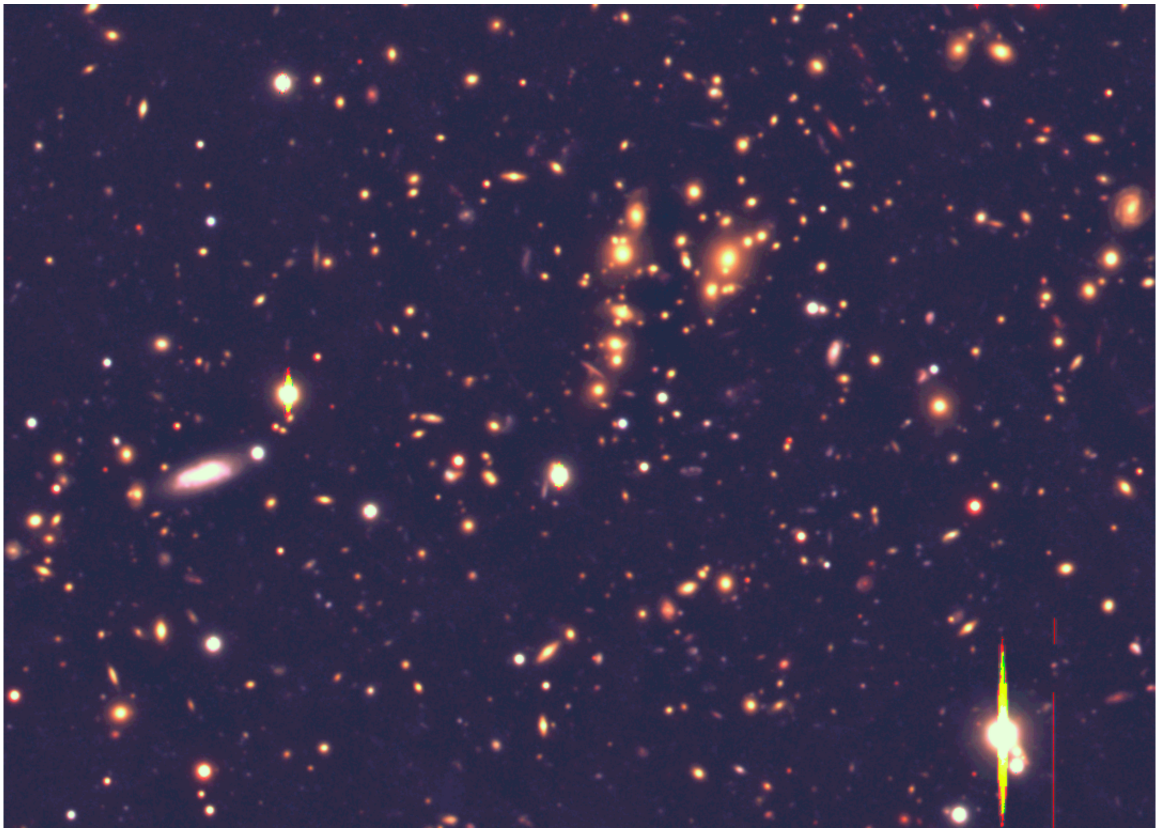

Figure 5.8: Color composite of the PLCK 100 cluster in r'-i'-g' filters.

Planck et al. (2011) [89], performing follow-up on the *Planck* SZ-detected cluster candidates with *XMM-Newton*, detected PLCK G100.2-30.4 in X-ray at 4.7 S/N, having found it at a S/N value of 5.5 in its *Planck*-HFI maps measuring SZ detection. They derive a spectroscopic X-ray redshift of $z_{\mathrm{Fe}} = 0.31$, fitting to the Fe contribution to the X-ray spectral profile, while observations by the CAMELOT camera at the 0.82-m IAC80 telescope (see Fig. 3.7a) calculate a photometric redshift of $z_{\mathrm{phot}} = 0.38 \pm 0.04$ using four bands of imaging ($griz$). While SDSS-derived optical spectral redshift finds a value in-between these at $z_{\mathrm{opt}} = 0.34 \pm 0.03$ [88].

The data in our sample is also drawn from four filters: $g'r'i'z'$ wavebands, with the vast majority coming in r', which is excellent for resolving background object shapes. All imaging (including that of PLCK 018 as well) consists of 180 sec exposures. The r' field consists of 19×180 sec exposures, 3420 sec total. 10 exposures in i' & g' totaled 1800 sec, and 7 z' exposures for 1260 sec.

No analysis is required to demonstrate that there is a massive cluster located in this part of the

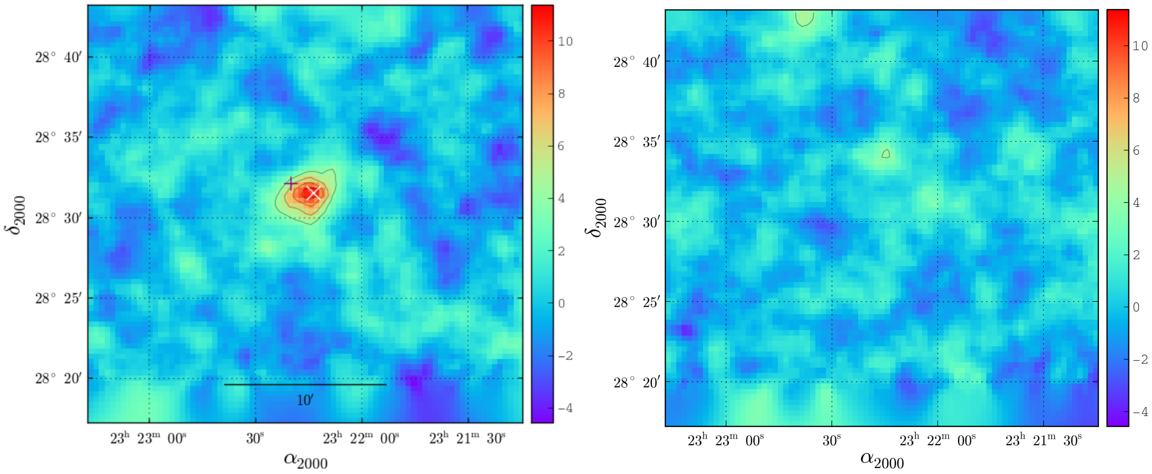

(a) (b)

Figure 5.9: 2D mass reconstruction maps of the PLCK 100 cluster. **(a)** *E*-mode S/N, peaking at 11.374 at the cluster center. (Contours at 4, 6, 8, & 10, and white at 11). X-ray and SZ detection locations [89] indicated by white and purple marks, respectively. **(b)** *B*-mode systematic check.

sky. Lensed and magnified galaxies are exceedingly evident in Fig. 5.11. Though the cluster center sits on the cusp of what we had chosen as our data sample cut-off in terms of galactic latitude, at coordinates, ℓ=100.243°, b=-30.354°, we do not find the region contaminated by an over-abundance of stars or foreground galactic extinction.

Using r'-band data, we detect this cluster at 11.69 S/N, $\sigma_{\rm fit}$=7.517±0.02, with a B-mode maximum of 4.84 at a different position (Fig. 5.9). Our peak center, at $23^h22^m14.7^s$ $+28°31'36.0''$ is in good agreement with the X-ray and SZ sources found by *XMM-Newton* and *Planck* [89] at $23^h22^m14.9^s$ $+28°31'13.5''$, and $23^h22^m21.4^s$ $+28°33'46.8''$, respectively. SZ detection is offset $1.4'$ from our central lensing peak. Further, this peak is consistently seen across the other independent ($g'i'z'$) bandpasses, at 8.24 S/N, 9.47 S/N, and 11.65 S/N. Applying seeing-correction, and placing further catalog cuts to filter the sample, we exclude objects with estimated $z < 0.40$, magnitude ($23.7 < mag < 26.3$), and very small size.

As mentioned above, there are two differing redshift values for this cluster, the variance of which has some influence over the derived mass measurements for our sample. We determine three M_{200} values, one for each possible z. Our fitted NFW profile returns best-fit estimates of:

- **X-ray Spectral ($z_{\rm Fe} = 0.31$):** $M_{200} = 7.22 \pm 1.85 \times 10^{14}\ M_\odot$. $\chi^2 = 0.59$.
- **SDSS Optical ($z_{\rm opt} = 0.34$):** $M_{200} = 7.67 \pm 2.02 \times 10^{14}\ M_\odot$. $\chi^2 = 0.59$.

- **Photometric ($z_{\text{Phot}} = 0.38$):** $M_{200} = 8.17 \pm 2.12 \times 10^{14}\ M_{\odot}$. $\chi^2 = 0.60$.

We also find R_{200} scale radii of 1.69 Mpc, 1.71 Mpc, and 1.72 Mpc, respectively. These values place our measurement in good agreement with that of the 2011 *Planck* team's *XMM-Newton* X-ray results, which are of $M_{500} = 5.63 \pm 0.22 \times 10^{14}\ M_{\odot}$, and $R_{500} = 1.13$ Mpc, which measures the smaller central region of the cluster [89]. M_{500} and R_{500} refer to values calculated in reference to the region of the cluster where mass concentration is greater than 500 times that of the universe's critical density (and likewise with regard to M_{200} and R_{200}). Therefore, we expect our figures, which correspond to a greater extent of the cluster, to be larger. We find our results to be a confirmation of the *XMM-Newton* values.

5.3.2 PLCK G 018.7+23.6

This region was also imaged in the same four wavebands, though several fields experienced imaging glitches. As in the previous instance, r' was the most heavily used filter, with 15 usable exposures of 180 sec for 2700 sec total. Those acceptable for lensing use totaled 1800 sec in i', g' and 1620 in z'.

Planck et al. (2011) [89] *Planck*-HFI maps find PLCK G018.7+23.6 at 5.6 S/N, while *XMM-Newton* detects it at 6.0 S/N. Despite a detection strength roughly on par with PLCK 100 by these metrics, we found a substantially different observational quality. The central component of PLCK 018 is essentially undetectable across all scales by WL analysis with the field of view we had access to. Instead, lower significance structures appear, widely separated from the published location.

Although we had hoped to find an unambiguous WL signal, it is unsurprising that we did not for several reasons. Firstly, X-ray spectroscopic redshift measurement places it significantly closer to us, at $z_{Fe} = 0.09$, on the near edge of the detectability region for weak lensing. Secondly, it lies several degrees within the galactic disk, at ℓ=18.759°, b=23.564°. Foreground extinction as well as a very star-heavy field, prevents successful imaging of enough background galaxies to make a firm detection of a signal. Though r'-band seeing of unglitched images was $0.66''$, which is adequate, there are far more large saturated stars compared to our other data. A higher fraction of the field is therefore obscured by them. Other bands of data possess worse seeing still, with g', i', & z' having stellar FWHM's of $0.86''$, $0.74''$, & $0.74''$, respectively. Thirdly, the WL signal itself would be likely to be relatively diffuse at this scale, because observations by *XMM-Newton* estimate mass

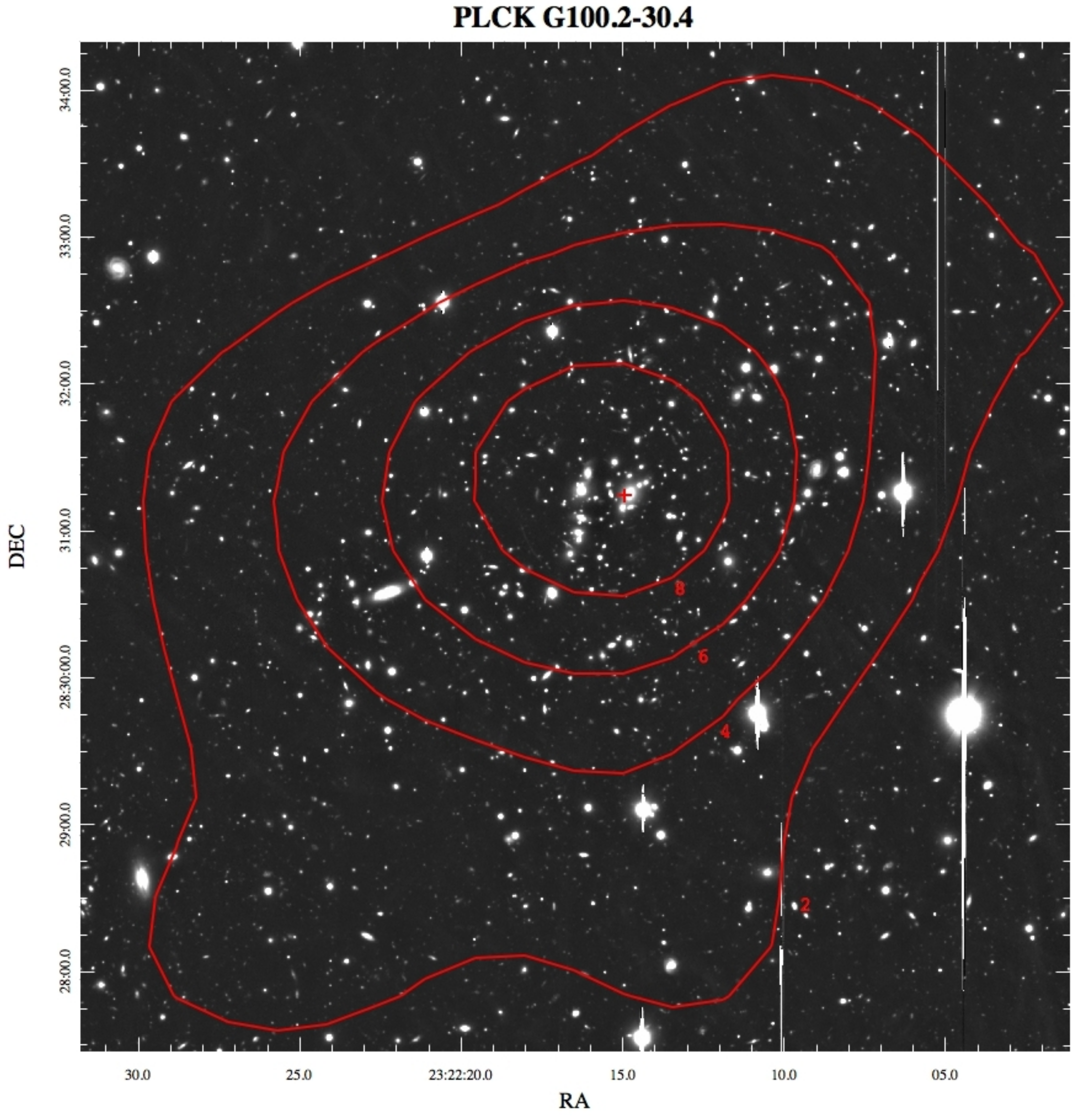

Figure 5.10: Convergence contours of the PLCK G 100 cluster center in the r' (main lensing) band. The cross marks the X-ray emissions peak of the *XMM* study of this field. [89]

and radial extent values of $M_{500} = 3.42 \pm 0.22 \times 10^{14}\ M_{\odot}$, $R_{500} = 1.03$ Mpc [89]. This translates to an angular scale of $\theta_{500} \simeq 10'$ (and thus, what would appear as a larger R_{200} in our measurements), while Suprime-Cam's imaging field is $24' {\times} 24'$. At this angular extent, but a lower estimated total mass than PLCK 100, a strong detection signal is a challenging prospect.

Despite these difficulties, it is remarkable that we found no signal whatsoever near the X-ray/SZ coordinates. Furthermore, inspection of the images indicates a galaxy richness profile which is not consistent with an intermediate-mass cluster at this redshift (Fig. B.1). Even with the dense star

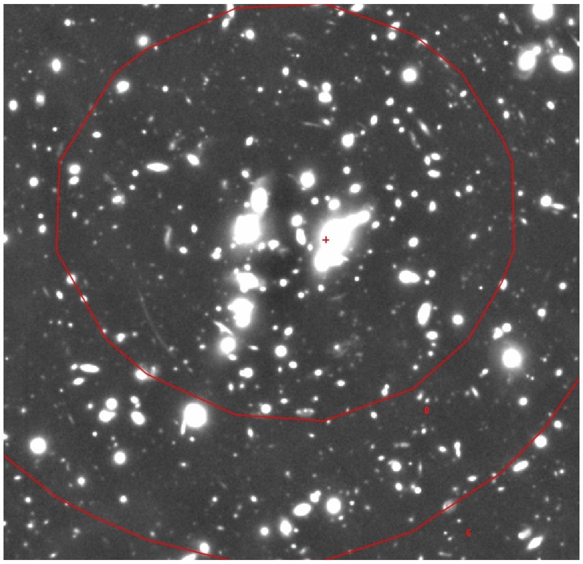

Figure 5.11: Central view of PLCK100 in r' (zoom from Fig. 5.9). Arcs are clearly visible.

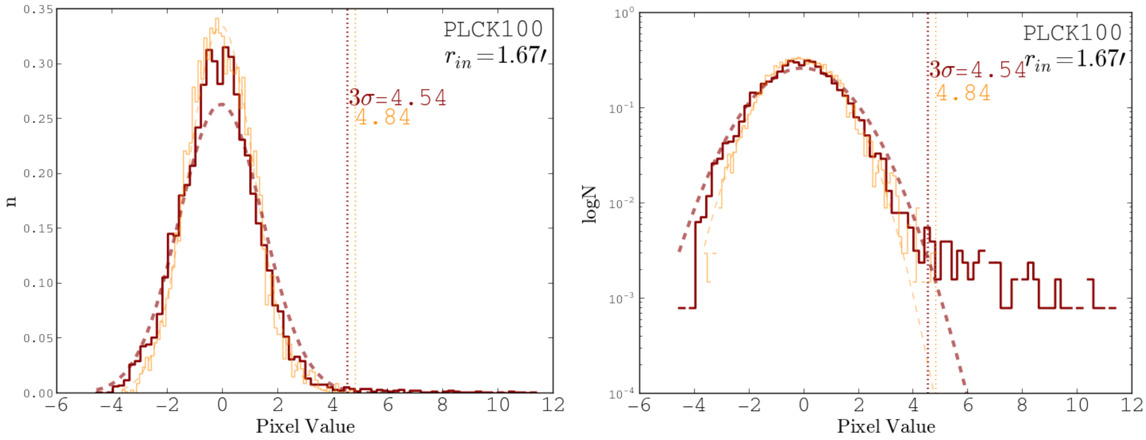

(a) (b)

Figure 5.12: PLCK 100 S/N distribution histograms in linear and logarithmic modes. E-mode in red, B-mode in orange, with vertical lines at B maxima and $3\sigma_{\text{fit}}$.

field, we might expect to find more large galaxies near the X-ray/SZ peak.

Nonetheless, it is possible we were able to glimpse a portion of the cluster's substructure. Though systematic issues are still problematic, we consistently detected a signal $\sim 7'$ displaced from the X-ray peak—within the potential extent of the cluster. Because these are present in 3 of the 4 wavebands imaged (Fig. 5.14 & Fig. B.2), data sets which constitute independent observations, they may indicate a valid detection of a substructure peak—however, the displacement from X-ray measurement is too significant to be considered a detection of the primary cluster.

Best-quality r'-band data find a 4.72 S/N peak at $17^h02^m01^s$ -00°54′27″, with a characteristic scale of 2.67′ (FIG. 5.14). B-mode measurement peaks at 3.06, while the non-gaussianity metric shows $\sigma_{\rm fit} = 3.26 \pm 0.03$. i' & z' data indicate this same peak, at S/N strengths of 4.04 & 4.06, while g' (the bandpass least suitable for lensing-quality shape resolution) locates a 4.17 S/N peak at $17^h01^m57^s$ -00°59′27″—somewhat closer (∼5′) to the X-ray and SZ coordinates, but decidedly offset from the candidate in the other three filters. (Additional $g'i'z'$ reconstruction maps are provided in §B.1, as well the image in r', marked with our detection and previous results.)

The general low quality of this field in terms of star density and convergence map signal strength, prevents us from making a NFW shear measurement, or of drawing any conclusions as to the detectability of this cluster via WL. Better quality data may have allowed us to attempt a halo measurement, however the unreliability of the field based on these metrics prohibits making such a determination with any certainty. Though SZ and X-ray results are in relatively good agreement, we do not have enough information to offer a firm explanation of our inability to find a WL signal. As mentioned above, it is intriguing that a cluster associated with this nearby redshift is so visually unremarkable. To reconcile these questions, further study is needed.

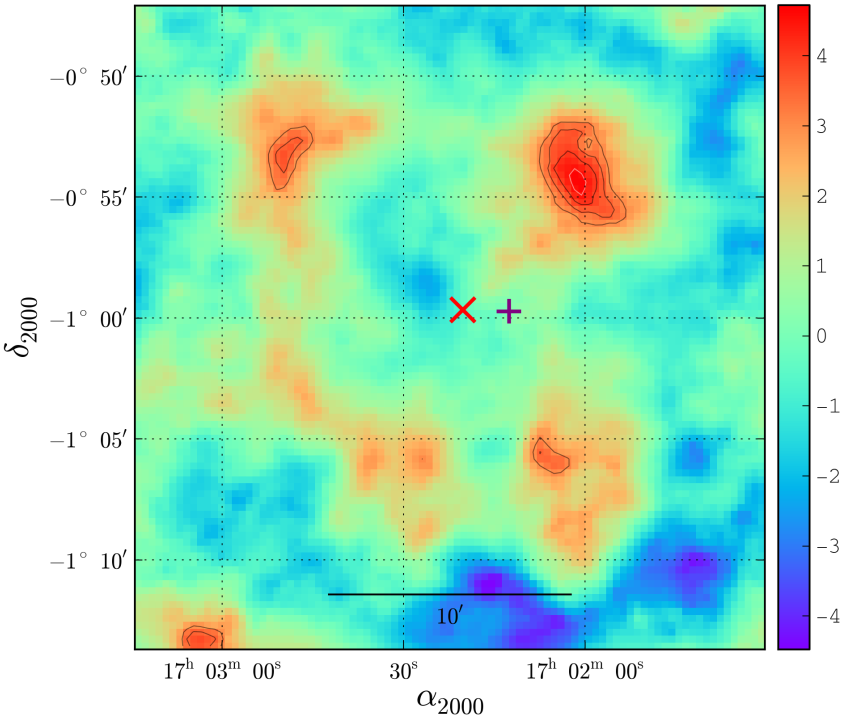

Figure 5.13: 2D mass reconstruction map of the PLCK 018 region. Contours at 3, 3.5, 4, 4.5 S/N, with peak value of 4.72 S/N. X-ray and SZ locations [89] shown in red and violet, respectively.

5.4 RXC J1651.1+0459

RXC J1651.1+0459[5], is a cluster of galaxies located at $16^h51^m10.0^s$ $+04°59'46''$, with an X-ray derived redshift of z =0.1540 [11]. Piffaretti *et al.* 2011 [86] used the MCXC X-ray luminosity meta-catalog to calculate a mass of $M_{500} = 3.76 \times 10^{14} M_\odot$, characteristic radius $R_{500} = 1.04$ Mpc, and X-ray luminosity $L_{500} = 3.23 \times 10^{44}$ erg/s. A cluster member contains a bright and well-studied active galactic nucleus, HERCULES A, at $16^h51^m08.2^s$ $+04°59'33''$, $z = 0.1549 \pm 0.0001$ [121, 131]. And the Northern Optical Cluster Survey likely identified RXC J1651.1+0459 as NSC J165058+050108, at the nearby coordinates of $16^h50^m58.15^s$ $+05°01'07.5''$ but at lower redshift $z \simeq 0.1086$ [39].

The RXC J1651.1+0459 cluster has an existing mass measurement, but only through X-ray observation, therefore, this poses an interesting target for a mass measurement through WL methods. The field itself sits right at the cusp of the SDSS observation area, with the imaged area passing directly through the center of the cluster.

Our sample consists of 2160 sec (nine 240 sec exposures) in i' taken by Smith, Jauzac & Okabe on April 4th, 2011 under Suprime-Cam proposal-ID "o11203". Fields possess seeing of 0.63″, filtered galaxy density $\langle n_{\rm gal}\rangle$=37.0 gal/arcmin^2, and a depth of 26.30 mag.

Convergence maps indicate an extended structure, with a larger central mass conglomeration at $16^h51^m04.4^s$ $+04°59'15''$, $\sim$1.5′ from the X-ray center, and a smaller secondary peak to the south-west of this around $16^h50^m54.7^s$ $+04°56'31''$. Peak signal is 5.39 S/N, with $\sigma_{\rm fit}$=3.94±0.02 non-gaussianity metric and B-mode peak 3.98.

We find $M_{200} = 3.37 \pm 1.96 \times 10^{14}$ $M_\odot$ at best-fit $\chi^2 = 0.511$, with characteristic radius $R_{200} =$ 1.39 Mpc. This value is slightly lower than would be expected compared to the X-ray mass, though still within statistical uncertainty. Given the extended nature of the signal it is possible that the NFW fit underestimates the mass. We also find that the convergence peak matches the X-ray measurement very well.

---

[5] Also identified as MCXC J1651.1+0459, NAME 3C 348, Hercules A Cluster, (as well as, in all likelihood, the extremely nearby optical cluster detection NSC J165058+050108).

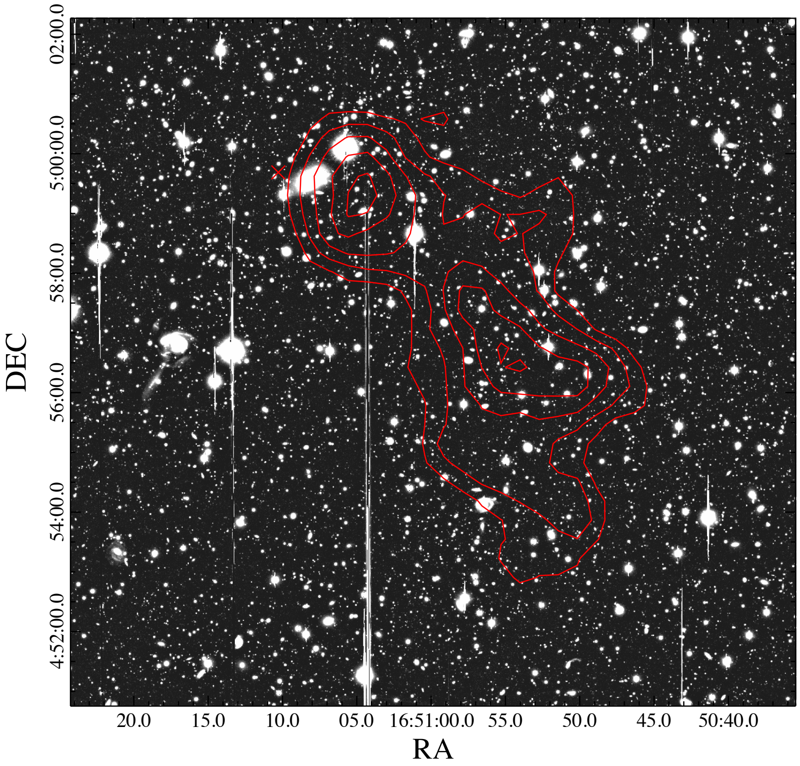

Figure 5.14: 2D mass reconstruction contours on the RXC J1651.1+0459 region. Contours at 3, 3.5, 4, 4.5, 5 S/N, with peak value of 5.39 S/N. (X-ray peak shown as “X”).

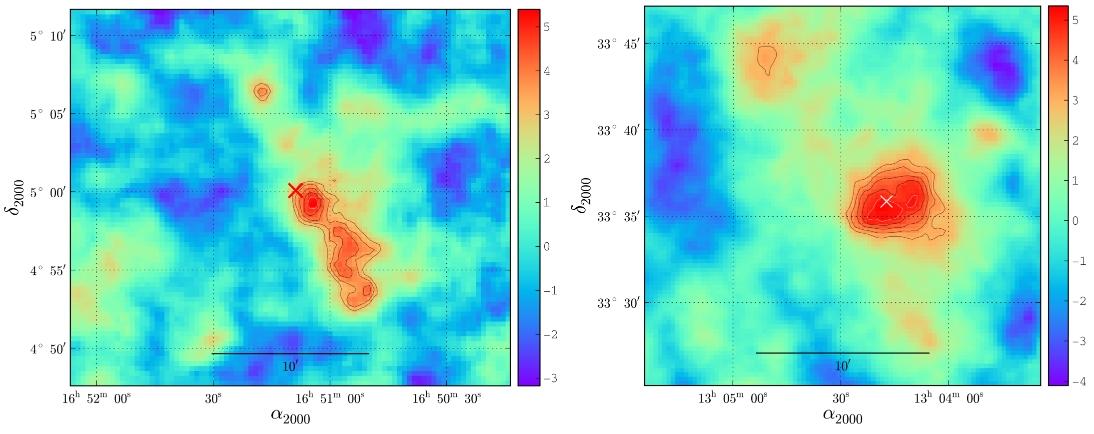

(a) (b)

Figure 5.15: 2D mass reconstruction maps of: **(a)** RXC J1651.1+0459, with a peak value of 5.39 S/N. **(b)** Abell 1672, with a peak of 5.34 S/N. **(Both)** Contours at 3, 3.5, 4, 4.5, 5 S/N, X-ray peaks marked by “X” [86].

5.5 Abell 1672

This cluster was first identified in 1958 as a rich cluster in the Abell catalog [1]. It has been studied in a variety of approaches, but not yet through weak gravitational lensing. It possesses an X-ray peak at

$13^h04^m20.4^s$ $+33°36'03''$ [85], and a redshift of z=0.1882 [4]. As with the previous cluster, Piffaretti *et al.* 2011 [86] employed X-ray luminosity measurements to estimate $M_{500} = 3.23 \times 10^{14} M_\odot$ with characteristic radius $R_{500} = 0.98$ Mpc.

This field was observed on the same date and by the same researchers as RXC J1651.1+0459, but with only eight lensing-quality frames for 1920 sec (8×240 sec) in i'-band instead of nine.

We find Abell 1672 to be characterized by an relatively compact central area with a distinct subcluster region to the northwest at smaller scales. We determine a primary lensing peak at $13^h04^m16.6^s$ $+33°35'40''$ (just $0.88'$ separated from the X-ray source) with S/N=5.34, $\sigma_{\rm fit}$=3.34±0.03, and maximum B-mode value 2.80. We calculate a mass of $M_{200} = 5.61 \pm 2.81 \times 10^{14} M_\odot$ at best-fit $\chi^2 = 0.449$, and characteristic radius $R_{200} = 1.63$ Mpc.

5.6 Summary

We demonstrate cluster mass estimation of four clusters, as well as report the non-detection of a fifth, PLCK 018, potentially due to inopportune lensing conditions. Our measurements of the calibration field, Abell 383, as well as PLCK 100 and Abell 1672 are in good agreement with prior measurements, while RXC J1651.1+0459 finds a slightly lower M_{200} mass than would be expected based on the prior X-ray based result.

Our 2D mass reconstructions are highly precise, matching the known X-ray emission peaks of four of the five clusters with excellent accuracy. We also confidently map mass distribution, finding PLCK 100 and Abell 1672 to be relatively compact, while RXC J1651.1+0459 presents a more extended structure leading off the primary cluster center. This suggests that a mass degeneracy effect may be responsible for a slightly lower WL-derived NFW mass than the one found via X-ray measurement. Quality statistics and final estimates are summarized on TABLE 5.1.

Successful measurements of intermediate-to-low mass clusters through an approach such as the one we have outlined is a key aspect of applying WL to cosmological pursuits, as their greater numbers provide a more sensitive determination of cosmologically significant structure parameters. Future studies employing enormous sets of imaging data will require tools, similar to those described in this work, to detect and study clusters on a large scale, while maintaining sensitivity to galaxy clusters on the lower end of the mass range.

Chapter 6

Conclusions and Future Directions

> *"...It's people like that who make you realize how little you've accomplished.*
> *It is a sobering thought, for example, that when Mozart was my age,*
> *he had been dead for two years."*
> Tom Lehrer (age 37)
> *Alma,* 1965.

This work constitutes a significantly large sample of lensing measurements. Similarly large WL studies are rare, due to their inherent difficulty and large computational requirements. We demonstrate proof-of-concept in our approach to archival data that accomplishes this goal with modest technological resources and (very) few personnel.

Results

- We make wide-field convergence measurements of $\sim$10.34 deg^2 of the sky, the majority of which has never been studied with weak lensing tools. We detect 90 clusters above $\gtrsim$ 3 S/N, with 47 presenting potential new cluster discoveries. We provide comparisons to previous cluster studies overlapping these fields.
- We make cluster mass estimates of the Abell 383, PLCK G 100.2-30.4, Abell 1672, and RXC J1651.1+0459 fields. 2D mass reconstruction of Abell 781 is accomplished as well, a partial follow-up of the work previously accomplished by this group. We also attempt WL detection

of a SZ cluster candidate, PLCK G 018.7+23.6, however, we are unable to find a reliable signal at the predicted coordinates.

- We develop a rapid and robust astronomical data pipeline for Subaru Telescope data, capable of going from raw data frames to refined galaxy catalogs and convergence maps within several hours, (with the majority of processing effort occurring automatically and without frequent human input).
- We create a highly accurate, magnitude-independent, automated star-selection routine—ideal for object shape analysis/correction and capable of adaptation to a broad array of astronomical imagers beyond Suprime-Cam.

Future Directions

- **Further exploration of archival fields:** There was such an abundance of potentially useful data that quality parameters were not always sufficient for truncating the scope of this work. Outside the highest impact data, a focus on areas by likelihood of being "understudied" defined our selection approach. Although we have indeed shed light on a great deal of regions and clusters unreached by WL study, further study of under-examined regions which were processed but not explored in-depth may yield interesting results.
- **Cluster mass detection thresholds:** Although data was selected primarily to include fields most likely to provide high significance detections, the issue of the boundary of detection ability for WL is ongoing. Selected tests of low-mass clusters within such a framework could potentially provide a measurement of this threshold.
- **Cluster mass function:** In concert with the previous item, low-mass clusters, which require large numbers of faint galaxies to convincingly detect and study, provide the strongest anchor to the cluster mass function. As such, quality-optimized compilations of large data sets capable of reaching them (as much of our sample consists of) may be profitably applied to this issue.

Outlook

Observational astrophysics, advanced largely by improvements in detector technology and computational power, is poised to enter an age of truly staggering data intake. As massive observatories such as the Large Synoptic Survey Telescope, the Giant Magellan Telescope, the European Extremely Large Telescope, and the Thirty Meter Telescope come online in the next decade, the light-gathering abilities of ground-based astronomy will scale upwards dramatically, as will the technical demands for the thorough analysis thereof. Weak lensing studies of large sections of the sky will become further refined in precision, and automated tools for aggregating vast amounts of data (similar to but on much larger scales than this work) will transition from convenience to necessity. Wide-field WL studies, such as this one, are providing essential calibration and methodology for the era which is about to come.

Appendix A

Complete Wide-Field Results

This appendix consists of extra figures and data for which only select portions were included in the main body of the dissertation. We include complete tables of every detected peak throughout all four examined scales, each convergence map covering this area, and additional images around signal peaks, for every one of the 53 pointings in this sample.

As in Figs. 4.9 & 4.10, the regions are color-coded and abbreviated as:

Lockman Hole (LH)

Elias North 1 (EN1)

CFHTLS Wide (W2 & W3)

Boötes (F)

A.1 Full Quality Statistics Figures

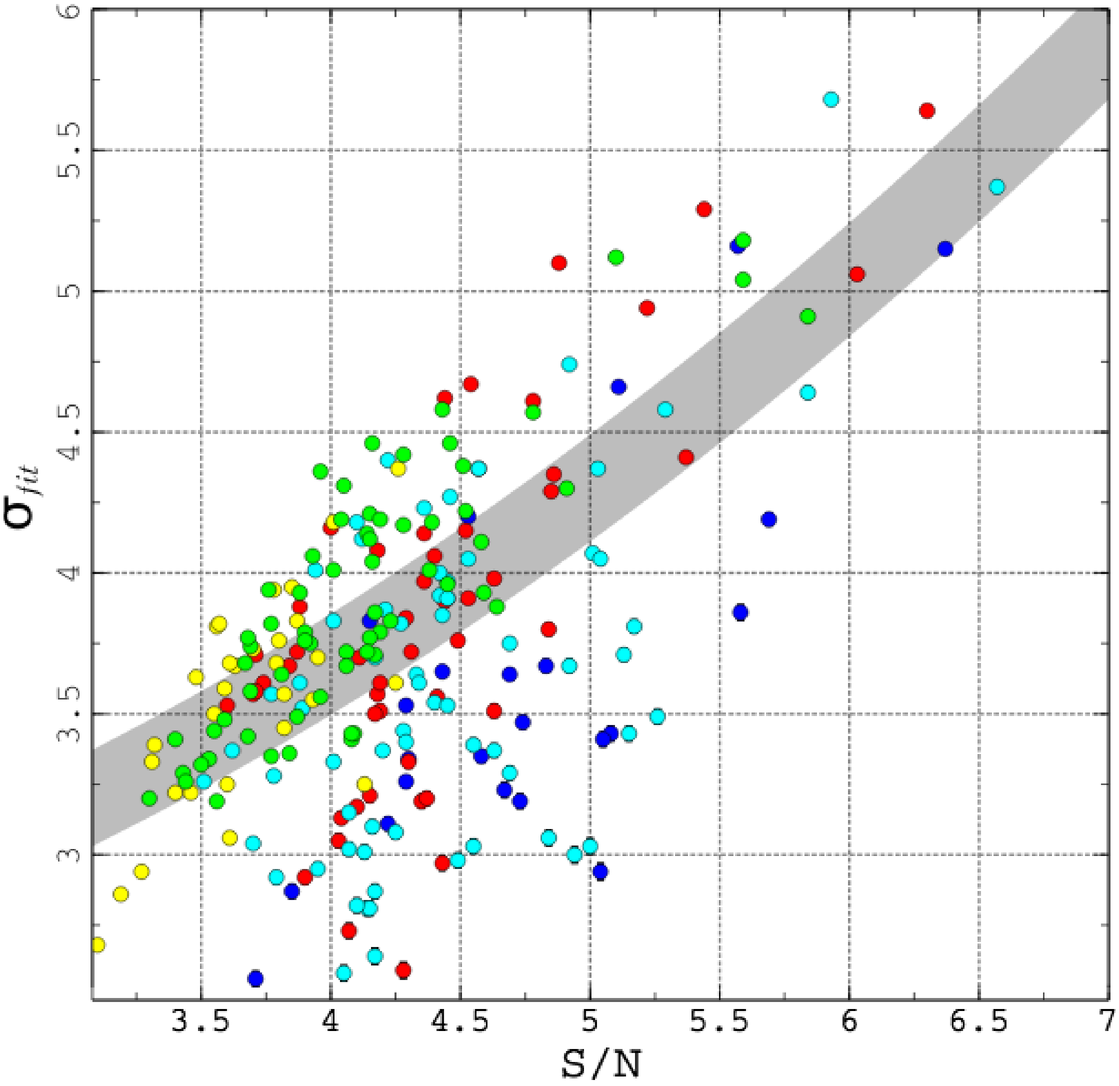

Figure A.1: Relation of S/N to σ_{fit} values for every of the 241 peaks found across the 4 characteristic scales, not only those chosen to represent represent the annular extent.

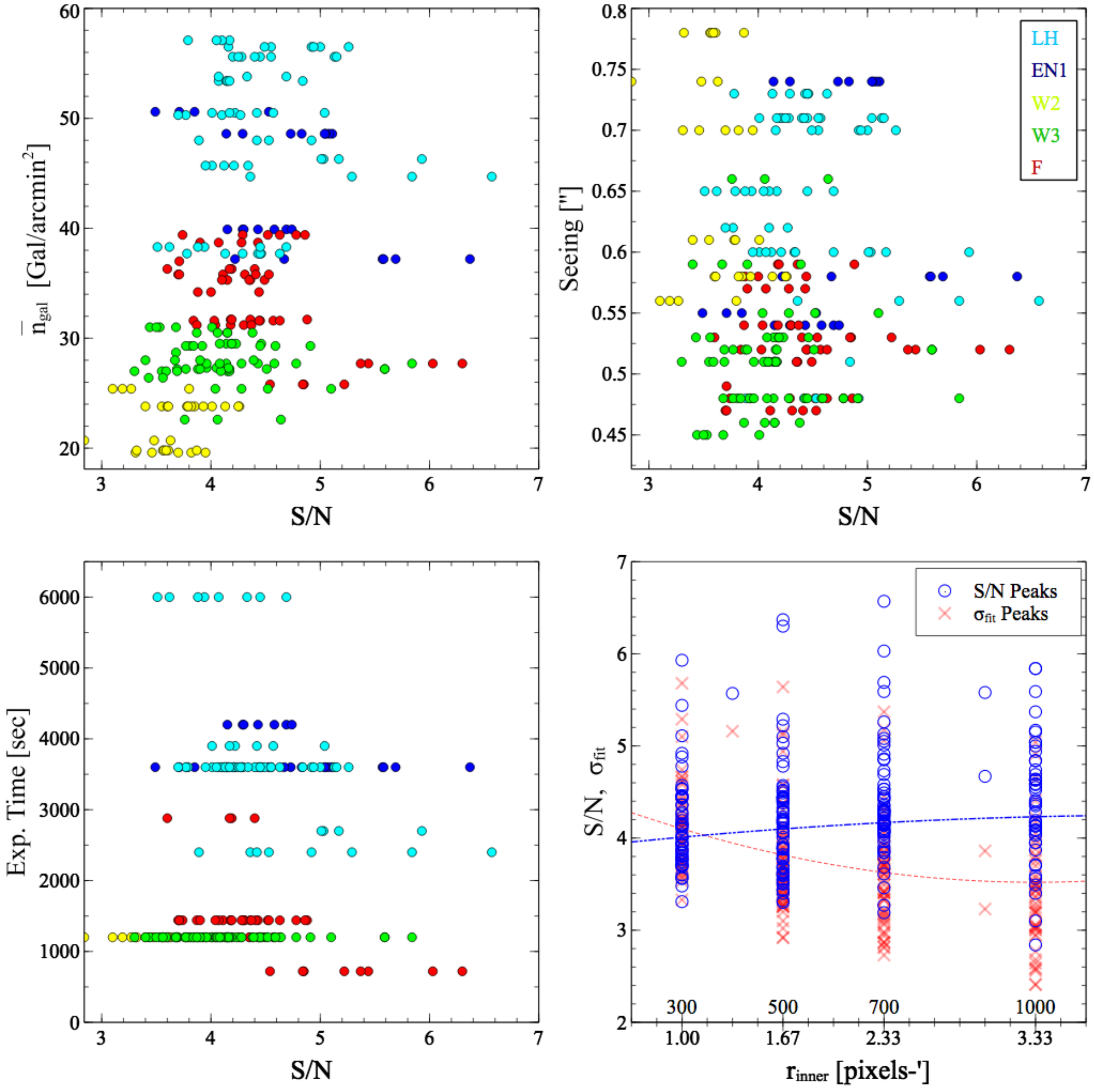

Figure A.2: Summary of **every** quality statistic for the 92 convergence peaks found at all 4 scales. Several peaks are duplicated because they appear in multiple scales at different strengths.

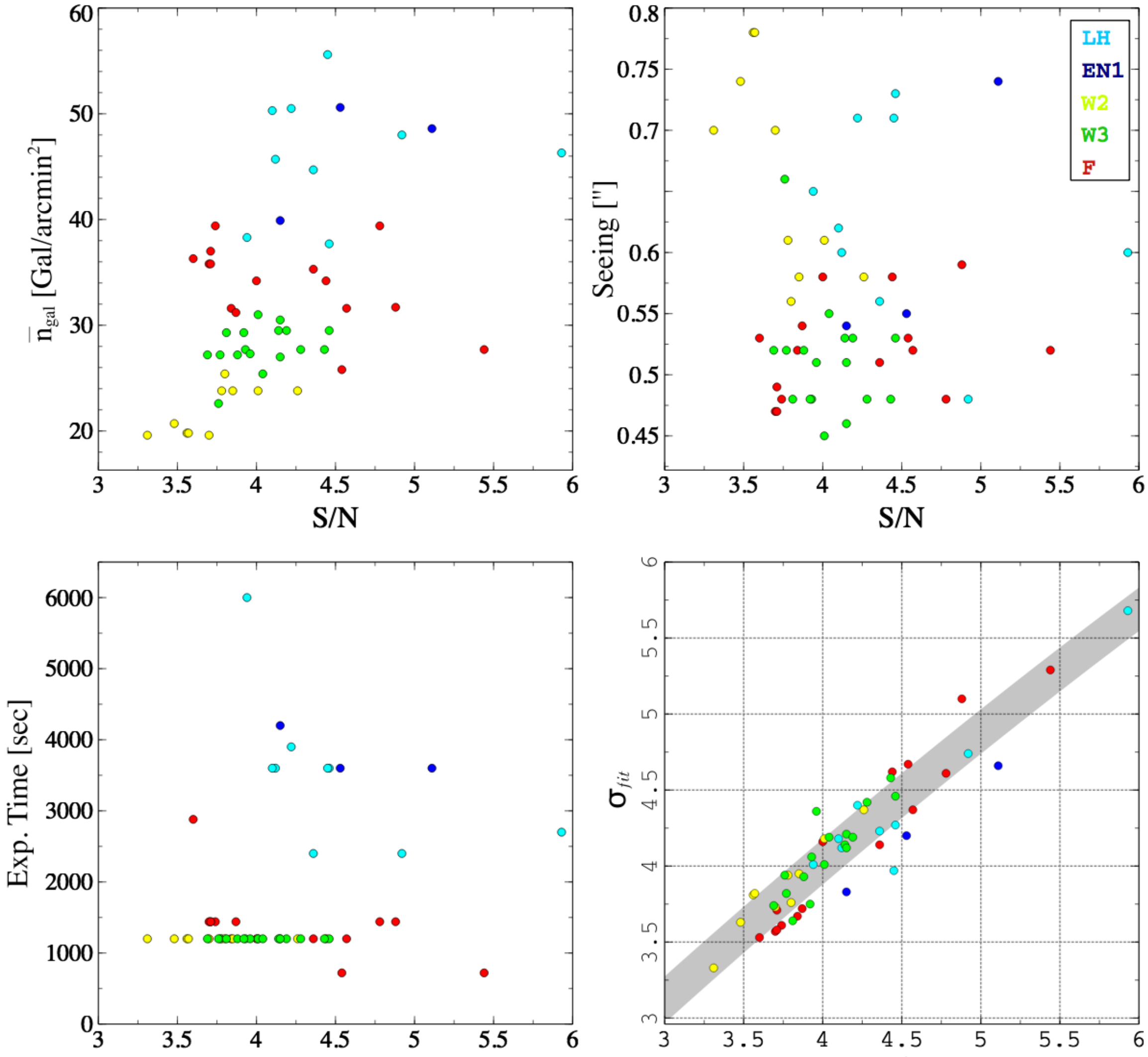

Figure A.3: Summary of quality statistics for the 64 convergence peaks found at $r_{\rm in} = 300$ pix ($1''$).

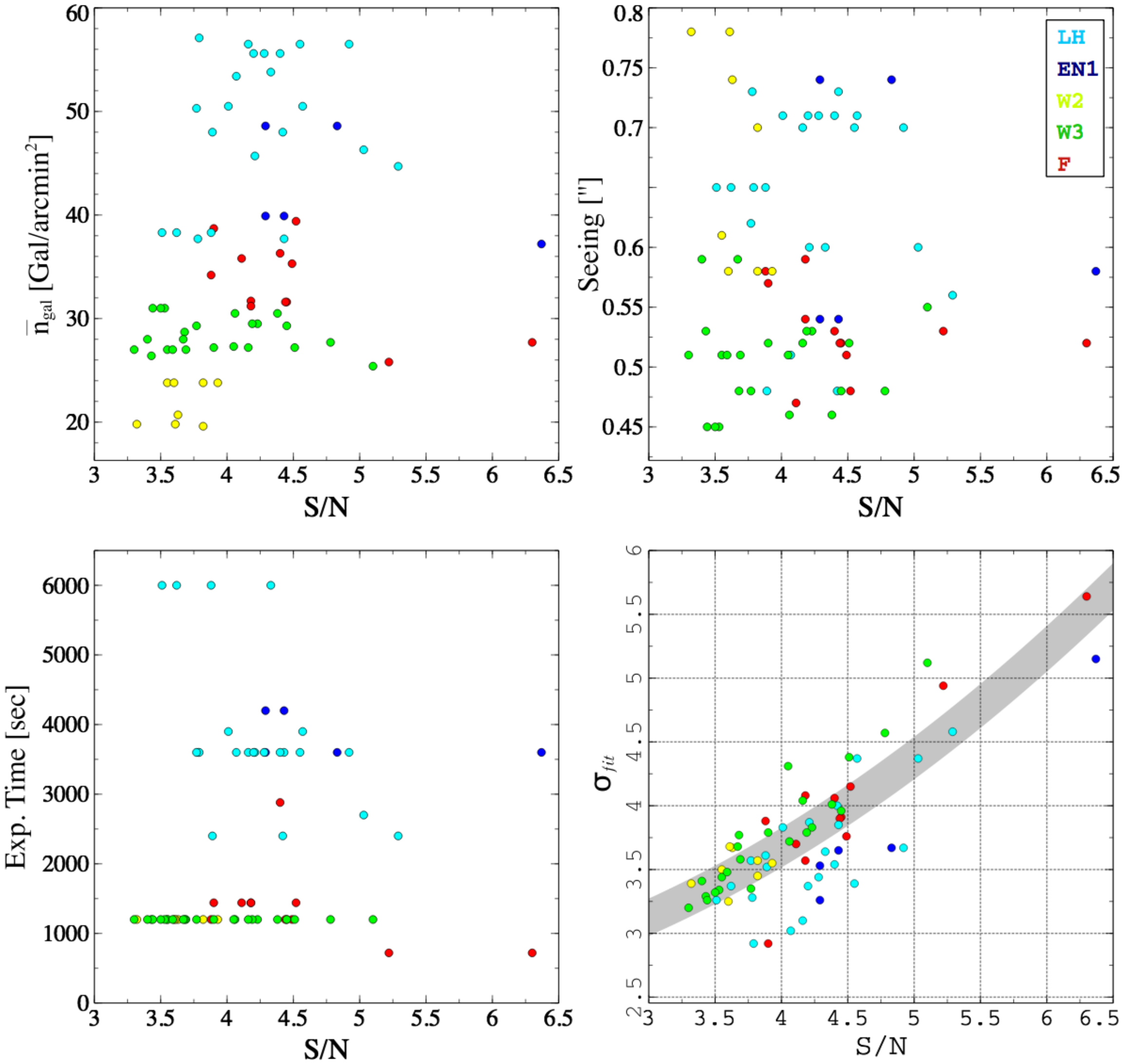

Figure A.4: Summary of quality statistics for the 70 convergence peaks found at $r_{\rm in}$ = 500 pix (1.67″).

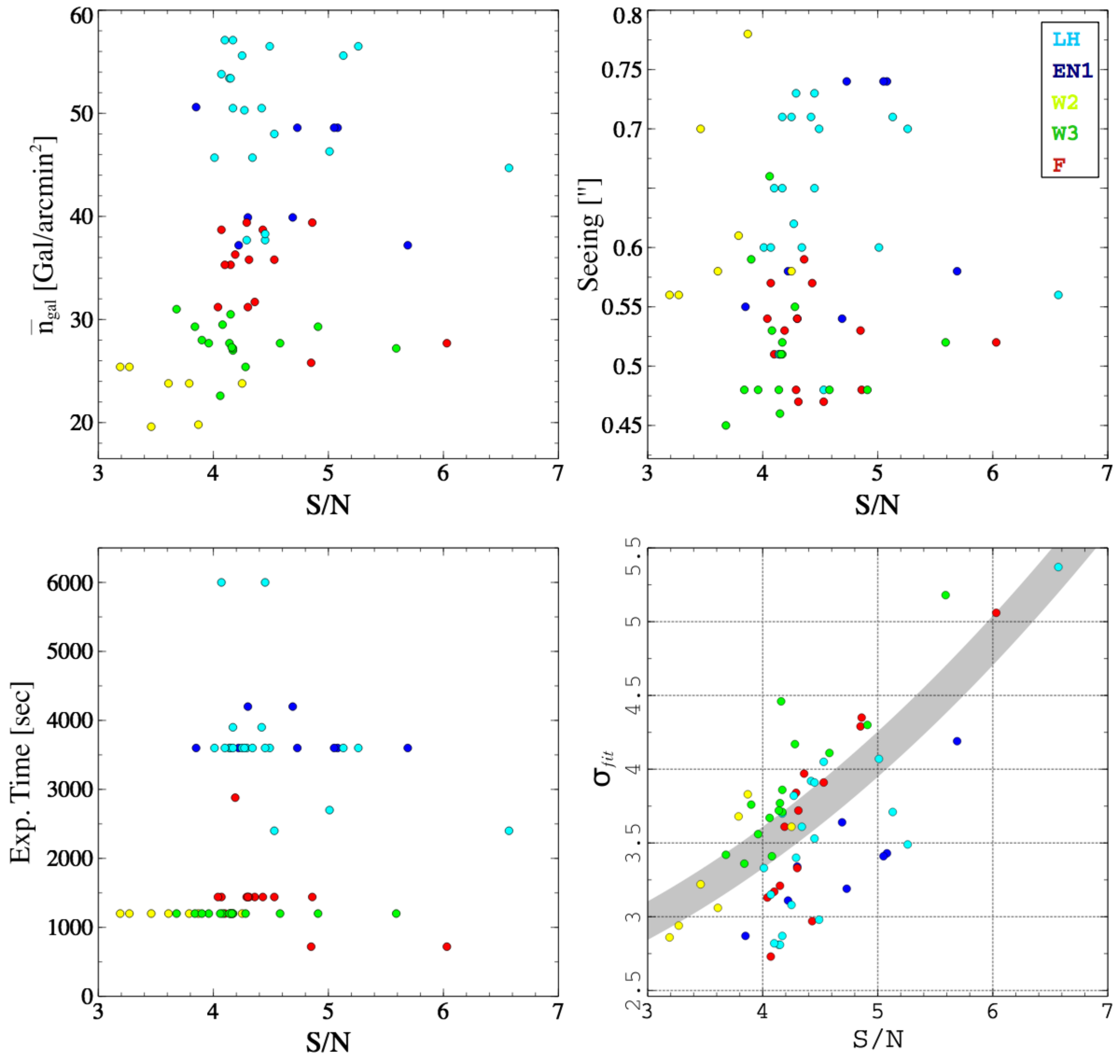

Figure A.5: Summary of quality statistics for the 64 convergence peaks found at $r_{\rm in} = 700$ pix (2.33″).

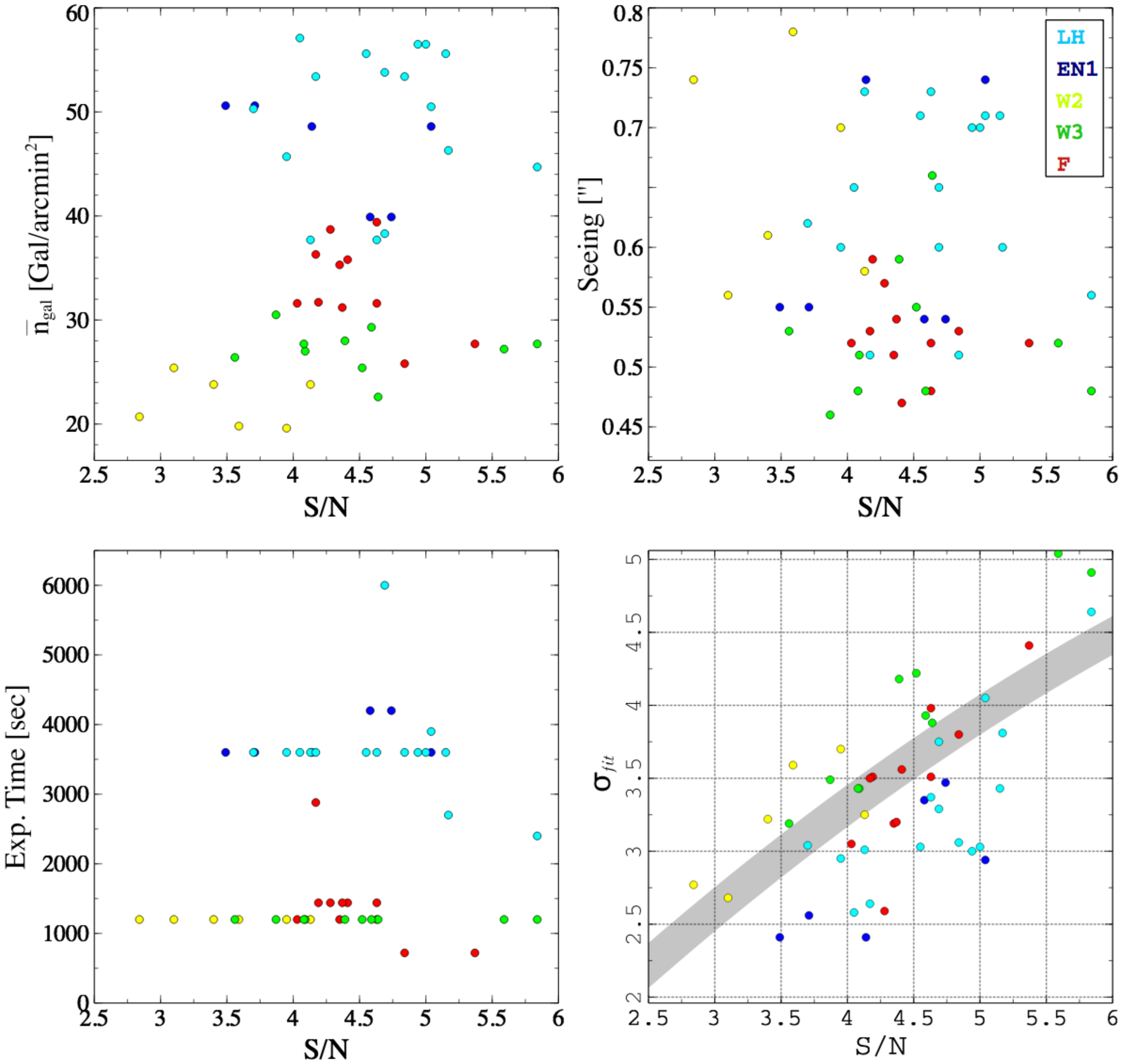

Figure A.6: Summary of quality statistics for the 50 convergence peaks found at $r_{\rm in}$ = 1000 pix (3.33″).

A.2 Lockman Hole

Region	S/N	RA	DEC	r_{in}	
		[J2000]	[J2000]	[pix]	[arcmin]
LHn1n1	5.93	10:52:35.246	+57:36:46.20	300	$1'$
LHn1p0	4.92	10:52:46.962	+58:05:35.51	300	$1'$
LHn2n2	4.22	10:55:48.088	+57:20:14.75	300	$1'$
LHp0n3	4.46	10:49:29.158	+57:04:54.29	300	$1'$
LHp0p1	4.36	10:48:48.908	+58:30:03.53	300	$1'$
LHp1n1	4.12	10:45:20.432	+57:56:45.06	300	$1'$
LHp1p0	4.45	10:45:08.409	+58:09:17.22	300	$1'$
LHp1p2	4.10	10:45:46.239	+58:56:18.72	300	$1'$
LHp2p2	3.94	10:40:52.151	+58:55:54.57	300	$1'$

Table A.1: Highest signal peaks in the LH field at $r_{in} = 300$.

Region	S/N	RA	DEC	r_{in}	
		[J2000]	[J2000]	[pix]	[arcmin]
LHn1n1	5.03	10:52:31.294	+57:35:46.32	500	$1.67'$
LHn1p0	4.42	10:52:46.588	+58:05:48.48	500	$1.67'$
LHn1p0	3.89	10:54:11.635	+58:05:48.00	500	$1.67'$
LHn2n2	4.57	10:58:12.022	+57:25:49.29	500	$1.67'$
LHn2n2	4.01	10:55:48.950	+57:20:34.07	500	$1.67'$
LHp0n2	4.92	10:49:56.021	+57:21:30.95	500	$1.67'$
LHp0n2	4.55	10:47:48.810	+57:21:01.96	500	$1.67'$
LHp0n2	4.16	10:48:15.144	+57:27:50.66	500	$1.67'$
LHp0n3	4.43	10:49:22.939	+57:05:06.88	500	$1.67'$
LHp0n3	3.78	10:49:25.443	+56:55:30.99	500	$1.67'$
LHp0p0	4.07	10:50:05.854	+58:22:12.66	500	$1.67'$
LHp0p0*	-5.73	10:49:08.972	+58:15:34.26	500	$1.67'$
LHp0p1	5.29	10:48:41.939	+58:32:28.08	500	$1.67'$
LHp1n1	4.21	10:45:18.545	+57:57:06.69	500	$1.67'$
LHp1p0	4.40	10:45:08.069	+58:09:19.72	500	$1.67'$
LHp1p0	4.28	10:46:32.961	+58:02:53.67	500	$1.67'$
LHp1p0	4.20	10:44:40.550	+58:07:47.09	500	$1.67'$
LHp1p1	3.79	10:45:12.682	+58:50:25.34	500	$1.67'$
LHp1p2	3.77	10:45:46.283	+58:55:03.28	500	$1.67'$
LHp2p1	4.33	10:41:53.252	+58:37:25.20	500	$1.67'$
LHp2p2	3.88	10:39:50.347	+58:54:51.77	500	$1.67'$
LHp2p2	3.62	10:40:51.787	+58:55:51.65	500	$1.67'$
LHp2p2	3.51	10:41:47.718	+58:59:15.11	500	$1.67'$

Table A.2: Highest signal peaks in the LH field at $r_{in} = 500$.

Region	S/N	RA	DEC	r_{in}	
		[J2000]	[J2000]	[pix]	[arcmin]
LHn1n1	5.01	10:52:35.134	+57:35:41.37	700	$2.33'$
LHn2n2	4.42	10:58:11.435	+57:25:15.89	700	$2.33'$
LHn2n2	4.17	10:55:45.960	+57:20:23.30	700	$2.33'$
LHn1p0	4.53	10:52:45.430	+58:05:55.41	700	$2.33'$
LHp0n2	5.26	10:49:56.802	+57:21:32.78	700	$2.33'$
LHp0n2	4.49	10:48:24.239	+57:29:22.74	700	$2.33'$
LHp0n3	4.45	10:49:28.057	+57:04:50.39	700	$2.33'$
LHp0n3	4.29	10:49:16.993	+56:55:09.09	700	$2.33'$
LHp0p0	4.14	10:50:59.288	+58:10:34.78	700	$2.33'$
LHp0p0	4.15	10:50:54.718	+58:08:55.75	700	$2.33'$
LHp0p1	6.57	10:48:40.687	+58:32:45.58	700	$2.33'$
LHp1n1	4.34	10:45:17.466	+57:57:22.65	700	$2.33'$
LHp1n1	4.01	10:44:08.315	+57:54:37.06	700	$2.33'$
LHp1p0	5.13	10:44:40.715	+58:08:20.01	700	$2.33'$
LHp1p0	4.25	10:46:32.498	+58:02:34.95	700	$2.33'$
LHp1p1	4.17	10:46:03.389	+58:38:53.37	700	$2.33'$
LHp1p1	4.10	10:45:13.219	+58:50:38.19	700	$2.33'$
LHp1p2	4.27	10:45:48.685	+58:56:06.38	700	$2.33'$
LHp2p1	4.07	10:41:47.783	+58:37:18.95	700	$2.33'$
LHp2p2	4.45	10:40:52.230	+58:55:54.88	700	$2.33'$

Table A.3: Highest signal peaks in the LH field at $r_{in} = 700$.

Region	S/N	RA	DEC	r_{in}	
		[J2000]	[J2000]	[pix]	[arcmin]
LHn1n1	5.17	10:52:36.904	+57:35:42.41	1000	$3.33'$
LHn2n2	5.04	10:58:15.457	+57:25:37.17	1000	$3.33'$
LHp0n2	5.00	10:48:19.763	+57:29:08.32	1000	$3.33'$
LHp0n2	4.94	10:49:55.970	+57:21:40.61	1000	$3.33'$
LHp0n3	4.63	10:49:03.940	+56:53:38.04	1000	$3.33'$
LHp0n3	4.13	10:49:28.523	+57:05:16.61	1000	$3.33'$
LHp0p0	4.84	10:50:55.872	+58:08:45.14	1000	$3.33'$
LHp0p0	4.17	10:50:18.869	+58:19:40.56	1000	$3.33'$
LHp0p0*	-6.03	10:49:08.373	+58:15:37.19	1000	$3.33'$
LHp0p1	5.84	10:48:41.110	+58:31:42.34	1000	$3.33'$
LHp1n1	3.95	10:45:12.988	+57:58:33.65	1000	$3.33'$
LHp1p0	5.15	10:45:31.871	+58:02:46.71	1000	$3.33'$
LHp1p0	4.55	10:44:44.192	+58:07:57.92	1000	$3.33'$
LHp1p1	4.05	10:45:12.132	+58:50:44.05	1000	$3.33'$
LHp1p2	3.70	10:45:46.227	+58:56:14.07	1000	$3.33'$
LHp2p1	4.69	10:41:48.595	+58:37:08.05	1000	$3.33'$
LHp2p2	4.69	10:40:54.287	+58:55:51.91	1000	$3.33'$

Table A.4: Highest signal peaks in the LH field at $r_{in} = 1000$.

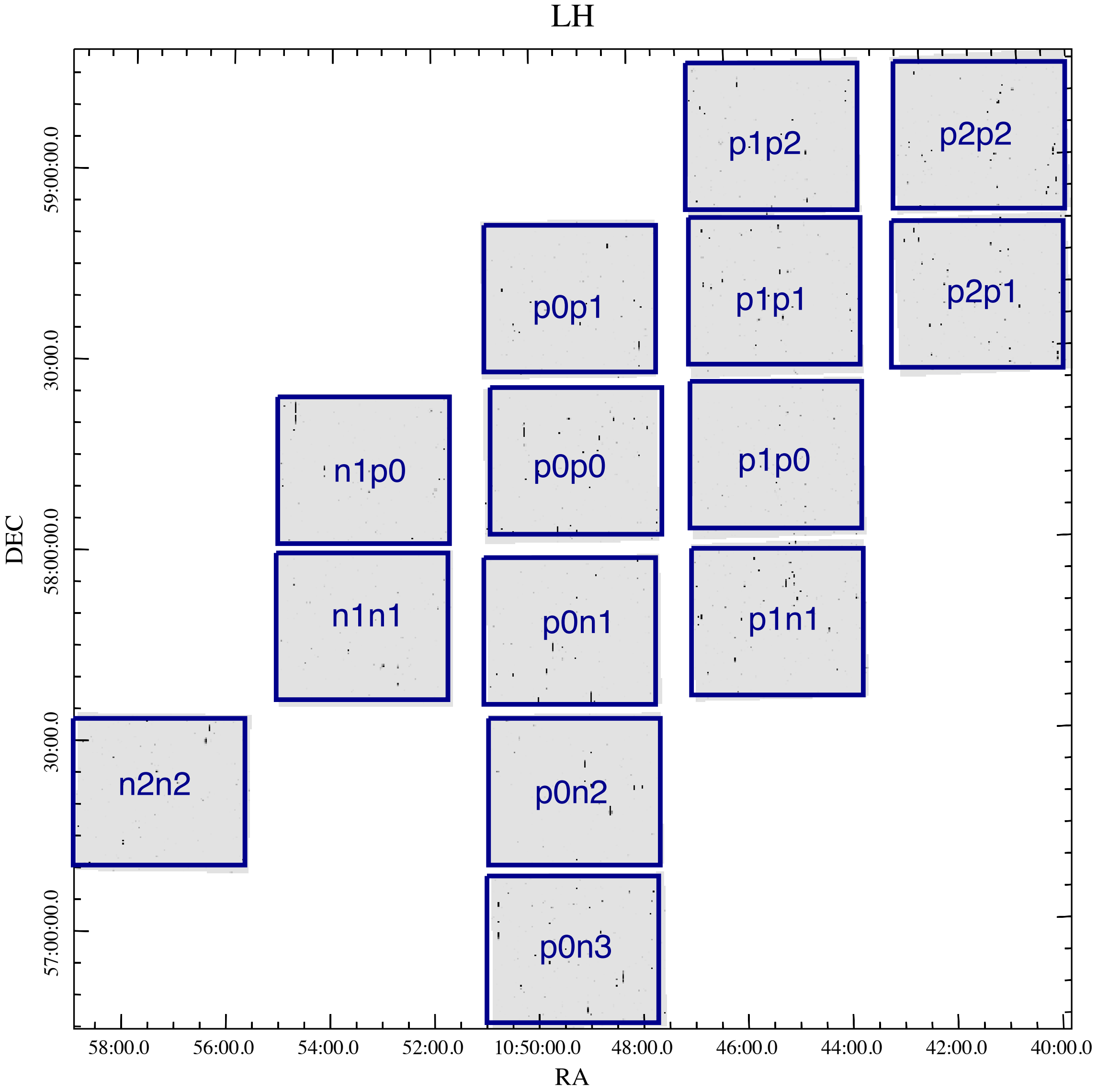

Figure A.7: Relative locations of LH fields.

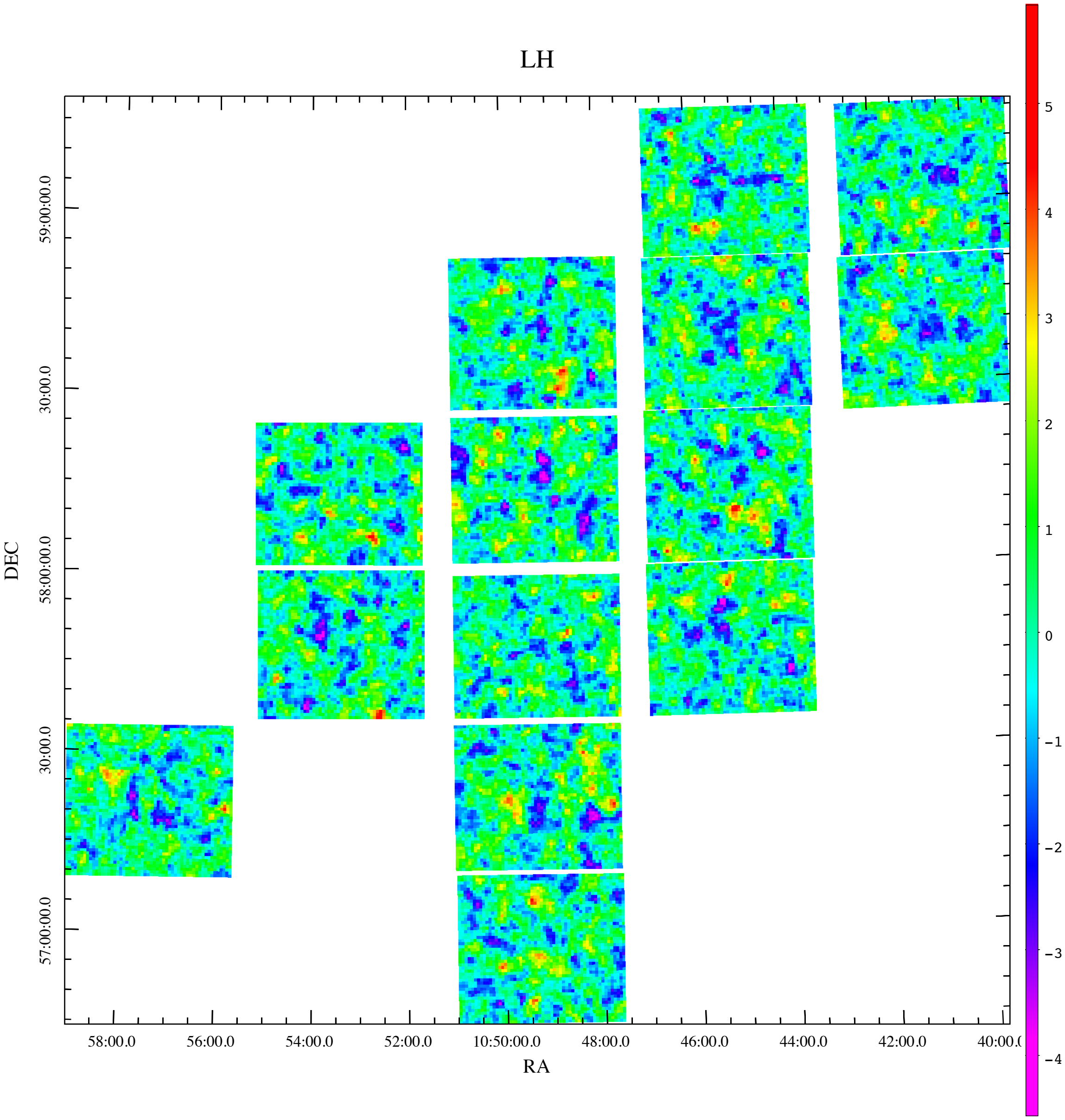

Figure A.8: $R_{\rm in} = 300$ pix convergence map of the Lockman Hole region.

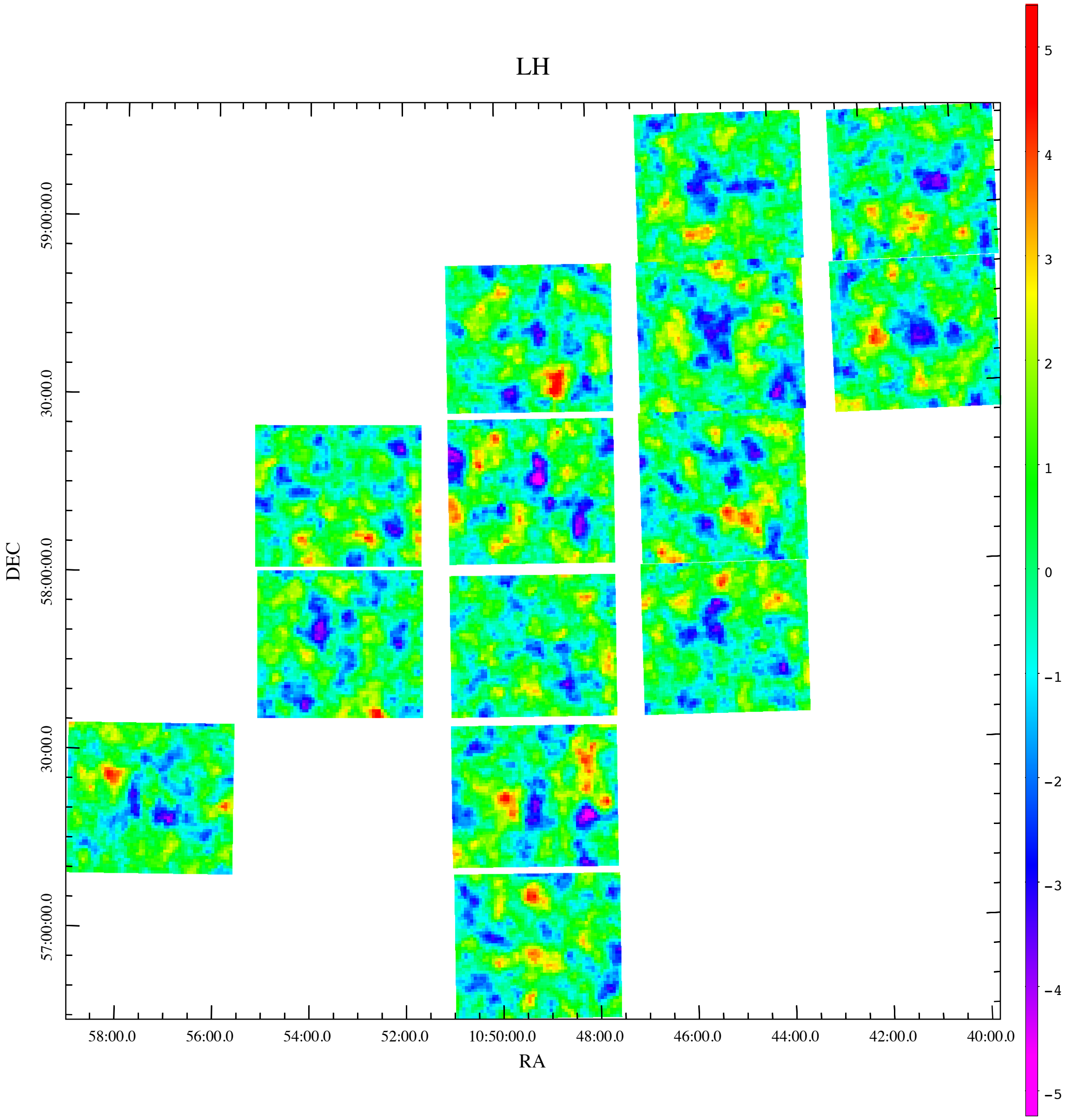

Figure A.9: $R_{\rm in} = 500$ pix convergence map of the Lockman Hole region.

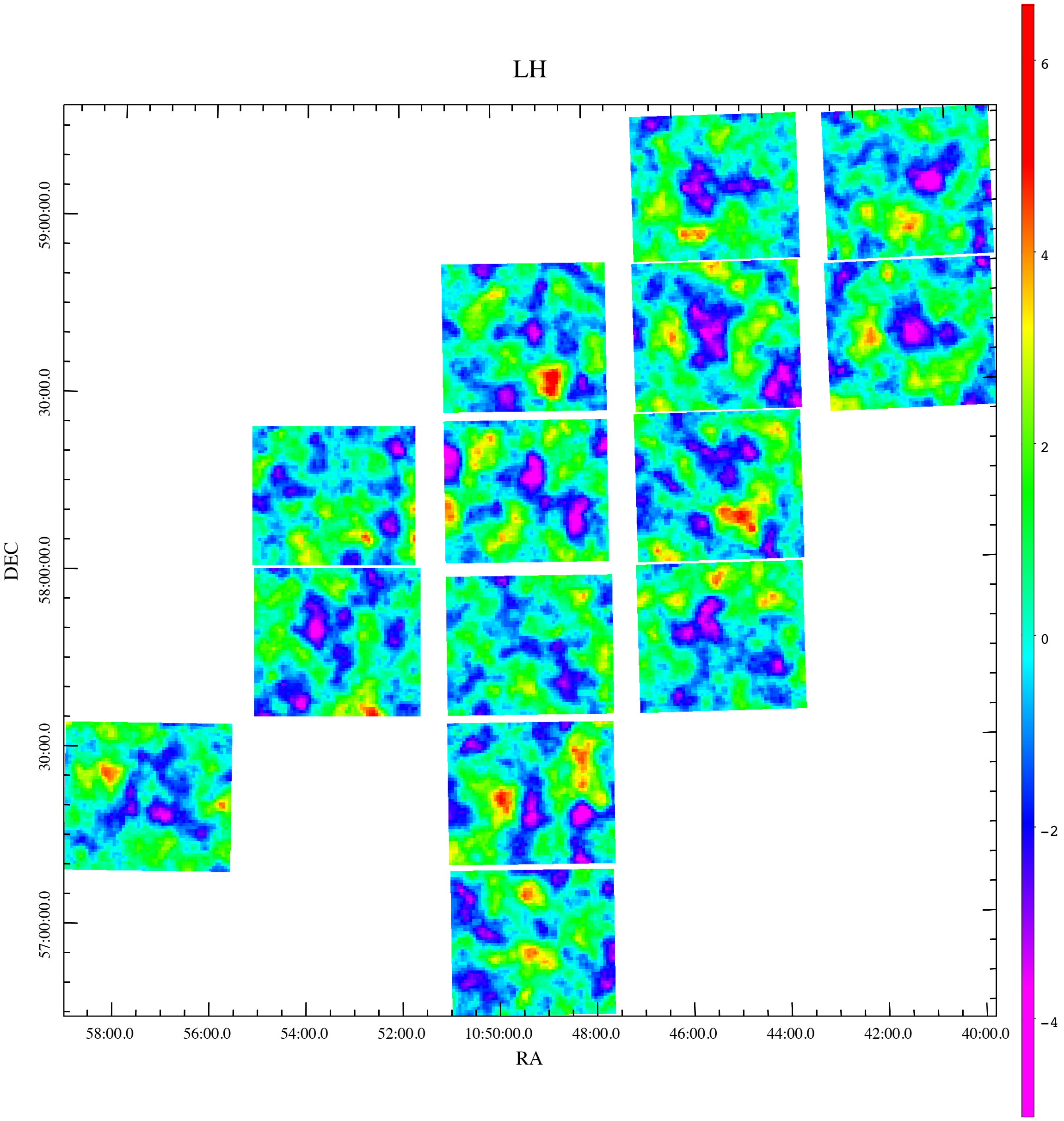

Figure A.10: $R_{\text{in}} = 700$ pix convergence map of the Lockman Hole region.

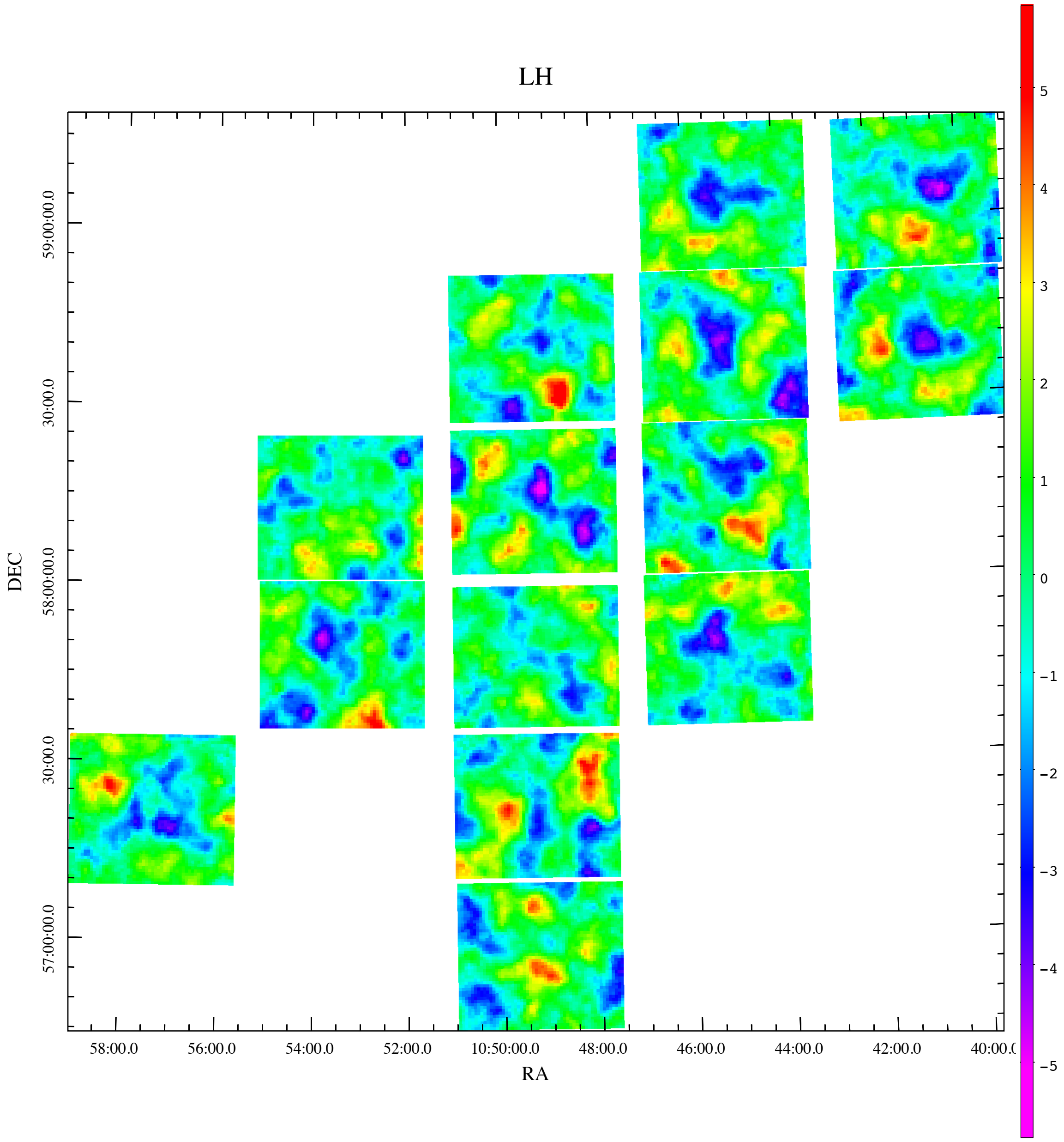

Figure A.11: $R_{\text{in}} = 1000$ pix convergence map of the Lockman Hole region.

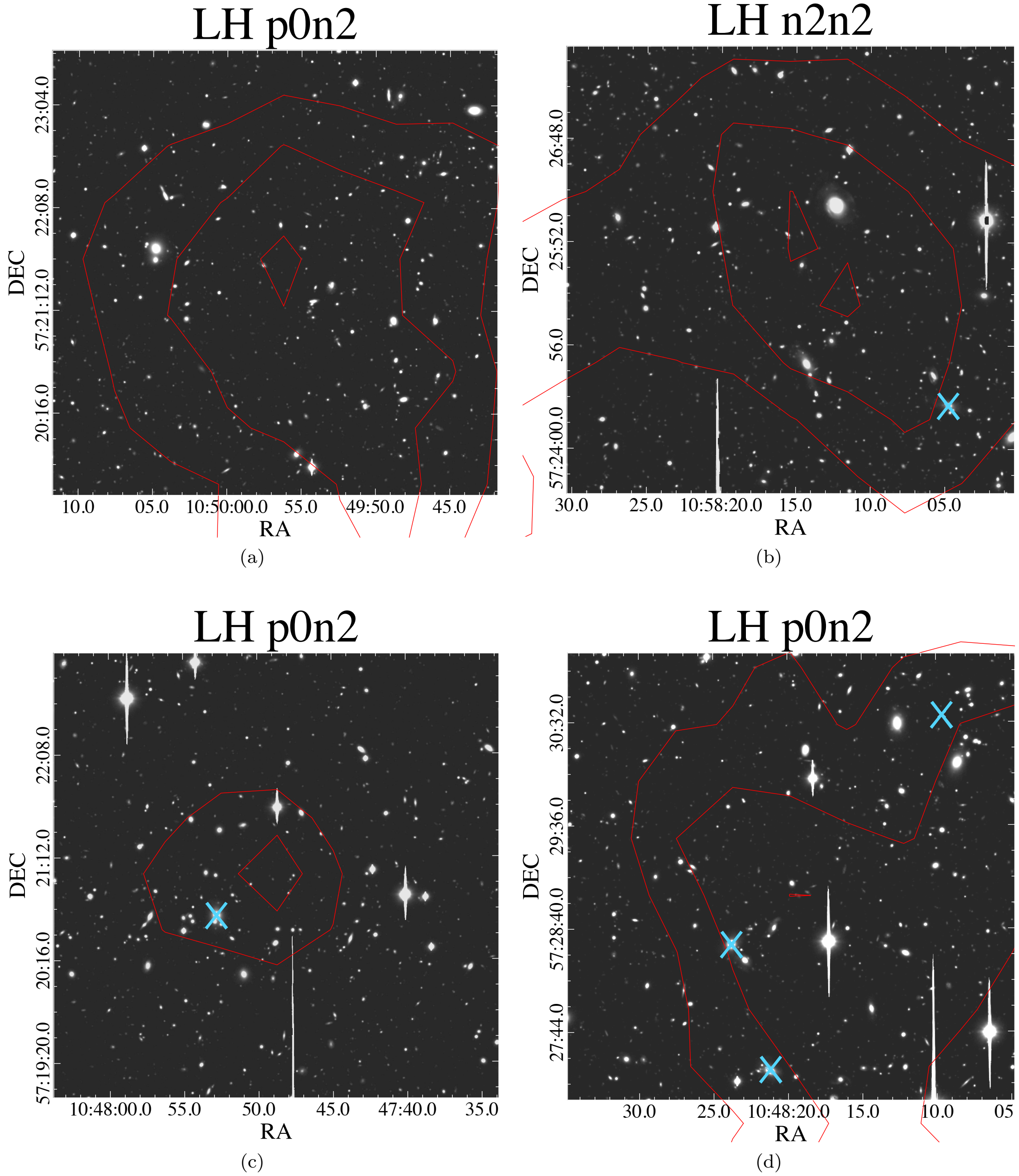

(a) (b) (c) (d)

Figure A.12: Signal peaks in the LH fields. **(a)** 5.26 S/N peak at 2.33′ scale (700 pix). Contours at 3, 4, 5. **(b)** 5.04 S/N peak at 3.33′ scale (1000 pix). Contours at 3, 4, 5. **(c)** 4.55 S/N peak at 1.67′ scale (500 pix). Contours at 3, 4. **(d)** 5.00 S/N peak at 3.33′(1000 pix). Contours at 3, 4, 5.

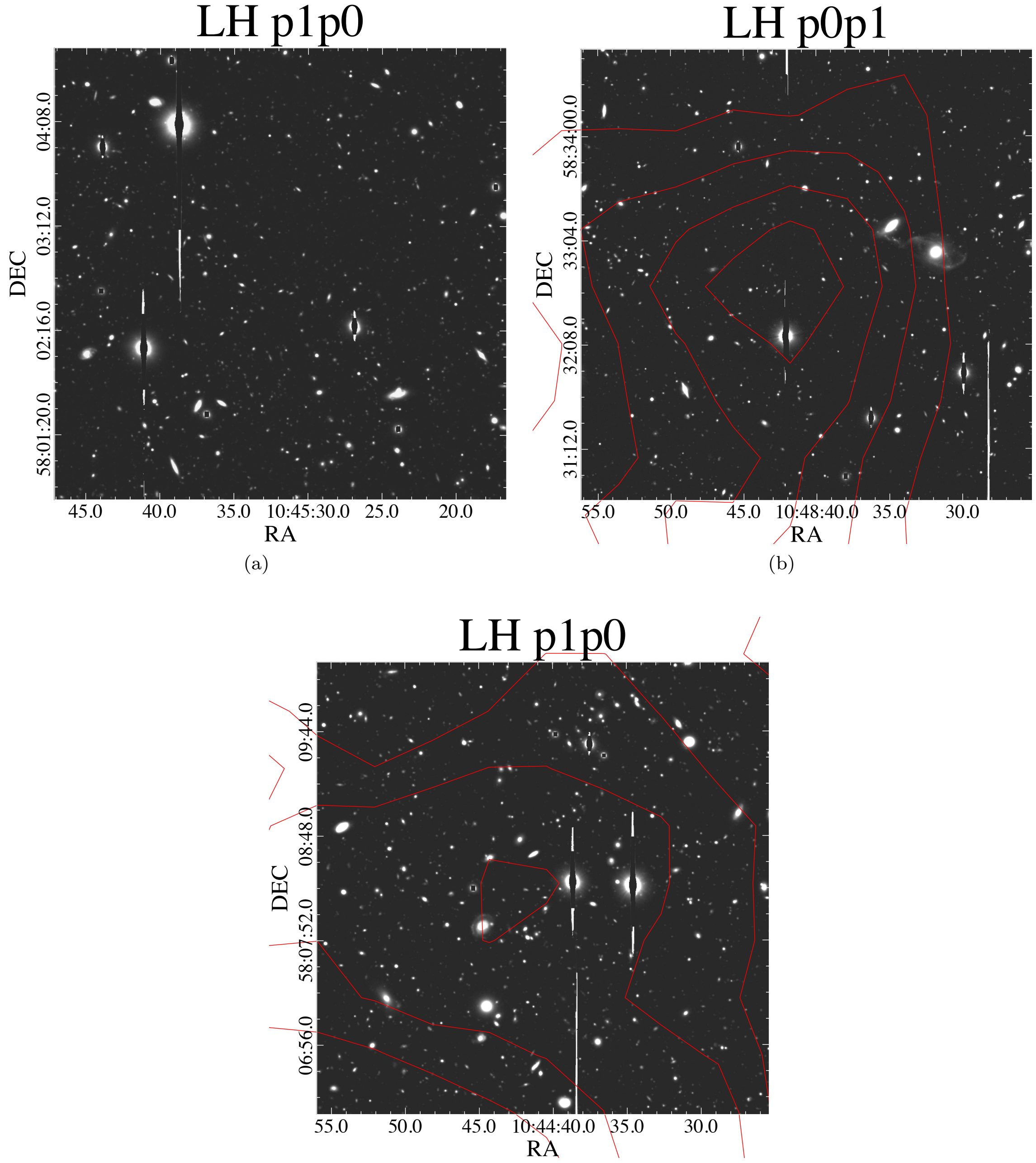

(a)

(b)

(c)

Figure A.13: Signal peaks in the LH fields. **(a)** 5.15 S/N peak at 3.33′ scale (1000 pix). Contours outside field of view. **(b)** 6.57 S/N peak at 2.33′ scale (700 pix). Contours at 3, 4, 5, 6. **(c)** 5.13 S/N peak at 2.33′ scale (700 pix). Contours at 3, 4, 5.

A.3 EN1 Region

Region	S/N	RA	DEC	r_{in}	
		[J2000]	[J2000]	[pix]	[arcmin]
en1n1n1	4.53	16:06:34.374	+53:54:05.96	300	$1'$
en1p0n1	5.57	16:10:33.206	+54:05:40.00	400	$1.33'$
en1p1n1	5.11	16:12:10.063	+54:00:45.36	300	$1'$
en1p2n1	4.15	16:15:45.754	+53:47:03.98	300	$1'$

Table A.5: Highest signal peaks in the EN1 field at $r_{in} = 300$.

Region	S/N	RA	DEC	r_{in}	
		[J2000]	[J2000]	[pix]	[arcmin]
en1n1n1*	-4.22	16:07:04.815	+53:57:03.79	500	$1.67'$
en1p0n1	6.37	16:10:33.144	+54:05:50.81	500	$1.67'$
en1p1n1	4.29	16:13:46.886	+54:02:45.77	500	$1.67'$
en1p1n1	4.83	16:12:11.263	+54:00:24.54	500	$1.67'$
en1p2n1	4.43	16:15:08.591	+54:08:58.40	500	$1.67'$
en1p2n1	4.29	16:15:46.490	+53:47:19.37	500	$1.67'$

Table A.6: Highest signal peaks in the EN1 field at $r_{in} = 500$.

Region	S/N	RA	DEC	r_{in}	
		[J2000]	[J2000]	[pix]	[arcmin]
en1n1n1	3.85	16:06:32.656	+53:53:49.33	700	$2.33'$
en1n1n1*	-4.78	16:07:09.014	+53:57:00.07	700	$2.33'$
en1p0n1	5.69	16:10:32.681	+54:06:14.51	700	$2.33'$
en1p0n1	4.22	16:10:04.975	+53:47:44.42	700	$2.33'$
en1p1n1	5.08	16:13:39.581	+54:02:53.05	700	$2.33'$
en1p1n1	5.05	16:13:42.094	+54:05:57.05	700	$2.33'$
en1p1n1	4.73	16:12:12.103	+54:00:28.12	700	$2.33'$
en1p1n1*	-4.85	16:11:45.666	+54:08:28.08	700	$2.33'$
en1p2n1	4.69	16:15:46.756	+53:47:24.07	700	$2.33'$
en1p2n1	4.30	16:15:15.910	+54:08:28.27	700	$2.33'$

Table A.7: Highest signal peaks in the EN1 field at $r_{in} = 700$.

Region	S/N	RA	DEC	r_{in}	
		[J2000]	[J2000]	[pix]	[arcmin]
en1n1n1	3.71	16:08:20.191	+53:54:32.02	1000	$3.33'$
en1n1n1	3.49	16:06:31.749	+53:53:21.18	1000	$3.33'$
en1n1n1*	-4.99	16:07:06.981	+53:56:57.14	1000	$3.33'$
en1p0n1	5.58	16:10:31.940	+54:05:45.43	900	$3'$
en1p0n1	4.67	16:10:05.473	+53:47:55.82	900	$3'$
en1p1n1	5.04	16:13:52.545	+54:04:01.93	1000	$3.33'$
en1p1n1	4.14	16:12:11.379	+54:00:26.84	1000	$3.33'$
en1p1n1*	-5.49	16:11:46.476	+54:08:41.82	1000	$3.33'$
en1p2n1	4.74	16:15:12.296	+54:08:25.19	1000	$3.33'$
en1p2n1	4.58	16:15:45.516	+53:47:48.12	1000	$3.33'$

Table A.8: Highest signal peaks in the EN field at $r_{in} = 1000$.

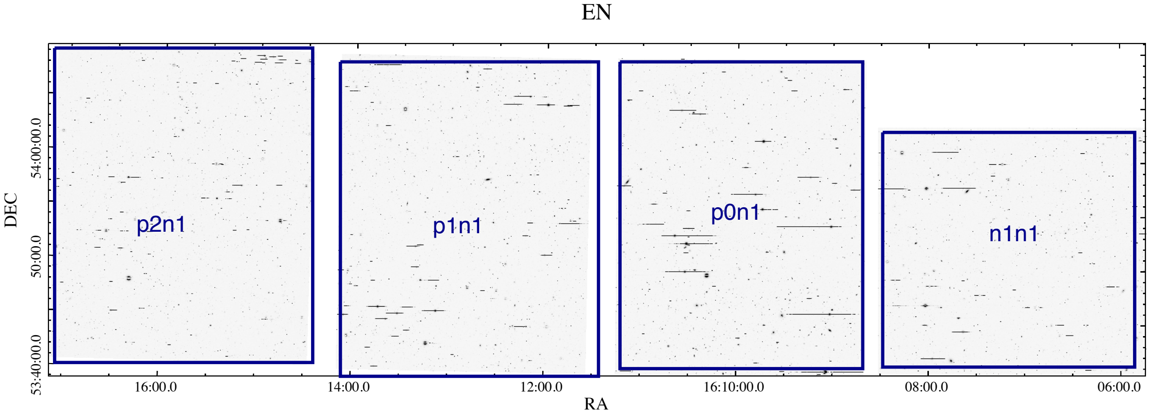

Figure A.14: Relative locations of EN1 fields.

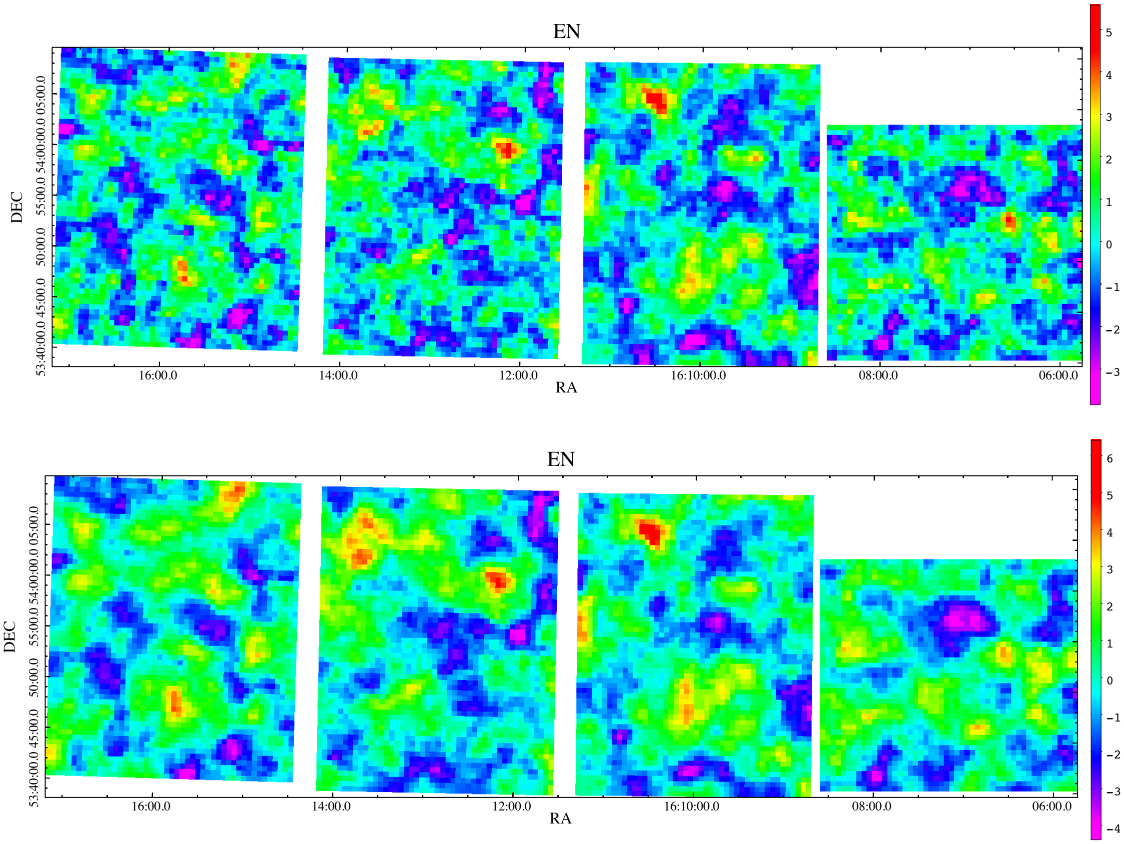

Figure A.15: Convergence maps of the EN region for r_{in} = 300 and 500 pix. (EN1p0n1 is 400 & 500 pix, respectively).

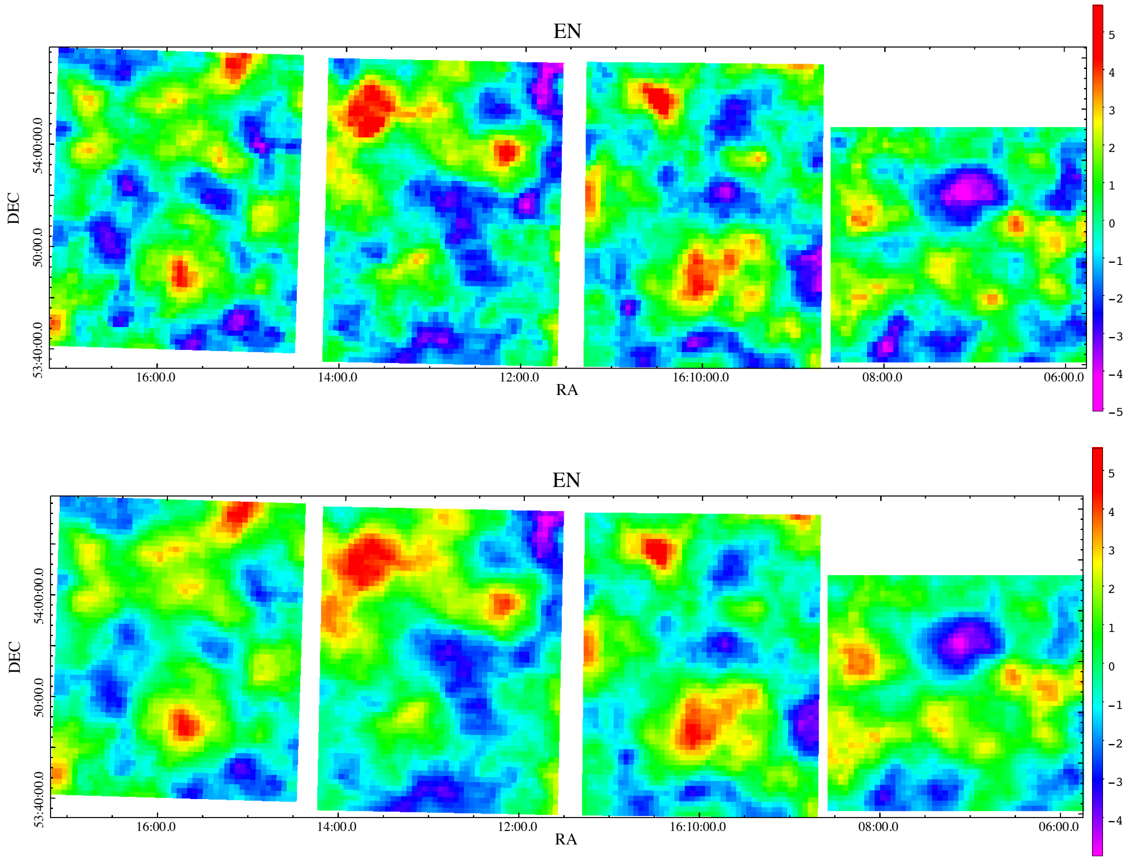

Figure A.16: Convergence maps of the EN region for r_{in} = 700 and 1000 pix. (Note: EN1p0n1 is 700 & 900 pix, respectively)

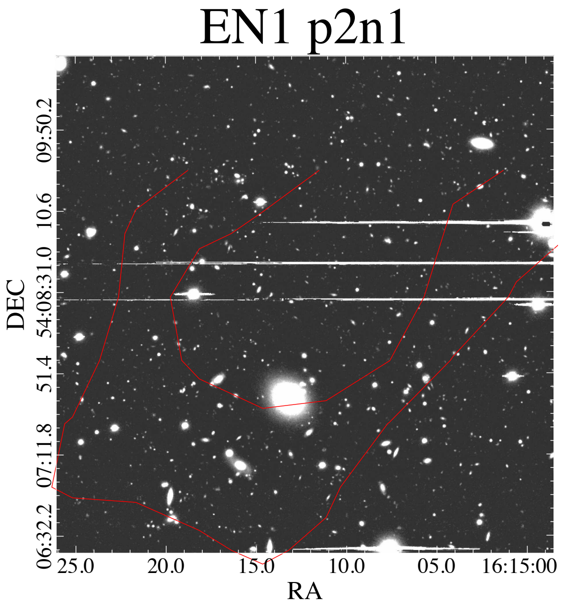

Figure A.17: 4.74 S/N peak at 3.33′ scale (1000 pix). Contours at 3, 4.

A.4 W2 Region

Region	S/N	RA	DEC	r_{in}	
		[J2000]	[J2000]	[pix]	[arcmin]
w2_61	3.48	9:01:53.562	-2:45:31.76	300	1′
w2_62	3.78	9:03:41.758	-3:01:15.76	300	1′
w2_62	4.01	9:04:32.552	-2:55:23.07	300	1′
w2_63	3.56	9:07:10.137	-3:01:20.45	300	1′
w2_63	3.57	9:06:33.857	-2:47:15.42	300	1′
w2_70	3.70	9:02:23.657	-2:24:30.40	300	1′
w2_70	3.31	9:01:17.355	-2:28:44.05	300	1′
w2_71	3.85	9:04:34.830	-2:21:12.55	300	1′
w2_71	4.26	9:03:26.204	-2:40:14.51	300	1′
w2_72	3.80	9:06:32.870	-2:36:34.49	300	1′

Table A.9: Highest signal peaks in the W2 field at $r_{in} = 300$.

Region	S/N	RA	DEC	r_{in}	
		[J2000]	[J2000]	[pix]	[arcmin]
w2_61	3.63	9:01:53.455	-2:45:34.05	500	$1.67'$
w2_62	3.55	9:04:31.610	-2:55:15.13	500	$1.67'$
w2_63	3.61	9:06:33.724	-2:47:11.33	500	$1.67'$
w2_63	3.32	9:07:10.245	-3:01:22.00	500	$1.67'$
w2_70	3.82	9:02:24.224	-2:24:31.38	500	$1.67'$
w2_71	3.82	9:03:41.842	-2:23:13.13	500	$1.67'$
w2_71	3.60	9:03:25.294	-2:40:35.98	500	$1.67'$
w2_71	3.93	9:04:38.537	-2:20:50.91	500	$1.67'$

Table A.10: Highest signal peaks in the W2 field at $r_{in} = 500$.

Region	S/N	RA	DEC	r_{in}	
		[J2000]	[J2000]	[pix]	[arcmin]
w2_62	3.79	9:04:33.892	-2:54:58.43	700	$2.33'$
w2_63	3.87	9:06:37.387	-2:47:03.96	700	$2.33'$
w2_70	3.46	9:02:26.901	-2:24:49.32	700	$2.33'$
w2_71	4.25	9:04:36.554	-2:21:23.12	700	$2.33'$
w2_71	3.61	9:03:40.993	-2:23:16.56	700	$2.33'$
w2_72	3.27	9:05:52.008	-2:22:13.84	700	$2.33'$
w2_72	3.19	9:06:33.909	-2:36:37.09	700	$2.33'$

Table A.11: Highest signal peaks in the W2 field at $r_{in} = 700$.

Region	S/N	RA	DEC	r_{in}	
		[J2000]	[J2000]	[pix]	[arcmin]
w2_61	2.84	9:01:41.646	-3:00:08.84	1000	$3.33'$
w2_62	3.40	9:04:34.374	-2:55:23.57	1000	$3.33'$
w2_63	3.59	9:06:35.228	-2:47:19.13	1000	$3.33'$
w2_70	3.95	9:02:27.123	-2:25:30.17	1000	$3.33'$
w2_71	4.13	9:04:36.027	-2:21:10.86	1000	$3.33'$
w2_72	3.10	9:05:50.816	-2:22:10.56	1000	$3.33'$

Table A.12: Highest signal peaks in the W2 field at $r_{in} = 1000$.

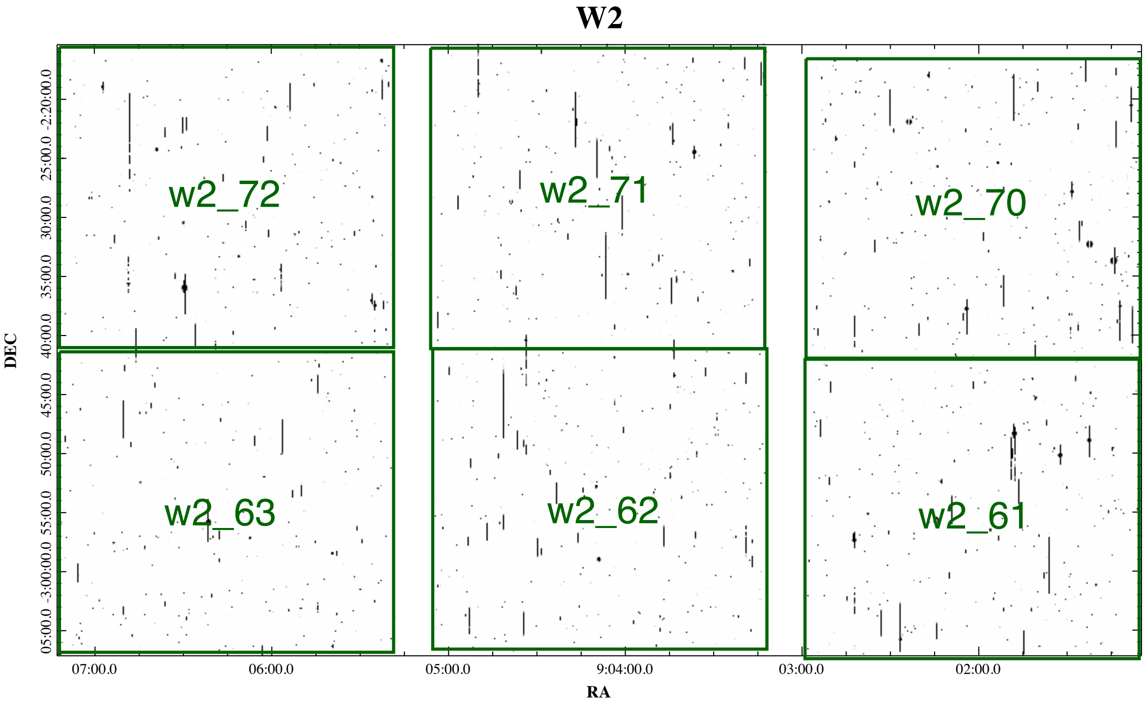

Figure A.18: Relative locations of W2 fields.

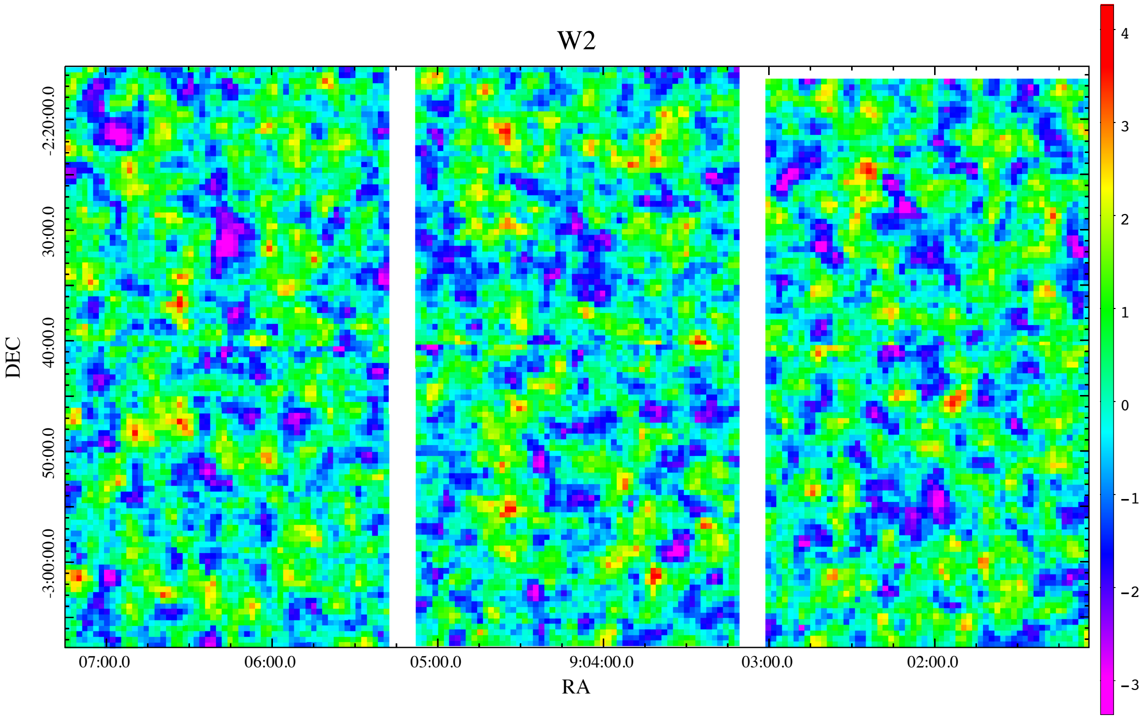

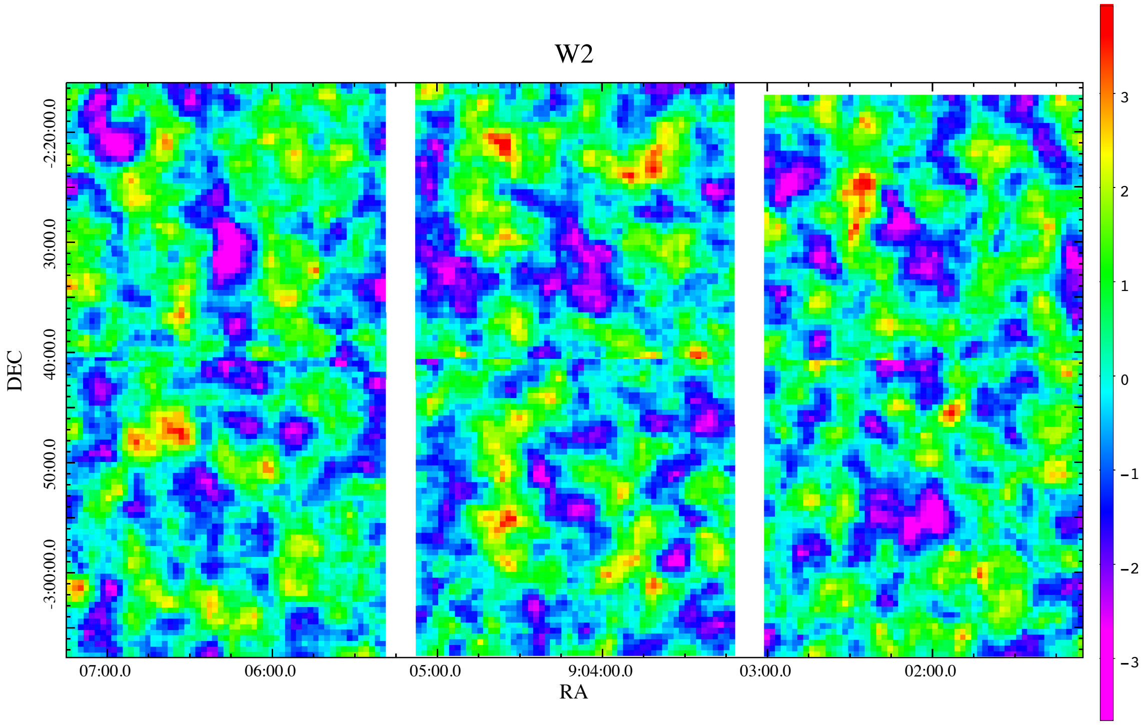

Figure A.19: $R_{\text{in}} = 300$ and 500 convergence maps of the W2 region.

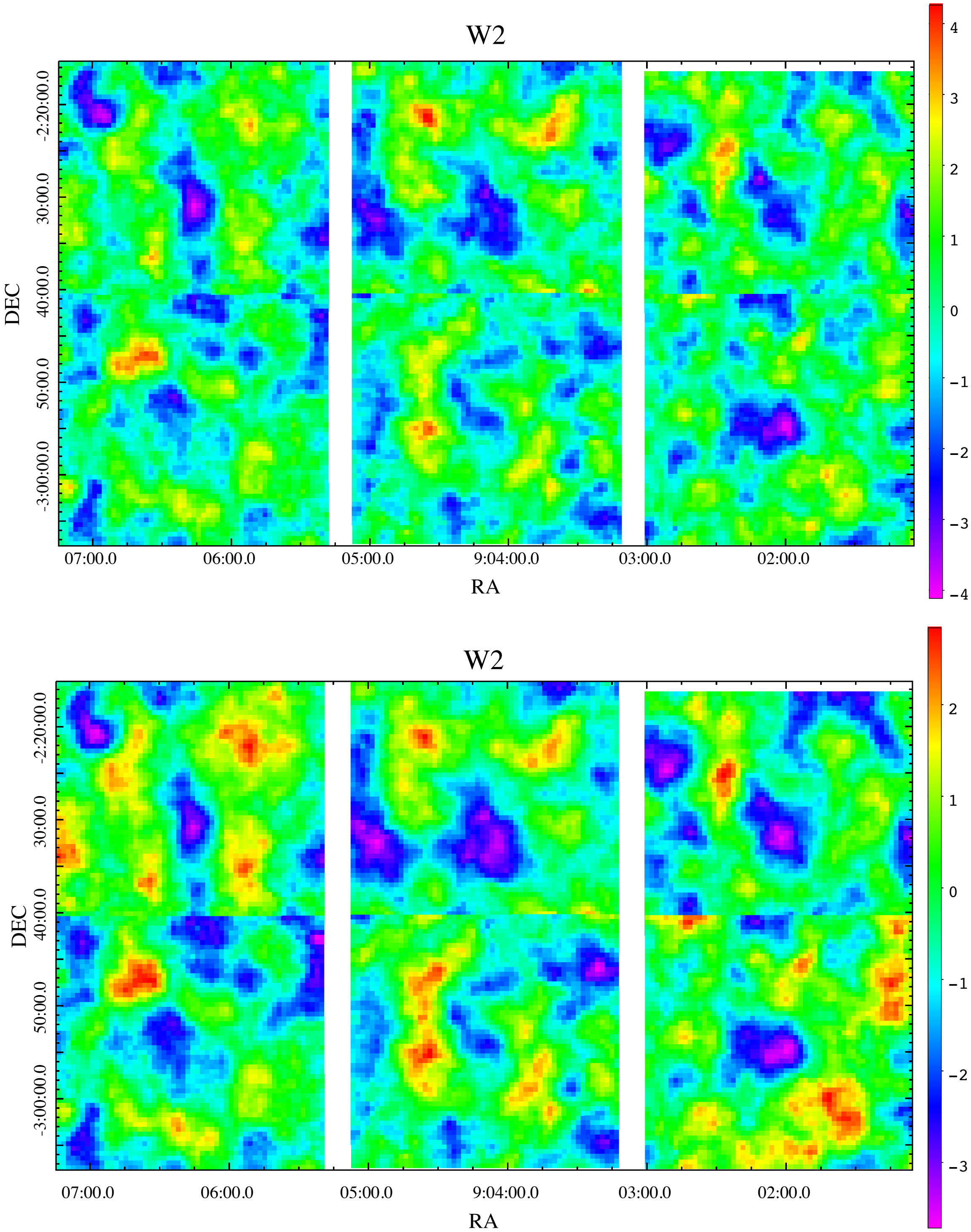

Figure A.20: $R_{\rm in} = 700$ and 1000 convergence maps of the W2 field region.

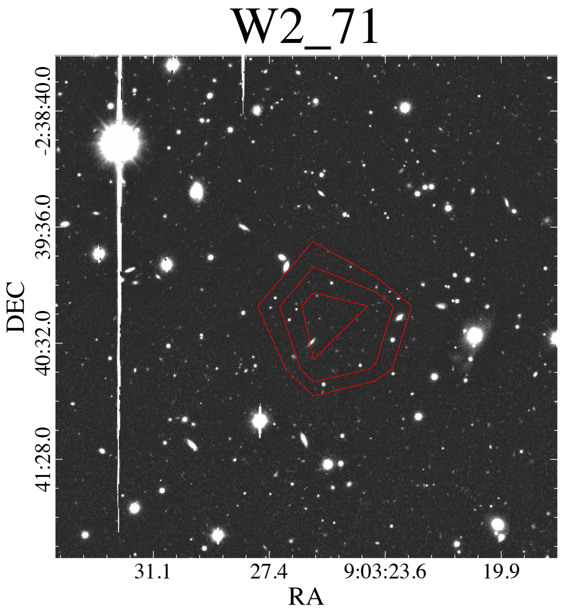

Figure A.21: 4.26 S/N peak at $1'$ scale (300 pix). Contours at 3, 3.5, 4.

A.5 W3 Region

Region	S/N	RA	DEC	r_{in}	
		[J2000]	[J2000]	[pix]	[arcmin]
w3_126	4.15	14:13:37	+56:19:52	300	$1'$
w3_127	4.14	14:17:13	+56:15:13	300	$1'$
w3_127	4.19	14:17:28	+56:08:42	300	$1'$
w3_127	4.46	14:18:38	+56:09:08	300	$1'$
w3_137	4.01	14:12:49	+56:38:17	300	$1'$
w3_138	4.15	14:17:09	+56:39:45	300	$1'$
w3_139	3.77	14:21:06	+56:47:37	300	$1'$
w3_139	3.69	14:22:18	+56:41:10	300	$1'$
w3_139	3.88	14:21:47	+56:31:50	300	$1'$
w3_150	3.93	14:23:20	+57:13:02	300	$1'$
w3_150	4.28	14:22:02	+57:02:55	300	$1'$
w3_150	4.43	14:20:41	+56:51:22	300	$1'$
w3_151	3.76	14:25:52	+57:07:02	300	$1'$
w3_159	4.04	14:13:05	+57:35:47	300	$1'$
w3_160	3.96	14:18:38	+57:29:53	300	$1'$
w3_161	3.92	14:22:18	+57:27:40	300	$1'$
w3_161	3.81	14:22:02	+57:28:09	300	$1'$

Table A.13: Highest signal peaks in the W3 field at $r_{in} = 300$.

Region	S/N	RA	DEC	r_{in}	
		[J2000]	[J2000]	[pix]	[arcmin]
w3_126	3.69	14:13:37.383	+56:19:48.36	500	$1.667'$
w3_126	3.55	14:15:58.909	+56:20:15.44	500	$1.667'$
w3_126	3.59	14:13:37.379	+56:20:03.07	500	$1.667'$
w3_126	3.30	14:13:16.415	+56:09:44.75	500	$1.667'$
w3_127	4.23	14:17:16.374	+56:15:30.40	500	$1.667'$
w3_127	4.19	14:18:38.555	+56:08:29.28	500	$1.667'$
w3_128	3.43	14:22:20.923	+56:19:33.58	500	$1.667'$
w3_137	3.53	14:14:41.383	+55:48:00.14	500	$1.667'$
w3_137	3.44	14:12:35.091	+56:28:35.73	500	$1.667'$
w3_137	3.50	14:13:33.305	+56:49:13.41	500	$1.667'$
w3_138	4.06	14:18:53.109	+56:41:33.25	500	$1.667'$
w3_138	4.38	14:17:04.015	+56:39:33.05	500	$1.667'$
w3_139	4.51	14:23:18.838	+55:39:54.49	500	$1.667'$
w3_139	4.16	14:21:09.868	+56:47:17.43	500	$1.667'$
w3_139	3.90	14:21:46.104	+56:31:27.83	500	$1.667'$
w3_149	3.68	14:16:27.492	+56:56:01.18	500	$1.667'$
w3_150	4.78	14:23:19.720	+57:13:15.33	500	$1.667'$
w3_159	5.10	14:13:04.964	+57:35:45.79	500	$1.667'$
w3_160	4.05	14:19:04.053	+57:25:24.27	500	$1.667'$
w3_161	3.77	14:20:23.285	+57:31:19.19	500	$1.667'$
w3_161	4.45	14:22:13.889	+57:27:30.04	500	$1.667'$
w3_162	3.67	14:23:48.401	+57:26:50.68	500	$1.667'$
w3_162	3.40	14:23:33.122	+57:38:26.71	500	$1.667'$

Table A.14: Highest signal peaks in the W3 field at $r_{in} = 500$.

Region	S/N	RA	DEC	r_{in}	
		[J2000]	[J2000]	[pix]	[arcmin]
w3_126	4.17	14:13:37.917	+56:19:35.02	700	2.33′
w3_127	4.08	14:18:37.143	+56:08:21.10	700	2.33′
w3_137	3.68	14:12:39.175	+56:28:07.16	700	2.33′
w3_138	4.15	14:17:20.969	+56:38:36.31	700	2.33′
w3_139	5.59	14:23:18.003	+56:39:46.96	700	2.33′
w3_139	4.17	14:21:06.808	+56:47:26.88	700	2.33′
w3_150	4.58	14:23:19.927	+57:12:59.27	700	2.33′
w3_150	4.14	14:20:42.211	+56:51:12.85	700	2.33′
w3_150	3.96	14:20:33.601	+57:12:25.89	700	2.33′
w3_151	4.06	14:25:03.379	+57:04:31.02	700	2.33′
w3_159	4.28	14:13:01.982	+57:35:36.29	700	2.33′
w3_160	4.16	14:19:04.813	+57:25:38.46	700	2.33′
w3_161	4.91	14:22:15.329	+57:27:39.29	700	2.33′
w3_161	3.84	14:20:27.059	+57:31:22.09	700	2.33′
w3_162	3.90	14:23:50.449	+57:26:17.25	700	2.33′

Table A.15: Highest signal peaks in the W3 field at $r_{in} = 700$.

Region	S/N	RA	DEC	r_{in}	
		[J2000]	[J2000]	[pix]	[arcmin]
w3_126	4.09	14:13:36.377	+55:19:52.58	1000	3.33′
w3_128	3.56	14:22:28.489	+55:19:52.22	1000	3.33′
w3_138	3.87	14:17:11.555	+56:39:44.07	1000	3.33′
w3_138	3.87	14:17:11.566	+56:39:44.07	1000	3.33′
w3_139	5.59	14:23:17.027	+56:40:47.81	1000	3.33′
w3_150	4.08	14:20:57.149	+56:49:23.63	1000	3.33′
w3_151	4.64	14:26:03.087	+57:05:23.57	1000	3.33′
w3_150	5.84	14:23:19.537	+57:12:59.72	1000	3.33′
w3_159	4.52	14:13:03.921	+57:35:36.53	1000	3.33′
w3_161	4.59	14:22:11.486	+57:27:47.67	1000	3.33′
w3_162	4.39	14:23:50.545	+57:26:47.33	1000	3.33′

Table A.16: Highest signal peaks in the W3 field at $r_{in} = 1000$.

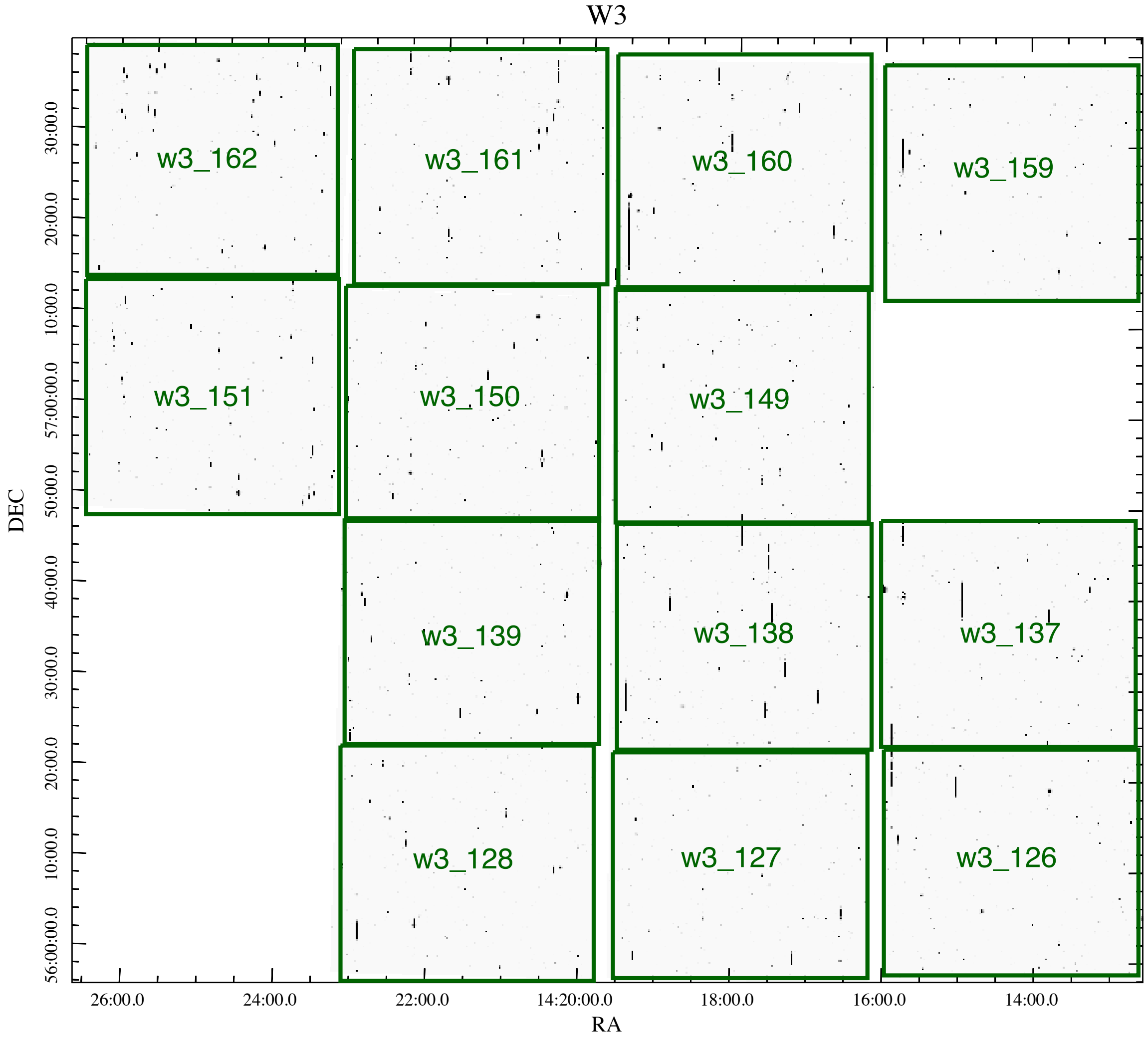

Figure A.22: Relative locations of W3 fields.

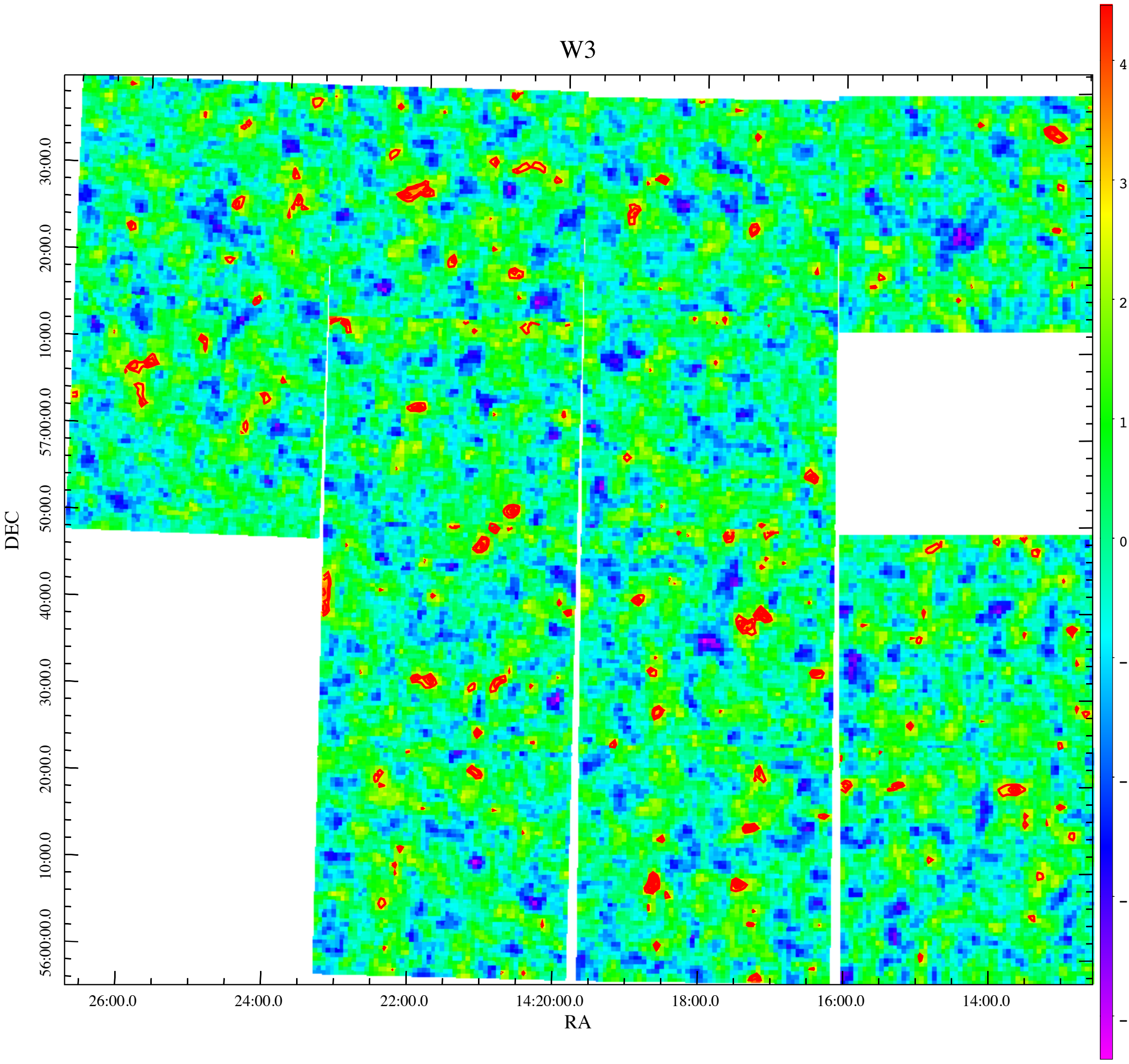

Figure A.23: $R_{\text{in}} = 300$ pix convergence map of the W3 field region. (Contours at 3, 4, and 5 S/N levels to make peaks discernible.)

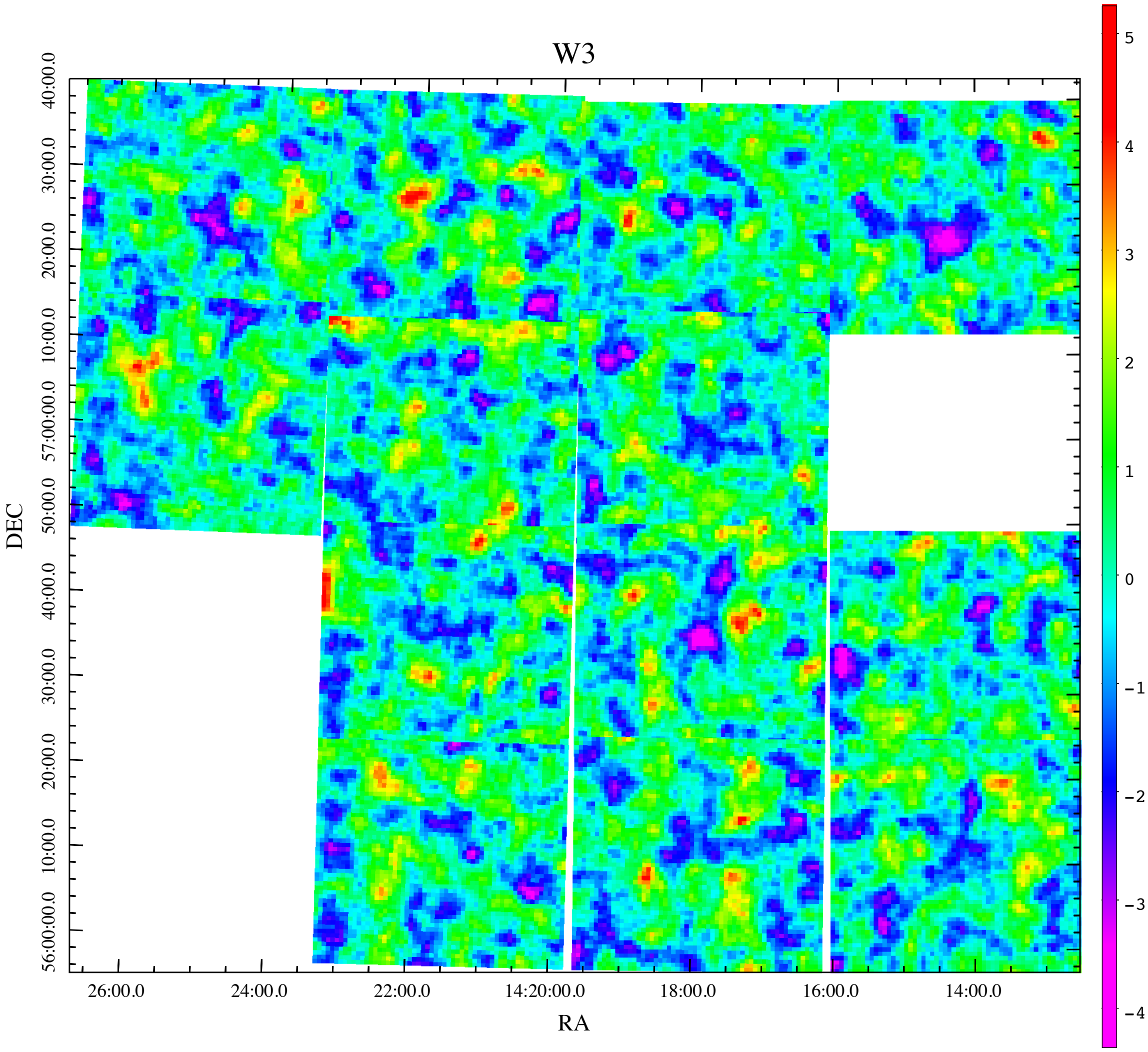

Figure A.24: $R_{\mathrm{in}} = 500$ pix convergence map of the W3 field region.

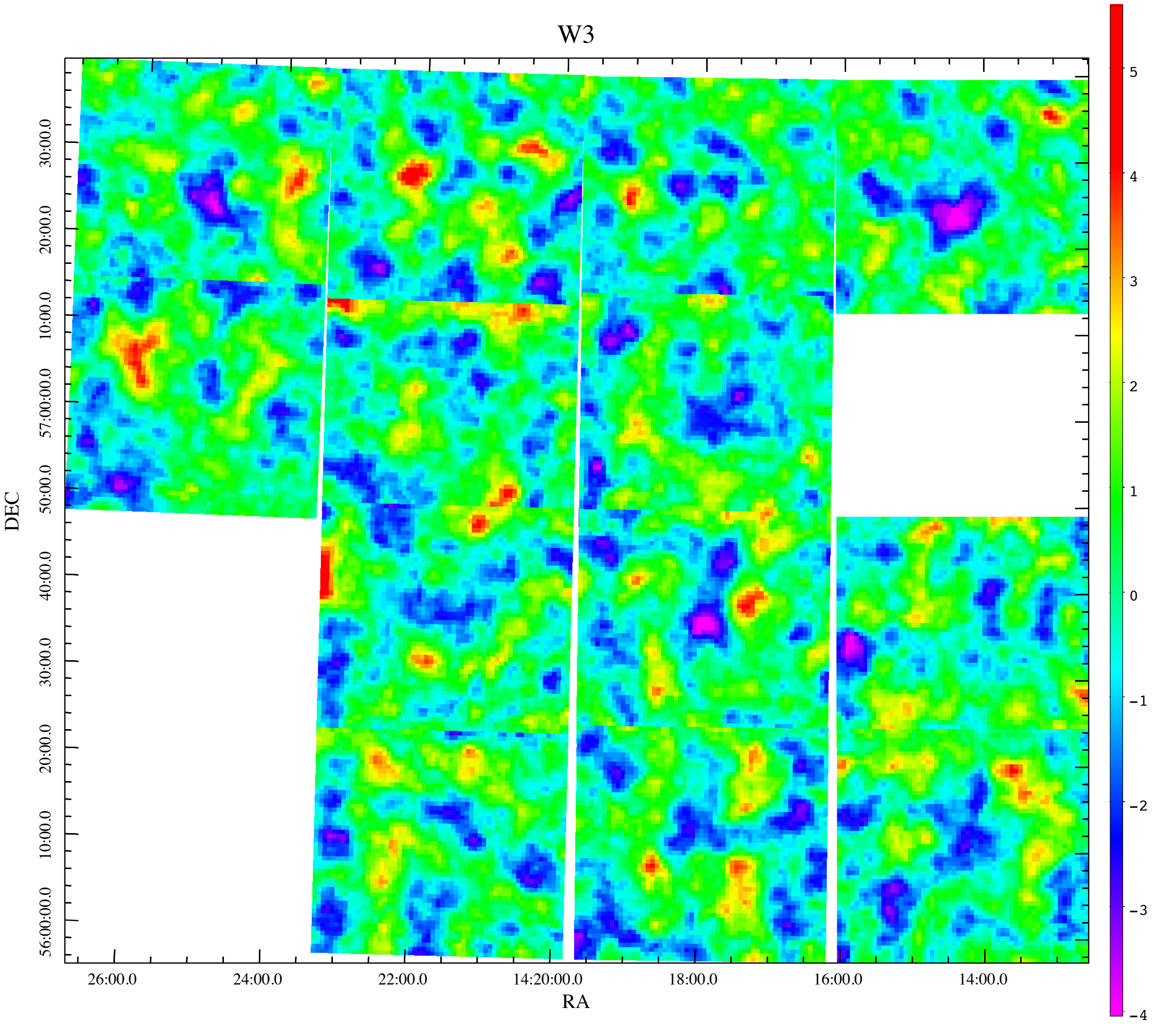

Figure A.25: $R_{\text{in}} = 700$ pix convergence map of the W3 field region.

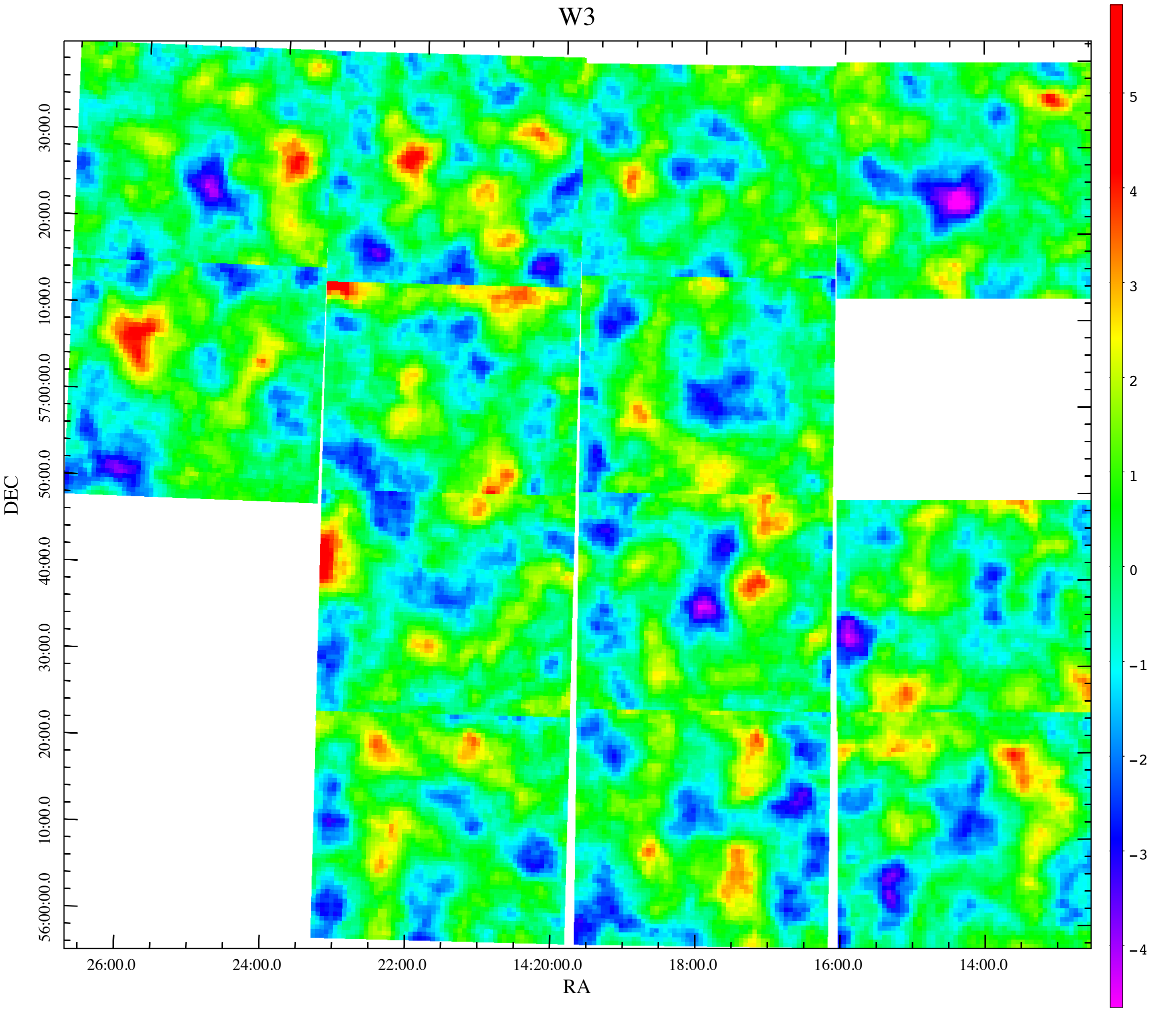

Figure A.26: $R_{\rm in} = 1000$ pix convergence map of the W3 field region.

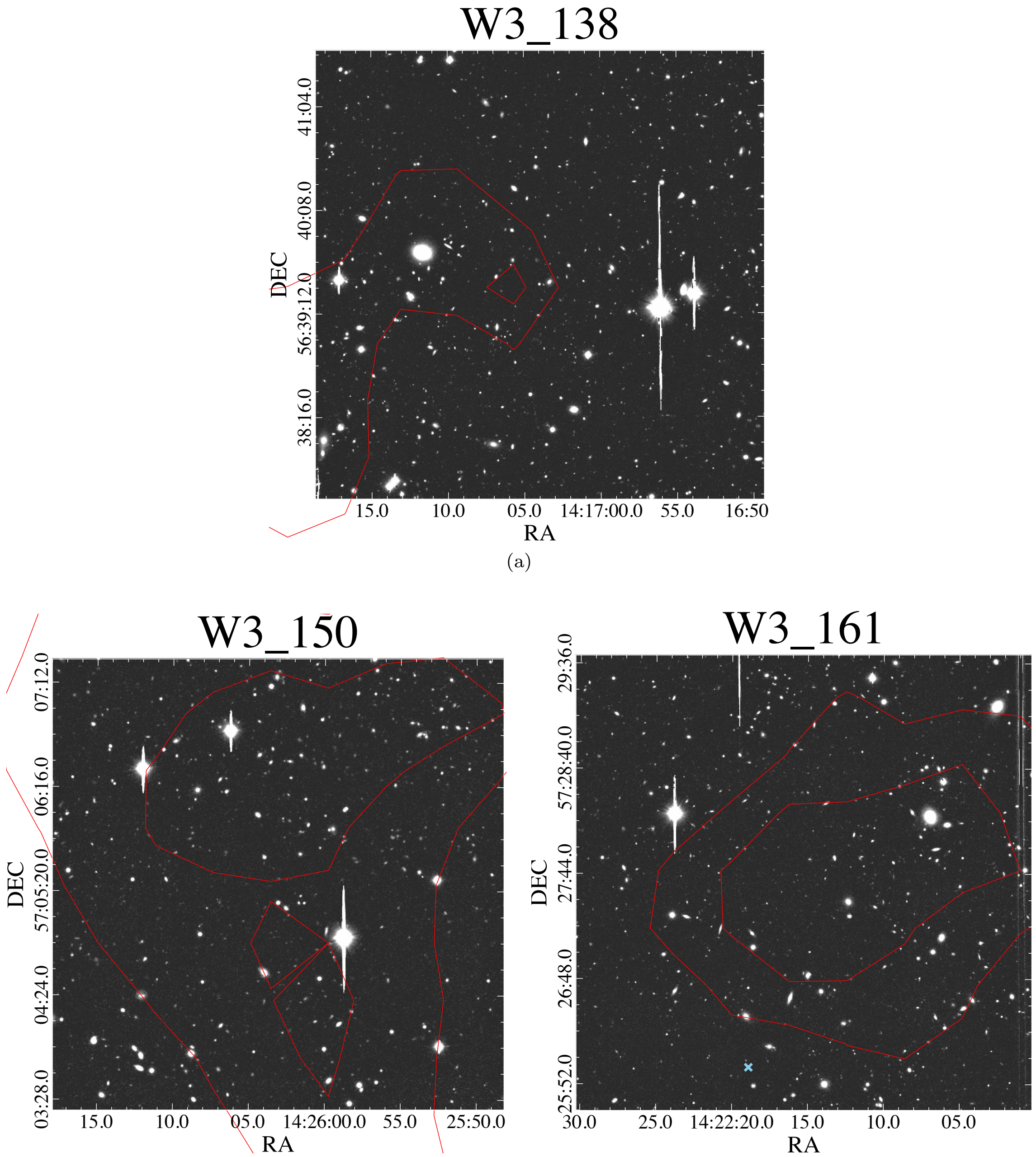

(a)

(b)

(c)

Figure A.27: Signal peaks in the W3 fields. **(a)** 4.38 S/N peak at 1.67′ scale (500 pix) contours at 3, 4. **(b)** 4.64 S/N peak at 3.33′ scale (1000 pix), contours at 3, 4. **(c)** 4.91 S/N peak at 2.33′ scale (700 pix), contours at 3, 4.

A.6 Boötes Void

Region	S/N	RA	DEC	r_{in}	
		[J2000]	[J2000]	[pix]	[arcmin]
f43	5.44	14:30:50.368	+34:20:58.54	300	$1'$
f46	4.78	14:37:07.733	+34:19:15.77	300	$1'$
f46	3.74	14:37:08.177	+34:24:44.50	300	$1'$
f52	4.36	14:28:08.074	+33:45:35.61	300	$1'$
f53	3.71	14:31:29.326	+33:53:45.90	300	$1'$
f54	4.00	14:33:07.982	+33:50:25.17	300	$1'$
f54	4.44	14:32:45.803	+34:01:00.13	300	$1'$
f56	4.88	14:38:18.198	+33:55:27.90	300	$1'$
f61	4.54	14:25:29.708	+33:14:52.51	300	$1'$
f63	3.60	14:32:02.789	+33:15:23.24	300	$1'$
f64	3.70	14:33:53.057	+33:30:15.63	300	$1'$
f64	3.71	14:34:34.551	+33:22:28.03	300	$1'$
f71	4.57	14:26:41.204	+33:00:25.59	300	$1'$
f71	3.84	14:25:41.517	+32:52:11.10	300	$1'$
f73	3.87	14:31:44.087	+32:59:47.09	300	$1'$

Table A.17: Highest signal peaks in the Boötes field at $r_{in} = 300$.

Region	S/N	RA	DEC	r_{in}	
		[J2000]	[J2000]	[pix]	[arcmin]
f43	6.30	14:30:50.963	+34:21:12.26	500	$1.67'$
f44	3.90	14:33:01.632	+34:21:30.41	500	$1.67'$
f44*	-6.14	14:32:43.669	+34:16:25.35	500	$1.67'$
f45*	-4.56	14:34:51.199	+34:15:59.67	500	$1.67'$
f46	4.52	14:37:07.859	+34:19:04.55	500	$1.67'$
f52	4.49	14:28:07.588	+33:45:22.93	500	$1.67'$
f54	3.88	14:33:07.524	+33:50:26.76	500	$1.67'$
f56	4.18	14:38:17.862	+33:55:44.15	500	$1.67'$
f61	5.22	14:25:29.145	+33:14:39.85	500	$1.67'$
f63	4.40	14:32:08.741	+33:15:10.44	500	$1.67'$
f63*	-4.51	14:31:05.306	+33:24:49.01	500	$1.67'$
f64	4.11	14:34:20.199	+33:26:49.93	500	$1.67'$
f71*	-5.32	14:25:01.257	+32:57:59.83	500	$1.67'$
f71	4.45	14:26:41.074	+33:01:08.44	500	$1.67'$
f71	4.44	14:25:41.136	+32:51:49.37	500	$1.67'$
f73	4.18	14:31:43.075	+32:59:16.13	500	$1.67'$

Table A.18: Highest signal peaks in the Boötes field at $r_{in} = 500$.

Region	S/N	RA	DEC	r_{in}	
		[J2000]	[J2000]	[pix]	[arcmin]
f43	6.03	14:30:52.566	+34:21:09.59	700	2.33′
f44	4.43	14:32:41.504	+34:27:04.70	700	2.33′
f44	4.07	14:33:01.280	+34:21:34.13	700	2.33′
f46	4.86	14:37:08.473	+34:19:05.32	700	2.33′
f46	4.29	14:37:08.182	+34:15:29.41	700	2.33′
f52	4.15	14:28:07.447	+33:45:06.01	700	2.33′
f52	4.10	14:29:14.046	+33:59:22.88	700	2.33′
f56	4.36	14:38:18.433	+33:55:31.52	700	2.33′
f61	4.85	14:25:28.425	+33:14:49.87	700	2.33′
f63	4.19	14:31:43.235	+33:31:45.96	700	2.33′
f64	4.53	14:34:19.251	+33:27:17.30	700	2.33′
f64	4.31	14:34:07.969	+33:31:35.70	700	2.33′
f73	4.30	14:31:50.756	+32:51:41.06	700	2.33′
f73	4.04	14:30:54.431	+32:49:29.14	700	2.33′

Table A.19: Highest signal peaks in the Boötes field at $r_{in} = 700$.

Region	S/N	RA	DEC	r_{in}	
		[J2000]	[J2000]	[pix]	[arcmin]
f43	5.37	14:30:50.388	+34:21:06.99	1000	3.33′
f44	4.28	14:33:03.291	+34:21:31.53	1000	3.33′
f44*	-6.92	14:32:40.574	+34:16:12.41	1000	3.33′
f46	4.63	14:37:07.903	+34:18:41.56	1000	3.33′
f52	4.35	14:29:19.539	+34:00:34.62	1000	3.33′
f56	4.19	14:38:16.736	+33:55:50.71	1000	3.33′
f61	4.84	14:25:28.289	+33:14:31.52	1000	3.33′
f63	4.17	14:32:05.903	+33:14:50.13	1000	3.33′
f64	4.41	14:34:21.772	+33:27:24.24	1000	3.33′
f71	4.63	14:26:41.494	+33:00:53.55	1000	3.33′
f71	4.03	14:25:28.865	+33:04:42.40	1000	3.33′
f73	4.37	14:31:50.6478	+32:51:44.53	1000	3.33′

Table A.20: Highest signal peaks in the Boötes field at $r_{in} = 1000$.

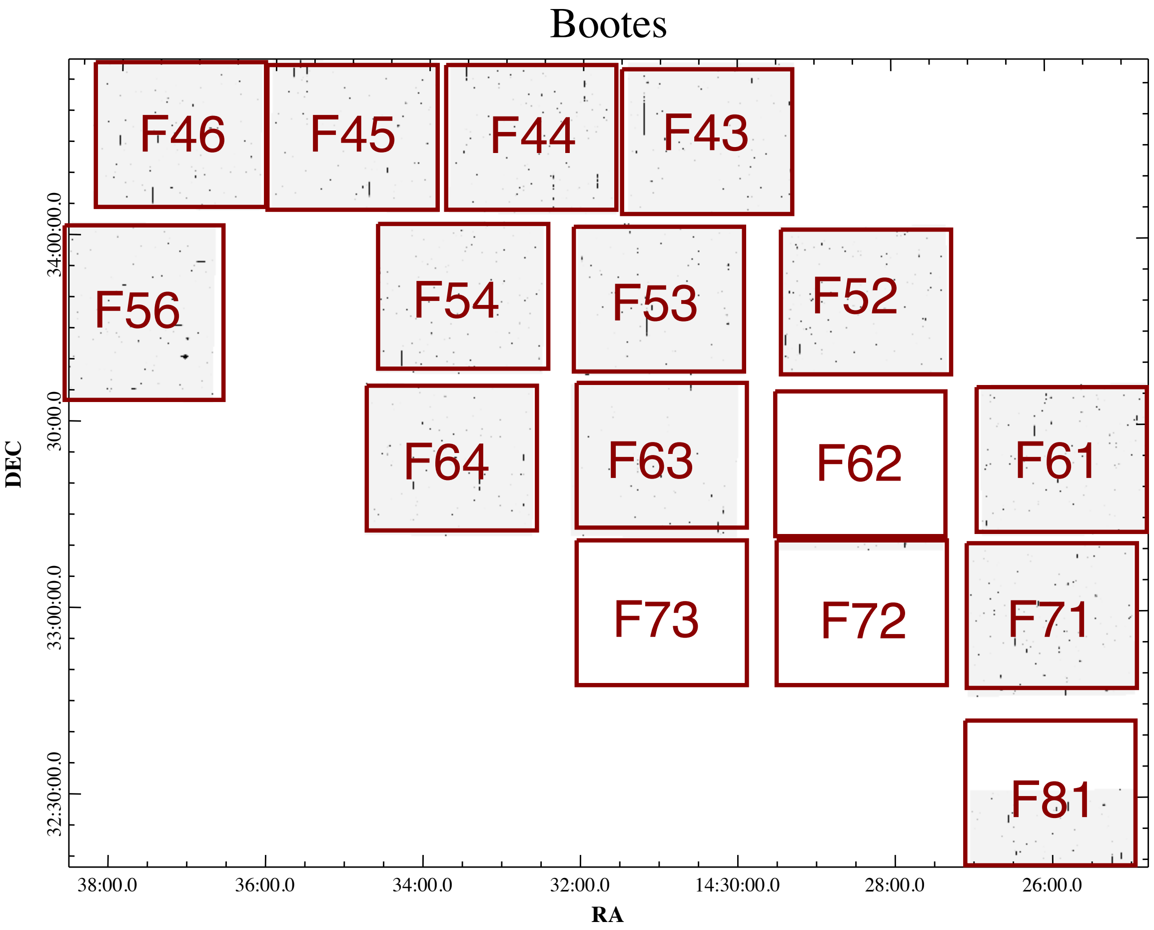

Figure A.28: Relative locations of Boötes fields.

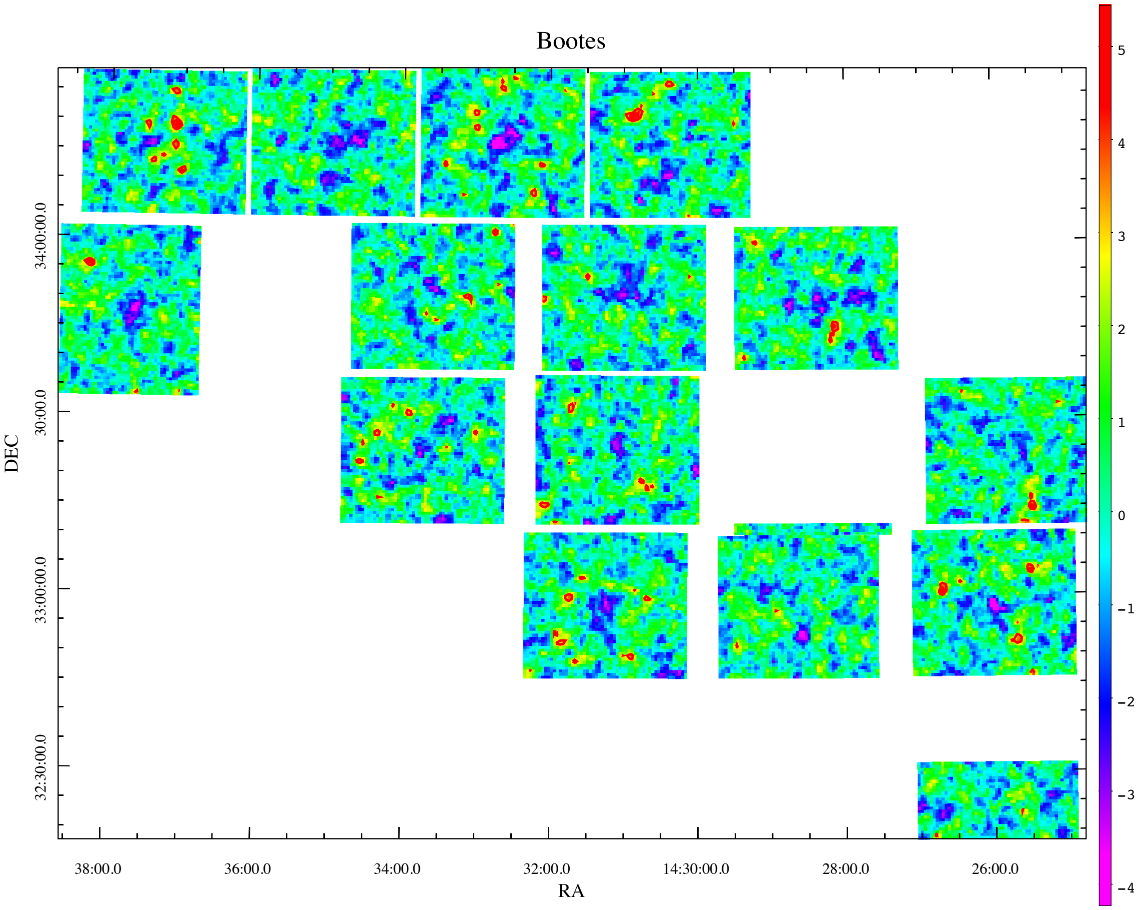

Figure A.29: $R_{\text{in}} = 300$ pix convergence map of the Boötes Void field region. (Contours at 3, 4, and 5 S/N levels to make peaks discernible.)

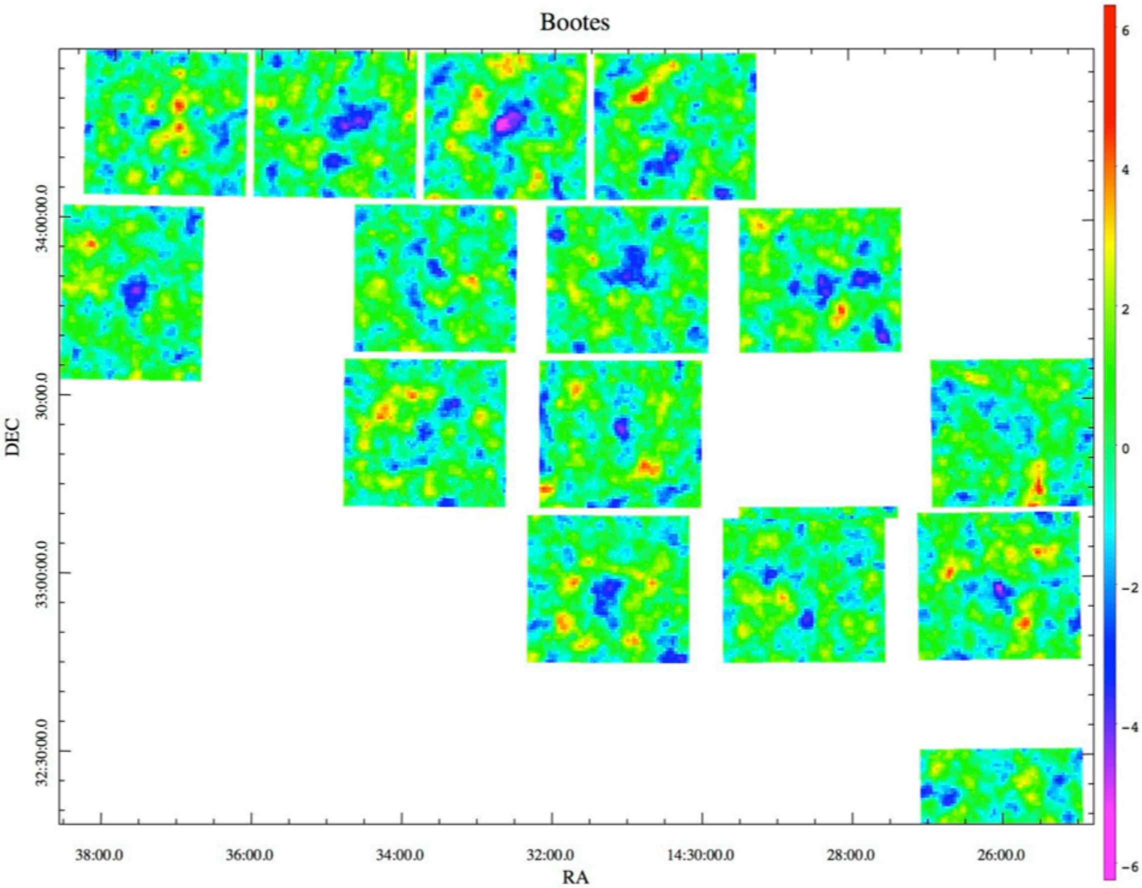

Figure A.30: $R_{\text{in}} = 500$ pix convergence map of the Boötes Void field region.

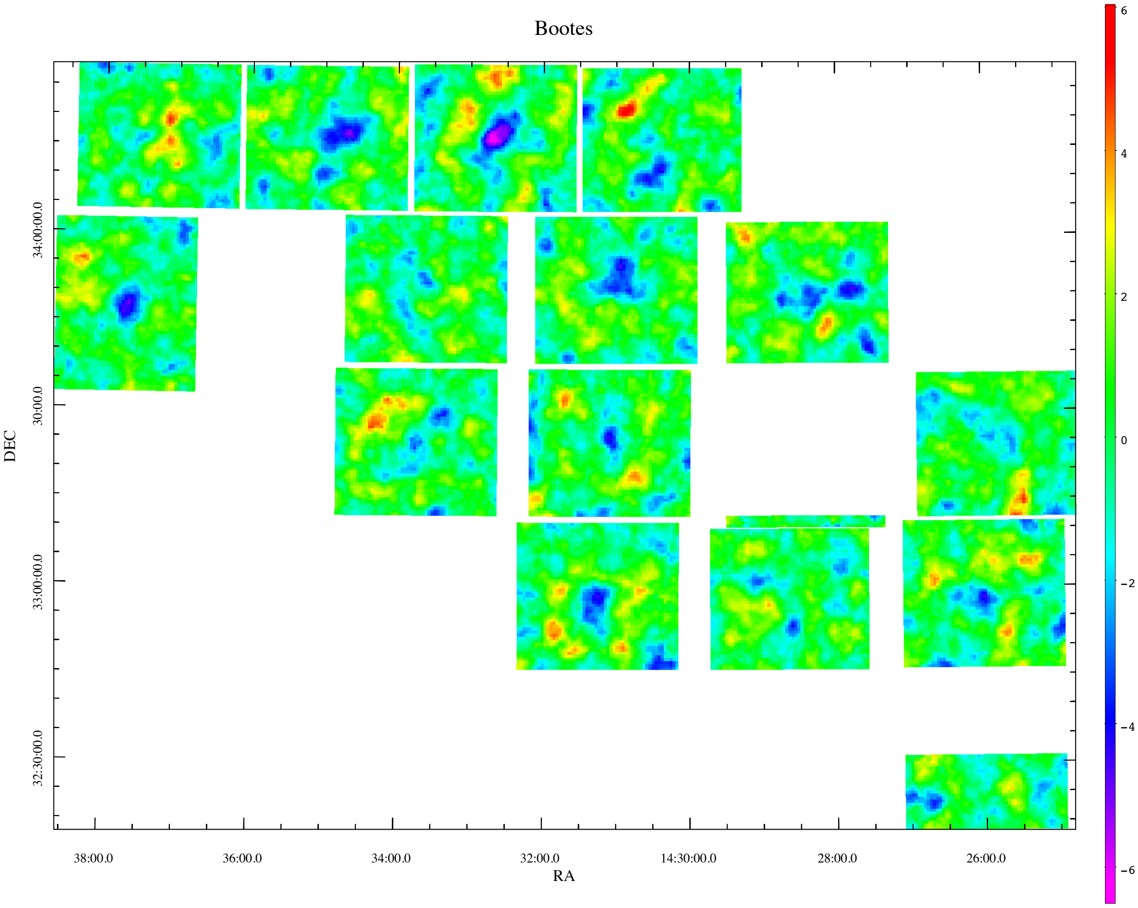

Figure A.31: $R_{\rm in} = 700$ pix convergence map of the Boötes Void field region.

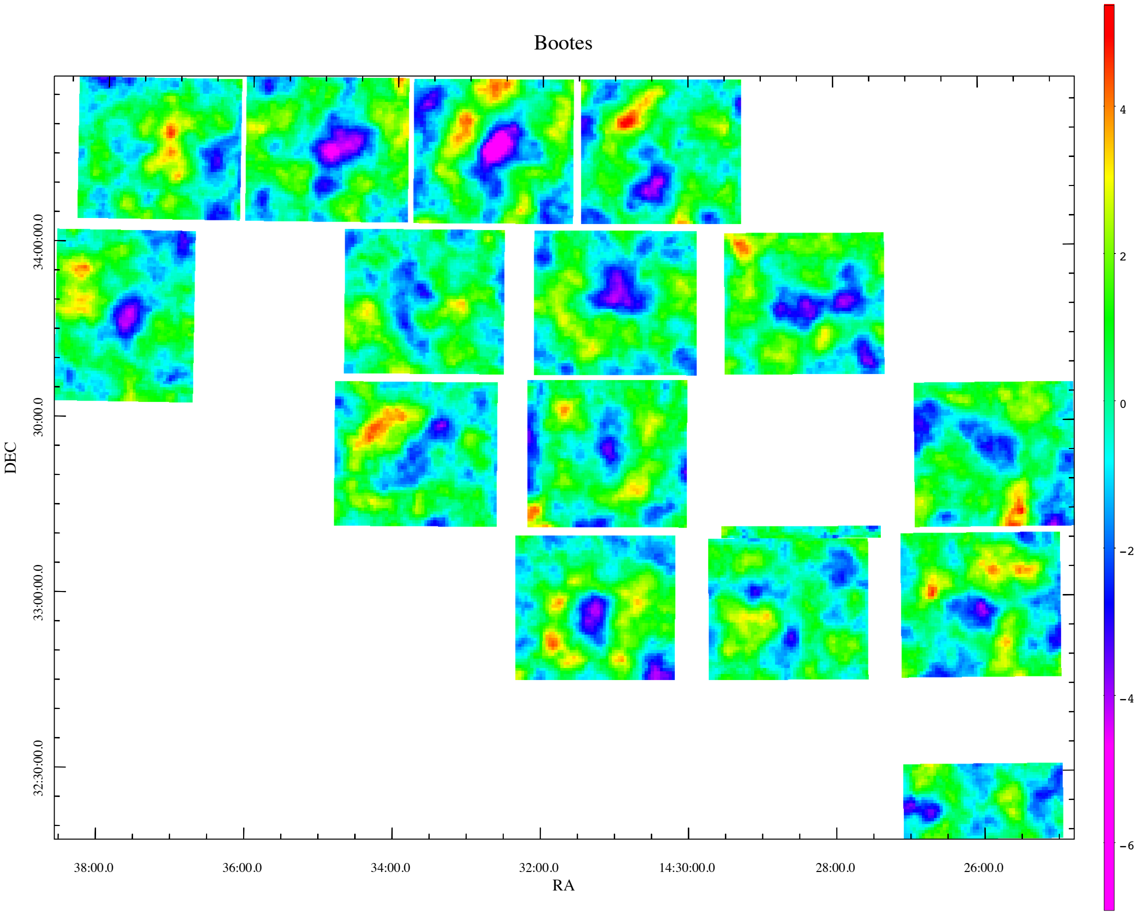

Figure A.32: $R_{\rm in} = 1000$ pix convergence map of the Boötes Void field region.

Appendix B

Additional Targeted Fields

Additional figures relating to the results of Ch. 5.

B.1 PLCK G 018.7+23.6

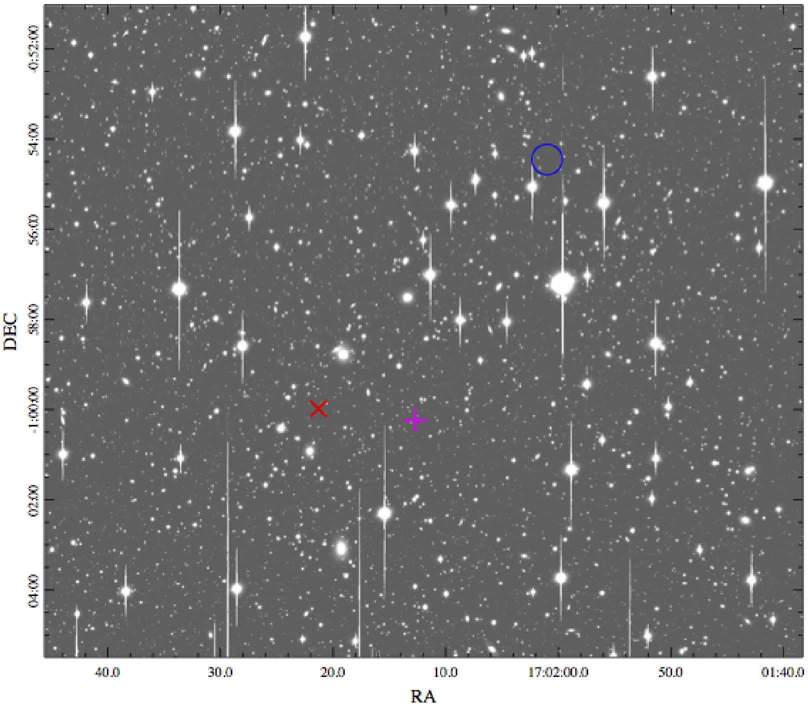

Figure B.1: PLCK 018 region in r'. X-ray, SZ, and our r'-band lensing peak marked with red "x," violet cross, and circle, respectively [89]. Few large ellipticals are visible, counter to expectations for a cluster located at this redshift.

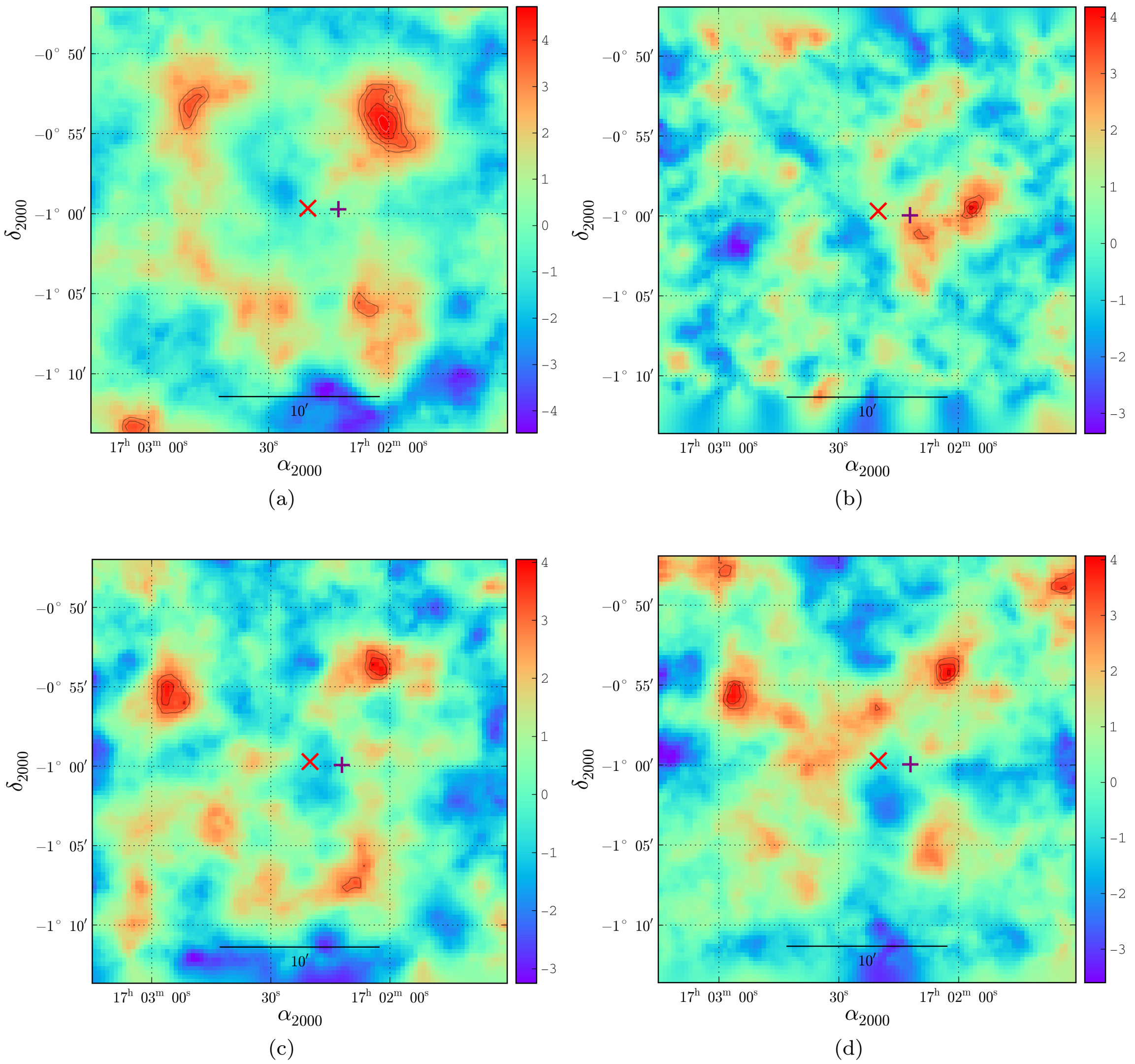

(a) (b)

(c) (d)

Figure B.2: PLCK 018 2D mass reconstruction maps in all filters. X-ray and SZ locations [89] shown in red and violet, respectively. (Contours at 3, 3.5, 4, 4.5 S/N). **(a)** r'-band. Peak 4.72 S/N (B-mode maximum at 3.06). **(b)** g'-band. Peak 4.17 S/N (B-mode maximum at 3.01). **(c)** i'-band. Peak 4.04 S/N (B-mode maximum at 3.51). **(d)** z'-band. Peak 4.06 S/N (B-mode maximum at 2.99).

Bibliography

[1] G. O. Abell, *The Distribution of Rich Clusters of Galaxies.*, ApJS **3** (1958), 211.

[2] D. S. Akerib, H. M. Araújo, X. Bai, A. J. Bailey, J. Balajthy, S. Bedikian, E. Bernard, A. Bernstein, A. Bolozdynya, A. Bradley, D. Byram, S. B. Cahn, M. C. Carmona-Benitez, C. Chan, J. J. Chapman, A. A. Chiller, C. Chiller, K. Clark, T. Coffey, A. Currie, A. Curioni, S. Dazeley, L. de Viveiros, A. Dobi, J. Dobson, E. M. Dragowsky, E. Druszkiewicz, B. Edwards, C. H. Faham, S. Fiorucci, C. Flores, R. J. Gaitskell, V. M. Gehman, C. Ghag, K. R. Gibson, M. G. D. Gilchriese, C. Hall, M. Hanhardt, S. A. Hertel, M. Horn, D. Q. Huang, M. Ihm, R. G. Jacobsen, L. Kastens, K. Kazkaz, R. Knoche, S. Kyre, R. Lander, N. A. Larsen, C. Lee, D. S. Leonard, K. T. Lesko, A. Lindote, M. I. Lopes, A. Lyashenko, D. C. Malling, R. Mannino, D. N. McKinsey, D.-M. Mei, J. Mock, M. Moongweluwan, J. Morad, M. Morii, A. S. J. Murphy, C. Nehrkorn, H. Nelson, F. Neves, J. A. Nikkel, R. A. Ott, M. Pangilinan, P. D. Parker, E. K. Pease, K. Pech, P. Phelps, L. Reichhart, T. Shutt, C. Silva, W. Skulski, C. J. Sofka, V. N. Solovov, P. Sorensen, T. Stiegler, K. O'Sullivan, T. J. Sumner, R. Svoboda, M. Sweany, M. Szydagis, D. Taylor, B. Tennyson, D. R. Tiedt, M. Tripathi, S. Uvarov, J. R. Verbus, N. Walsh, R. Webb, J. T. White, D. White, M. S. Witherell, M. Wlasenko, F. L. H. Wolfs, M. Woods, C. Zhang, and LUX Collaboration, *First Results from the LUX Dark Matter Experiment at the Sanford Underground Research Facility*, Physical Review Letters **112** (2014), no. 9, 091303.

[3] C. Alcock, R. A. Allsman, D. R. Alves, T. S. Axelrod, A. C. Becker, D. P. Bennett, K. H. Cook, N. Dalal, A. J. Drake, K. C. Freeman, M. Geha, K. Griest, M. J. Lehner, S. L. Marshall, D. Minniti, C. A. Nelson, B. A. Peterson, P. Popowski, M. R. Pratt, P. J. Quinn, C. W. Stubbs, W. Sutherland, A. B. Tomaney, T. Vandehei, and D. Welch, *The MACHO Project:*

Microlensing Results from 5.7 Years of Large Magellanic Cloud Observations, ApJ **542** (2000), 281–307.

[4] S. W. Allen, A. C. Edge, A. C. Fabian, H. Bohringer, C. S. Crawford, H. Ebeling, R. M. Johnstone, T. Naylor, and R. A. Schwarz, *Optical spectroscopy of the ROSAT X-ray brightest clusters*, MNRAS **259** (1992), 67–81.

[5] A. Amara, *Cosmic Lensing/Cosmic Shear, PBSworks*, `http://gravitationallensing.pbworks.com/w/page/15553245/Cosmic\%5C\%20Lensing`, Accessed: 2014.

[6] D. E. Applegate, A. von der Linden, P. L. Kelly, M. T. Allen, S. W. Allen, P. R. Burchat, D. L. Burke, H. Ebeling, A. Mantz, and R. G. Morris, *Weighing the Giants - III. Methods and measurements of accurate galaxy cluster weak-lensing masses*, MNRAS **439** (2014), 48–72.

[7] S. Bardeau, G. Soucail, J.-P. Kneib, O. Czoske, H. Ebeling, P. Hudelot, I. Smail, and G. P. Smith, *A CFH12k lensing survey of X-ray luminous galaxy clusters. II. Weak lensing analysis and global correlations*, A&A **470** (2007), 449–466.

[8] G. M. Bernstein and M. Jarvis, *Shapes and Shears, Stars and Smears: Optimal Measurements for Weak Lensing*, AJ **123** (2002), 583–618.

[9] E. Bertin and S. Arnouts, *SExtractor: Software for source extraction.*, A&AS **117** (1996), 393–404.

[10] M. R. Blanton, D. W. Hogg, and SDSS Collaboration, *Low-redshift Evolution of Galaxies in the SDSS*, American Astronomical Society Meeting Abstracts #200, Bulletin of the American Astronomical Society, vol. 34, May 2002, p. 679.

[11] H. Böhringer, W. Voges, J. P. Huchra, B. McLean, R. Giacconi, P. Rosati, R. Burg, J. Mader, P. Schuecker, D. Simiç, S. Komossa, T. H. Reiprich, J. Retzlaff, and J. Trümper, *The Northern ROSAT All-Sky (NORAS) Galaxy Cluster Survey. I. X-Ray Properties of Clusters Detected as Extended X-Ray Sources*, ApJS **129** (2000), 435–474.

[12] E. F. Bunn and M. White, *The 4 Year COBE Normalization and Large-Scale Structure*, ApJ **480** (1997), 6–21.

[13] Canada-France-Hawaii Telescope Legacy Survey, *Deep & Wide Surveys*, `http://www.cfht.hawaii.edu/Science/CFHLS/cfhtlsdeepwidefields.html`, Accessed: 2014.

[14] P. Capak, H. Aussel, M. Ajiki, H. J. McCracken, B. Mobasher, N. Scoville, P. Shopbell, Y. Taniguchi, D. Thompson, S. Tribiano, S. Sasaki, A. W. Blain, M. Brusa, C. Carilli, A. Comastri, C. M. Carollo, P. Cassata, J. Colbert, R. S. Ellis, M. Elvis, M. Giavalisco, W. Green, L. Guzzo, G. Hasinger, O. Ilbert, C. Impey, K. Jahnke, J. Kartaltepe, J.-P. Kneib, J. Koda, A. Koekemoer, Y. Komiyama, A. Leauthaud, O. Le Fevre, S. Lilly, C. Liu, R. Massey, S. Miyazaki, T. Murayama, T. Nagao, J. A. Peacock, A. Pickles, C. Porciani, A. Renzini, J. Rhodes, M. Rich, M. Salvato, D. B. Sanders, C. Scarlata, D. Schiminovich, E. Schinnerer, M. Scodeggio, K. Sheth, Y. Shioya, L. A. M. Tasca, J. E. Taylor, L. Yan, and G. Zamorani, *The First Release COSMOS Optical and Near-IR Data and Catalog*, ApJS **172** (2007), 99–116.

[15] S. M. Carroll, *Spacetime and geometry. An introduction to general relativity*, Addison Wesley, 2004.

[16] D. Clowe, M. Bradač, A. H. Gonzalez, M. Markevitch, S. W. Randall, C. Jones, and D. Zaritsky, *A Direct Empirical Proof of the Existence of Dark Matter*, ApJ **648** (2006), L109–L113.

[17] M. Colless, B. A. Peterson, C. Jackson, J. A. Peacock, S. Cole, P. Norberg, I. K. Baldry, C. M. Baugh, J. Bland-Hawthorn, T. Bridges, R. Cannon, C. Collins, W. Couch, N. Cross, G. Dalton, R. De Propris, S. P. Driver, G. Efstathiou, R. S. Ellis, C. S. Frenk, K. Glazebrook, O. Lahav, I. Lewis, S. Lumsden, S. Maddox, D. Madgwick, W. Sutherland, and K. Taylor, *The 2dF Galaxy Redshift Survey: Final Data Release*, ArXiv Astrophysics e-prints (2003).

[18] E. Contini, G. De Lucia, and S. Borgani, *Statistics of substructures in dark matter haloes*, MNRAS **420** (2012), 2978–2989.

[19] R. I. Cook, *Measuring Weak Lensing Sensitivity and Systematics*, Ph.D. thesis, Brown University, May 2012.

[20] R. I. Cook and I. P. Dell'Antonio, *The Missing Weak Lensing Mass in A781*, ApJ **750** (2012), 153.

[21] R. H. Cyburt, B. D. Fields, K. A. Olive, and E. Skillman, *New BBN limits on physics beyond the standard model from* ^4He, Astroparticle Physics **23** (2005), 313–323.

[22] S. Das, R. de Putter, E. V. Linder, and R. Nakajima, *Weak lensing cosmology beyond* ΛCDM, JCAP **11** (2012), 11.

[23] G. de Vaucouleurs, *Recherches sur les Nebuleuses Extragalactiques*, Annales d'Astrophysique **11** (1948), 247.

[24] E. Del Nobile, G. B. Gelmini, P. Gondolo, and J.-H. Huh, *Update on light WIMP limits: LUX, lite and light*, JCAP **3** (2014), 14.

[25] I. Dell'Antonio, R. Cook, R. Michney, P. Huwe, and V. Dao, *High Source Density Tests of Cluster Evolution via Weak Gravitational Lensing*, November 2011, NSF Proposal.

[26] I. Dell'Antonio, J. McCleary, R. Michney, and P. Huwe, *Measuring the Evolution of mass substructures in clusters: Substructure at z=0.25*, August 2013, NOAO Proposal, p. 399.

[27] S. Dicker, P. Ade, J. Brock, J. Cung, E. Chapin, M. Devlin, M. Giffin, J. Gunderson, M. Halpern, P. Hargrave, D. Hughes, J. Klein, C. MacTavish, G. Marsden, P. Mauskopf, B. Netterfield, L. Olmi, M. Rex, D. Scott, G. Tucker, M. Truch, and M. Viero, *BLAST - A New Balloon-Borne Submillimeter Telescope*, Thirteenth International Symposium on Space Terahertz Technology, March 2002, p. 153.

[28] A. R. Duffy, J. Schaye, S. T. Kay, and C. Dalla Vecchia, *Dark matter halo concentrations in the Wilkinson Microwave Anisotropy Probe year 5 cosmology*, MNRAS **390** (2008), L64–L68.

[29] F. Durret, C. Adami, A. Cappi, S. Maurogordato, I. Márquez, O. Ilbert, J. Coupon, S. Arnouts, C. Benoist, J. Blaizot, T. M. Edorh, B. Garilli, L. Guennou, V. Le Brun, O. Le Fèvre, A. Mazure, H. J. McCracken, Y. Mellier, C. Mezrag, E. Slezak, L. Tresse, and M. P. Ulmer, *Galaxy cluster searches based on photometric redshifts in the four CFHTLS Wide fields*, A&A **535** (2011), A65.

[30] A. S. Eddington, *The Deflection of Light during a Solar Eclipse*, Nature **104** (1919), 372.

[31] ———, *The total eclipse of 1919 May 29 and the influence of gravitation on light*, The Observatory **42** (1919), 119–122.

[32] P. R. Eisenhardt, D. Stern, M. Brodwin, G. G. Fazio, G. H. Rieke, M. J. Rieke, M. W. Werner, E. L. Wright, L. E. Allen, R. G. Arendt, M. L. N. Ashby, P. Barmby, W. J. Forrest, J. L. Hora, J.-S. Huang, J. Huchra, M. A. Pahre, J. L. Pipher, W. T. Reach, H. A. Smith, J. R. Stauffer, Z. Wang, S. P. Willner, M. J. I. Brown, A. Dey, B. T. Jannuzi, and G. P. Tiede, *The Infrared Array Camera (IRAC) Shallow Survey*, ApJS **154** (2004), 48–53.

[33] I. N. Evans, F. A. Primini, K. J. Glotfelty, C. S. Anderson, N. R. Bonaventura, J. C. Chen, J. E. Davis, S. M. Doe, J. D. Evans, G. Fabbiano, E. C. Galle, D. G. Gibbs, II, J. D. Grier, R. M. Hain, D. M. Hall, P. N. Harbo, X. (Helen He, J. C. Houck, M. Karovska, V. L. Kashyap, J. Lauer, M. L. McCollough, J. C. McDowell, J. B. Miller, A. W. Mitschang, D. L. Morgan, A. E. Mossman, J. S. Nichols, M. A. Nowak, D. A. Plummer, B. L. Refsdal, A. H. Rots, A. Siemiginowska, B. A. Sundheim, M. S. Tibbetts, D. W. Van Stone, S. L. Winkelman, and P. Zografou, *The Chandra Source Catalog*, ApJS **189** (2010), 37–82.

[34] T. S. Fetisova, D. Y. Kuznetsov, V. A. Lipovetskij, A. A. Starobinskij, and R. P. Olowin, *Characteristics of the spatial distribution of rich clusters of galaxies in the northern and southern galactic hemispheres*, Astronomy Letters **19** (1993), 198–202.

[35] P. Fischer and J. A. Tyson, *The Mass Distribution of the Most Luminous X-Ray Cluster RXJ 1347.5-1145 From Gravitational Lensing*, AJ **114** (1997), 14–24.

[36] D. J. Fixsen, *The Temperature of the Cosmic Microwave Background*, ApJ **707** (2009), 916–920.

[37] J. Frieman and Dark Energy Survey Collaboration, *The Dark Energy Survey: Overview*, American Astronomical Society Meeting Abstracts #221, American Astronomical Society Meeting Abstracts, vol. 221, January 2013, p. 335.

[38] H. Furusawa, Y. Okura, S. Mineo, T. Takata, F. Nakata, M. Tanaka, N. Katayama, R. Itoh, N. Yasuda, S. Miyazaki, Y. Komiyama, Y. Utsumi, T. Uchida, and H. Aihara, *First On-Site Data Analysis System for Subaru/Suprime-Cam*, PASJ **63** (2011), 585–.

[39] R. R. Gal, R. R. de Carvalho, P. A. A. Lopes, S. G. Djorgovski, R. J. Brunner, A. Mahabal, and S. C. Odewahn, *The Northern Sky Optical Cluster Survey. II. An Objective Cluster Catalog for 5800 Square Degrees*, AJ **125** (2003), 2064–2084.

[40] R. R. Gal, R. R. de Carvalho, S. C. Odewahn, S. G. Djorgovski, and V. E. Margoniner, *The Northern Sky Optical Cluster Survey. I. Detection of Galaxy Clusters in DPOSS*, AJ **119** (2000), 12–20.

[41] M. J. Geller, M. J. Kurtz, I. P. Dell'Antonio, M. Ramella, and D. G. Fabricant, *SHELS: Testing Weak-Lensing Maps with Redshift Surveys*, ApJ **709** (2010), 832–850.

[42] T. Hamana, M. Takada, and N. Yoshida, *Searching for massive clusters in weak lensing surveys*, MNRAS **350** (2004), 893–913.

[43] J. Hao, T. A. McKay, B. P. Koester, E. S. Rykoff, E. Rozo, J. Annis, R. H. Wechsler, A. Evrard, S. R. Siegel, M. Becker, M. Busha, D. Gerdes, D. E. Johnston, and E. Sheldon, *A GMBCG Galaxy Cluster Catalog of 55,424 Rich Clusters from SDSS DR7*, ApJS **191** (2010), 254–274.

[44] C. Heymans, L. Van Waerbeke, L. Miller, T. Erben, H. Hildebrandt, H. Hoekstra, T. D. Kitching, Y. Mellier, P. Simon, C. Bonnett, J. Coupon, L. Fu, J. Harnois Déraps, M. J. Hudson, M. Kilbinger, K. Kuijken, B. Rowe, T. Schrabback, E. Semboloni, E. van Uitert, S. Vafaei, and M. Velander, *CFHTLenS: the Canada-France-Hawaii Telescope Lensing Survey*, MNRAS **427** (2012), 146–166.

[45] H. Hoekstra, Y. Mellier, L. van Waerbeke, E. Semboloni, L. Fu, M. J. Hudson, L. C. Parker, I. Tereno, and K. Benabed, *First Cosmic Shear Results from the Canada-France-Hawaii Telescope Wide Synoptic Legacy Survey*, ApJ **647** (2006), 116–127.

[46] Z. Huang, M. Radovich, A. Grado, E. Puddu, A. Romano, L. Limatola, and L. Fu, *A weak-lensing analysis of the Abell 383 cluster*, A&A **529** (2011), A93.

[47] P. M. Huwe, *Dark Matter Substructure in High Redshift Clusters of Galaxies*, Ph.D. thesis, Brown University, May 2013.

[48] S.-I. Ichikawa, *Data archive systems: MOKA and SMOKA*, Astronomical Herald **95** (2002), 266–271.

[49] R. Ikerd and Wahi Pana Photography, *Subaru Telescope Dome at Sunset*, `www.wahipanaphoto.com`, 2010, Accessed: 2014.

[50] B. T. Jannuzi, A. Dey, and NDWFS Team, *The NOAO Deep Wide-Field Survey*, American Astronomical Society Meeting Abstracts #194, Bulletin of the American Astronomical Society, vol. 31, May 1999, p. 979.

[51] P. Jetzer, D. Puy, M. Signore, and C. Tortora, *Limits on decaying dark energy density models from the CMB temperature-redshift relation*, General Relativity and Gravitation **43** (2011), 1083–1093.

[52] N. Kaiser and G. Squires, *Mapping the dark matter with weak gravitational lensing*, ApJ **404** (1993), 441–450.

[53] P. L. Kelly, A. von der Linden, D. E. Applegate, M. T. Allen, S. W. Allen, P. R. Burchat, D. L. Burke, H. Ebeling, P. Capak, O. Czoske, D. Donovan, A. Mantz, and R. G. Morris, *Weighing the Giants - II. Improved calibration of photometry from stellar colours and accurate photometric redshifts*, MNRAS **439** (2014), 28–47.

[54] R. P. Kirshner, A. Oemler, Jr., P. L. Schechter, and S. A. Shectman, *A million cubic megaparsec void in Bootes*, ApJ **248** (1981), L57–L60.

[55] B. P. Koester, T. A. McKay, J. Annis, R. H. Wechsler, A. Evrard, L. Bleem, M. Becker, D. Johnston, E. Sheldon, R. Nichol, C. Miller, R. Scranton, N. Bahcall, J. Barentine, H. Brewington, J. Brinkmann, M. Harvanek, S. Kleinman, J. Krzesinski, D. Long, A. Nitta, D. P. Schneider, S. Sneddin, W. Voges, and D. York, *A MaxBCG Catalog of 13,823 Galaxy Clusters from the Sloan Digital Sky Survey*, ApJ **660** (2007), 239–255.

[56] J. M. Kubo, H. Khiabanian, I. P. Dell'Antonio, D. Wittman, and J. A. Tyson, *Dark Matter Structures in the Deep Lens Survey*, ApJ **702** (2009), 980–988.

[57] J. M. Kubo, A. Stebbins, J. Annis, I. P. Dell'Antonio, H. Lin, H. Khiabanian, and J. A. Frieman, *The Mass of the Coma Cluster from Weak Lensing in the Sloan Digital Sky Survey*, ApJ **671** (2007), 1466–1470.

[58] M. J. Kurtz, M. J. Geller, Y. Utsumi, S. Miyazaki, I. P. Dell'Antonio, and D. G. Fabricant, *Testing Weak-lensing Maps with Redshift Surveys: A Subaru Field*, ApJ **750** (2012), 168.

[59] F. J. Lockman, K. Jahoda, and D. McCammon, *The structure of galactic HI in directions of low total column density*, ApJ **302** (1986), 432–449.

[60] C. Lonsdale, T. Conrow, F. Fang, A. Franceschini, N. Gautier, M. Griffin, F. Masci, G. Morrison, J. O'Linger, S. Oliver, D. Padgett, I. Perez-Fournon, M. Pierre, R. Puetter, M. Rowan-Robinson, D. Shupe, H. Smith, G. Stacey, J. Surace, and C. Xu, *The SIRTF Wide-area InfraRed Extragalactic Survey*, Spitzer Proposal, September 2004, p. 142.

[61] C. J. Lonsdale, H. E. Smith, M. Rowan-Robinson, J. Surace, D. Shupe, C. Xu, S. Oliver, D. Padgett, F. Fang, T. Conrow, A. Franceschini, N. Gautier, M. Griffin, P. Hacking, F. Masci,

G. Morrison, J. O'Linger, F. Owen, I. Pérez-Fournon, M. Pierre, R. Puetter, G. Stacey, S. Castro, M. d. C. Polletta, D. Farrah, T. Jarrett, D. Frayer, B. Siana, T. Babbedge, S. Dye, M. Fox, E. Gonzalez-Solares, M. Salaman, S. Berta, J. J. Condon, H. Dole, and S. Serjeant, *SWIRE: The SIRTF Wide-Area Infrared Extragalactic Survey*, PASP **115** (2003), 897–927.

[62] P. A. A. Lopes, R. R. de Carvalho, R. R. Gal, S. G. Djorgovski, S. C. Odewahn, A. A. Mahabal, and R. J. Brunner, *The Northern Sky Optical Cluster Survey. IV. An Intermediate-Redshift Galaxy Cluster Catalog and the Comparison of Two Detection Algorithms*, AJ **128** (2004), 1017–1045.

[63] LSST Dark Energy Science Collaboration, *Large Synoptic Survey Telescope: Dark Energy Science Collaboration*, ArXiv e-prints (2012).

[64] V. Luković, P. Cabella, and N. Vittorio, *Dark matter in cosmology*, International Journal of Modern Physics A **29** (2014), 43001.

[65] G. Mangano and P. D. Serpico, *A robust upper limit on N from BBN, circa 2011*, Physics Letters B **701** (2011), 296–299.

[66] A. B. Mantz, A. von der Linden, S. W. Allen, D. E. Applegate, P. L. Kelly, R. G. Morris, D. A. Rapetti, R. W. Schmidt, S. Adhikari, M. T. Allen, P. R. Burchat, D. L. Burke, M. Cataneo, D. Donovon, H. Ebeling, S. Shandera, and A. Wright, *Weighing the Giants IV: Cosmology and Neutrino Mass*, ArXiv e-prints (2014).

[67] J. C. Mather, E. S. Cheng, D. A. Cottingham, R. E. Eplee, Jr., D. J. Fixsen, T. Hewagama, R. B. Isaacman, K. A. Jensen, S. S. Meyer, P. D. Noerdlinger, S. M. Read, L. P. Rosen, R. A. Shafer, E. L. Wright, C. L. Bennett, N. W. Boggess, M. G. Hauser, T. Kelsall, S. H. Moseley, Jr., R. F. Silverberg, G. F. Smoot, R. Weiss, and D. T. Wilkinson, *Measurement of the cosmic microwave background spectrum by the COBE FIRAS instrument*, ApJ **420** (1994), 439–444.

[68] M. Maturi, M. Meneghetti, M. Bartelmann, K. Dolag, and L. Moscardini, *An optimal filter for the detection of galaxy clusters through weak lensing*, A&A **442** (2005), 851–860.

[69] J.-C. Mauduit, M. Lacy, D. Farrah, J. A. Surace, M. Jarvis, S. Oliver, C. Maraston, M. Vaccari, L. Marchetti, G. Zeimann, E. A. Gonzáles-Solares, J. Pforr, A. O. Petric, B. Henriques, P. A. Thomas, J. Afonso, A. Rettura, G. Wilson, J. T. Falder, J. E. Geach, M. Huynh, R. P.

Norris, N. Seymour, G. T. Richards, S. A. Stanford, D. M. Alexander, R. H. Becker, P. N. Best, L. Bizzocchi, D. Bonfield, N. Castro, A. Cava, S. Chapman, N. Christopher, D. L. Clements, G. Covone, N. Dubois, J. S. Dunlop, E. Dyke, A. Edge, H. C. Ferguson, S. Foucaud, A. Franceschini, R. R. Gal, J. K. Grant, M. Grossi, E. Hatziminaoglou, S. Hickey, J. A. Hodge, J.-S. Huang, R. J. Ivison, M. Kim, O. LeFevre, M. Lehnert, C. J. Lonsdale, L. M. Lubin, R. J. McLure, H. Messias, A. Martínez-Sansigre, A. M. J. Mortier, D. M. Nielsen, M. Ouchi, G. Parish, I. Perez-Fournon, M. Pierre, S. Rawlings, A. Readhead, S. E. Ridgway, D. Rigopoulou, A. K. Romer, I. G. Rosebloom, H. J. A. Rottgering, M. Rowan-Robinson, A. Sajina, C. J. Simpson, I. Smail, G. K. Squires, J. A. Stevens, R. Taylor, M. Trichas, T. Urrutia, E. van Kampen, A. Verma, and C. K. Xu, *The Spitzer Extragalactic Representative Volume Survey (SERVS): Survey Definition and Goals*, PASP **124** (2012), 714–736.

[70] J. McCleary, I. dell'Antonio, and P. Huwe, *Mass Substructure in Abell 3128*, ArXiv e-prints (2015).

[71] Y. Mellier, *Probing the Universe with Weak Lensing*, ARA&A **37** (1999), 127–189.

[72] R. J. Michney, *Anisotropy in the Cosmic Neutrino Background*, Dartmouth College Undergraduate Honors Thesis, June 2006.

[73] R. J. Michney and R. R. Caldwell, *Anisotropy of the cosmic neutrino background*, JCAP **1** (2007), 14.

[74] S. Miyazaki, T. Hamana, R. S. Ellis, N. Kashikawa, R. J. Massey, J. Taylor, and A. Refregier, *A Subaru Weak-Lensing Survey. I. Cluster Candidates and Spectroscopic Verification*, ApJ **669** (2007), 714–728.

[75] S. Miyazaki, Y. Komiyama, M. Sekiguchi, S. Okamura, M. Doi, H. Furusawa, M. Hamabe, K. Imi, M. Kimura, F. Nakata, N. Okada, M. Ouchi, K. Shimasaku, M. Yagi, and N. Yasuda, *Subaru Prime Focus Camera – Suprime-Cam*, PASJ **54** (2002), 833–853.

[76] ———, *Subaru Prime Focus Camera – Suprime-Cam*, PASJ **54** (2002), 833–853.

[77] D. G. Monet, S. E. Levine, B. Canzian, H. D. Ables, A. R. Bird, C. C. Dahn, H. H. Guetter, H. C. Harris, A. A. Henden, S. K. Leggett, H. F. Levison, C. B. Luginbuhl, J. Martini, A. K. B. Monet, J. A. Munn, J. R. Pier, A. R. Rhodes, B. Riepe, S. Sell, R. C. Stone, F. J. Vrba, R. L.

Walker, G. Westerhout, R. J. Brucato, I. N. Reid, W. Schoening, M. Hartley, M. A. Read, and S. B. Tritton, *The USNO-B Catalog*, AJ **125** (2003), 984–993.

[78] M. J. Mortonson, D. H. Weinberg, and M. White, *Dark Energy: A Short Review*, ArXiv e-prints (2014).

[79] S. S. Murray, A. Kenter, W. R. Forman, C. Jones, P. J. Green, C. S. Kochanek, A. Vikhlinin, D. Fabricant, G. Fazio, K. Brand, M. J. I. Brown, A. Dey, B. T. Jannuzi, J. Najita, B. McNamara, J. Shields, and M. Rieke, *XBootes: An X-Ray Survey of the NDWFS Bootes Field. I. Overview and Initial Results*, ApJS **161** (2005), 1–8.

[80] F. Nakata, R. S. Furuya, and Subaru Telescope Support Staff, *Subaru Data Reduction Cookbook: Optical Imaging with Suprime-Cam (SDFRED2)*, 2012.

[81] J. F. Navarro, C. S. Frenk, and S. D. M. White, *A Universal Density Profile from Hierarchical Clustering*, ApJ **490** (1997), 493–508.

[82] S. Noda, J. Furusawa, R. Furusho, Y. Yamada, H. Furusawa, T. Ozawa, T. Takata, and S.-I. Ichikawa, *PSF analysis of 7 years Subaru/Suprime-Cam data.*, Publications of the National Astronomical Observatory of Japan **13** (2010), 71–81.

[83] K.A. Olive et al., *Review of Particle Physics*, Chin.Phys. **C38** (2014), 090001.

[84] M. Ouchi, K. Shimasaku, S. Okamura, H. Furusawa, N. Kashikawa, K. Ota, M. Doi, M. Hamabe, M. Kimura, Y. Komiyama, M. Miyazaki, S. Miyazaki, F. Nakata, M. Sekiguchi, M. Yagi, and N. Yasuda, *Subaru Deep Survey. V. A Census of Lyman Break Galaxies at z=4 and 5 in the Subaru Deep Fields: Photometric Properties*, ApJ **611** (2004), 660–684.

[85] P. Patel, S. Maddox, F. R. Pearce, A. Aragón-Salamanca, and E. Conway, *An imaging survey of a uniform sample of brightest cluster galaxies and intracluster light*, MNRAS **370** (2006), 851–883.

[86] R. Piffaretti, M. Arnaud, G. W. Pratt, E. Pointecouteau, and J.-B. Melin, *The MCXC: a meta-catalogue of x-ray detected clusters of galaxies*, A&A **534** (2011), A109.

[87] Planck Collaboration, P. A. R. Ade, N. Aghanim, C. Armitage-Caplan, M. Arnaud, M. Ashdown, F. Atrio-Barandela, J. Aumont, C. Baccigalupi, A. J. Banday, and et al., *Planck 2013 results. XVI. Cosmological parameters*, ArXiv e-prints (2013).

[88] Planck Collaboration, N. Aghanim, M. Arnaud, M. Ashdown, F. Atrio-Barandela, J. Aumont, C. Baccigalupi, A. Balbi, A. J. Banday, R. B. Barreiro, J. G. Bartlett, E. Battaner, K. Benabed, J.-P. Bernard, M. Bersanelli, H. Böhringer, A. Bonaldi, J. R. Bond, J. Borrill, F. R. Bouchet, H. Bourdin, M. L. Brown, C. Burigana, R. C. Butler, P. Cabella, J.-F. Cardoso, P. Carvalho, A. Catalano, L. Cayón, A. Chamballu, R.-R. Chary, L.-Y. Chiang, G. Chon, P. R. Christensen, D. L. Clements, S. Colafrancesco, S. Colombi, A. Coulais, B. P. Crill, F. Cuttaia, A. Da Silva, H. Dahle, R. J. Davis, P. de Bernardis, G. de Gasperis, G. de Zotti, J. Delabrouille, J. Démoclès, F.-X. Désert, J. M. Diego, K. Dolag, H. Dole, S. Donzelli, O. Doré, M. Douspis, X. Dupac, T. A. Enßlin, H. K. Eriksen, F. Finelli, I. Flores-Cacho, O. Forni, P. Fosalba, M. Frailis, S. Fromenteau, S. Galeotta, K. Ganga, R. T. Génova-Santos, M. Giard, J. González-Nuevo, R. González-Riestra, K. M. Górski, A. Gregorio, A. Gruppuso, F. K. Hansen, D. Harrison, A. Hempel, C. Hernández-Monteagudo, D. Herranz, S. R. Hildebrandt, A. Hornstrup, K. M. Huffenberger, G. Hurier, T. Jagemann, J. Jasche, M. Juvela, E. Keihänen, R. Keskitalo, T. S. Kisner, R. Kneissl, J. Knoche, L. Knox, H. Kurki-Suonio, G. Lagache, A. Lähteenmäki, J.-M. Lamarre, A. Lasenby, C. R. Lawrence, S. Leach, R. Leonardi, A. Liddle, P. B. Lilje, M. López-Caniego, G. Luzzi, J. F. Macías-Pérez, D. Maino, N. Mandolesi, R. Mann, F. Marleau, D. J. Marshall, E. Martínez-González, S. Masi, M. Massardi, S. Matarrese, F. Matthai, P. Mazzotta, P. R. Meinhold, A. Melchiorri, J.-B. Melin, L. Mendes, A. Mennella, M.-A. Miville-Deschênes, A. Moneti, L. Montier, G. Morgante, D. Mortlock, D. Munshi, P. Naselsky, P. Natoli, H. U. Nørgaard-Nielsen, F. Noviello, S. Osborne, F. Pasian, G. Patanchon, O. Perdereau, F. Perrotta, F. Piacentini, E. Pierpaoli, S. Plaszczynski, P. Platania, E. Pointecouteau, G. Polenta, N. Ponthieu, L. Popa, T. Poutanen, G. W. Pratt, J.-L. Puget, J. P. Rachen, R. Rebolo, M. Reinecke, M. Remazeilles, C. Renault, S. Ricciardi, T. Riller, I. Ristorcelli, G. Rocha, C. Rosset, M. Rossetti, J. A. Rubiño-Martín, B. Rusholme, M. Sandri, G. Savini, B. M. Schaefer, D. Scott, G. F. Smoot, J.-L. Starck, F. Stivoli, R. Sunyaev, D. Sutton, J.-F. Sygnet, J. A. Tauber, L. Terenzi, L. Toffolatti, M. Tomasi, M. Tristram, L. Valenziano, B. Van Tent, P. Vielva, F. Villa, N. Vittorio, B. D. Wandelt, J. Weller, S. D. M. White, D. Yvon, A. Zacchei, and A. Zonca, *Planck intermediate results. I. Further validation of new Planck clusters with XMM-Newton*, A&A **543** (2012), A102.

[89] Planck Collaboration, N. Aghanim, M. Arnaud, M. Ashdown, J. Aumont, C. Baccigalupi,

A. Balbi, A. J. Banday, R. B. Barreiro, M. Bartelmann, and et al., *Planck early results. IX. XMM-Newton follow-up for validation of Planck cluster candidates*, A&A **536** (2011), A9.

[90] R. V. Pound and G. A. Rebka, *Gravitational red-shift in nuclear resonance*, Phys. Rev. Lett. **3** (1959), 439–441.

[91] R. Powell, *The Boötes Void*, `http://www.atlasoftheuniverse.com/superc/boo.html`, Accessed: 2014.

[92] William H. Press, Saul A. Teukolsky, William T. Vetterling, and Brian P. Flannery, *Numerical recipes 3rd edition: The art of scientific computing*, 3 ed., Cambridge University Press, New York, NY, USA, 2007.

[93] M. Richmond, *Properties of Stars in the Subaru Deep Field*, PASJ **57** (2005), 969–976.

[94] E. S. Rykoff, B. P. Koester, E. Rozo, J. Annis, A. E. Evrard, S. M. Hansen, J. Hao, D. E. Johnston, T. A. McKay, and R. H. Wechsler, *Robust Optical Richness Estimation with Reduced Scatter*, ApJ **746** (2012), 178.

[95] D. J. Sand, T. Treu, G. P. Smith, and R. S. Ellis, *The Dark Matter Distribution in the Central Regions of Galaxy Clusters: Implications for Cold Dark Matter*, ApJ **604** (2004), 88–107.

[96] S. Schlamminger, K.-Y. Choi, T. A. Wagner, J. H. Gundlach, and E. G. Adelberger, *Test of the Equivalence Principle Using a Rotating Torsion Balance*, Physical Review Letters **100** (2008), no. 4, 041101.

[97] D. Schlegel, D. Finkbeiner, and M. Davis, *Application of SFD Dust Maps to Galaxy Counts and CMB Experiments*, Wide Field Surveys in Cosmology (S. Colombi, Y. Mellier, and B. Raban, eds.), 1998, p. 297.

[98] R. W. Schmidt and S. W. Allen, *The dark matter haloes of massive, relaxed galaxy clusters observed with Chandra*, MNRAS **379** (2007), 209–221.

[99] A. Schwope, G. Hasinger, I. Lehmann, R. Schwarz, H. Brunner, S. Neizvestny, A. Ugryumov, Y. Balega, J. Trümper, and W. Voges, *The ROSAT Bright Survey: II. Catalogue of all high-galactic latitude RASS sources with PSPC countrate...*, Astronomische Nachrichten **321** (2000), 1–52.

[100] Science Software Branch at STScI, *PyRAF: Python alternative for IRAF*, July 2012, Astrophysics Source Code Library.

[101] N. Sehgal, J. P. Hughes, D. Wittman, V. Margoniner, J. A. Tyson, P. Gee, and I. dell'Antonio, *Probing the Relation Between X-Ray-Derived and Weak-Lensing-Derived Masses for Shear-Selected Galaxy Clusters. I. A781*, ApJ **673** (2008), 163–175.

[102] H. Shan, J.-P. Kneib, C. Tao, Z. Fan, M. Jauzac, M. Limousin, R. Massey, J. Rhodes, K. Thanjavur, and H. J. McCracken, *Weak Lensing Measurement of Galaxy Clusters in the CFHTLS-Wide Survey*, ApJ **748** (2012), 56.

[103] T. R. Slatyer, N. Padmanabhan, and D. P. Finkbeiner, *CMB constraints on WIMP annihilation: Energy absorption during the recombination epoch*, Phys. Rev. D **80** (2009), no. 4, 043526.

[104] D. R. Smith, G. M. Bernstein, P. Fischer, and M. Jarvis, *Weak-Lensing Determination of the Mass in Galaxy Halos*, ApJ **551** (2001), 643–650.

[105] D. N. Spergel, R. Bean, O. Doré, M. R. Nolta, C. L. Bennett, J. Dunkley, G. Hinshaw, N. Jarosik, E. Komatsu, L. Page, H. V. Peiris, L. Verde, M. Halpern, R. S. Hill, A. Kogut, M. Limon, S. S. Meyer, N. Odegard, G. S. Tucker, J. L. Weiland, E. Wollack, and E. L. Wright, *Three-Year Wilkinson Microwave Anisotropy Probe (WMAP) Observations: Implications for Cosmology*, ApJS **170** (2007), 377–408.

[106] V. Springel, C. S. Frenk, and S. D. M. White, *The large-scale structure of the Universe*, Nature **440** (2006), 1137–1144.

[107] V. Springel, S. D. M. White, A. Jenkins, C. S. Frenk, N. Yoshida, L. Gao, J. Navarro, R. Thacker, D. Croton, J. Helly, J. A. Peacock, S. Cole, P. Thomas, H. Couchman, A. Evrard, J. Colberg, and F. Pearce, *Simulations of the formation, evolution and clustering of galaxies and quasars*, Nature **435** (2005), 629–636.

[108] D. Stern, A. Amblard, M. Ashby, J. Bock, C. Borys, K. Brand, M. Brodwin, M. J. I. Brown, R. Cool, A. Cooray, S. Croft, A. Dey, P. Eisenhardt, D. Eisenstein, A. Gonzalez, V. Gorjian, N. Grogin, R. Ivison, J. Jacob, B. Jannuzi, C. Kochanek, A. Mainzer, L. Moustakas, H. Roettgering, H. A. Smith, A. Stanford, I. S. Sullivan, S. Willner, E. L. (. Wright, and

W. van Breugel, *SDWFS: The Spitzer Deep, Wide-Field Survey*, Spitzer Proposal, May 2007, p. 40839.

[109] M. F. Struble and H. J. Rood, *A Compilation of Redshifts and Velocity Dispersions for ACO Clusters*, ApJS **125** (1999), 35–71.

[110] Subaru Telescope NAOJ, *SMOKA: The Data Archive of NAOJ Telescopes*, `http://www.naoj.org/Topics/2005/05/11/index.html`, Accessed: 2014.

[111] ———, *Subaru Telescope Distribution of Seeing, 2000-2008*, `http://www.naoj.org/Observing/Telescope/ImageQuality/Seeing/`, Accessed: 2014.

[112] ———, *Subaru Telescope Observing Schedule*, `http://www.naoj.org/cgi-bin/opecenter/schedule.cgi`, See "List of Accepted Proposals." Accessed: 2014.

[113] ———, *Suprime-Cam General Filters*, `http://www.naoj.org/Observing/Instruments/SCam/sensitivity.html`, Accessed: 2014.

[114] T Subaru Telescope NAOJ, Armandroff, *Keck/Subaru Exchange Program, 2011*, `http://subarutelescope.org/Science/SubaruUM/SubaruUM2010/files/Armandorff_Subaru_Keck_Jan_2011v2.pdf`, Accessed: 2014.

[115] The Super-Kamiokande Collaboration, :, K. Abe, Y. Hayato, K. Iyogi, J. Kameda, M. Miura, S. Moriyama, M. Nakahata, S. Nakayama, R. A. Wendell, H. Sekiya, M. Shiozawa, Y. Suzuki, A. Takeda, Y. Takenaga, K. Ueno, T. Yokozawa, H. Kaji, T. Kajita, K. Kaneyuki, K. P. Lee, K. Okumura, T. McLachlan, L. Labarga, E. Kearns, J. L. Raaf, J. L. Stone, L. R. Sulak, M. Goldhaber, K. Bays, G. Carminati, W. R. Kropp, S. Mine, A. Renshaw, M. B. Smy, H. W. Sobel, K. S. Ganezer, J. Hill, W. E. Keig, J. S. Jang, J. Y. Kim, I. T. Lim, J. B. Albert, K. Scholberg, C. W. Walter, T. Wongjirad, T. Ishizuka, S. Tasaka, J. G. Learned, S. Matsuno, S. N. Smith, T. Hasegawa, T. Ishida, T. Ishii, T. Kobayashi, T. Nakadaira, K. Nakamura, K. Nishikawa, Y. Oyama, K. Sakashita, T. Sekiguchi, T. Tsukamoto, A. T. Suzuki, Y. Takeuchi, K. Ieki, M. Ikeda, H. Kubo, A. Minamino, A. Murakami, T. Nakaya, Y. Fukuda, K. Choi, Y. Itow, G. Mitsuka, M. Miyake, P. Mijakowski, J. Hignight, J. Imber, C. K. Jung, I. Taylor, C. Yanagisawa, H. Ishino, A. Kibayashi, Y. Koshio, T. Mori, M. Sakuda, J. Takeuchi, Y. Kuno, S. B. Kim, H. Okazawa, Y. Choi, K. Nishijima, M. Koshiba, Y. Totsuka,

M. Yokoyama, K. Martens, L. Marti, Y. Obayashi, M. R. Vagins, S. Chen, H. Sui, Z. Yang, H. Zhang, K. Connolly, M. Dziomba, and R. J. Wilkes, *Search for Proton Decay via* $p \to \nu K^+$ *using 260 kiloton·year data of Super-Kamiokande*, ArXiv e-prints (2014).

[116] S. A. Thomas, F. B. Abdalla, and O. Lahav, *Upper Bound of 0.28 eV on Neutrino Masses from the Largest Photometric Redshift Survey*, Physical Review Letters **105** (2010), no. 3, 031301.

[117] D. Tody, *IRAF in the Nineties*, Astronomical Data Analysis Software and Systems II (R. J. Hanisch, R. J. V. Brissenden, and J. Barnes, eds.), Astronomical Society of the Pacific Conference Series, vol. 52, January 1993, p. 173.

[118] J. A. Tyson, R. A. Wenk, and F. Valdes, *Detection of systematic gravitational lens galaxy image alignments - Mapping dark matter in galaxy clusters*, ApJ **349** (1990), L1–L4.

[119] K. Umetsu, E. Medezinski, M. Nonino, J. Merten, M. Postman, M. Meneghetti, M. Donahue, N. Czakon, A. Molino, S. Seitz, D. Gruen, D. Lemze, I. Balestra, N. Benítez, A. Biviano, T. Broadhurst, H. Ford, C. Grillo, A. Koekemoer, P. Melchior, A. Mercurio, J. Moustakas, P. Rosati, and A. Zitrin, *CLASH: Weak-lensing Shear-and-magnification Analysis of 20 Galaxy Clusters*, ApJ **795** (2014), 163.

[120] J.-P. Uzan, *Varying Constants, Gravitation and Cosmology*, Living Reviews in Relativity **14** (2011), 2.

[121] M.-P. Véron-Cetty and P. Véron, *A catalogue of quasars and active nuclei: 13th edition*, A&A **518** (2010), A10.

[122] A. Vikhlinin, A. V. Kravtsov, R. A. Burenin, H. Ebeling, W. R. Forman, A. Hornstrup, C. Jones, S. S. Murray, D. Nagai, H. Quintana, and A. Voevodkin, *Chandra Cluster Cosmology Project III: Cosmological Parameter Constraints*, ApJ **692** (2009), 1060–1074.

[123] A. von der Linden, M. T. Allen, D. E. Applegate, P. L. Kelly, S. W. Allen, H. Ebeling, P. R. Burchat, D. L. Burke, D. Donovan, R. G. Morris, R. Blandford, T. Erben, and A. Mantz, *Weighing the Giants - I. Weak-lensing masses for 51 massive galaxy clusters: project overview, data analysis methods and cluster images*, MNRAS **439** (2014), 2–27.

[124] D. Walsh, R. F. Carswell, and R. J. Weymann, *0957 + 561 A, B - Twin quasistellar objects or gravitational lens*, Nature **279** (1979), 381–384.

[125] Z. L. Wen and J. L. Han, *Galaxy Clusters at High Redshift and Evolution of Brightest Cluster Galaxies*, ApJ **734** (2011), 68.

[126] Z. L. Wen, J. L. Han, and F. S. Liu, *Galaxy Clusters Identified from the SDSS DR6 and Their Properties*, ApJS **183** (2009), 197–213.

[127] ______, *Erratum: "Galaxy Clusters Identified from the Sloan Digital Sky Survey DR6 and their Properties"*, ApJS **187** (2010), 272–273.

[128] D. Wittman, W. Dawson, and B. Benson, *Shedding light on the matter of Abell 781*, MNRAS **437** (2014), 3578–3585.

[129] D. Wittman, I. P. Dell'Antonio, J. P. Hughes, V. E. Margoniner, J. A. Tyson, J. G. Cohen, and D. Norman, *First Results on Shear-selected Clusters from the Deep Lens Survey: Optical Imaging, Spectroscopy, and X-Ray Follow-up*, ApJ **643** (2006), 128–143.

[130] D. M. Wittman, J. A. Tyson, I. P. Dell'Antonio, A. Becker, V. Margoniner, J. G. Cohen, D. Norman, D. Loomba, G. Squires, G. Wilson, C. W. Stubbs, J. Hennawi, D. N. Spergel, P. Boeshaar, A. Clocchiatti, M. Hamuy, G. Bernstein, A. Gonzalez, P. Guhathakurta, W. Hu, U. Seljak, and D. Zaritsky, *Deep lens survey*, Survey and Other Telescope Technologies and Discoveries (J. A. Tyson and S. Wolff, eds.), Society of Photo-Optical Instrumentation Engineers (SPIE) Conference Series, vol. 4836, December 2002, pp. 73–82.

[131] J.-H. Woo, C. M. Urry, R. P. van der Marel, P. Lira, and J. Maza, *Black Hole Masses and Host Galaxy Evolution of Radio-Loud Active Galactic Nuclei*, ApJ **631** (2005), 762–772.

[132] C. O. Wright and T. G. Brainerd, *Gravitational Lensing by NFW Halos*, ApJ **534** (2000), 34–40.

[133] L. Xu and Y Chang, *Equation of state of dark matter after Planck data*, Phys. Rev. D **88** (2013), 127301.

[134] A. Zitrin, Y. Rephaeli, S. Sadeh, E. Medezinski, K. Umetsu, J. Sayers, M. Nonino, A. Morandi, A. Molino, N. Czakon, and S. R. Golwala, *Cluster-cluster lensing and the case of Abell 383*, MNRAS **420** (2012), 1621–1629.